# From above, see below: High-resolution detection of subsurface anomalies from air and space






Major Adam Morley RE
St Cross College
University of Oxford

A thesis submitted for the degree of
*Doctor of Philosophy*
Michaelmas 2025

# Author's Declaration

I declare that the work in this thesis was carried out in accordance with the University of Oxford's Regulations and Code of Practice for Research Degree Programmes. Unless indicated by specific references, the work herein is the result of the candidate's own independent research, performed in the Department of Earth Sciences, University of Oxford, between 1 October 2022 and 30 November 2025.

Adam Morley

# Abstract

Recent advances in spatial, spectral, radiometric and temporal resolution reveal new opportunities and innovative ways to remotely sense the Earth's subsurface from air and space. In this thesis, I explore the tangible, subsurface detection capabilities of high-resolution and very-high-resolution (VHR) datasets and in doing so, I devise a series of new and remote, subsurface detection regimes.

To begin, I categorise the ground indicators and potential field characteristics of a subsurface anomaly, before reviewing over seventy air and space subsurface detection techniques using: photogrammetry, multispectral and hyperspectral imaging, thermal infrared, synthetic aperture radar (SAR), airborne light detection and ranging (LiDAR), airborne gravity and aeromagnetics. I then use geophysical observations from a shallow, Iron Age tunnel (fogou) in the ancient settlement of Carn Euny in Cornwall, UK, to statistically validate and reprioritise the detection efficiency of several broadband vegetation indices (VIs) in high-resolution, multispectral satellite imagery. With the assistance of false colour composites (FCCs) and Sobel edge detection filters, a multispectral image processing workflow is produced to detect shallow, subsurface features in temperate, vegetated terrain. Using statistical thresholds, VI reflection profiles from this workflow are analysed, revealing an underground passage between the Cistercian abbey of Aunay and a medieval grange in Normandy, France. The workflow is then combined with a new, LiDAR hillshade sequence to reveal the location of several near-surface features in the abbey's largest field enclosure. When compared to an eighteenth-century site plan, these subsurface anomalies reveal the structural features of a seventeenth-century garden. High-resolution LiDAR elevation differencing, average elevation-change profiles, high-resolution multispectral imagery analyses and VHR thermal observations are then used, in a multi-sensor approach, to detect and interpret statistically abnormal, linear subsurface features around Glastonbury Tor in Somerset, UK.

Relationships between spectral behaviour and near-surface geophysical properties demonstrate the detection potential of the Red/Blue reflectance ratio. In temperate, vegetated terrain, the Iron Oxide index, Soil Salinity Index 7 (SI7), the Structure Insensitive Pigment Index (SIPI), and their gradient magnitudes, accentuate anomalous iron oxide concentrations, soil salinity levels and chlorophyll production in the ground above a subsurface feature. Their average reflection profiles, with statistical benchmarks, are also capable of revealing the location of subsurface anomalies beneath linear features like field boundaries. Similarly, high-resolution datasets from various sensor types permit the formation of average change profiles across linear, subsurface anomalies, exposing those with abnormal ground behaviour. For multispectral detection, it is best to observe during or after adverse weather events; for LiDAR elevation differencing, observe at different times of year and several years apart; for heat retention analyses, observe during extreme periods of ground warming and ground cooling. Only then will you begin to see below, from above.

# Acknowledgements

Studying for the degree of Doctor of Philosophy at the University of Oxford, and producing this thesis in three years, has been a truly rewarding experience. However, I have not performed this journey in isolation, nor have I steered the ship single-handedly.

Underpinning the success of any scientific research is a need for good-quality data, and in support of this integrated thesis, I have been blessed. All high-resolution panchromatic and multispectral satellite imagery were kindly supplied by Maxar Technologies Inc. (now rebranded to Vantor), for which I am so very grateful. In particular, I would like to thank Maxar's Paulo Godinho for making this happen. I would also like to thank the Institut National de l'Information Géographique et Forestière (IGN) in France, and the UK Environment Agency, for kindly providing the necessary high and very-high-resolution (VHR) elevation data, and Bristol Water for their pipeline dataset of Glastonbury.

In support of site access, I would like to thank Historic England South West for approving the conduct of a geophysical survey in Carn Euny Ancient Village. For accommodating numerous pedestrian and geophysical surveys in the private, medieval estate of La Garenne, a special thanks goes to the landowners in Normandy, France; without their engagement and dedication, the research on Aunay Abbey and its environs would not have been possible. In equal measure, I am also grateful to the National Trust for approving a geophysical survey and a drone survey in and above the fields north of Glastonbury Tor.

Away from the field, my location for reading, writing, analysing and evaluating must not go unnoticed, so thank you Oxford for being such a wonderful city and such a resourceful university. In particular, thank you Bodleian Libraries for your professional services and thank you Nick Millea (Bodleian map curator), for sourcing an eighteenth-century site plan of Aunay Abbey in Normandy, France.

Even so, none of this would have been possible without funding. For DPhil funding, I thank the British Army External Placements (Academic) programme; what an opportunity this has been. For fieldwork funding, I thank the Burdett-Coutts Foundation, the Centre for Observation and Modelling of Earthquakes, Volcanoes and Tectonics (COMET), the Near Surface Geophysics Group (NSGG) and St Cross College. Without their financial support, site visits, fieldwork and subsurface verification procedures would not have been possible.

Finally, and most importantly, I want to thank my crewmates. For geophysical expertise, a special thanks must go to Dr Antony Butcher from the University of Bristol and Mr Matthew Bunting, the

Director of GPR Team. Without Antony's assistance, I would not have been able to perform gravity or resistivity surveys, and without Matthew's investment, I would not have been able to use ground penetrating radar (GPR). I would also like to thank James Fleming and Oliver Savill, two accomplished drone operators from AtkinsRéalis. Their planning, preparation and flying aptitude prior to and during an airborne survey around Glastonbury Tor was exemplary. It also goes without saying that I am eternally grateful for meeting and collaborating with the author of 'Glastonbury Underground', Mr Geoff Stray; his book inspired a chapter in this thesis and his knowledge of Glastonbury, past and present, has been so very useful. I would also like to thank Tesfahiwet for our lunches, Amanda for the college coffee, and Sasha for our regular conversations on tunnels, monks and pilgrims.

Now for those most important. To begin, I must thank my supervisors Mike, David and Tamsin for their wisdom, their humility and their steady, guiding hand. Mike, thank you for believing in me and thank you for the opportunity and the freedoms to design, innovate and prioritise my own research. David and Tamsin, thank you so much for your timely advice, your sound feedback and your expert reviewing and editing – it made all the difference. I would also like to thank my parents for their outstanding support and encouragement. In particular, I would like to thank my Dad for his genuine interest in this research and his incredulous, unwavering support in the field. I could not have wished for a better field assistant or a better friend in wet, muddy tunnels and dry, sunny fields. And finally, my biggest thank you goes to my wife Beth, and my two bean heads Alma and Wilf. Research is less fun if children don't habitually sneak into the study and scare the living daylights out of their father whilst he works. Research is also less fun if you don't have an amazing wife by your side. One who is accepting and supportive of time away on fieldwork, early starts and late finishes, and typing in bed. And even when all of this happens at once, the amazing wife still brings the best lunches to the study the next day. I had a very fun time researching this thesis; I am very lucky.

“This is the real secret of life - to be completely
engaged with what you are doing in the here and now.
And instead of calling it work, realise it is play”
- Alan Watts -

# Table of Contents


Author's Declaration ii
Abstract iii
Acknowledgements iv
List of Figures xii
List of Tables xvi
List of Abbreviations xviii

**1 Introduction 1**
1.1 Remote sensing the subsurface ..... 1
1.2 Advances in remote sensing ..... 3
1.3 Motivation and aims ..... 5
1.4 Thesis outline ..... 6

**2 Detecting shallow subsurface anomalies with airborne and spaceborne remote sensing: A review 8**
2.1 Introduction ..... 9
2.2 Motivations for remotely sensing the subsurface ..... 11
2.2.1 Archaeological prospecting ..... 11
2.2.2 Environmental risk mitigation ..... 12
2.2.3 Natural resource exploration ..... 13
2.2.4 Defence and security ..... 13
2.2.5 Speleological research ..... 14
2.3 Characterisation of subsurface anomalies ..... 15
2.3.1 Visual identification ..... 15
2.3.2 Soil matrix irregularity ..... 15
2.3.3 Anomalous groundwater behaviour ..... 16
2.3.4 Surface elevation change ..... 16
2.3.5 Heat retention anomaly ..... 17
2.3.6 Subsurface density change ..... 18
2.3.7 Magnetic field variation ..... 18
2.4 Remote sensing the subsurface: overview ..... 19
2.5 Visual identification ..... 20
2.5.1 Using photogrammetry ..... 20
2.5.2 Using multispectral imaging ..... 22
2.5.3 Using hyperspectral imaging ..... 24
2.5.4 Using airborne LiDAR ..... 24

2.5.5 Using SAR ..... 25
2.6 Detecting soil matrix irregularities ..... 27
2.6.1 Using multispectral imaging ..... 27
2.6.2 Using hyperspectral imaging ..... 30
2.6.3 Using SAR ..... 32
2.7 Detecting anomalous groundwater behaviour ..... 34
2.7.1 Using photogrammetry and multispectral imaging ..... 34
2.7.2 Using thermal infrared ..... 34
2.7.3 Using hyperspectral imaging ..... 35
2.7.4 Using airborne LiDAR ..... 35
2.7.5 Using SAR ..... 35
2.8 Detecting surface elevation change ..... 36
2.8.1 Using photogrammetry ..... 36
2.8.2 Using airborne LiDAR ..... 37
2.8.3 Using SAR ..... 39
2.9 Detecting heat retention anomalies ..... 40
2.9.1 Using thermal infrared ..... 40
2.9.2 Using hyperspectral imaging ..... 45
2.10 Detecting subsurface density anomalies ..... 46
2.10.1 Using airborne gravity ..... 46
2.10.2 Using SAR ..... 47
2.11 Detecting magnetic field variation ..... 49
2.11.1 Using aeromagnetics ..... 49
2.11.2 Using airborne electromagnetics ..... 51
2.12 Verifying remote sensing observations of the subsurface ..... 52
2.12.1 Ground reconnaissance ..... 52
2.12.2 Field spectroscopy ..... 54
2.12.3 Geophysical survey ..... 54
2.12.4 Integrated approach ..... 55
2.13 Future perspectives ..... 56
2.13.1 Very-high-resolution (VHR) time series analyses ..... 57
2.13.2 Multi-branch convolutional neural networks (CNNs) on multi-sensor data ..... 57
2.13.3 Active remote sensing in variable potential fields ..... 58
2.14 Concluding remarks ..... 58

**3 Using gravity, ground penetrating radar and vegetation indices to derive a multispectral recipe for subsurface detection 60**
3.1 Introduction ..... 61
3.2 Control Site ..... 65

3.3 Methodology ..... 66
3.3.1 Image acquisition ..... 66
3.3.2 Validating Vegetation Indices (VIs) ..... 67
3.3.2.1 Correlation with gravity ..... 68
3.3.2.2 Correlation with Ground Penetrating Radar (GPR) ..... 69
3.3.3 Subsurface detection ..... 71
3.3.3.1 Using False Colour Composites (FCCs) ..... 71
3.3.3.2 Using Edge Detection ..... 71
3.4 Results ..... 72
3.4.1 Vegetation Index (VI) selection using gravity ..... 72
3.4.2 VI validation using GPR ..... 74
3.4.3 Subsurface detection – FCC analysis ..... 75
3.4.4 Subsurface detection – Edge Detection analysis ..... 77
3.5 Discussion ..... 79
3.5.1 Subsurface detection workflow ..... 84
3.5.1.1 Design ..... 84
3.5.1.2 Test ..... 85
3.6 Concluding remarks ..... 88

**4 Remote sensing of the subsurface between a Cistercian abbey and a medieval grange 91**
4.1 Introduction ..... 92
4.2 Aunay Abbey ..... 94
4.3 Methodology ..... 97
4.3.1 Data acquisition ..... 97
4.3.1.1 Multispectral imagery ..... 97
4.3.1.2 Light detection and ranging (LiDAR) digital surface model (DSM) ..... 98
4.3.2 Inspecting the Abbey-Grange Boundary ..... 98
4.3.3 Inspecting the Abbey Field ..... 100
4.3.3.1 With multispectral imagery ..... 101
4.3.3.2 With airborne LiDAR ..... 102
4.4 Results ..... 103
4.4.1 Abbey-Grange Boundary ..... 103
4.4.1.1 East Wall ..... 104
4.4.1.2 North Wall ..... 106
4.4.2 Abbey Field ..... 108
4.4.2.1 Using multispectral False Colour Composites (FCCs) ..... 108
4.4.2.2 Using multispectral Edge Detection ..... 112
4.4.2.3 Using LiDAR hillshade analysis ..... 114
4.5 Interpreting the Abbey Field ..... 116

4.6 Discussion ..... 120
4.6.1 Tunnel detection ..... 120
4.6.2 Garden detection ..... 123
4.7 Concluding remarks ..... 126

**5 Remote detection of linear subsurface features around Glastonbury Tor: A multi-sensor approach 129**
5.1 Introduction ..... 130
5.2 Methodology ..... 132
5.2.1 Light Detection and Ranging (LiDAR) elevation differencing ..... 133
5.2.2 Multispectral analysis ..... 134
5.2.3 Thermal analysis ..... 135
5.2.4 Electrical Resistivity Tomography (ERT) ..... 135
5.3 Results ..... 136
5.3.1 LiDAR ..... 137
5.3.2 Multispectral ..... 138
5.3.3 Thermal ..... 140
5.4 Interpretation ..... 141
5.4.1 Linear Anomaly 4 (LA4) ..... 142
5.4.2 Linear Anomaly 6 (LA6) ..... 144
5.5 Discussion ..... 145
5.6 Concluding remarks ..... 149

**6 Conclusions 151**
6.1 Summary of chapter conclusions ..... 154
6.1.1 Detecting shallow subsurface anomalies with airborne and spaceborne remote sensing: A review ..... 154
6.1.2 Using gravity, ground penetrating radar and vegetation indices to derive a multispectral recipe for subsurface detection ..... 155
6.1.3 Remote sensing of the subsurface between a Cistercian abbey and a medieval grange ..... 156
6.1.4 Remote detection of linear subsurface features around Glastonbury Tor: A multi-sensor approach ..... 157
6.2 Summary of algorithms and workflows ..... 157
6.2.1 Algorithms ..... 157
6.2.2 Workflows ..... 158
6.3 Future work ..... 160
6.3.1 With different high-resolution remote detection regimes ..... 160
6.3.2 At other sites ..... 161
6.4 Final word ..... 162

**Appendices** **164**

**A Major spaceborne imaging sensors for passive Earth observation** **165**
**B Major spaceborne imaging sensors for active Earth observation** **170**
**C Search strategy and paper statistics** **173**
**D Principles of air and space remote sensing** **175**
**E Maxar image metadata for Carn Euny** **180**
**F Broadband vegetation indices** **181**
**G Modelling gravity across Carn Euny's fogou** **185**
**H Maxar image metadata for Aunay Abbey** **186**
**J Example catalogue of black, grey and white (BGW) graded imagery using multispectral FCCs, edge detection and LiDAR hillshade analysis** **187**
**K Multispectral image processing workflow** **189**
**M Electrical Resistivity Tomography (ERT) profiles** **191**

**References** **194**

# List of Figures


1.1 Examples of anthropogenic and geologic subsurface anomalies ..... 2
1.2 Spatial resolution of passive spaceborne imaging sensors since 1972 ..... 3
1.3 Spatial resolution of active spaceborne imaging sensors since 1978 ..... 4
1.4 Location map showing sites used in this research ..... 7

2.1 Location map showing subterranean sites reviewed ..... 11
2.2 Motivations for remote sensing the subsurface ..... 12
2.3 Anomalous ground characteristics from three general subsurface structures ..... 17
2.4 Bubble chart showing type of sensor used to detect subsurface anomaly characteristics in peer-reviewed publications ..... 20
2.5 Example of using aerial photography to detect near-surface anomalies ..... 21
2.6 Soil detection results from tunnel excavations long USA-Mexico border using a four-layer convolutional neural network (CNN) ..... 23
2.7 SAR backscatter anomaly from a partially buried archaeological structure ..... 26
2.8 Temporal variation in Normalised Difference Vegetation Index (NDVI) at Alampra in Cyprus ..... 28
2.9 Eighteen vegetation indices ranked from most to least effective using information theory and hyperspectral data of Selinunte in Sicily ..... 31
2.10 Detecting sinkholes in a forested karst landscape in Slovak National Park using airborne LiDAR ..... 36
2.11 Airborne LiDAR point-cloud data of the ancient Maya site of Caracol in Belize ..... 38
2.12 Temperature anomaly map of the La Pacana caldera geothermal field in Chile ..... 41
2.13 Four airborne thermal images of an 18th Century buried building foundation in the Enfield Shaker Village in New Hampshire, US ..... 44
2.14 Range-line SAR echographic tomography profile in Somma Vesuvius ..... 48
2.15 Image map showing faults, contacts and dykes associated with gold mineralisation beneath Wadi El-Saqia study region in Central Eastern Desert, Egypt ..... 50
2.16 A cave opening inside a sinkhole in the Las Cuevas study site in Belize ..... 53
2.17 Principal geophysical methods and the subsurface properties they exploit ..... 55

3.1 Anomalous ground characteristics from three general subsurface structures ..... 62
3.2 Carn Euny Ancient Village and Iron Age fogou ..... 66
3.3 Residual gravity survey and ground penetrating radar (GPR) survey of control site above Iron Age fogou ..... 69
3.4 Normalised bouguer anomaly and normalised vegetation index (VI) profiles along A-A' for all VIs with correlation coefficients > |0.7| ..... 73

3.5 Image similarity assessment using the Enhanced Vegetation Index (EVI) image subset and a GPR C-scan of the control site ..... 74
3.6 GPR reference image and example false colour composites (FCCs) from a six-layer multiband raster built for subsurface detection ..... 77
3.7 Edge detection analysis of the gradient magnitude (Gmag) Soil Salinity Index 7 (SI7) image subset ..... 79
3.8 Variation in Red, Green, Blue, Near Infrared (NIR) and [Red-Blue] reflectance values from smooth stalked meadow grass above Carn Euny's fogou ..... 81
3.9 Temporal spectral analysis of Iron Oxide and the Structure Insensitive Pigment Index (SIPI) "on" and "off" the fogou gravity anomaly in Carn Euny ..... 83
3.10 Multispectral image processing workflow for shallow subsurface detection in a temperate landscape with cool-season vegetation ..... 85
3.11 Applying the high-resolution multispectral subsurface detection workflow on two experimental sites ..... 86

4.1 Tintern Abbey and nearby tunnel in Wales, UK ..... 92
4.2 Location of Aunay Abbey, La Garenne, the Abbey Field and the Abbey-Grange boundary wall in Normandy, France ..... 96
4.3 Location of spatial profiles along the Abbey-Grange boundary wall in northeastern corner of Abbey Field ..... 99
4.4 Image processing workflow used to inspect high-resolution multispectral satellite imagery of the Abbey Field ..... 102
4.5 Multi-directional and multi-altitude hillshade sequence used to analyse a very-high-resolution (VHR) light detection and ranging (LiDAR) digital surface model (DSM) of the Abbey Field ..... 103
4.6 Average subsurface detection index profiles along the east wall of the Abbey-Grange Boundary (E-E') and a stacked column chart revealing reflection outliers along E-E' ..... 105
4.7 Average subsurface detection index profiles along the north wall of the Abbey-Grange Boundary (N-N') and a stacked column chart revealing reflection outliers along N-N' ..... 107
4.8 Subsurface anomalies detected in the Abbey Field using FCCs from the six-layer image stack of subsurface detection indices ..... 111
4.9 Subsurface anomalies detected in the Abbey Field using Sobel edge detection filters on subsurface detection indices in the six-layer image stack ..... 113
4.10 LiDAR hillshade analysis and micro-relief anomalies in the Abbey Field ..... 116
4.11 Subsurface anomalies detected beneath the Abbey Field using high-resolution multispectral satellite imagery and VHR airborne LiDAR ..... 117
4.12 An eighteenth-century garden plan of the Abbey Field and the subsurface features found using multispectral satellite imagery and airborne LiDAR ..... 119

4.13 Rubble stone tunnel found under east wall of Abbey-Grange boundary in the grounds of Aunay Abbey and La Garenne, Normandy, France ..... 122
4.14 Comparison between concealed garden features in Abbey Field and garden features mapped in Aunay Abbey's eighteenth-century garden plan..... 125

5.1 Glastonbury Tor and its environs, including the Tor's border fields, soil coverage and the 2016 Lypyatt Lane "well house" excavation ..... 131
5.2 Airborne thermal survey and electrical resistivity tomography (ERT) survey of border fields north of Glastonbury Tor..... 136
5.3 Results of LiDAR elevation differencing in border fields north of Glastonbury Tor ..... 137
5.4 Average elevation-change profiles across each linear anomaly (LA) north of Glastonbury Tor ..... 139
5.5 Photographs and high-resolution multispectral observations of statistically anomalous linear elevation-change anomalies in fields north of Glastonbury Tor..... 140
5.6 Red-Green-Blue (RGB) and thermal imagery of linear anomaly 4 (LA4) and linear anomaly 6 (LA6); taken with a DJI M300 rotary drone ..... 141
5.7 Averaged and normalised elevation-change profile, vegetation indices and relative heat loss profile across LA4, superimposed with 2D ERT profile..... 143
5.8 Averaged and normalised elevation-change profile, vegetation indices and relative heat loss profile across LA6, superimposed with 2D ERT profile..... 145
5.9 Near-surface inspection along Field 2, north of Glastonbury Tor, using 2D ERT and GPR ..... 148

6.1 Generalised data processing workflow for high and VHR subsurface detection..... 154
6.2 Word cloud showing most used words in the abstracts from Chapters 2, 3, 4 and 5 ..... 163

A1 Spatial resolution of passive spaceborne imaging sensors since 1972 ..... 169

B1 Spatial resolution of active spaceborne imaging sensors since 1978..... 172

C1 Three-dimensional reference matrix for documenting peer-reviewed publications and paper statistics..... 174

D1 Information graphic showing principles of air and space photogrammetry ..... 175
D2 Information graphic showing principles of multispectral imaging ..... 176
D3 Information graphic showing principles of thermal infrared imaging ..... 176
D4 Information graphic showing principles of hyperspectral imaging..... 177
D5 Information graphic showing principles of airborne gravity ..... 177
D6 Information graphic showing principles of airborne magnetics..... 178

D7 Information graphic showing principles of airborne light detection and ranging (LiDAR).....178
D8 Information graphic showing principles of synthetic aperture radar (SAR).....179

G1 Modelling residual gravity over the fogou in Carn Euny Ancient Village .....185

J1 Catalogue of imagery examples featuring black, grey and white (BGW) subsurface detection ratings with multispectral FCCs, Sobel edge detection raster images and hillshaded DSM FCCs.....188

K1 Multispectral image processing workflow used to inspect LA4 in Field 2 and LA6 in Field 9, north of Glastonbury Tor.....190

M1 Location and orientation of ERT profiles across LA4 and LA6 .....191
M2 2D ERT profiles across LA4 and LA6 .....192

# List of Tables


1.1 Subsurface anomaly characteristics used to detect and verify the location of subsurface anomalies ..... 6

2.1 Ground indicators, potential field characteristics and typical field observations generated by a subsurface anomaly ..... 19
2.2 Airborne and spaceborne remote sensing techniques used for visual identification ..... 27
2.3 Airborne and spaceborne remote sensing techniques used to detect soil matrix irregularities ..... 33
2.4 Airborne and spaceborne remote sensing techniques used to detect anomalous groundwater behaviour ..... 37
2.5 Airborne and spaceborne remote sensing techniques used to detect surface elevation change ..... 40
2.6 Airborne and spaceborne remote sensing techniques used to detect heat retention anomalies ..... 45
2.7 Airborne and spaceborne remote sensing techniques used to detect subsurface density anomalies ..... 48
2.8 Airborne and spaceborne remote sensing techniques used to detect magnetic field variation ..... 52

3.1 Image similarity results for pansharpened image subsets of high-performing vegetation indices and ground penetrating radar (GPR) C-scan of the control site at Carn Euny ..... 75
3.2 Image similarity results for the 20 false colour composites (FCCs) and the 0.48 m deep GPR C-scan of the control site ..... 76
3.3 Image similarity results for greyscale, Sobel edge detection filtered VI image subsets and the 0.48 m deep GPR C-scan of the control site ..... 78

4.1 Percentage of reflection outliers from average subsurface detection index profiles along the east wall, E-E', of the Abbey-Grange Boundary ..... 104
4.2 Percentage of reflection outliers from average subsurface detection index profiles along the north wall, N-N', of the Abbey-Grange Boundary ..... 106
4.3 Black, Grey and White (BGW) subsurface anomaly detection rating of 20 FCCs of the Abbey Field, from each of six different high-resolution multispectral satellite images ..... 109

4.4 BGW subsurface anomaly detection rating of six Sobel edge detection VI raster images of the Abbey Field, from each of six different high-resolution multispectral satellite images....112
4.5 BGW subsurface anomaly detection rating of 20 hillshaded digital surface model (DSM) FCCs of the Abbey Field, taken from the six-layer DSM stack and repeated for nine different sun altitudes....115

A1 Major spaceborne imaging sensors for passive Earth observation, ordered by launch year....165

B1 Major spaceborne imaging sensors for active Earth observation, ordered by launch year....170

E1 Maxar high-resolution image bundles of Carn Euny used in this research, with supporting metadata; ordered by image acquisition day and month....180

F1 Broadband vegetation indices (VIs) assessed in this research, accompanied by VI abbreviations, VI equations, example references and correlation coefficients with gravity across the fogou in Carn Euny....182

H1 Maxar high-resolution image bundles of Aunay Abbey used in this research, with supporting metadata; ordered by image acquisition day and month....186

# List of Abbreviations

| | |
|---|---|
| **1D** | One Dimension / One Dimensional |
| **2D** | Two Dimensions / Two Dimensional |
| **3D** | Three Dimensions / Three Dimensional |
| **AD** | Anno Domini |
| **A-DInSAR** | Advanced-Differential InSAR |
| **AOI** | Area of Interest |
| **ARD** | Analysis Ready Data |
| **AS** | Analytic Signal |
| **BBA** | Bundle Block Adjustment |
| **BC** | Before Christ |
| **BGW** | Black-Grey-White |
| **CBT** | Cross Border Tunnel |
| **CCD** | Coherent Change Detection |
| **CCE** | Candidate Cave Entrance |
| **CET** | Centre for Exploration Targeting |
| **CNN** | Convolutional Neural Networks |
| **COMET** | Centre for Observation and Modelling of Earthquakes, Volcanoes and Tectonics |
| **COOP** | Crustal Onshore/Offshore Project |
| **CSV** | Comma-Separated Value |
| **CTBTO** | Comprehensive Nuclear-Test-Ban Treaty Organisation |
| **DEM** | Digital Elevation Model |
| **DGPS** | Differential Global Positioning System |
| **DInSAR** | Differential InSAR |
| **DJI** | Da-Jiang Innovations |
| **DSM** | Digital Surface Model |
| **DST** | Dead Sea Transform |
| **DTM** | Digital Terrain Model |
| **EA** | Environment Agency |
| **EM** | Electromagnetic / Electromagnetism |
| **ERDAS** | Earth Resources Data Analysis System |
| **ERT** | Electrical Resistivity Tomography |
| **ESA** | European Space Agency |
| **EVI** | Enhanced Vegetation Index |
| **FCC** | False Colour Composite |
| **FTG** | Full Tensor Gradiometry |

| | |
|---|---|
| **FVD** | First-order Vertical Derivative |
| **GAFEM** | Ground-Airborne Frequency domain Electromagnetic Method |
| **GGI** | Gravity Gradient Instruments |
| **GIS** | Geographic Information System |
| **GLCM** | Grey Level Co-occurrence Matrix |
| **Gmag** | Gradient Magnitude |
| **GNN** | Graph Neural Network |
| **GNSS** | Global Navigation Satellite System |
| **GPR** | Ground Penetrating Radar |
| **GPS** | Global Positioning System |
| **HPF** | High-Pass Filter |
| **HTEM** | Helicopter-borne Time-domain Electromagnetic Method |
| **ICD** | Incoherent Change Detection |
| **IED** | Improvised Explosive Device |
| **IGN** | l'Information Géographique et Forestière |
| **IMU** | Inertial Measurement Unit |
| **InSAR** | Interferometric Synthetic Aperture Radar |
| **IO** | Iron Oxide |
| **IQR** | Interquartile Range |
| **IRIS** | Incorporated Research Institutions for Seismology |
| **LA** | Linear Anomaly |
| **LiDAR** | Light Detection and Ranging |
| **LRM** | Local Relief Model |
| **LULC** | Land Use / Land Cover |
| **LWIR** | Longwave Infrared |
| **MATLAB** | MATrix LABoratory |
| **MEQ** | Mausoleum of the Emperor Qinshihuang |
| **MS** | Multispectral |
| **MSL** | Mean Sea Level |
| **NASA** | National Aeronautics and Space Administration |
| **NDVI** | Normalised Difference Vegetation Index |
| **NDWI** | Normalized Difference Water Index |
| **NIR** | Near Infrared |
| **NND** | Nearest Neighbour Diffusion |
| **NOI** | Negative Openness Index |
| **NSGG** | Near Surface Geophysics Group |
| **OBIA** | Object-Based Image Analysis |
| **PCA** | Principal Component Analysis |
| **PDF** | Probability Density Function |
| **POI** | Positive Openness Index |

| | |
|---|---|
| **Q1** | First Quartile |
| **Q3** | Third Quartile |
| **REIP** | Red Edge Inflection Point |
| **RGB** | Red-Green-Blue |
| **RMSE** | Root Mean Square Error |
| **SAM** | Spectral Angle Mapper |
| **SAR** | Synthetic Aperture Radar |
| **SATEM** | Semi-Airborne Transient Electromagnetic Method |
| **SI5** | Soil Sanity Index 5 |
| **SI6** | Soil Salinity Index 6 |
| **SI7** | Soil Salinity Index 7 |
| **SIMAV** | Similarity Average |
| **SIPI** | Structure Insensitive Pigment Index |
| **SMA** | Spectral Mixture Analysis |
| **SR** | Simple Ratio |
| **SRTM** | Shuttle Radar Topography Mission |
| **SSI** | Spectral Separability Index |
| **SSIM** | Structural Similarity Index Measurement |
| **SSIMVAL** | Structural Similarity Index Measurement Value |
| **STC** | Sensitive Time Control |
| **SWIR** | Short-Wave Infrared |
| **TA** | Tilt Angle |
| **TCARI** | Transformed Chlorophyll Absorption in Reflectance Index |
| **TD** | Tilt Derivative |
| **THD** | Total Horizontal Derivative |
| **TIFF** | Tagged Image File Format |
| **TIR** | Thermal Infrared |
| **TOLP** | Take Off and Landing Position |
| **TPI** | Topographic Position Index |
| **TRI** | Topographic Ruggedness Index |
| **UAV** | Unpiloted Aerial Vehicle |
| **VES** | Vertical Electrical Sounding |
| **VHR** | Very High Resolution |
| **VI** | Vegetation Index |
| **VLOS** | Visual Line of Sight |
| **VNIR** | Visible to Near Infrared |
| **WV1** | WorldView-1 |
| **WV2** | WorldView-2 |
| **WV3** | WorldView-3 |
| **WV4** | WorldView-4 |

# 1

# Introduction

## 1.1 Remote sensing the subsurface

Advances in airborne and spaceborne platform and sensor technologies are transforming our ability to remotely sense the Earth's subsurface. Modern imaging systems now provide extensive spatial coverage, frequent data acquisition, and exceptionally high spatial, spectral, radiometric and temporal resolution, expediting the detection of near-surface anomalies with impressive accuracy. These capabilities offer unprecedented opportunities for numerous disciplines worldwide, including archaeology, environmental management, natural resource exploration, defence and security, and speleological research, particularly in regions that are inaccessible, hazardous or unknown.

By definition, remote sensing is the practice of obtaining information about the Earth's land and water surfaces from images acquired with a top-down perspective, using reflected or emitted electromagnetic (EM) radiation (Campbell et al., 2023). In this thesis, I review, design, apply, analyse and evaluate the utility of airborne and spaceborne remote sensing in the detection of shallow subsurface anomalies. For the purpose of this research, the subsurface is defined as the region immediately below the Earth's surface, extending tens or hundreds of metres below ground level. However, the suite of techniques I employ and the workflows I devise predominantly focus on the detection of features in the *near surface*, defined in this thesis as being the first 10 m below the Earth's surface.

Much of the work in this thesis refers to 'subsurface anomalies', which are described as below ground causative bodies constituting: 1) different material properties to that of the surrounding soil and rock; 2) a different density; 3) a different magnetic susceptibility. If the subsurface anomaly is geologic, the anomalous structure is usually tens or hundreds of metres deep and tens or hundreds of metres wide, adopting numerous forms like dyke intrusions, ore deposits, volcanic conduits, karstic caves, salt domes, buried valleys, structural faults, fracture zones, granite plutons, shallow hydrocarbon prospects and geothermal reservoirs (Figure 1.1). However, if the subsurface anomaly is anthropogenic, it is generally much shallower and usually found at depths and widths of

1 – 10 m. Anthropogenic subsurface anomalies are broad in scope; common examples include archaeological features, pipelines, drainage systems, tunnels, mines, buried trenches and landfills (Figure 1.1).

The size of these subsurface anomalies is also important, because it governs the spatial resolution needed by the remote sensor prescribed for detection. Therefore, for the purpose of detecting subsurface anomalies from air *and* space, low spatial resolution is considered to be greater than 20 m; medium spatial resolution is 3 – 20 m; high spatial resolution is 0.5 – 3 m; very high spatial resolution is less than 0.5 m. Given the limitations of these spatial resolutions and the size and nature of the subsurface anomalies under detection, I review the use of eight different sensor types. These are: photographic, multispectral, thermal, hyperspectral, synthetic aperture radar (SAR), airborne light detection and ranging (LiDAR), airborne gravity and aeromagnetics. Following the review, I then use high-resolution multispectral imaging sensors, high resolution and very-high-resolution (VHR) LiDAR sensors and a VHR thermal imaging sensor to detect shallow subsurface anomalies.




**Figure 1.1**. Examples of anthropogenic and geologic subsurface anomalies considered in this thesis. Buried anthropogenic features and structures are generally found in the near surface which, in this thesis, is the first 10 m below ground. Geologic subsurface anomalies are typically much deeper, existing tens or hundreds of metres deep.

The motives for remote sensing the subsurface from air and space are considerable. These are discussed comprehensively in the review at Chapter 2, where a number of communities are shown to benefit, including archaeologists, environmental agencies, earth scientists, defence and security personnel, speleologists, and academics worldwide (e.g., Bernatek-Jakiel and Jakiel, 2021; Du et al., 2022; El-Behaedi, 2021; Lasaponara et al., 2016; Mathew et al., 2023; Ottesen et al., 2020; Pisani and De Waele, 2021; Richemond-Barak, 2018; Wynne et al., 2021).

*How* subsurface anomalies are identified from air and space is also a fundamental question. The review in Chapter 2 reveals the various ways and means to achieve this. However, underpinning these detection techniques is one essential concept: shallow structures, features and objects beneath the Earth's surface will produce unique ground characteristics, abnormal surface expressions and anomalous potential fields directly above them (e.g., El-Raouf et al., 2023; Hofierka et al., 2018; Jamaludin et al., 2021; Lasaponara and Masini, 2007; Luo et al., 2019; Scoular et al., 2020). These unique ground indicators and potential field characteristics are used to remotely detect the location of subsurface anomalies (e.g., Abdel Zaher et al., 2018; Barla et al., 2016; Dana Negula et al., 2020; Gaber et al., 2020; Hill et al., 2020; Saha, 2022). I group these distinct subsurface anomaly characteristics into seven categories: 1) visual identification; 2) soil matrix irregularity; 3) anomalous groundwater behaviour; 4) surface elevation change; 5) heat retention anomaly; 6) subsurface density change; 7) magnetic field variation. In Chapter 2, the remote sensing techniques most suitable for the detection of each subsurface anomaly characteristic are tabulated in seven distinct technique tables. Using high-resolution and VHR datasets, and in variable amounts, this thesis seeks the detection of each.

## 1.2 Advances in remote sensing

Technical advances in airborne and spaceborne sensor technology are providing new ways to remotely sense the Earth's subsurface. Fast and frequent image acquisition and high spectral, spatial and radiometric resolution are now allowing spaceborne multispectral imaging systems to detect, with considerable accuracy, the unique ground characteristics of shallow subsurface anomalies (e.g., Luo et al., 2019). For example, Airbus's Pléiades Neo satellite constellation is now capable of acquiring a panchromatic image at 0.3 m spatial resolution and a six-band multispectral image at 1.2 m resolution (Figure 1.2 and Appendix A).

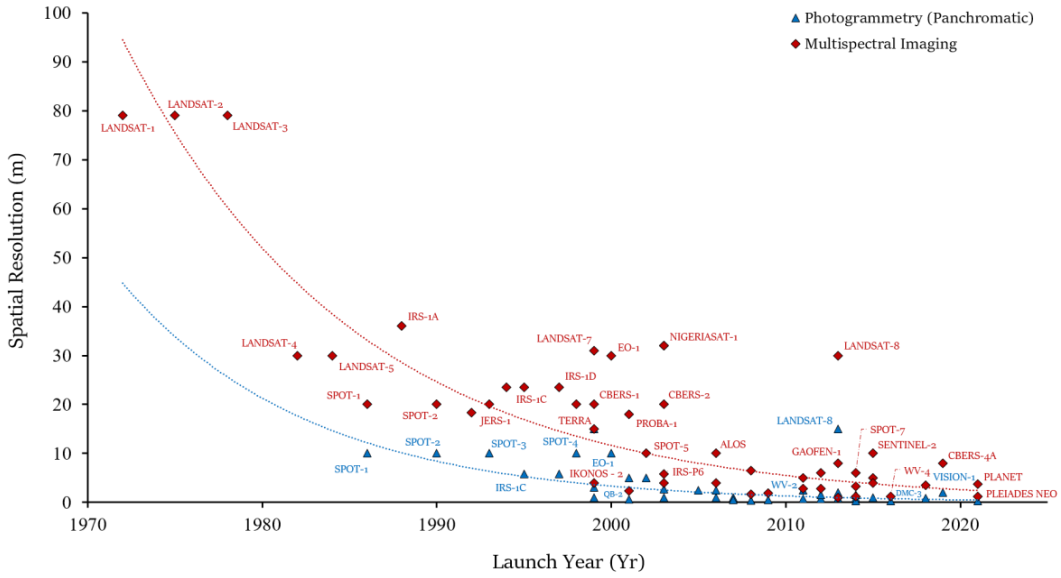



**Figure 1.2**. Spatial resolution of passive spaceborne imaging sensors since 1972. The list of passive imaging sensors used in this scatter plot is not exhaustive; all data points are sourced from the European Space Agency's 'Satellite Mission Catalogue' on the eoPortal (ESA, 2023) and are tabulated in Table A1, Appendix A.

Temporally, Planet's Super Dove constellation now provide a continuous, eight-band multispectral view of the entire Earth's surface every day (Sakuma and Yamano, 2020). Spaceborne hyperspectral imaging capabilities are also advancing. According to Pixxel (2023), a constellation of 30+ hyperspectral smallsats will soon be in orbit, capable of acquiring imagery with 300 spectral values per pixel, at 5 m spatial resolution and daily global coverage.

Since the development and implementation of new SAR imaging modes, the spatial resolution of spaceborne SAR has also improved (Figure 1.3 and Appendix B), unlocking new subsurface detection capabilities. There are now numerous high-resolution satellite missions (e.g., TerraSAR-X, TanDEM-X, COSMO-SkyMed, ICEYE, Capella X-SAR) which acquire imagery in different acquisition modes (e.g., stripMap, spotlight, scanSAR) and different polarisations (Tapete and Cigna, 2019), achieving spatial resolutions of 1 m or less (Table B1, Appendix B). A significant volume of spaceborne SAR data has also become freely available to the general public (e.g., Sentinel-1 data), and it is becoming increasingly more common for commercial space agencies to share high-resolution commercial SAR data under third party mission agreements. Larger fractions of the remote sensing community are also embracing the operational flexibility, revisit time and observational capabilities of aerial SAR. New lightweight and compact SAR sensors are now mounted on even smaller aircraft, allowing new observation configurations to exploit the latest advancements in multifrequency, multiantenna and multiplatform SAR technology (Frey et al., 2022).

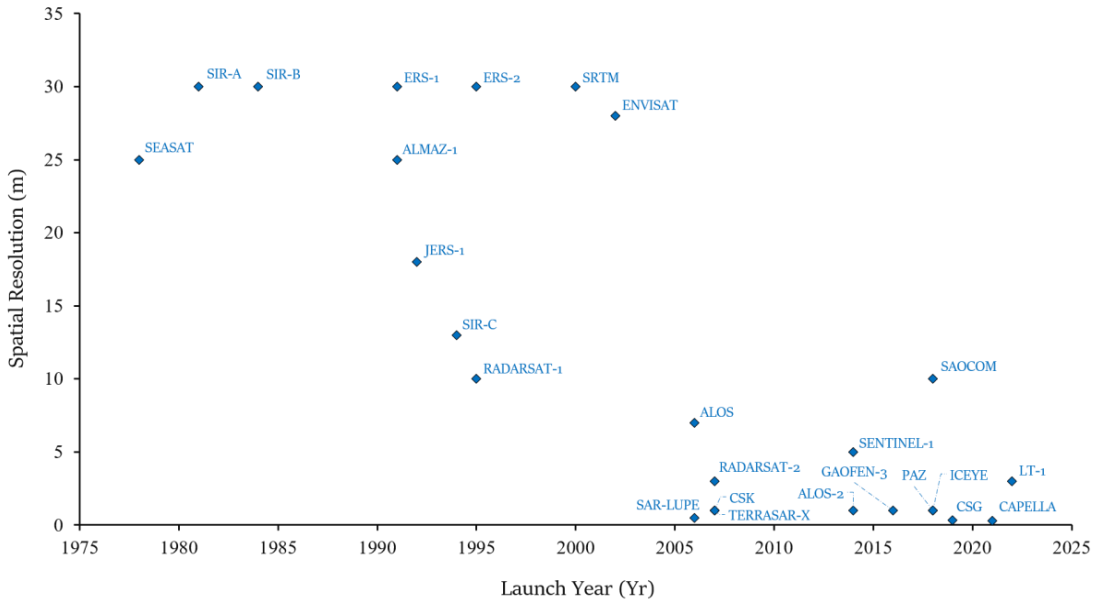



**Figure 1.3**. Spatial resolution of active spaceborne imaging (i.e. SAR) sensors since 1978. The implementation of new SAR imaging modes from 2000 onwards has significantly increased the spatial resolution of spaceborne SAR. The list of SAR sensors used in this scatter plot is not exhaustive; all data points are sourced from the European Space Agency's 'Satellite Mission Catalogue' on the eoPortal (ESA, 2023) and are tabulated in Table B1, Appendix B.

Government funded LiDAR acquisition programmes are also becoming increasingly common, supporting at scale, the generation of high and VHR digital elevation models (DEMs).

Consequently, more high-resolution LiDAR-derived elevation data is becoming publicly available and free to download from national-level environment agencies, geospatial organisations and mapping bureaus (e.g., Leonardi and Guerreschi, 2021). In parallel, recent advances in airborne LiDAR imaging systems have witnessed the introduction of multispectral lasers, higher point cloud densities, single-photon-sensitive receiver arrays and online/offline full-waveform processing (Lohani and Ghosh, 2017; Mandlburger, 2019).

In support of airborne gravity surveys, gravity gradiometers can record gravity tensor data that support the imaging of shallow, subsurface targets in high definition and during turbulent air conditions (Bell Geospace, 2021). It is also increasingly more feasible to jointly conduct airborne gravity and aeromagnetic drape surveys. These can enrich the detection accuracy, the reliability and the interpretation of geologic subsurface anomalies in regional landscapes, resolving geological anomalies 50 – 100 m in diameter (Fairhead et al., 2017; Walter et al., 2019).

Finally, advances in unpiloted aerial vehicle (UAV / drone) technology and photogrammetric processing software are transforming subsurface detection regimes (e.g., Hill et al., 2020; James et al., 2020; Masini et al., 2022). In particular, a new generation of UAV-optimized multispectral, hyperspectral and thermal infrared sensors have become routinely capable of acquiring VHR datasets (Casana, 2021). Technical improvements in high-quality inertial measurement units (IMUs) and global navigation satellite systems (GNSS) have also increased the speed and ease of georeferencing imagery, negating the need to survey ground control points before or after image acquisition (Loots et al., 2022).

## 1.3 Motivation and aims

Accelerations in platform, sensor and software capability (Section 1.2) present new opportunities to analyse and evaluate the utility of airborne and spaceborne remote sensing in subsurface detection. To seize these opportunities, I explore the capabilities of high resolution and VHR datasets and in return, assess their benefits and limitations. To increase the likelihood of detecting subsurface anomalies in high-resolution imagery, I devise a series of optimised image processing workflows and a catalogue of recommendations for best practice.

To begin, I: 1) collectively review the effectiveness of general subsurface detection from air and space; 2) assemble useful air and space subsurface detection techniques from major sensor types; 3) identify research trends in motive, sensor type and subsurface anomaly characteristics. I then examine the utility of various multispectral image processing techniques in their detection of near-surface features. During this practice, I devise a multispectral image processing workflow which is tailored to the high-resolution detection of subsurface features. I then augment this detection regime with a bespoke, multi-directional and multi-altitude LiDAR hillshade workflow which, by design, exhibits resilience in its detection of micro-relief anomalies from near-surface features. I

also explore the detection efficiency of high-resolution LiDAR elevation differencing and VHR thermal analyses to find and validate linear elevation-change anomalies from near-surface structures like tunnels, pipes and drains. To verify these remotely sensed observations, I conduct a series of pedestrian surveys and near-surface geophysical surveys with gravity, ground penetrating radar (GPR) and electrical resistivity tomography (ERT).

## 1.4 Thesis outline

In this thesis I present five chapters, each an original contribution to the study of subsurface detection from air and space.

The chapters develop coherently, beginning with a review in Chapter 2 of subsurface detection using airborne and spaceborne remote sensing; published as Morley et al. (2025a). In Chapter 3, geophysical observations across an Iron Age tunnel in Cornwall, UK, are used to reset and statistically validate the detection efficiency of broadband VIs in high-resolution multispectral satellite imagery (Table 1.1 and Figure 1.4). The study culminates in a multispectral image processing workflow which is correctly calibrated for subsurface detection in temperate, vegetated terrain (Morley et al., 2025b). In Chapter 4, this workflow, and a graphical and statistical inspection of its VI reflection profiles, are then augmented with a revised VHR LiDAR hillshade workflow to reveal several subsurface anomalies between a Cistercian abbey and a medieval grange in Normandy, France (Table 1.1 and Figure 1.4). Finally, in Chapter 5, high-resolution LiDAR elevation differencing, elevation-change profiles, high-resolution multispectral imagery analyses and VHR thermal observations are used, in a multi-sensor approach, to detect and interpret linear subsurface features around Glastonbury Tor in Somerset, UK (Table 1.1 and Figure 1.4). The thesis concludes with Chapter 6, which summarises the key findings and significant observations from previous chapters. This chapter also summarises the algorithms and workflows produced in support of this research, and suggests several avenues for future work.

**Table 1.1**
The subsurface anomaly characteristics used to *detect* and *verify* the location of subsurface anomalies at each site and in each thesis chapter.

| Chapter and location of subsurface anomalies | Subsurface anomaly characteristic detected (D) using airborne or spaceborne remote sensing; Subsurface anomaly characteristic verified (V) with pedestrian or geophysical survey[1] | | | | | | |
|---|---|---|---|---|---|---|---|
| | Visual identification | Soil matrix irregularity | Anomalous groundwater behaviour | Surface elevation change | Heat retention anomaly | Subsurface density change | Magnetic field variation |
| §3 Carn Euny | V | D | D | | | V | V |
| §4 Aunay Abbey | V | D | D | D | | | |
| §5 Glastonbury Tor | | D | D | D | D | V | |

[1] The letter 'D' signifies a subsurface anomaly characteristic used to remotely *'detect'* the location of subsurface features from air and space. The letter 'V' signifies a subsurface anomaly characteristic used to *'verify'* the location of subsurface features using pedestrian or geophysical survey.

At the time of writing, Chapter 2 has been published; Chapter 3 is under review; Chapter 4 is in preparation for publication; and Chapter 5 has become a technical report for the National Trust, Europe's largest conservation charity. Figure 1.4 is a location map showing the sites used in support of the remote sensing investigations in Chapters 3, 4 and 5 of this thesis. Within the relevant chapters, these site names also appear as page headers, thereby easing navigation through the thesis.




**Figure 1.4**. A map of southern UK and northern France (F). Sites used in this research for airborne and spaceborne subsurface detection are shown as red stars. Chapter 3 remotely detects the location of an Iron Age fogou (stone-walled underground passage) in the ancient village of Carn Euny in Cornwall, UK; Chapter 4 uses airborne and spaceborne remote sensing to detect several, high-resolution underground structures in Aunay Abbey, Normandy, France; Chapter 5 uses a multi-sensor approach to locate linear, subsurface features around Glastonbury Tor in Somerset, UK.

# 2

# Detecting shallow subsurface anomalies with airborne and spaceborne remote sensing: A review

Published as: *Morley, A.M., Mather, T.A., Pyle, D.M. and Kendall, J.M., 2025. Detecting shallow subsurface anomalies with airborne and spaceborne remote sensing: A review. Science of Remote Sensing, 11, 100187*

**Abstract**

Advances in air and space sensor technology reveal new opportunities and innovative ways to remotely sense the Earth's subsurface. Considerable spatial coverage, fast and frequent image acquisition and very high radiometric, spectral, spatial and temporal resolution imaging systems can now detect near subsurface anomalies with impressive accuracy. The merits are extensive, with archaeological prospecting, environmental risk mitigation, natural resource exploration, defence and security and speleological research all benefitting from subsurface imaging capabilities over unknown territory, difficult terrain, hazardous environments and inaccessible ground. In this paper, we categorise the ground indicators and potential field characteristics of a general subsurface anomaly before reviewing and documenting over seventy air and space subsurface detection techniques using: photogrammetry, multispectral sensors, thermal infrared, hyperspectral imaging, synthetic aperture radar (SAR), airborne light detection and ranging (LiDAR), airborne gravity and aeromagnetics. The capabilities of each technique are evaluated by reviewing their ability to detect specific characteristics from subsurface anomalies and then they are tabulated by investigable feature and sensor type in seven technique tables. Research trends in motive, sensor type and subsurface anomaly characteristic are discussed and a short review of the major ground-truthing techniques used to verify airborne and spaceborne observations is considered. To close,

we take a brief look at future research opportunities with very-high-resolution (VHR) datasets, multi-branch convolutional neural networks (CNNs) and active remote sensing in variable potential fields.

## 2.1 Introduction

Remote sensing is a field of techniques which use non-direct contact devices from land, air and space to observe targets of interest on or below the Earth's surface (Omali, 2021). In this review, we consider the applications and techniques of airborne and spaceborne remote sensing to identify subsurface anomalies where, for the purpose of this research, the subsurface is defined as the region immediately below the Earth's surface, and extending tens or hundreds of metres below ground level. We appraise the value of rapid image acquisition, large spatial coverage and high spectral, spatial, radiometric and temporal resolution datasets across 113 academic papers and 91 use cases (Figure 2.1). These use cases vary, representing different examples of subsurface detection in archaeological prospecting, environmental risk mitigation, natural resource exploration, defence and security and speleological research. Given this diversity, we generically define a subsurface anomaly as a near-surface causative body constituting: 1) different material properties to that of the surrounding soil and rock; 2) a different density; 3) a different magnetic susceptibility. If the subsurface anomaly is geologic, the anomalous structure is usually hundreds of metres deep, adopting numerous forms like dyke intrusions, ore deposits, volcanic conduits, karstic caves, salt domes, buried valleys, structural faults, fracture zones, granite plutons, shallow hydrocarbon prospects and geothermal reservoirs. However, if the subsurface anomaly is anthropogenic, it is generally much shallower, usually existing at depths of 1 – 10 m and rarely deeper than 50 m. Although our compilation is not exhaustive, we find that anthropogenic subsurface anomalies presented in the published literature are typically buried archaeological features, pipelines, drainage systems, tunnels, mines, adits, buried trenches and landfills.

Some of the most common, versatile and accessible forms of air and space remote sensing use photogrammetry and multispectral imagery to detect subsurface irregularities (Pisani and De Waele, 2021). Over the past 20 years, the potential of thermal and hyperspectral imagery, airborne light detection and ranging (LiDAR), synthetic aperture radar (SAR), airborne gravity and aeromagnetics have become well recognised and widely applied as subsurface remote sensing techniques (Casana et al., 2017; Chen et al., 2017; Fairhead et al., 2017; Jia et al., 2020; Luo et al., 2019). Consequently, shallow subsurface features are now identified from numerous air and space sensor types in significant degrees of detail and assurance.

Recent advances in platform and sensor technology, data processing algorithms and open access data policies have begun to unlock the true potential of air and space remote sensing. Airborne and spaceborne optical sensors can acquire data at very high spatial, spectral, radiometric and temporal resolution, unlocking the ability to process, analyse and interpret high-quality 2D and high-density 3D data from remote platforms (Gruen, 2021). For example, Airbus' Pléiades Neo satellite

constellation is capable of acquiring panchromatic images at 0.3 m spatial resolution and six-band multispectral images at 1.2 m resolution (Appendix A). Planet's Super Dove constellation is one of several multispectral revisit platforms, providing a continuous eight band spaceborne view of the entire Earth's surface every day (Sakuma and Yamano, 2020). Similarly, since the development of new SAR imaging modes, the spatial resolution of SAR has dramatically increased (Appendix B), unlocking new subsurface detection capabilities. There are numerous high-resolution satellite missions (e.g., TerraSAR-X, TanDEM-X, COSMO-SkyMed, ICEYE, Capella X-SAR) which acquire imagery in different acquisition modes (e.g., stripMap, spotlight, scanSAR) and different polarisations (Tapete and Cigna, 2019), achieving spatial resolutions of 1 m or less (Appendix B).

Such advances in sensor technology and data acquisition present new opportunities to apply sophisticated remote sensing capabilities to challenging subsurface detection problems like the remote detection of: subsurface magmatic features and volcanic conduits (Biondi, 2022), cross border tunnel excavation (Perez et al., 2017), ancient settlements (e.g., Dana Negula et al., 2020), unexplored cave systems (e.g., Moyes and Montgomery, 2019), geothermal potential (Abdel Zaher et al., 2018), mining activity (Ammirati et al., 2020), ore deposits (El-Raouf et al., 2023) and underground coal fires (e.g., Du et al., 2022).

To date, there is no review of the utility and success of detecting geological *and* anthropogenic structures below ground with airborne and spaceborne remote sensing. Until now, single imaging techniques from a lone sensor type or single application are most common. More recently, research has begun to explore datasets from multiple sensor types but again, the application of various remote sensing techniques therein is only considered in one particular research field. Given the recent advances in aircraft, satellite and sensor technology, it is timely to: 1) collectively review the effectiveness of general subsurface detection from air and space; 2) assemble useful air and space subsurface detection techniques from major sensor types; 3) identify research trends in motive, sensor type and subsurface anomaly characteristics.

By reviewing 113 academic papers and 91 use cases (Figure 2.1), our study reveals the principal motivations for remote sensing the subsurface. The paper then introduces a categorisation scheme for the specific ground indicators and potential field characteristics of a subsurface anomaly, setting the conditions for a systematic appraisal of remote subsurface detection using airborne and spaceborne: photogrammetry, multispectral, thermal and hyperspectral imaging, SAR, airborne LiDAR, airborne gravity and aeromagnetics. The application of various datasets from each sensor type are reviewed in separate sections, ordered by the subsurface characteristic being investigated and then by the type of sensor used. The various subsurface detection techniques for each sensor are documented in a series of technique tables (Tables 2.2 - 2.8), initially structured by the subsurface anomaly characteristic being pursued and then the investigable feature being studied (Tables 2.2 – 2.8). Major research trends in the utility and application of remote sensing the subsurface are then assessed. To close, the paper considers the major ground-truthing techniques

needed to verify air and space observations followed by a brief examination of some promising future research themes.

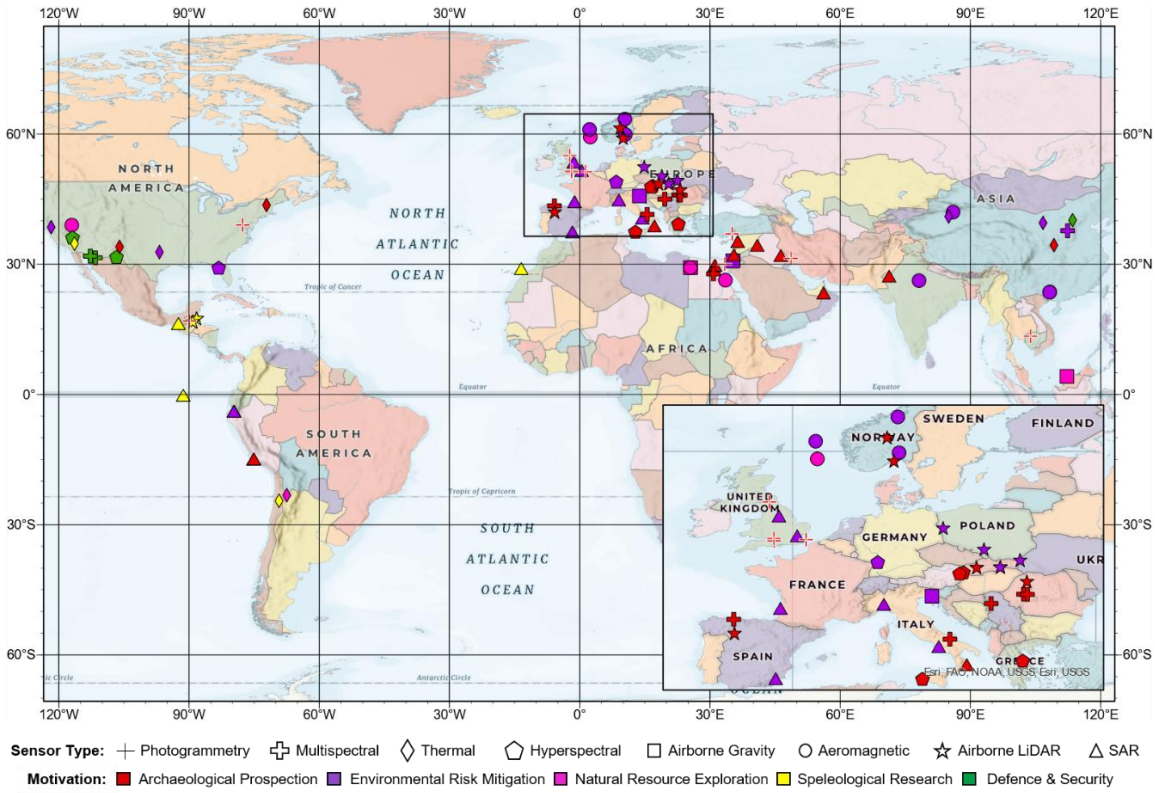



**Figure 2.1**. Location of subterranean sites (use cases) reviewed in this paper, showing the remote sensor used (symbol shape – as shown in the legend) and the motive for their detection (symbol colour – as shown in the legend).

## 2.2 Motivations for remotely sensing the subsurface

From air and space, five overarching motivations for remote sensing the subsurface have been identified in this review (Figure 2.2). Each research motive is discussed in descending order of prevalence, acknowledging our assumption that the sample of papers reviewed is representative of the body of subsurface remote sensing publications. The specific number of papers reviewed in support of each motivation and supporting statistics are presented in Figure C1 (Appendix C), where search strings were used to systematically trawl for publications by sensor category and subsurface target type.

### 2.2.1 Archaeological prospecting

The most popular research motive (38% of the papers reviewed; Appendix C) is archaeological prospecting. Here, the detection, cataloguing, differentiation and classification of ancient subsurface structures and the gathering of information, at scale and at speed, is greatly beneficial to the archaeological research community (Luo et al., 2019). Airborne and spaceborne remote sensing can unlock the ability to conduct large scale archaeological investigations without

expensive (and sometimes impossible due to scale or location) field studies. This reduces the need for pedestrian survey in the early phases of an archaeological project and enables archaeologists to detect and prioritise prospective sites before deploying (Figure 2.2).

As discussed by authors like El-Behaedi (2021), air and space remote sensing is a useful means to detect, classify and monitor archaeological sites without significant ground disturbance or destruction to the archaeological area (Figure 2.2). Harnessing air and space remote sensing techniques also allows archaeologists to conduct large scale archaeological investigations over areas which are often inaccessible by foot, broadening the number, type and size of landscape in which they are able to conduct archaeological research (Pisani and De Waele, 2021). From a preservation perspective, quick and frequent spaceborne acquisition methods allow an archaeologist to locate, manage and preserve cultural heritage sites from urbanisation, industrialisation, looting and rising water levels (Dana Negula et al., 2020; Trier et al., 2015; Trier and Pilø, 2012). Aerial and spaceborne studies of archaeological features may also reveal spatial characteristics and geometrical relationships with surrounding archaeological sites; observations which would often be imperceptible from the ground (Zanni and De Rosa, 2019).

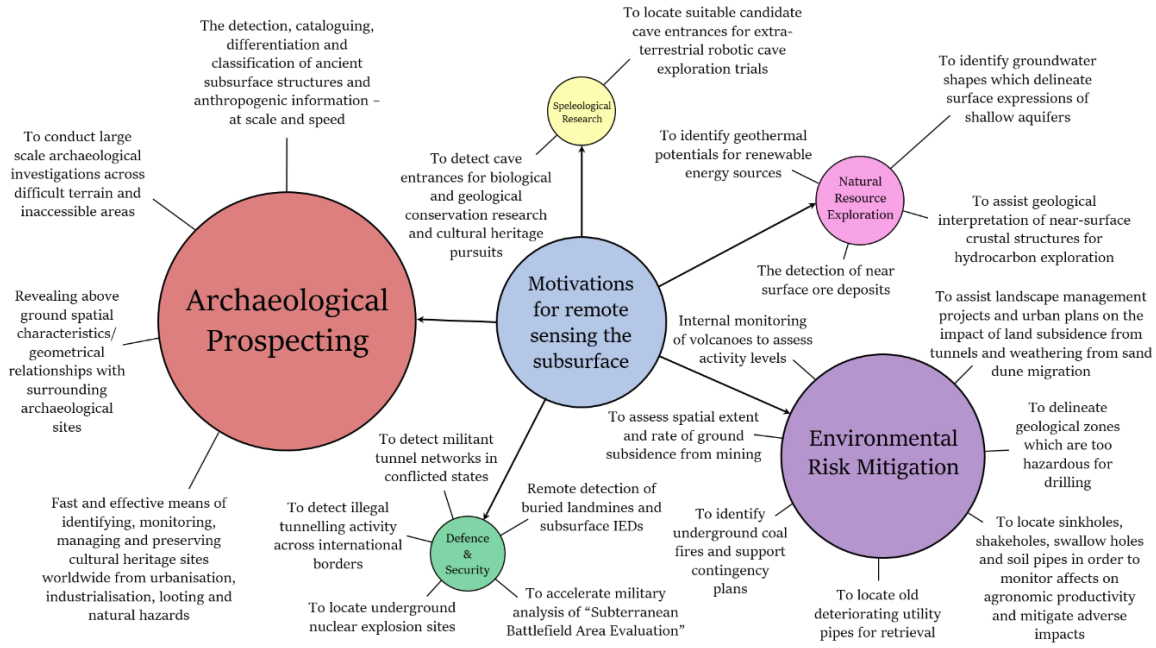



**Figure 2.2**. Motivations for remote sensing the subsurface; motivation bubble is proportional, in size, to the quantity of papers appraised in this review as per the paper statistics in Figure C1, Appendix C.

### 2.2.2 Environmental risk mitigation

One of the most diverse research motives in airborne and spaceborne remote sensing of the subsurface is environmental risk mitigation (31% of appraised papers; Appendix C). The use of various remote sensing techniques to locate sinkholes, shake holes, swallow holes, soil pipes and land subsidence in karstic rich environments and above voids is a popular research objective (Barla

et al., 2016; Bernatek-Jakiel and Jakiel, 2021; Hofierka et al., 2018; Zhang et al., 2023). Once detected, air and space remote sensing can be used to monitor the spatial extent and depression rate of ground subsidence in order to manage and mitigate any adverse impacts on urban development projects, tunnel construction and agronomic productivity (Bonì et al., 2017; Braitenberg et al., 2016; Sun et al., 2023). Other remote sensing objectives include the detection and behaviour of underground coal fires and sand dune migration (Du et al., 2022; Grandjean et al., 2001; Wang et al., 2015), the internal monitoring of volcanoes (Biondi, 2022) and the identification of specific geological structures which present drilling hazards during exploration programmes e.g. tunnel valleys containing shallow gas (Ottesen et al., 2020).

Hartshorn et al. (2022) present an interesting use case for the aerial detection of old utility pipes which, prior to retrieval, can have a detrimental effect on nearby ground conditions. Alternatively, Kuzia (2018) and Mi et al. (2019) consider the utility of airborne and spaceborne remote sensing to monitor the secondary impacts of underground mining (Figure 2.2).

### 2.2.3 Natural resource exploration

The remote detection of near-surface natural resources comprises 13% of the academic papers reviewed in this study (Appendix C). Research objectives include the detection and demarcation of subsurface ore deposits (El-Raouf et al., 2023) and the remote identification of shallow geothermal regions; the former supporting national economic levels and the latter supporting national ambitions to transition to renewable energy sources (Abdel Zaher et al., 2018). Air and space remote sensing techniques are also seen to detect unique groundwater shapes, patterns, tones and textures, revealing drainage patterns and surface lineament characteristics which delineate surface expressions from shallow aquifers (Gaber et al., 2020; Waters et al., 1990). This research motive also reveals the utility of airborne and spaceborne remote sensing as an augmentation toolset, where the execution of niche acquisition surveys like airborne gravity can assist with the geological interpretation and characterisation of crustal structures like faults, fracture zones, domes and tunnel valleys, all in direct support of shallow-subsurface hydrocarbon exploration (Jamaludin et al., 2021).

### 2.2.4 Defence and security

In total, 11% of the papers appraised in this review present a defence and security research motive (Appendix C). Given the sensitive nature of these applications, other studies will exist but are not necessarily published openly in international journals. Among the most important of these applications is that of tunnel detection, where the motivation to detect clandestine tunnel activity under built-up areas and international borders is considerable (Figure 2.2).

In conflict, tunnels allow combatants to move between fighting positions safely and freely. Urban tunnel networks and more widely, cross border tunnels (CBTs), also provide covert lines of

communication for transporting hostages, human trafficking, asylum seekers and drug smuggling (Figure 2.2). They are also useful for the concealment of weapons, soldiers, insurgents, food and water supplies (Richemond-Barak, 2018). In modern-day conflict, CBTs are specifically known to exist between Israel and Lebanon; Israel and Syria; Israel and Gaza; Egypt and Gaza; North and South Korea; Cambodia and Vietnam; US and Mexico; India and Pakistan (Olson and Speidel, 2020; Richemond-Barak, 2018).

Airborne and spaceborne remote sensing are useful for several defence and security-related applications. These techniques can, at scale and at speed, locate and prevent hostile militant activity and clandestine CBT exchanges by employing specialised change detection techniques (Kwan, 2019) and feature detection algorithms like the identification of excavated spoil heaps (Perez et al., 2017). Further, remote sensing is used to accelerate the military analysis of 'subterranean battlefield area evaluation', allowing armed forces to observe, orient, decide and act off the interpretation of high-resolution imagery that is up-to-date and readily available across the chain of command (Olson and Speidel, 2020). Additionally, multispectral and hyperspectral imagery is frequently used by various Defence and Government Intelligence experts to classify adversary vehicles, equipment and troops near tunnels and caves and under forested terrain and camouflage constructs (Shimoni et al., 2019). Pending burial depth and specific ground conditions, buried landmine and improvised explosive device (IED) detection is also achievable using specialist air and space remote sensing techniques (Shimoni et al., 2019). Similar specialism is also replicated by the Comprehensive Nuclear-Test-Ban Treaty Organisation (CTBTO) who can, during on-site inspections, perform multi-sensor subsurface detection routines to locate underground nuclear explosion sites (Mathew et al., 2023).

### 2.2.5 Speleological research

The effective employment of airborne and spaceborne remote sensing to detect cave entrances is the focus of 7% of the papers reviewed (Appendix C). The generation of various algorithms and workflows to detect candidate cave entrances (CCEs) offer several advantages to speleological research. For example, the detection of new cave systems in select and often restricted parts of the world can accelerate research prospects for conservation biologists and geologists, recognising that caves can host rare species, fragile ecosystems and unusual geological formations (Wynne et al., 2021). In support of speleological studies and ancient cultural heritage investigations, the ability to detect cave systems remotely in steep and rugged terrain, dense vegetation and relatively remote regions of the world is extremely beneficial (e.g. Moyes and Montgomery, 2019). Here, the remote detection of CCEs allows specific sites to be prioritised for follow-up ground investigation and in parallel, suitable access routes can be identified using the remotely sensed imagery (Weishampel et al., 2011).

In order to inform future robotic cave exploration missions on extra-terrestrial bodies like the Moon and Mars, the need to detect suitable CCEs on Earth is also gaining momentum (Figure 2.2).

Several papers in this review employ air and space remote sensing techniques to identify suitable cavernous training sites for robotic exploration trials (Carrer et al., 2015). The motivation to explore extra-terrestrial caves is multifaceted. Research objectives include: the search for water, dry ice, brines and organic matter, the need to understand the subsurface geology of extra-terrestrial bodies and the detection of prospective human outposts safe from cosmic radiation (Pisani and De Waele, 2021).

## 2.3 Characterisation of subsurface anomalies

Whether natural or anthropogenic, shallow structures and objects beneath the Earth's surface can produce unique ground characteristics and surface proxies directly above the ground anomaly, which can then be used for detection. We group these distinct subsurface anomaly characteristics into seven categories: 1) visual identification; 2) soil matrix irregularity; 3) anomalous groundwater behaviour; 4) surface elevation change; 5) heat retention anomaly; 6) subsurface density change; 7) magnetic field variation. The field observations related to each category are reviewed in the following subsections, summarised in Table 2.1 and illustrated in Figure 2.3.

### 2.3.1 Visual identification

Several visible features on and above the ground can signify the presence of subsurface structures and underground anthropogenic activity. By definition, these are visible indicators which can be seen in situ with the naked eye or, pending the spatial resolution of the air or spaceborne remote sensor, identified in visible Red-Green-Blue (RGB) imagery. Typical indicators include changes in land use and land cover (Mi et al., 2019), prominent and regular shaped crop marks (Melillos et al., 2019) and geomorphic surface anomalies like sinkholes (Hofierka et al., 2018), shake holes, soil pipes (Bernatek-Jakiel and Jakiel, 2021), lava tubes and skylights (Carrer et al., 2015). Pending the size of the opening and the amount of concealment, vertical and horizontal entrances to tunnels, mines and caves (Moyes and Montgomery, 2019) can also be detected remotely. Finally, any objects or features which depict clear signs of underground excavation are usually clear evidence of subsurface activity. These include: the formation of new tracks in sensitive regions, spoil heaps, tunnel boring machinery, plant vehicles and field generators (Olson and Speidel, 2020).

### 2.3.2 Soil matrix irregularity

An ancient underground structure like a wall or a road, or the presence of a shallow stone-lined tunnel, will directly influence the soil structure above it (Dana Negula et al., 2020). Often poor and/or excessive drainage conditions are introduced to the soil matrix above an anthropogenic structure and geochemical alterations within the soil are intensified by the mineralogical leaching of the subsurface structure, which can exacerbate with time. This results in detrimental modifications to the soil density, soil moisture content and soil composition above and around a subsurface anomaly (Rowlands and Sarris, 2007). Consequently, the growth and health status of any

vegetation at the surface is expected to deteriorate (Lasaponara and Masini, 2007). Furthermore, the presence of a very shallow underground structure is expected to restrict the absorption rates of chlorophyll, chlorophyll abundance and green leaf scattering in plants and grassland, because the subsurface anomaly will impede root development and disrupt soil salinity levels (Allbed and Kumar, 2013; James et al., 2020). Such activity will typically result in stressed crops (crop marks) and soil discolouration (soil marks) over buried anthropogenic structures, and pronounced crop marks over buried ditches and paleo channels (Figure 2.3). The vegetation response to soil matrix irregularity and subsurface heterogeneity is particularly useful for air and space remote sensing, where near-infrared (NIR) wavelengths are well reflected by vigorous vegetation and absorbed by stressed vegetation, and red wavelengths are absorbed by vigorous vegetation and well reflected by stressed vegetation (Luo et al., 2019).

### 2.3.3 Anomalous groundwater behaviour

Lateral variations in rock permeability from tunnel excavation and mining activity can activate fracturing, affecting groundwater percolation around tunnels and mines. According to Waters et al. (2019), underground tunnelling can trigger the formation of an excavation damage zone (Figure 2.3) which contains a series of newly formed radial and concentric fractures around the excavation. In turn, these fractures are expected to redistribute the rock stress in the near-surface, realign rock crystal structures and reroute groundwater percolation regimes. In particular, underground voids (e.g. tunnels) can often behave like drains, accelerating and/or disrupting soil drainage rates which then locally change the groundwater level (Lv et al., 2020; Zeng et al., 2023). Subsequently, these altered groundwater regimes have the potential to reveal anomalous drainage behaviour and lineament characteristics at the surface. Furthermore, any geochemical alterations in the soil matrix around a geological and anthropogenic subsurface anomaly can affect the water storage and recharge rates from infiltration (Gaber et al., 2020), again resulting in anomalous drainage patterns and watersheds.

### 2.3.4 Surface elevation change

Near-surface features like archaeological remains and buried river channels can produce micro-relief anomalies in the ground above (Chase et al., 2017). These small adjustments in surface elevation and topography are rarely noticed by the naked eye, but aerial reconnaissance and high-resolution air and space remote sensing can reveal subtle height distinctions (Lieskovský et al., 2022). Soil degradation, soil consolidation, variable drainage rates and the swelling and shrinkage of clay soils around subsurface anomalies are expected to contribute to surface uplift and surface slumps over shallow subsurface features (Bernatek-Jakiel and Jakiel, 2021). Also, naturally occurring ground subsidence from deeper deformation activity, groundwater withdrawal, aquifer compaction and karstic behaviour can symbolise the presence of underground inconsistencies. In parallel, human induced land subsidence can trigger similar field observations, where anomalous

surface depressions can signify the location of underground solid and fluid extraction, lateral and vertical mining activity and tunnel excavation (Anantrasirichai et al., 2021).

### 2.3.5 Heat retention anomaly

Micro-relief anomalies (e.g. localised surface depressions and ground uplift) above subsurface anomalies can instigate differential heating effects across a scene (James et al., 2020), where slopes directly facing the Sun capture more heat energy than slopes facing away from the Sun. Corrections must therefore be made for the Sun's azimuth, elevation and local ground conditions. Additionally, differences in the density, chemical composition and moisture content of the ground above a subsurface feature can cause the ground surface to absorb, emit, transmit and reflect thermal infrared (TIR) radiation at different rates from that of the surrounding ground (Casana et al., 2017). This is due to anomalous thermal emissivity contrasts in the subsurface, generated by the materials constituting that particular subsurface entity. Such anomalous geologic and anthropogenic entities have distinct diurnal radiant temperature curves which are defined by the subsurface anomaly's 'thermal conductivity', 'thermal capacity' and 'thermal inertia' (Lillesand et al., 2015). As illustrated in Figure 2.3, this thermal inertia is a measure of the response of a material to temperature change and in general, subsurface features with high thermal inertia (e.g., buried ditches) express greater uniform surface temperatures throughout the day than subsurface bodies that introduce low thermal inertia properties into the surrounding ground (e.g., buried walls and air-filled tunnels). Crop marks created by shallow subsurface objects can also generate heat retention anomalies, where they express unique variations in evapotranspiration (Tan et al., 2006).

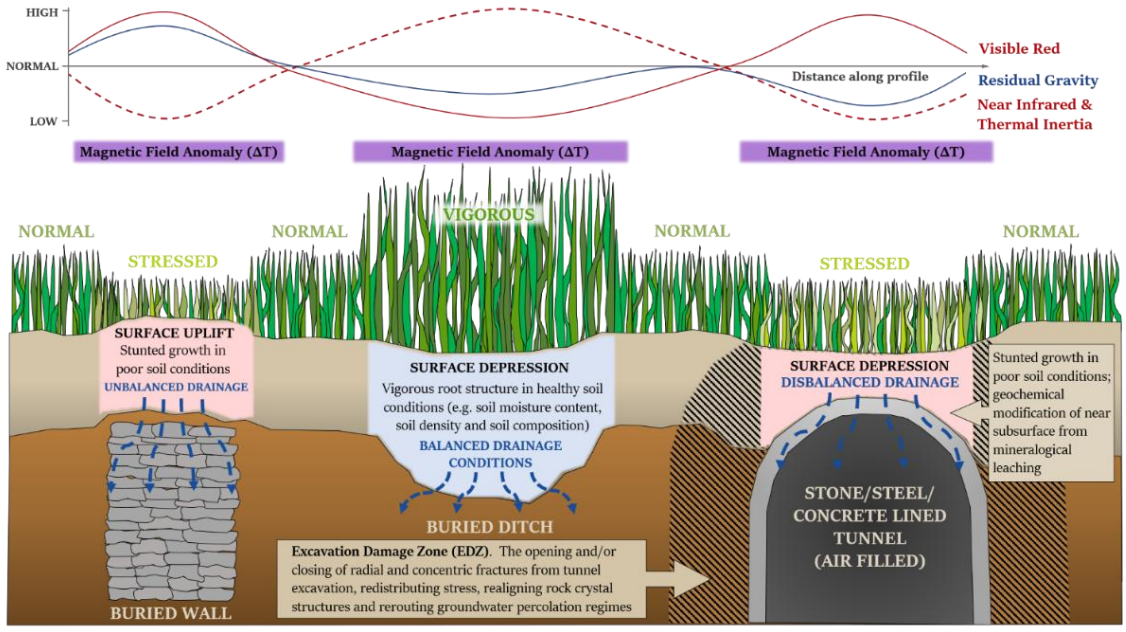



**Figure 2.3**. Anomalous ground characteristics of three general subsurface structures that can be detected using remote sensing. An underground wall (left), buried ditch (centre) and air-filled tunnel (right) are used as examples. Top diagram illustrates how visible red light, near infrared, thermal inertia and residual gravitational field strength vary across these structures. Purple bars denote locations of total magnetic field anomalies ($\Delta T$); $\Delta T$ is dependent on the subsurface distribution of magnetic susceptibility and the orientation of the Earth's Magnetic Field. Vegetation, topographic and drainage variations are also illustrated pictorially, although some or all may not be present in every real-world scenario.

### 2.3.6 Subsurface density change

Geological and anthropogenic subsurface anomalies can be identified on the basis of variations in the Earth's gravitational field, arising from differences in density between the target subsurface object and the surrounding ground (Kearey et al., 2002). A causative subsurface structure like a large air-filled cave will present a lower density than its bulk 'soil and rock' surroundings, generating a subsurface zone of anomalous mass and a localised perturbation in the Earth's gravitational field known as a gravity anomaly (Milsom, 2003). A wide range of geological and anthropogenic settings will generate zones of anomalous mass which in turn, will produce residual gravitational field strength anomalies. Geological structures expected to generate residual gravitational field strength anomalies include caves, salt domes, buried valleys, structural faults, fracture zones, granite plutons, shallow hydrocarbon prospects and geothermal reservoirs (Jamaludin et al., 2021). Anthropogenic subsurface structures expected to generate residual gravitational field strength anomalies include archaeological features, tunnels, mines and adits (Butler, 2008).

### 2.3.7 Magnetic field variation

Near-surface structures like concrete lined tunnels or ancient walls can present significant alterations in magnetic susceptibility ($\kappa$) underground. Magnetic susceptibility ($\kappa$) is a measure of how susceptible a material is to becoming magnetised (Persico et al., 2019). Depending on the concentration of ferro and ferro-magnetic minerals in the geological or anthropogenic subsurface anomaly, varying levels of magnetic susceptibility are introduced to the near-surface. Furthermore, this subsurface anomaly will, to a greater or lesser extent, feature an induced and remnant magnetisation different from the surrounding ground. Therefore, above the Earth's surface, these magnetisations will generate a resultant vector known as the 'intensity of magnetisation ($J$)' which is unique and representative of the underlying geological or anthropogenic body (Reynolds, 1997). When interpreting the magnitude and shape of the magnetic anomaly above the Earth's surface, it is important to understand that the resultant anomaly is a product of the interaction (superimposition) between the magnetic field of the subsurface body and the Earth's Magnetic Field (Campbell, 2003). Geological features which are expected to generate residual magnetic field strength anomalies include dykes, large basic intrusions, magnetite ore deposits, fracture zones, weak rock units, shallow hydrocarbon prospects, shallow geothermal reservoirs and faulted, folded and truncated lava flows (Everett, 2013). Anthropogenic structures which are expected to generate residual magnetic field strength anomalies include buried pipelines, buried archaeological features, stone, steel or concrete lined tunnels, buried trenches and landfills (Křivánek, 2017).

**Table 2.1**
Ground indicators, potential field characteristics and typical field observations generated by a subsurface anomaly, as illustrated in Figure 2.3.

| Subsurface Anomaly Characteristic | Field Observations | Example References |
|---|---|---|
| Visual identification | Changes in land use/land cover; geomorphic surface anomalies (e.g. sinkholes, shake holes, soil pipes, lava tubes, skylights); prominent and regular shaped crop marks; entry points to tunnels, mines and caves; tunnelling indicators (e.g. new tracks, spoil heaps, tunnel boring machinery, plant vehicles, hand/power tools, field generators) | Carrer et al., 2015; Dao et al., 2017; Mi et al., 2019; Moyes and Montgomery, 2019; Saha, 2022; Bernatek-Jakiel and Jakiel, 2021 |
| Soil matrix irregularity | Crop marks – tall/vigorous over buried ditches, short/stressed over buried archaeological features, stone intrusions and lined tunnels; steady drainage, soil moisture content and soil composition over buried ditches; excessive drainage over buried features, stone intrusions and lined tunnels; soil marks; mineralogical modification from migration of leachates | Lasaponara and Masini, 2007; Rowlands and Sarris, 2007; Dana Negula et al., 2020; El-Behaedi, 2021 |
| Anomalous groundwater behaviour | Lateral variations in rock permeability from excavation activity triggers fracturing and affects ground water percolation; altered groundwater regimes reveal anomalous drainage behaviour and lineament characteristics at the surface; underground voids can behave like drains, affecting groundwater level; alterations in chemical composition of soil affects water storage and recharge rates from infiltration | Grandjean et al., 2001; Finn et al., 2011; Waters et al., 2019; Gaber et al., 2020; Lv et al., 2020 |
| Surface elevation change | Micro-relief from near-surface features and soil degradation activity; land subsidence from superficial and deep deformations e.g. swelling/shrinkage of clay soils, soil consolidation, aquifer compaction, solid and fluid extraction; ground subsidence from mining and tunnelling | Barla et al, 2016; Boni et al., 2017; Luo et al., 2019; Scoular et al., 2020; Macchiarulo et al., 2021 |
| Heat retention anomaly | Differential heating of Earth's surface from micro-relief variations; crop marks affecting heat retention due to variations in evapotranspiration; thermal inertia distinctions and thermal emissivity contrasts above subsurface structures and at tunnel, mine and cave entrances | Kvamme, 2005; Tan et al., 2006; Rowlands and Sarris, 2007; Hill et al., 2020; Wynne et al., 2021 |
| Subsurface density change | Residual gravitational field strength anomalies (using microgravity profiling) from buried archaeological features, cave systems, tunnels, mines, adits, salt domes, buried valleys, structural faults, fracture zones, granite plutons, shallow hydrocarbon prospects and geothermal reservoirs | Braitenberg et al., 2016; Abdel Zaher et al., 2018; Jamaludin et al., 2021 |
| Magnetic field variation | Residual magnetic field strength anomalies from dykes, large basic intrusions, magnetite ore deposits, fracture zones, weak rock units, shallow hydrocarbon prospects, shallow geothermal reservoirs, buried pipelines, archaeological features, stone, steel or concrete lined tunnels and buried trenches/infills | Ottesen et al., 2020; Hartshorn et al., 2022; El-Raouf et al., 2023; Zhang et al., 2023 |

## 2.4 Remote sensing the subsurface: overview

Case studies demonstrating the remote detection of subsurface anomalies are considered systematically, ordered by the subsurface characteristic being investigated and then by the type of sensor used. All papers reviewed are documented in a three-dimensional reference matrix (Figure C1), where each paper is registered by sensor type, authors' motivation and the subsurface anomaly characteristic being pursued (Appendix C). In support of each subsection are a series of information graphics (Appendix D), each communicating the respective principles of the air and space remote sensors reviewed.

By assuming the 113 papers reviewed are representative of the total population of subsurface remote sensing publications, several trends in the utility and application of remote sensing the subsurface are revealed. As summarised in Figure 2.4, 78% of reviewed photogrammetry papers study the visible indicators across archaeological sites; 43% of multispectral papers identify soil matrix irregularities over buried archaeological features; anomalous groundwater behaviour is analysed using 6/8 sensor types; heat retention anomalies are a suitable proxy for all research motives; changes in subsurface density are detected (or assisted) using airborne gravity, airborne

LiDAR and SAR; and 57% of LiDAR papers and 50% of SAR papers exploit changes in surface elevation.

In the remainder of this review, over 70 air and space subsurface detection techniques are summarised across seven technique tables (Tables 2.2 – 2.8). In each technique table, relevant acquisition methods and detection techniques are documented by subsurface anomaly characteristic, investigable feature and sensor type. Our hope is that this organisation will maximise their value in priming future research and future subsurface detection studies.

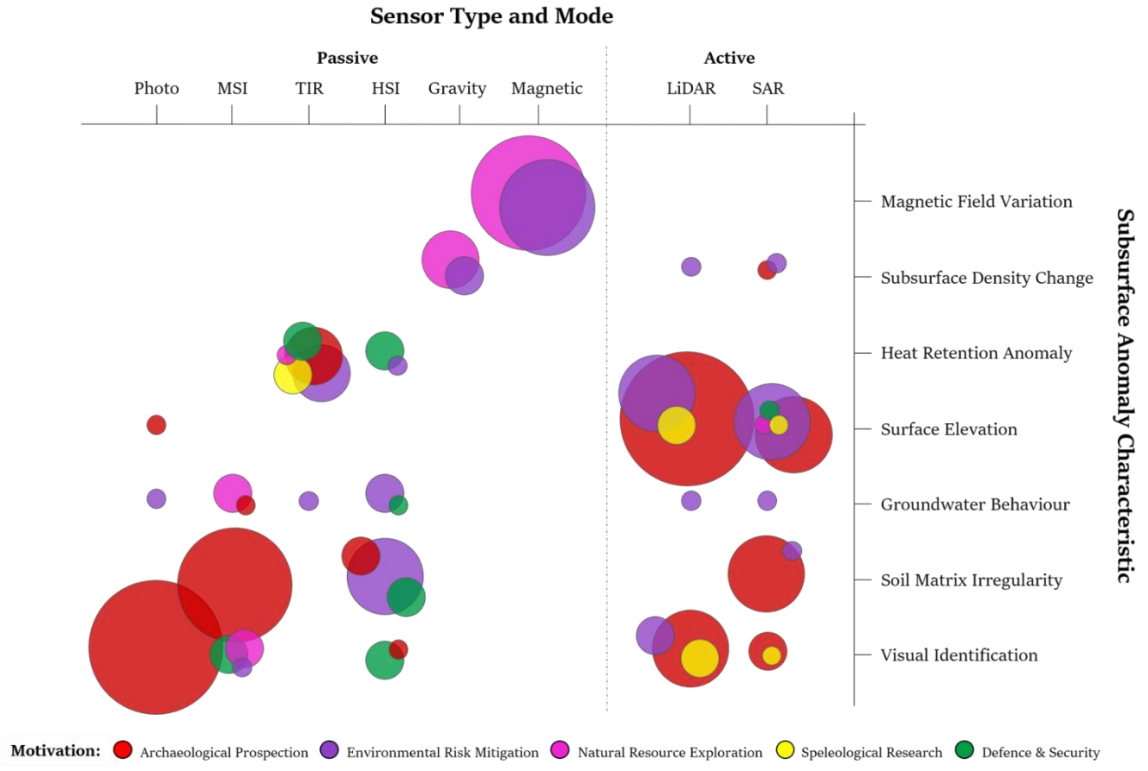



**Figure 2.4**. Bubble chart showing the type of sensor used to detect the characteristics of subsurface anomalies for each paper in this review. The size and colour of each data bubble represents the quantity of papers applicable and the author's primary motivation. In total, 113 papers were reviewed in six months. Specific paper counts and supporting statistics are recorded in Figure C1, Appendix C.

## 2.5 Visual identification

### 2.5.1 Using photogrammetry

When visually inspecting the ground for unique characteristics from subsurface features, the principles of photogrammetry can assist considerably. Examples include the detection and analysis of anomalous groundwater regimes over and around subterranean features (Sharafi and Khazaei, 2013) and the visual detection and geometrical measurement of micro-relief patterns, crop marks and soil marks (Lasaponara and Masini, 2014). In support of visually detecting micro-relief

anomalies, air and space photography can also be used as stereopairs to create digital elevation models (Luo et al., 2019).

The benefits of using aerial photogrammetry in subsurface detection were first conceived in 1906 when archaeological features around the ancient UK monument of Stonehenge were identified from an aerial photograph taken from a military balloon (Bewley, 2003). Since then, developments in photography and aerial photogrammetry have accelerated and consequently, the discipline of 'aerial archaeology' began to flourish. By the 1970s, the use of infrared and multispectral photography started to detect variations in soil moisture and crop growth across historical sites (Verhoeven, 2012) and by the 1990s, aerial reconnaissance of larger study regions was beginning to identify numerous geometrical patterns across regional landscapes. For example, an aerial survey across England in 1996 revealed the distinct discolouration of plants and crops in numerous geometrical shapes, later confirmed to be crop marks from subsurface objects. These crop marks had been accentuated by the hot, dry summers across the UK from 1989 to 1996 (Featherstone et al., 1999). Using various image enhancement filters, the crop marks in multiple images revealed several new archaeological sites (Featherstone et al., 1999), with many then confirmed as Iron Age through to Roman settlements over excessively well drained limestone and ironstone foundations (Figure 2.5).




**Figure 2.5**. Example of using aerial photography to detect near subsurface anomalies. Red dashed box contains several crop marks at a site in Hougham in Lincolnshire, revealing a settlement which developed from the Iron Age to Roman period. The aerial photo was taken during an aerial archaeology study in 1996, funded by the Royal Commission on the Historical Monuments of England (RCHME). Figure adapted from Featherstone et al. (1999).

Subsurface detection regimes using photogrammetry require pixel level delineation techniques. Such techniques, combined with a holistic perspective of the study area from air or space, can equip the user with a broader contextual view of the landscape. This is often crucial for the location of subsurface features like tunnels, trenches and archaeological foundations. The linear trends and geometrical patterns generated in the terrain from such subsurface features are not readily seen

on the ground but aerial and space photography can reveal subtle patterns through variations in soil colour, relief shadow and the tone of overlying vegetation (Deng et al., 2010).

Weber and Yool (1999) explore some of these delineation techniques using two different spatial contrast enhancement filters on four scanned historical photographs of Idalion, an ancient archaeological site in the Nicosia District of Cyprus. They compared the performance of median and locally adaptive spatial contrast filters (Table 2.2) in the detection of new archaeological features. The former operates in a neighbourhood mode which reduces image noise and smooths differently valued pixels within a group of similar valued pixels (Gonzalez and Wintz, 1987). They are also “edge preserving, smoothing” filters (Pratt, 1991), where their noise reduction qualities can produce a more interpretable image. In contrast, the locally adaptive spatial contrast filters increase the resolution of spatial detail by using local neighbourhood statistics to maximize local contrast and stretch the range of pixel brightness values across a region of interest (Fahnestock and Schowengerdt, 1983). In using the locally adaptive spatial contrast filter, Weber and Yool (1999) enhanced the radiometric resolution of the low contrast air photos and managed to detect the foundations of five towers along a 9.6 km long defensive wall of Idalion.

The subsurface detection capabilities of spaceborne photogrammetry soon followed after the successful application of airborne photogrammetry. Kennedy (1998) performed the first inspection of CORONA space photography for a virtual investigation of the Euphrates Valley in Turkey. Ur (2003) went on to examine CORONA space photography to locate archaeological sites and road foundations in northern Syria, successfully detecting the latter. Before long, subsurface prospecting using space photogrammetry migrated to commercial satellite cameras. In 2003, several buried archaeological features in Cilicia, southern Turkey, were identified using digitally processed and spatially enhanced IKONOS-2 panchromatic and colour photography. On the ground, these sites were obscured by overlying vegetation including maquis and garrigue, and by agricultural terraces supporting wheat and orchards. However, crop marks and micro-relief patterns could be identified from the IKONOS-2 space photography which were later verified with archaeological excavation as 150 BC – 650 AD building foundations (Kucukkaya, 2004).

### 2.5.2 Using multispectral imaging

Notable changes in land use and land cover can reveal structural alterations in the subsurface. Mi et al. (2019) use a continuous Landsat imagery classification (Table 2.2) with a random forest classifier to monitor changes in land use/land cover (LULC) across the Nanjiao mining area in Shanxi Province, China between 1987 and 2017. Initially, they use a data smoothing filter and normalised difference vegetation index (NDVI) to detect the temporal and spatial changes in cultivated forest, natural forest, buildings and farmland. They then used LULC classification techniques to reveal significant regions of LULC change from grasslands and buildings to cultivated forest, revealing regional (and spatial) trends in village abandonment from the lived effects of ground subsidence from coal mining. Temporal analyses of the spectral content in multispectral

data can reveal subsurface drivers for change in LULC, benefitting regional land plans, ecological restoration strategies and the development of environmentally friendly management policies in sensitive milieus like mining districts.

Inspecting temporal change across consecutive multispectral images is also a useful technique for identifying the presence of new subterranean structures like cross border tunnels (Table 2.2). Kwan (2019) reviews a series of change detection algorithms, commonly employed across a full suite of multispectral and hyperspectral imaging case studies. Referring to the detection of changes between images collected at two different points in time, Kwan (2019) highlights the benefits of employing 'Direct Subtraction', 'Principal Component Analysis (PCA)' and 'Band Ratio' comparisons to detect clandestine tunnel activity across contested borders like USA–Mexico.

Li et al. (2019) also investigated the use of change detection, where change detection maps from existing unsupervised change detection methods were used to train a deep Convolutional Neural Network (CNN). Allowing deep learning to succeed without the use of supervised training data can reduce the data burden and computational time. Similarly, Perez et al. (2017) explore the utility of deep learning on multispectral data, where they use WorldView-2 (WV2) multispectral imagery and a CNN model to identify fresh soil trails and spoil heaps from cross border tunnels along the USA-Mexico border (Table 2.2). WorldView-2 satellite images in the visible to near infrared (VNIR) range were pansharpened to increase the spatial resolution of the eight VNIR bands to 0.31 m. A four-layer CNN was then configured and trained to classify image patches into 14 different classes (e.g., soil, building, road) using both the spatial and spectral information in the multispectral data. Once trained, the neural network could perform in real-time, computing the probability of an image patch belonging to excavated tunnel soil. A novel method for handling the imbalance in training data was also employed, overcoming the challenge of having a limited number of positive excavated tunnel soil data samples versus an unlimited number of negative training samples. Experimental results showed that the CNN successfully detected a high to low probability plot of excavated tunnel soil (Figure 2.6), suggesting that the Perez et al. (2017) imbalance learning technique improved the CNN detection performance.

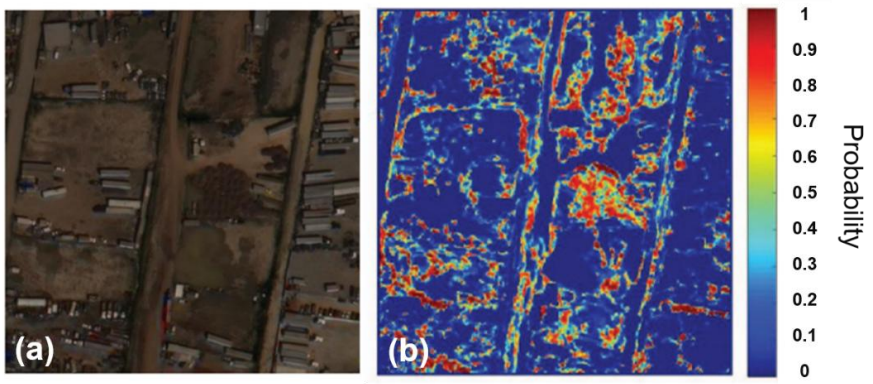



**Figure 2.6**. Soil detection results from the excavation of clandestine tunnels along the USA-Mexico border using a four-layer CNN. a). The WV2 test image in RGB. b). A soil class probability map, where a CNN is trained as a 14-class multispectral soil classifier and then used to map the likelihood of soil deposits originating from excavated cross border tunnels. Figure adapted from Perez et al. (2017).

### 2.5.3 Using hyperspectral imaging

In support of cross border tunnel (CBT) surveillance operations, the routine use of automated feature recognition algorithms and VHR imagery to detect new tracks, spoil heaps, tunnel boring equipment and heavy plant machinery will mitigate the illegal use of CBTs (Richemond-Barak, 2018). In particular, hyperspectral imagery is well placed to support these automated feature recognition algorithms (Davis, 2019), especially when used in collaboration with image resolution enhancement algorithms (Table 2.2) like single super-resolution and multi-image fusion techniques (Kwan, 2018). Kwan (2018) also present a band synthesis technique for generating high resolution hyperspectral images from multispectral imagery, showcasing spectral interoperability between different sensor types.

In support of the visual detection of buried objects, Shimoni et al. (2019) consider a slightly different approach, where discrepancies in longwave infrared (LWIR) and the quartz absorption line are used as a proxy for detecting buried landmines (Table 2.2). In a review on 'Hyperspectral Imaging for Military and Security Applications' they observe physical, chemical and thermal changes in the exposure of bare subsurface soil after landmines were buried across a battlefield (McFee et al., 2005). Changes in reflectance value from quartz particles were observed from the compact soil above a buried landmine and the disturbed soil around it (Shimoni et al., 2019). Further, if a buried landmine lay undetonated for prolonged periods, leakage of the explosive compounds into the environment could contaminate the surrounding soil and vegetation, stressing the physiology of vegetation in ways that can lead to different spectral responses to those affected by natural conditions like drought and salinity (Kalderis et al., 2011).

### 2.5.4 Using airborne LiDAR

A LiDAR derived digital elevation model (DEM), digital terrain model (DTM) and digital surface model (DSM) can be inspected for the visual traces of micro-relief proxies from subsurface anomalies (Lasaponara and Masini, 2009). This typically requires the implementation of a suitable relief visualisation technique (Table 2.2). Within the steep and forested archaeological site of Porolissum in Romania, Roman et al. (2017) identified 79 subsurface sections of a defensive system from the ancient Roman Empire frontiers. Using PCA (Devereux et al., 2008), local relief models (LRMs) (Moyes and Montgomery, 2019), sky-view factor (SVF) (Zakšek et al., 2011) and positive openness (Yokoyama et al., 2002), the surface expression of the ancient remains supported the hypothesis that the site was once extensively deforested by the Romans for strategic purposes. Similarly, in Slovakia, ancient cultural landscape features were detected in the near-surface by identifying micro-relief anomalies in LRMs, SVF, slope gradient and colour blending (Lieskovský et al., 2022). According to Štular et al. (2012), optimal visualisation techniques are dependent on the terrain type and so for effective employment, they should be selected carefully and systematically from an all-encompassing catalogue of thirteen different visualization methods.

Airborne LiDAR systems can also capture reflectance percentages (i.e., amplitudes) from the returning pulses, more commonly known as LiDAR intensity. The intensity of returning LiDAR pulses vary with the wavelength of the source energy and the composition of the material reflecting the incoming signal. The LiDAR measurements of these reflectance percentage values can be used to produce a georeferenced raster image that both identifies and classifies broad land cover types. During a LiDAR detection study of river valley floors in the Trent Valley of the English Midlands, UK, Challis et al. (2011) examine the various factors which influence LiDAR intensity and explore several processing steps which can be undertaken to enhance the utility of LiDAR intensity analysis. Their results suggest that LiDAR intensity imagery can assist in the interpretation of airborne LiDAR data, where an intensity analysis could be used to augment the qualitative understanding of land cover, the burial environment of archaeological remains and the identification of anthropogenic archaeological crop marks (Table 2.2). According to Challis et al. (2008) in Bennett et al. (2010), LiDAR intensity data could also become a potential proxy for, or comparable to, conventional geophysical techniques like earth resistivity and Ground Penetrating Radar (GPR), where the relationship between LiDAR intensity and soil moisture values could be exploited.

Notwithstanding, Stott et al. (2015) consider a different approach. They experimented with multi-temporal airborne LiDAR and single-date full waveform LiDAR to detect variations in canopy biomass over archaeological features. Although some detection was achieved using metrics of the full waveform data, it was the multi-temporal method using discrete return data which showed the most potential in detecting and characterising archaeological vegetation marks.

### 2.5.5 Using SAR

Entrance points to cross border tunnels and urban tunnel networks change with time. Therefore, SAR change detection routines are a useful technique for identifying subsurface entry points, especially in regions where illicit subsurface activity is high. In particular, multi-date SAR products such as interferometric coherence and RGB multi-temporal composites are effective at monitoring this type of change (Chen et al., 2016). According to Tapete and Cigna (2019), one of the best methods to capture the dynamic change of a landscape is to ratio the radar backscatter signal between pairs of SAR scenes from a long time series. In turn, this will depict the spatial extent and distribution of any change. Alternatively, radar backscatter correlations around cross border tunnel sites could be calculated between pairs of SAR images, where correlation images are then generated (Table 2.2). High coherence values indicate high homogeneity and no change whereas low coherence could indicate the presence of clandestine activity along borders. This technique is more commonly termed ‘Coherent Change Detection’ (CCD), where both amplitude and phase are considered. However, ‘Incoherent Change Detection’ (ICD) also shows promise in identifying freshly buried objects (Airbus, 2022), where only changes in amplitude are analysed using high spatial resolution commercial SAR with short revisit times and low (penetrable) microwave frequency. Similar change detection techniques have also been used to locate anomalous change

in soil moisture content, vegetation cover, roughness, elevation and geomorphology over archaeological sites and mining regions prone to looting (Comer et al., 2017).

Chen et al. (2014) highlight four surface characteristics from subsurface features that can be observed in SAR imagery. These are “shadow marks”, “crop marks”, “soil marks” and “damp marks”. Shadow marks are found where very steep slopes generate shadows or when surface roughness contrasts significantly with the flatter surroundings. Crop marks over buried features can be identified when backscattering anomalies appear during a temporal analysis of a plant’s phenological cycle and soil and damp marks are found when strong, anomalous back scatter returns are seen from increased groundwater content over a subsurface discrepancy. Figure 2.7 depicts the clear distinction of a backscattering anomaly in bare ground, imaged over a subsurface archaeological structure by the COSMO-SkyMed constellation.

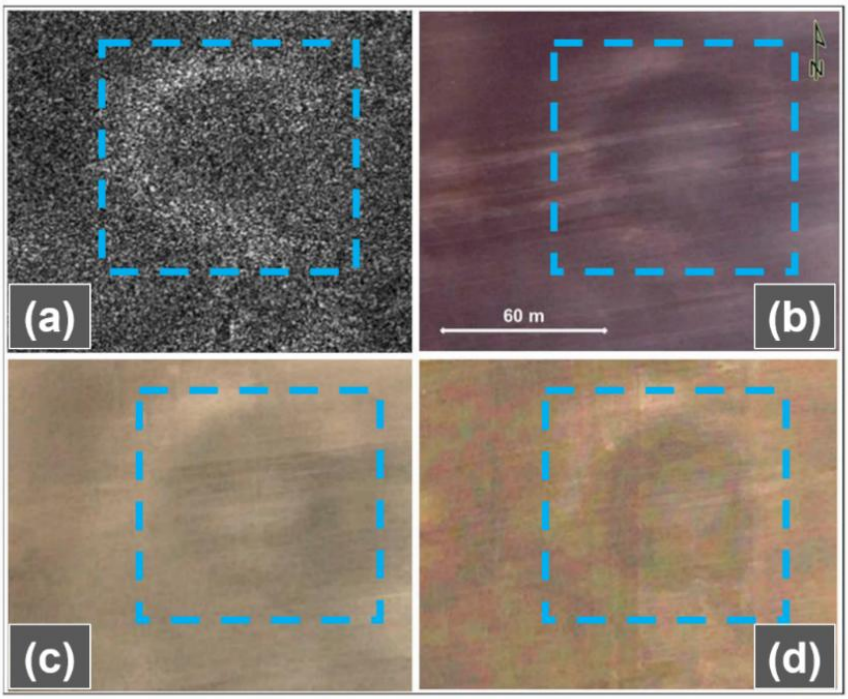



**Figure 2.7**. a). SAR backscatter anomaly from a partially buried archaeological structure, observed in a COSMO-SkyMed Enhanced Spotlight image at 1 m ground resolution and 39° incidence angle. The soil/damp mark is also visible in Maxar high-resolution optical satellite imagery acquired in b). summer, c). autumn and d). winter. Blue dashed box contains location and circular shape of partially buried archaeological feature. Figure adapted from Tapete and Cigna (2019).

**Table 2.2**
Airborne and spaceborne remote sensing techniques used for *visual identification*.

| Investigable Feature | Sensor Type | Remote Sensing Detection Technique | Example References |
|---|---|---|---|
| • Topographic relief patterns from buried subsurface structures<br>• Anomalous tone, height and density of crop marks<br>• Soil marks / discolouration anomalies | Photographic | 1. Geometrical measurements of anomalous visual indicators<br>2. Creation of digital elevation models (DEMs) from stereopairs<br>3. Image enhancement filters<br>4. Spatial contrast enhancement filters | 1. Sharafi and Khazaei (2013); Lasaponara and Masini (2014)<br>2. Luo et al. (2019)<br>3. Featherstone et al. (1999); Bewley (2003); Kucukkaya (2004)<br>4. Weber and Yool (1999); Deng et al. (2010) |
| • Changes in land use / land cover related to subsurface activity<br>• Spoil heaps and soil tracks from recent excavation of tunnels / mines<br>• New track formation and heavy plant equipment for tunnelling | Multispectral | 1. Spectral classification regimes<br>2. Change detection algorithms<br>3. Convolutional neural networks (CNNs) | 1. Mi et al. (2019)<br>2. Kwan (2019)<br>3. Perez et al. (2017); Li et al. (2019) |
| • Disturbed earth from tunnel excavation or object burial (e.g. landmines) | Hyperspectral | 1. Image resolution enhancement algorithms e.g. single super-resolution and multi-image resolution algorithms<br>2. Examine soil reflectance spectra for anomalies e.g. anomalous mineral radiance values along typical absorption lines | 1. Kwan (2018)<br>2. Shimoni et al. (2019) |
| • Anthropogenic micro-relief patterns<br>• Crop marks from subsurface abnormalities e.g. archaeological | Airborne LiDAR | 1. DEM/DTM/DSM relief visualisation techniques e.g. analytical hillshading, colour gradient elevation, slope analysis, 3D visualisation, contour analysis, local relief models (LRMs), Openness, Sky View Factor (SVF) and Principal Component Analysis (PCA)<br>2. LiDAR classification studies incl LiDAR intensity, multi-temporal LiDAR and LiDAR full waveform analysis | 1. Devereux et al. (2008); Zakšek et al. (2011); Roman et al. (2017); Moyes and Montgomery (2019); Lieskovský et al. (2022)<br>2. Challis et al. (2008); Lasaponara and Masini (2009); Challis et al. (2011); Stott et al. (2015) |
| • Human activity at subsurface entry points e.g. cross border tunnels<br>• Anomalous changes in vegetation cover, surface roughness and elevation over suspected subsurface features | SAR | 1. SAR change detection routines e.g. Coherent Change Detection (CCD), Incoherent Change Detection (ICD), RGB multi-temporal composites, correlation and ratio analysis between SAR scenes<br>2. Temporal analysis of backscattering anomalies throughout a plant's phenological cycle | 1. Chen et al. (2016); Comer et al. (2017); Tapete and Cigna (2019); Airbus (2022)<br>2. Chen et al. (2014) |

## 2.6 Detecting soil matrix irregularities

### 2.6.1 Using multispectral imaging

High levels of mineralogical leaching and poor and/or excessive drainage conditions in the soil matrix above near subsurface objects (like buried archaeological features) can degrade soil quality and stunt the growth of overlying vegetation (Figure 2.3). These irregularities in soil condition are frequently expressed in the health and reflectance characteristics of overlying vegetation and crops (Pascucci et al., 2010). Traditionally, these proxies have been documented in visible light as contrasting areas of grass or crop development, commonly referred to as cropmarks (James et al., 2020). However, a reliance on the visible electromagnetic spectrum has inherent limitations on what can be documented. Therefore, multispectral sensors with the ability to measure reflectance values outside visible bandwidths can enhance the detection of near subsurface anomalies under grassland (Bennett et al., 2012) and crops (Moriarty et al., 2019).

James et al. (2020) demonstrated this using two UAV mounted multispectral surveys over an archaeological site in eastern Scotland to produce vegetation index (VI) maps which assess the effectiveness of detecting anomalous crop responses in a temperate climate. The VI maps were analysed visually and statistically, comparing reflectance values on and off the buried archaeological foundations. Resultantly, the VIs statistically showed the potential to detect general crop stress from archaeological features across the site (Table 2.3).

The timing of a multispectral survey is also important. For example, Agapiou et al. (2013a) suggest the optimal time-window for monitoring accentuated barley and wheat crop marks over subsurface anomalies in Cyprus (and the wider Mediterranean region) is the first 15 days of their boot stage, a critical juncture and growing stage in the barley and wheat reproductive phase (Figure 2.8). They also use spectral separability indices (SSIs) like 'Euclidean Distance, 'Jeffries-Matusita (J-M) Distance', 'Mahalanobis Distance' and 'Cosine Similarity' to probabilistically assess the spectral separation of reflectance values from vegetation over known subsurface anomalies and those from the surrounding area (Table 2.3). The results indicate that spectral regions around the red edge and NIR spectrum (700 and 800 nm respectively) are the most effective at distinguishing soil matrix irregularities and crop marks from subsurface features in multispectral imagery.

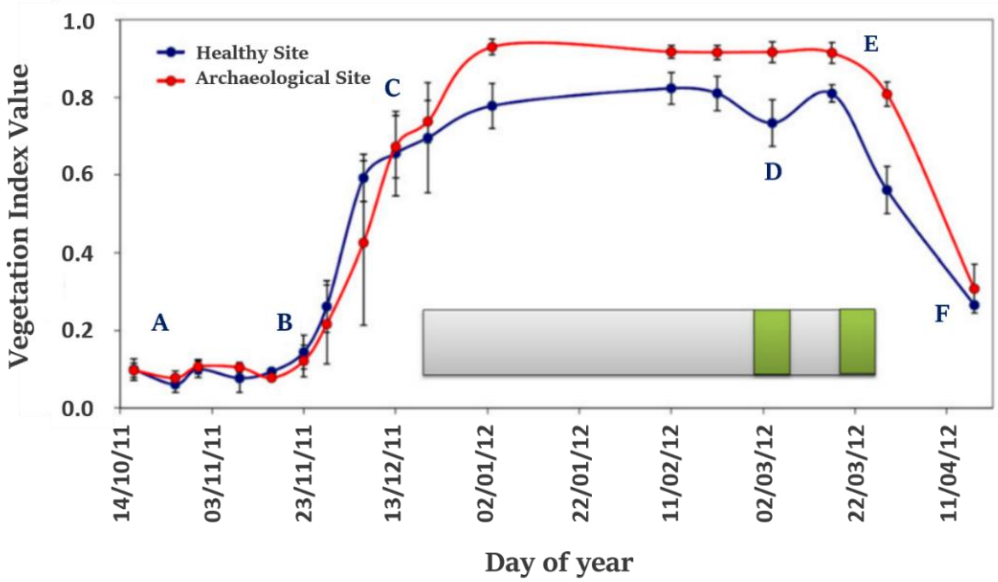



**Figure 2.8**. Temporal variation in vegetation index values (Normalised Difference Vegetation Index - NVDI) at Alampra in Cyprus reveal the phenological cycle of barley crops. The optimal period for remotely detecting crop marks over buried archaeological features is indicated by the grey bar. This is where the separability of the phenological cycles over buried archaeological objects (red line) and regular, healthy soil and crops (blue line) are at their greatest. The best phenophase for detecting accentuated spectral responses from crop marks over subsurface anomalies is shown in green. The time between these green markers denotes the boot stage - where crop development is significant during the reproductive phase of barley. Figure adapted from Agapiou et al. (2013a).

Temporal observations were also recorded by Dana Negula et al. (2020), who monitored temporal changes in the Normalised Difference Vegetation Index (NDVI), the Simple Ratio (SR) vegetation index and the Normalized Difference Water Index (NDWI) over the Micia and Germisara archaeological sites in Romania using Sentinel-2A multispectral imagery. Due to stressed crop

growth seen using the NDVI and SR, traces of a buried road were found connecting the Cigmău Fort to the baths in Geoagiu–Băi. The NDWI results were also useful, where the near-infrared (NIR) and short-wave infrared (SWIR) wavelengths were used to detect the North-East wall of the Micia Roman Fort. This latter index showcases the effectiveness of NDWI and the sensitivities of moisture content in plants and soil across a subsurface feature.

Agapiou et al. (2013b) take a slightly different approach, introducing linear orthogonal equations for several multispectral satellite sensors. Using PCA to create the initial eigenspace, eigenvalues were used to define the initial feature space before rotating into a new 3D orthogonal space. These linear transformations were able to re-project the visible to near infrared (VNIR) bands of a satellite image to a new 3D coordinate system where the first component became the “crop mark”, the second component “vegetation” and the third component “soil”. In all trials conducted by Agapiou et al. (2013b), the proposed equations were able to enhance the detection of soil matrix discrepancies and their respective crop marks (Table 2.3).

Stepping away from spectral transformations, Calleja et al. (2018) consider a multi-acquisition approach for detecting anomalous change in soil matrix. Here, they combine the use of multispectral imagery from WV2 with RGB and NIR cameras on a UAV to detect buried archaeological remains across Llanera, an ancient Roman population centre on the Iberian Peninsula in Spain. Dual mounted with a GNSS, the UAV data was used to generate true colour composites and a high precision DSM which, in conjunction with WV2 NDVI calculations, generated an archaeological binary map. This archaeological binary map subsequently contained pixels of anomalous NDVI value and normalized threshold elevation value which were thought to represent the location of buried archaeological remains. In total, seven crop marks associated with buried Roman structures were identified, reliant on the premise that buried archaeological remains exist at locations that exhibit both crop and microrelief marks with a similar shape. Therefore, integrating high-resolution and very-high-resolution (VHR) multispectral sensors from air and space can significantly enhance subsurface detection routines.

If needed, high-resolution multispectral imagery can also be pansharpened to guarantee even higher spatial fidelity (Table 2.3). Further, image fusion with temporally rich sensors like those on a Planet Dove satellite could be used to generate several high-resolution multispectral images over short time periods (Dao et al., 2017; Perez et al., 2017).

Alternatively, spectral enhancement indices and edge detection filtering can be used to improve the spatial resolution of an image and the chances of successfully detecting a subsurface discrepancy (Table 2.3). El-Behaedi (2021) uses multispectral enhancement indices to detect ground matrix irregularities at the ancient Egyptian site of Hermopolis. Using WorldView-3 (WV3) satellite imagery and edge-detection spatial filtering, the study uses the WorldView New Iron Index to identify iron oxide anomalies across the site. According to Nicholson and Shaw (2009), unfired mudbrick was

the most common building material in ancient Egypt and often used for the construction of various domestic installations. Sun-dried mudbricks comprise large amounts of clay, of which 5-6% is iron oxide ($Fe_2O_3$) (Hool and Johnson, 2010). Therefore, detecting the presence of iron oxide using multispectral imagery assisted El-Behaedi (2021) in the identification of seven subterranean structures. Similarly, Allbed and Kumar (2013) review several soil salinity indices which can be used to detect and map soil salinity and the anomalous groundwater behaviour above subsurface features. The indices have, according to Allbed and Kumar (2013), been employed with varying degrees of success although in general, a multispectral approach continues to showcase much promise in detecting halophytic plants, salt properties in soil and other salt-tolerant crops.

### 2.6.2 Using hyperspectral imaging

From studying the reflectance and emission spectrums over subsurface structures, hyperspectral radiance spectrums can be compared with spectra from the surrounding landscape to identify anomalies in reflectance or emission at particular wavelengths. This has numerous benefits in near subsurface exploration, where spectral returns in hyperspectral data can show anomalies in soil condition (Alexakis et al., 2009). These can be cross-referenced with various spectral libraries to determine specific ground conditions, chemical signatures and soil moisture properties (Thenkabail et al., 2014).

Doneus et al. (2014) explore this concept in detail, devising two new subsurface detection algorithms for hyperspectral imagery:

(i) The first algorithm, termed the Red Edge Inflection Point (REIP), identifies the wavelength, radiance value and maximum gradient in the 'Red Edge' transition zone for every pixel in a hyperspectral image. For healthy soil and vegetation, this transition zone is usually found at 700 nm, where a steep slope along the spectral reflectance curve denotes high absorption rates from chlorophyll pigments in the far-Red spectrum and high NIR reflection rates from spongy mesophyll (Doneus et al., 2014). However, when vegetation is stressed over subsurface objects, this 'Red Edge' transition shifts towards the shorter wavelengths, an effect which is more commonly termed a "Blue shift" of the 'Red Edge' (Horler et al., 1983; Gitelson et al., 1996). By identifying the location of the highest gradient in the Red Edge spectral profile for each pixel, the REIP algorithm can generate a three-band image visualising the optimal wavelength, steepest gradient and reflectance value of the REIP for every pixel in a scene (Doneus et al., 2014). In turn, this can delineate the location of stressed soil, stunted vegetation and anomalous subsurface entities (Table 2.3).

(ii) The second algorithm named 'Distribution Fitting' generates, for each hyperspectral pixel, a frequency histogram of the radiance values along the pixel's spectral signature, prior to fitting the histogram with a predefined Probability Density Function (PDF). In probability theory, various PDFs are used to mathematically describe the specific distribution of a random variable which in this case, are the reflectance values from the hyperspectral image. Once an optimal PDF is assigned across

each pixel (e.g., Normal, Gaussian, Rayleigh, Exponential, Weibull, Beta, Gamma), the algorithm parameterises the PDF and then the resultant parameters form the digital numbers (pixel values) of the newly generated image. Subsequently, the number of image layers equates to the number of parameters of the chosen PDF (Verhoeven et al., 2013). The resulting image can be used to depict clear contrasts between vigorous and stressed soil and in particular, vegetation and soil irregularities from buried objects (Doneus et al., 2014).

Studying VIs with hyperspectral data, Cerra et al. (2018) objectively estimated the suitability of several VIs for subsurface detection using Information Theory. They were able to compute the statistical mutual dependence between the extracted vegetation anomalies and a digital map (Table 2.3) which indicated the presence of buried archaeological structures from previous ground surveys. Based on the obtained scores over known archaeological features, the various VIs were ranked at each site and the most suitable were selected to assist in the discovery of previously undetected crop marks. Theoretical mutual information measurements using 'Shannon's Probabilistic Point of View' (Cover and Thomas, 1991) were then used to quantitatively estimate the mutual dependence of a given vegetation index and the location of buried archaeological features. Seen using a subset of the VI results from Selinunte in Sicily (Figure 2.9), the results show a clear gradation in VI effectiveness.

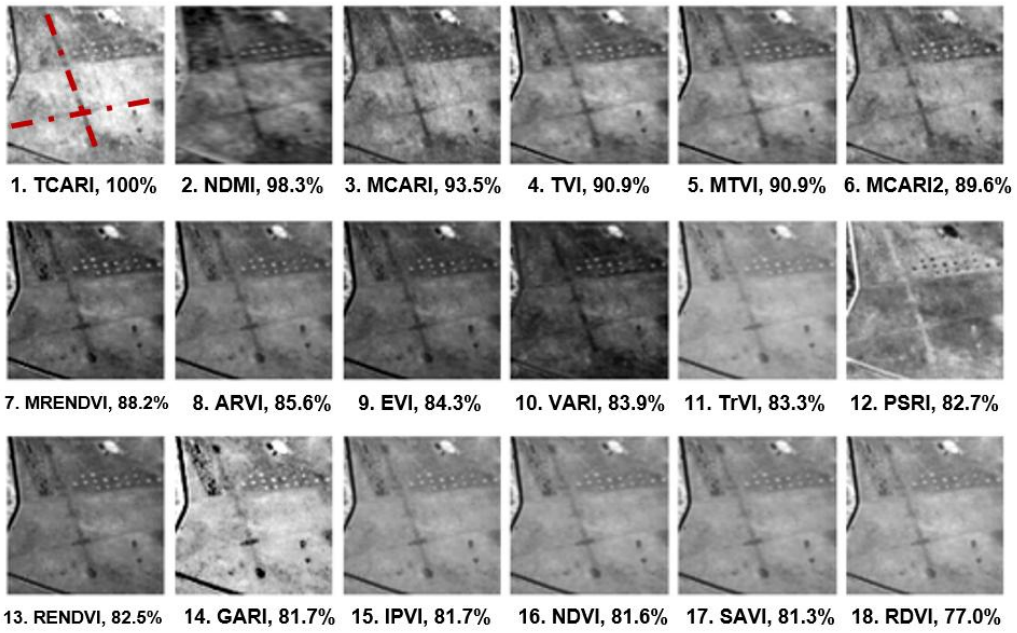



**Figure 2.9**. Eighteen vegetation (spectral) indices ranked from most effective (1) to least effective (18) using information theory and hyperspectral data over an area of an ancient buried crossroad at the Selinunte cultural heritage site in Sicily. An ancient crossroad (denoted by red dashed line in the TCARI image) is visible under the fields, detected when the mutual information value from the vegetation index scores highly. The buried crossroad then becomes less evident as the mutual information value decreases. Figure adapted from Cerra et al. (2018).

Another method for determining hyperspectral bandwidths sensitive to soil condition and subsurface irregularity is the application of SSIs (Bassani et al., 2009; Lasaponara et al., 2016).

Similarly, Spectral Angle Mapper (SAM) and Spectral Mixture Analysis (SMA) can be employed (Cavalli et al., 2009). The SAM determines spectral similarity on the basis of spectral shape, where the angular difference between the spectrum of every "quarantine pixel" *and* the spectrum of a pixel related to a subsurface feature is examined (Savage et al., 2012). Conversely, the SMA deconvolves an image using a spectral library over known buried objects to reveal the likelihood of a subsurface anomaly being present - for every pixel in an image (Savage et al., 2012).

### 2.6.3 Using SAR

The penetration capabilities of microwaves for mapping subsurface heterogeneities in soil, lithology, moisture and sedimentary structure have been explored by several authors like Grandjean et al. (2001). Experimental sites like the mobile Pyla Dunes near Bordeaux in France are ideal for such analysis, where significant deposits of low-loss sandy material frequently form from the erosion of the Pyrénées and the Massif Central. This weathering activity can produce large subsurface targets featuring multiple paleosols at varying depths (Grandjean et al., 2001).

By conducting a polarimetric analysis of airborne SAR data in the L-band, Grandjean et al. (2001) detect subsurface scattering effects from soil dielectric discontinuities at several places across the Pyla Dune. A series of surface roughness profiles were generated across the sand dunes which were then augmented using ground penetrating radar (GPR). The subsurface structures revealed by the GPR were seen to align with those detected by subsurface scattering from the polarimetric data analysis, allowing them to characterise the geometric and dielectric properties of the subsurface soil structure. The observed GPR profiles were then matched with simulated GPR profiles to produce a subsurface dielectric model adequate for inserting into their SAR scattering model. Consequently, SAR penetration depths were estimated by inverting the SAR scattering model, proving the effective subsurface penetration of L-band SAR. In parallel, the study also revealed the ground moisture detection potential of lower frequencies like P-band, which is capable of detecting subsurface moisture discontinuities up to 10 m deep.

Similar to the detection efficiency of multispectral VIs, SAR VIs are also sensitive to soil moisture content and the physiological conditions of overlying vegetation (Table 2.3). In Gonenc et al. (2019), remotely sensed correlations from agricultural study areas in Dicle University, Turkey, were observed between the Radar Vegetation Index (RVI) from a Radarsat-2 image and the NDVI from a Landsat-8 image. Zhang et al. (2024) have since progressed these observations, revealling a new SAR VI method for soil moisture retrieval over cropland; introduced as a novel dual-polarization SAR vegetation index (DRVI). Their research reveals successful DRVI trials in four different crop covered areas in the Carman test site in Canada, thereby showcasing DRVIs potential in the detection of shallow, subsurface anomalies in vegetated terrain.

Spaceborne SAR has also been used for imaging ground matrix irregularities in arid regions, where archaeological prospecting is frequently undertaken using L-band SAR sensors (Chen et al., 2017).

However, Wiig et al. (2018) demonstrate that shorter-wavelength SAR can also penetrate the subsurface. Using the C-band and X-band information from VV polarization TerraSAR-X bistatic and Radarsat-2 images at low incidence angles (30 to 40 degrees), they identify a subsurface paleo-channel 0.6 m – 0.7 m deep at the Iron Age archaeological site of Uqdat al-Bakrah (Safah) in Oman. To visually enhance the subsurface anomaly, they sum the images to increase the signal-to-noise ratio, apply a low pass 3 x 3 pixel window filter and a Grey Level Co-occurrence Matrix (GLCM) texture analysis to reduce the speckle and accentuate the location of the subsurface paleo-channel (Table 2.3). To improve the resolution of the study, Wiig et al. (2018) also recommend a follow-up investigation using even higher spatial resolution C-band and X-band SAR data (from a staring spotlight acquisition mode) and several multi-polarized products.

**Table 2.3**
Airborne and spaceborne remote sensing techniques used to detect *soil matrix irregularities*.

| Investigable Feature | Sensor Type | Remote Sensing Detection Technique | Example References |
|---|---|---|---|
| • Anomalous change in soil condition and vegetation health<br>• Contrasting areas of grass and crop development (crop marks)<br>• Soil marks / discolouration / soil salinity<br>• Anomalous concentrations of chemical compounds in soil e.g. Iron Oxide | Multispectral | 1. Statistically analysing vegetation index (VI) maps<br>2. Temporal analysis and statistical separability indices (SSIs) of reflectance values from VIs “on” and “off” suspected subsurface features<br>3. Linear transforms / orthogonal equations using spectral reflectance values<br>4. Integrating high-resolution datasets from several multispectral sensors<br>5. Image enhancement in spatial domain using image fusion and pansharpening techniques<br>6. Bespoke spectral enhancement indices (e.g. chemical compounds, soil salinity etc) and edge detection spatial filtering | 1. James et al. (2020)<br>2. Agapiou et al. (2013a); Dana Negula et al. (2020)<br>3. Agapiou et al. (2013b)<br>4. Calleja et al. (2018)<br>5. Lasaponara and Masini (2014); Dao et al. (2017); Perez et al. (2017); Kwan (2018)<br>6. Allbed & Kumar (2013); El-Behaedi (2021) |
| • Stressed vegetation and stressed soil | Hyperspectral | 1. Use spectral libraries to select optimal hyperspectral narrow bands for the identification of specific soil conditions and ground proxies<br>2. Examine spectral content for a "blue shift" of the Red Edge Inflection Point (REIP) and/or 'Distribution Fitting' using Probability Density Functions (PDFs)<br>3. Examine VIs and statistically assess mutual dependence or correlation between vegetation anomalies and ground truth datasets<br>4. Calculate and assess Spectral Separability Indices (SSI) between reflectance profiles from pixels “on” and “off” suspected subsurface anomalies<br>5. Use Spectral Angle Mapper (SAM) or Spectral Mixture Analysis (SMA) to detect the likely presence of a subsurface anomaly | 1. Thenkabail et al. (2014)<br>2. Doneus et al. (2014)<br>3. Cerra et al. (2018)<br>4. Bassani et al. (2009); Lasaponara et al. (2016)<br>5. Cavalli et al. (2009); Savage et al. (2012) |
| • Soil dielectric discontinuities in paleosols<br>• Soil moisture retrieval and vegetation growth<br>• Subsurface paleo-channels<br>• Buried archaeological features in arid environments | SAR | 1. Polarimetric data analysis using backscatter information from penetrable SAR bands<br>2. SAR vegetation indices (VIs) e.g., RVI, DRVI<br>3. Accentuate backscatter anomalies from penetrable SAR bands by employing image stacking (image summation) techniques, noise reduction filters and a Grey Level Co-occurrence Matrix (GLCM) analysis<br>4. SAR image enhancement using multi-looking, multi-temporal averaging and specialist noise filtration algorithms e.g. nonlocal-SAR noise reduction | 1. Grandjean et al. (2001); Patruno et al. (2013)<br>2. Gonenc et al. (2019); Zhang et al. (2024)<br>3. Wiig et al. (2018); Tapete and Cigna (2019)<br>4. Chen et al. (2016) |

According to Luo et al. (2019), numerous studies have used the frequency, polarization, incidence angle and scale of SAR to detect soil matrix irregularities and subsurface discrepancies. Both Patruno et al. (2013) and Chen et al. (2016) in Luo et al. (2019) trial different SAR bands, incidence

angles and imaging modes for the polarimetric analysis and detection of buried archaeological features in arid environments. To reduce speckle and improve the visibility of these features, SAR image enhancement methods were then used, comprising multi-looking, multi-temporal averaging and image filtration (Table 2.3).

## 2.7 Detecting anomalous groundwater behaviour

### 2.7.1 Using photogrammetry and multispectral imaging

Several early attempts to detect geomorphic surface anomalies for natural resource exploration (e.g., Mahajan et al.,1984; Mitra and Agarwal, 1991; Berger, 1994) were conducted using multispectral imaging. Waters et al. (1990) used various photographic and multispectral imagery enhancement techniques to identify unique groundwater patterns, tones and textures that locate subsurface structures like faults, joints, ductile shears, folds, dyke intrusions and veins. An assured location of these geological subsurface structures would, in turn, increase the likelihood of performing a successful groundwater exploration survey. Waters et al. (1990) also describe early applications of multispectral imaging to locate shallow aquifers where, in arid and semi-arid regions, multispectral classification methods helped identify areas of anomalous vegetation vigour which subsequently represented the presence of near-surface aquifers and buried river channels. However, due consideration to the season of imagery acquisition should be considered, where the low sun elevation in winter imagery is particularly useful in emphasising ground structure, geomorphology and areas of sustained near-surface moisture.

More recently, Saha (2022) reviewed some applications of airborne multispectral imaging in hydrocarbon exploration. When combined with geophysical and geochemical surveys, the multispectral study successfully identified several anomalous geomorphic features and groundwater regimes related to subsurface reservoirs. The study used spatial filtering techniques, spectral band ratios and PCA to identify anomalous drainage patterns and surface lineament characteristics that delineated the surface expressions of hydrocarbon tied structural traps (faults, fractures and domes) and multiple fracture zones (Table 2.4).

### 2.7.2 Using thermal infrared

Abdel-Hardy (1970) illustrated several early applications of anomalous groundwater detection using airborne TIR imaging. One component of the study used an 8 – 14 µm TIR image of a buried wet stream channel under a field in the campus of the University of California Davis. The TIR image depicted the outline of a buried stream channel which was bright and light in tone (high emissivity), contrasting with the darker tone (low emissivity) of the surrounding area. This revealed the higher specific heat capacity of the wetter soil in the buried stream channel, explaining why the channel remained warmer at night in comparison to the surrounding soil (which was drier and cooling at

greater rates). Abdel-Hardy (1970) also presented similar thermal applications in the detection of underground water conduits for civilian and military reconnaissance. Here, a TIR image was recorded in the early evening using the 8-14 µm TIR range, revealing a buried water conduit under Interstate Highway 35 near Dallas in Texas, US. When inspecting the imagery, the conduit under the paved highway generated a surface temperature along the overlying ground that was different to the adjacent paved sections of the highway, visualised as a linear anomaly in surface emissivity (Table 2.4).

### 2.7.3 Using hyperspectral imaging

In 2011, hyperspectral sensors with high spatial resolution and narrow spectral bands were used to quantify soil moisture levels across the Little River Experimental Watershed in Georgia (Finn et al., 2011). Spectral observations from airborne hyperspectral data containing SWIR information were statistically correlated with soil moisture probe data at 5.08 cm, 20.32 cm and 30.48 cm in depth. Results showed that the SWIR bands could determine values and variations in soil moisture at depths to 5.08 cm but less likely at greater depths. In particular, SWIR wavelengths in the 1300 nm to 1670 nm range were particularly sensitive to soil moisture levels (Table 2.4), achieving 'coefficient of determination' values ($R^2$ values) above 0.70 (Finn et al., 2011). Keller et al. (2018) then take this even further, using hydrological, geophysical and hyperspectral data in a supervised machine learning approach to estimate, with some success, the subsurface soil moisture across a grassland site in Linkenheim-Hochstetten, Germany (Keller et al., 2018).

### 2.7.4 Using airborne LiDAR

Given the breadth of visual and textural analysis tools available to LiDAR, Hofierka et al. (2018) adopt a combined visual and textural approach to locate and map karst sinkholes in the Slovak National Park in Slovakia. They considered four very different approaches: contour mapping, DEM sink-filling, numerical water flow simulation and a manual inspection of hillshaded DEMs (Figure 2.10). Each method identified varying numbers of sinkholes with varying spatial extents. These detections were then verified with a supporting field investigation. Such ground reconnaissance is often crucial, especially when detecting generically shaped surface depressions across large study regions.

### 2.7.5 Using SAR

The identification of strong, anomalous backscatter returns from increased ground water content in SAR imagery can reveal the location of soil and damp marks over near-surface objects (Chen et al., 2014). Also, polarimetric data analysis using backscatter information from penetrable SAR bands can detect anomalous subsurface moisture variations in and above subsurface anomalies (Grandjean et al., 2001; Patruno et al., 2013). A hydrological analysis using SAR-derived DEM products (Bubenzer and Bolten, 2008) could also be considered (Table 2.4). As an example, Luo

et al. (2017) used a DEM derived from the Shuttle Radar Topography Mission (SRTM) to generate a groundwater model. They then use a series of GIS hydrological analysis tools to reveal an ancient moat system under the Panlongcheng archaeological site in China.

In contrast, Ghorbani et al. (2022) adopt a very different approach. They use an Interferometric Synthetic Aperture Radar (InSAR) technique to detect regional-scale land subsidence across the Ardabil Plain in Iran. This revealed significant groundwater withdrawal from reduced rainfall and active pumping. Similar InSAR techniques are reviewed in Section 2.8.3.

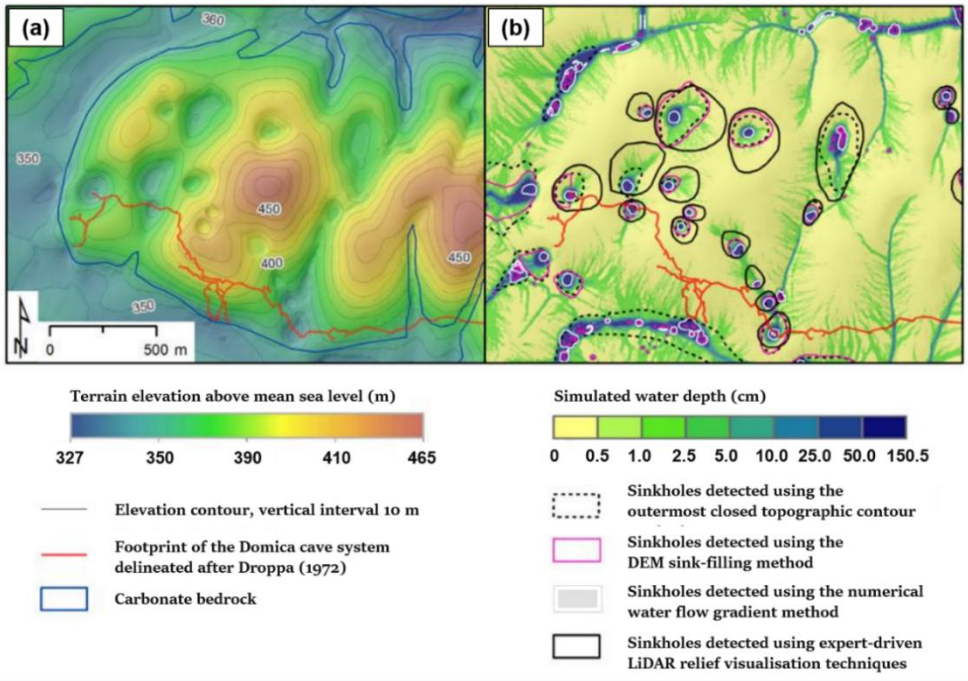



**Figure 2.10**. Detecting sinkholes in a forested karst landscape in Slovak National Park using airborne LiDAR. a). Hillshaded DEM of the study area showing contours at 10 m intervals, the footprint of the Domica cave system and the spatial extent of the carbonate bedrock. b). Sinkholes detected in LiDAR derived DEM using four different methods: contour mapping (dashed polygons), DEM sink-filling (pink polygons), water flow simulation (polygons with white outline and light grey fill) and a manual inspection of hillshaded DEMs (black polygons). Figure adapted from Hofierka et al. (2018).

## 2.8 Detecting surface elevation change

### 2.8.1 Using photogrammetry

Air and space photogrammetry allow an object's height to be determined using relief displacement from both a single vertical photograph and in the overlapping section of a stereopair. Topographic maps and DEMs can be generated from the same principle, producing useful products that can assist with the identification of subsurface features, especially when investigating localised changes in surface elevation and ground subsidence. Various DEM visualisation techniques can then be used to accentuate surface elevation change over subsurface features (Table 2.5). Such techniques include hillshade analysis, colour gradient elevation, slope analysis and shadow pattern analysis (Luo et al., 2019).

**Table 2.4**
Airborne and spaceborne remote sensing techniques used to detect *anomalous groundwater behaviour*.

| Investigable Feature | Sensor Type | Remote Sensing Detection Technique | Example References |
|---|---|---|---|
| • Underground drainage<br>• Subsurface moisture system | Photographic | 1. Image enhancement filters to identify unique groundwater shapes, patterns, tones and textures | 1. Waters et al. (1990) |
| • Geomorphic surface anomalies (e.g. sinkholes, shake holes)<br>• Anomalous drainage patterns | Multispectral | 1. Imagery enhancement using spatial filtering techniques<br>2. Multispectral classification, spectral band ratios and PCA | 1. Waters et al. (1990); Berger (1994)<br>2. Saha (2022) |
| • Buried stream channel (wet fill)<br>• Underground drainage systems | Thermal Infrared | 1. Time of image planned to maximise emissivity contrast between subsurface water/moisture target and surrounding area | 1. Abdel-Hady (1970) |
| • Soil moisture anomalies | Hyperspectral | 1. Inspect spectral behaviour of SWIR bands between 1300 - 1670 nm for radiance anomalies | 1. Finn et al. (2011) |
| • Karst sinkholes | Airborne LiDAR | 1. Contour analysis<br>2. DEM sink-filling<br>3. Numerical water flow simulation across DEM<br>4. LiDAR relief visualisation techniques | 1. Hofierka et al. (2018) |
| • Anomalous soil and damp marks over near-surface objects<br>• Soil dielectric discontinuities and subsurface moisture variations in paleosols<br>• Ancient subsurface hydrological systems e.g. moats<br>• Groundwater withdrawal; significant changes to groundwater level | SAR | 1. The identification of strong, anomalous backscatter returns from increased ground water content<br>2. Polarimetric data analysis using backscatter information from penetrable SAR bands<br>3. Building and analysing groundwater models using SAR derived DEMs and specialist GIS analysis tools<br>4. Time series Interferometric Synthetic Aperture Radar (InSAR) techniques | 1. Chen et al. (2014)<br>2. Grandjean et al. (2001); Patruno et al. (2013)<br>3. Bubenzer and Bolten (2008); Luo et al. (2017)<br>4. Ghorbani et al. (2022) |

### 2.8.2 Using airborne LiDAR

Recent airborne LiDAR applications recognise the importance of filtering and classifying ground and non-ground data points, especially when detecting surface elevation change from subsurface features. In archaeological prospecting, small surface elevation discrepancies can reveal the presence of significant underground entities and it is therefore crucial to filter and classify the raw data correctly before generating accurate DTMs for subsurface interpretation. According to Meng et al. (2010), filtering methods can be grouped into six operating categories: segmentation-based, morphological-based, directional scanning, contour-based, triangulated irregular network-based and interpolation-based. If specific characteristics of the study area are unknown, experimenting with all filtering modes is pragmatic, as is the experimentation with various interpolation methods used to create the DEM, DTM or DSM (Table 2.5). The most well practiced interpolation techniques for shallow subsurface detection include inverse distance weighting (IDW), kriging, minimum curvature, the modified Shepard's Method, natural and nearest neighbour, polynomial regression, radial basis function, triangulation with linear interpolation, moving average and local polynomial (Luo et al., 2019 and references therein). Again, the most suitable technique depends on specific research objectives and the physical characteristics of the study area.

If data availability allows, LiDAR derived DEMs can also be used temporally to detect and quantify changes in the three-dimensional position, shape and volume of objects and surfaces (Lillesand et al., 2015). By acquiring repeat LiDAR datasets over subsurface targets at multiple points in time, fine-scale topographic changes in land subsidence can be recorded (Table 2.5). Often termed 'DEMs of difference (DoD)', such techniques can be used to detect ground subsidence over near-surface tunnels, mining districts, sinkholes and shake holes (James et al., 2012). In the Bieszczady Mountains in Poland, many soil piping-related depressions were found using these DEM subtraction techniques. Initially, a LiDAR derived DEM was "sink-filled" and then it was subtracted from the raw DEM (Bernatek-Jakiel and Jakiel, 2021) to reveal a series of prospective piping-related ground depressions (Table 2.5).

In karst landscapes, Weishampel et al. (2011) chose to use LiDAR derived DEMs a little differently, using a 1-m resolution DEM of the ancient Maya site of Caracol in western Belize with a gradient elevation index (Topographic Position Index – TPI) to detect geomorphological features like vertical shafts, depressions and cave entrances across 200 km$^2$ of forested landscape (Figure 2.11). Weishampel et al. (2011) located 61 depressions with at least 10 m elevation change in circular areas of no more than 25 m radius. Trier and Pilø (2012) pursue similar objectives by convolving a DEM with small elevation templates of the surface expression of a subsurface target. This technique was put to good effect when they generated a series of hemispherical elevation templates of iron age pit structures which were then convolved with a DEM to reveal the likely location of ancient pit structures across Oppland County, Norway. This process was acknowledged by the Norwegian Directorate for Cultural Heritage as a cost-effective method for detecting, monitoring and protecting cultural heritage sites from mining, agricultural production, urbanisation and national energy programmes.

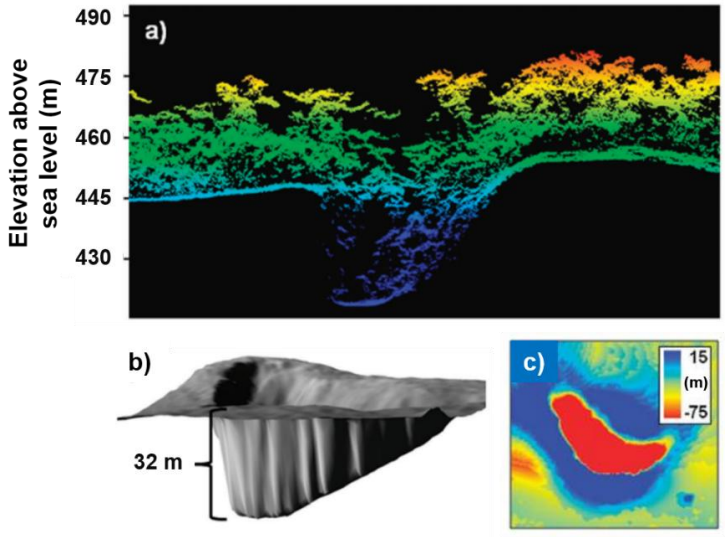



**Figure 2.11**. a). Airborne LiDAR point-cloud data of the ancient Maya site of Caracol in Belize, depicting the forest canopy and ground surface along a transect across one of 61 vertical depressions (caves, mines and sinkholes) discovered using the Topographic Position Index (TPI). b). 3D rendering of LiDAR derived DEM around same depression. c). Aerial view of the TPI image, depicting relative elevation of the same vertical depression in meters. Figure adapted from Weishampel et al. (2011).

### 2.8.3 Using SAR

The backscattering characteristics from air and spaceborne SAR can identify subsurface entry points across large study regions (Table 2.5). Carrer et al. (2015) explore this concept using high resolution commercial SAR data from the Capella Space X-band microsatellite radar constellation to resolve various cave geometries and accessibility characteristics across the Volcan de La Corona Region in Spain, the Volcan Wolf and Volcan Ecuador Region and the Sotano de la Lucha sinkhole in Mexico. The study was configured to detect cave systems with skylights, thereby making full use of SAR's side-looking acquisition geometry to determine whether the skylight can provide access to a cave or if in fact it simply represents a closed depression with no subsurface extension. They use a bespoke radar backscattering model and various radiometric conditions which are defined by the reflected signal, backscattering coefficient, local incidence angle and slant range. As a result, quantitative metrics of the subterranean cave size were retrieved for caves accessible by skylights, allowing the authors to assess the feasibility of human or robotic access for geological and ecological research purists.

Phase information in SAR data can also be used to accurately measure changes in surface elevation using a process called SAR Interferometry (InSAR). This process generates a SAR interferogram by computing the phase difference between two SAR images of the same area at different dates and time. This SAR interferogram subsequently reveals changes in phase for each pixel in the image which in turn, depicts an increase or decrease in the distance from the ground pixel to the SAR platform along the acquisition platform's line of sight (Ferretti et al., 2021). A temporal analysis using successive interferograms (often termed as differential InSAR - DInSAR) is then used to accurately measure the rate of ground subsidence over, for example, sinkholes and tunnels (Scoular et al., 2020) or groundwater extraction sites (Ng et al., 2018).

DInSAR has been used to preserve, manage and protect urban landscapes, mining districts, cultural heritage sites and various tunnels worldwide (Barla et al., 2016; Alberti et al., 2017; Da Lio and Tosi, 2018; Scoular et al., 2020; Aljammaz et al., 2021; Macchiarulo et al., 2021; Ramirez et al., 2022). For example, from knowing that ore bodies in soft rock can trigger unexpected surficial collapse at the surface, Ammirati et al. (2020) employed DInSAR to detect illegitimate gold mining in Ecuador. Using 89 ascending images and 51 descending images from Sentinel 1 data collected between 2015 and 2019, they generated 793 ascending interferograms and 271 descending interferograms which were then used to calculate ground subsidence from illegal artisanal mining in Zaruma, Ecuador.

Advanced DInSAR techniques (A-DInSAR) have also been used to detect subsurface features (Table 2.5). Bonì et al. (2017) evaluated these techniques over three test sites in Europe, where linear, non-linear and seasonal land subsidence anomalies were identified. Seasonal movements were detected using A-DInSAR in conjunction with a PCA, and new information about the deformation typology of the Alto Guadalentín aquifer in Spain was deduced. Another A-DInSAR

approach was undertaken by Anantrasirichai et al. (2021), where deep learning CNNs were used with sparse satellite InSAR data to detect: several areas of coal mining subsidence, uplift due to dewatering, slate quarries, landslides and tunnel engineering works across the UK. A pre-trained CNN was adapted to detect the ground deformation from national scale ground velocity maps from 2015 to 2019. The sparsity of measurement points and the presence of spike noise was overcome using spatial interpolation, enhanced over-wrapping techniques and a synthetic training dataset of a UK velocity map. The results show much potential in the generation of automated ground motion analysis systems with CNNs.

**Table 2.5**
Airborne and spaceborne remote sensing techniques used to detect *surface elevation change*.

| Investigable Feature | Sensor Type | Remote Sensing Detection Technique | Example References |
|---|---|---|---|
| • Buried archaeological feature / infrastructure<br>• Subsidence over sinkholes, shake holes and near subsurface tunnels and caves | Photographic | 1. DEM creation from stereopairs and DEM visualisation techniques (e.g. hillshade, colour gradient elevation, slope analysis etc) | 1. Luo et al. (2019) |
| • Buried archaeological features<br>• Buried ditches, pits and water channels<br>• Vertical depressions e.g. sinkholes and sumps over near-surface tunnels<br>• Horizontal and vertical cave entrances<br>• River valley floors | Airborne LiDAR | 1. Ground filtering of LiDAR point cloud data to determine returns from ground and non-ground surfaces<br>2. DEM, DTM and DSM generation using different interpolation algorithms<br>3. DEM subtraction (DEMs of difference) using multiple LiDAR derived DEMs from different acquisition dates or via "sink-filling" DEM prior to subtraction<br>4. Surface elevation detection techniques e.g. Topographic Position Index (TPI), Topographic Ruggedness Index (TRI), positive and negative openness indices (POI/NOI) and DEM convolution with small elevation templates of surface expression from subsurface target | 1. Meng et al. (2010)<br>2. Luo et al. (2019)<br>3. James et al. (2012); Bernett-Jakiel and Jakiel (2021)<br>4. Weishampel et al. (2011); Trier and Pilo (2012); Bernett-Jakiel and Jakiel (2021) |
| • Surface roughness from partially buried objects (e.g. archaeological)<br>• Land subsidence in karstic environments, urban zones, mining districts and tunnel sites<br>• Cave geometries with skylights in lava tubes and karstic sinkholes<br>• Deformation typology of underground aquifers<br>• Elevation change from groundwater extraction regimes | SAR | 1. Generating radar backscattering models with variable radiometric conditions<br>2. Differential InSAR (DInSAR) and Advanced DInSAR (A-DInSAR)<br>3. Deep learning CNNs and DInSAR data for automated ground motion analysis and automated indicators and warnings for land subsidence | 1. Carrer et al. (2015)<br>2. Barla et al. (2016); Alberti et al. (2017); Boni et al. (2017); Da Lio and Tosi (2018); Ammirati et al. (2020); Scoular et al. (2020); Aljammaz et al. (2021); Macchiarulo et al. (2021); Ramirez et al. (2022)<br>3. Anantrasirichai et al. (2021) |

## 2.9 Detecting heat retention anomalies

### 2.9.1 Using thermal infrared

Given the spatial resolution limitations of spaceborne thermal remote sensing, any heat retention anomaly detected from space must come from a significantly large subsurface feature or

widespread underground activity (Sabins, 1997). That said, Van der Meer et al. (2014) undertook a comprehensive review on the TIR detection of geothermal resources. They explored various direct and indirect TIR detection methods that were sensitive to specific geothermal surface proxies like alteration mineralogy, heat fluxes, geobotanical anomalies and Earth surface deformation. These surface manifestations revealed the approximate location and extent of geothermal reservoirs below ground, where meteoric water in the various permeable and porous rock formations is trapped.

Using a case study from the La Pacana caldera geothermal field in the Chilean Andes, Van der Meer et al. (2014) used daytime and night-time Advanced Spaceborne Thermal Emission and Reflection Radiometer (ASTER) imagery to conduct a comprehensive geologic interpretation of the mineralogy and emissivity. Geothermal anomalies were mapped using the night-time ASTER images, where the complexities of differential solar heating were reduced (Figure 2.12).

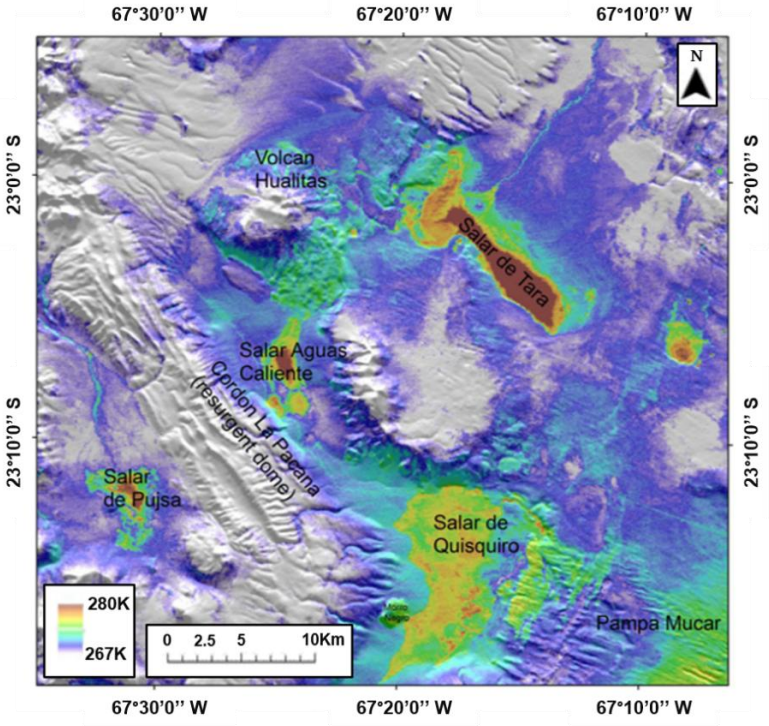



**Figure 2.12**. Temperature anomaly map of the La Pacana caldera geothermal field, Chile. The empirical topographic temperature correction from Ulusoy, Labazuy and Aydar (2012) was used on ASTER night-time imagery to reveal the location of several thermal anomalies from subsurface geothermal reservoirs near and under the salt flats (salars). Figure adapted from Van der Meer et al. (2014).

As expected, the tops of volcanoes showed low temperature values due to high altitude, and the steep flanks of the volcanoes showed higher temperature values due to residual differential heating from the day. To correct for these effects, Van der Meer et al. (2014) used an empirical topographic temperature correction from Ulusoy et al. (2012) which used terrain elevation, slope and aspect derivatives from SRTM data to develop empirical relationships between the topographic parameters

and measured surface temperatures. The result was a relative temperature map (Figure 2.12), where the effect of topography was suppressed and the temperature anomalies were made relative to the mean temperature, revealing several thermal anomalies from subsurface geothermal reservoirs near and under the salt flats (salars). In parallel, the daytime ASTER imagery was used to map clay, silica anomalies and other alteration minerals. By using various band ratio techniques to enhance absorption features (including the five TIR bands), and from studying pseudo reflectance curves, different mineral assemblages associated with near-surface thermal systems were identified across the caldera and consequently, the location of suspected geothermal reservoirs below ground were identified (Table 2.6).

Another common subsurface heat signature is underground coal fire, identified as both a heat source and a combustion site. The heat energy produced is transferred by air convection through cracks and holes in the ground and by conduction through bulk rocks, forming different types of thermal anomaly at the surface. Field observations and temperature measurements show that localized high-temperature thermal anomalies are typically related to holes and cracks (c.1 – 10 m long and c.1 – 30 cm wide) while low-temperature thermal anomalies are generated by thermal conduction, often producing regional scale thermal anomalies proportional to the size and depth of the underground fire (Wang et al., 2015).

In China, recent coal fire investigations have been done from space. Du et al. (2022) use the TIR bands in night-time ASTER images of the Huangbaici and Wuhushan mining areas in the Wuda coalfield in Inner Mongolia, China, from 2002, 2003, 2005 and 2007 to understand and monitor the way underground coal fires spread across a region. An adaptive-edge-threshold algorithm was used to detect and perform a time-series analysis on the underground coal fires across the study area (Table 2.6).

China is also invested in thermal airborne surveys of archaeological sites. In 2002, a project entitled ‘Synthetic Archaeological Studies with Remote Sensing and Geophysics Survey’ on the Mausoleum of the Emperor Qinshihuang (MEQ) (259–210 BC) was incorporated into the National High Technology Research and Development Program of China (Tan et al., 2006). The project employed thermal remote sensing techniques and geophysical survey to map the distribution of various historic artefacts and detect the architecture of an underground palace. In 2003 both daytime and night-time thermal images of the MEQ were acquired using an Operative Modular Imaging Spectrometer (OMISII) on a fixed wing aircraft. Thermal anomalies were identified over a pyramid shaped mound which were confirmed, using magnetics, to delineate the extent of the underground palace (Tan et al., 2006). Furthermore, the “thermal high” from the compacted soil which buried an ancient tomb was easily distinguishable from the surrounding soil matrix because densely packed soil has a stronger heat conductivity than the lightly packed soil in surrounding areas.

Casana et al. (2017) have also undertaken and reviewed several subsurface investigations using airborne TIR. They promote the efficiency of UAVs, using drones and specialist camera configurations for subsurface investigations. Here, the UAVs are flown at fixed altitudes and constant speeds whilst suppressing flight vibrations. They also use specialist software to control UAV speed, camera orientation and flight plans with Global Positioning System (GPS) guided waypoints (Table 2.6). Casana et al. (2014) trialled UAV thermal imaging over a pre-historic Chaco-period archaeological site named 'Blue J', located in New Mexico, US. They used Agisoft PhotoScan software to produce both colour and thermal ortho-imagery via the extraction of numerous still images from the video feeds recorded by the camera. The software used feature extraction and matching capabilities with traditional aero-triangulation to create accurate orthorectified thermal imagery and digital surface models from the overlapping two-dimensional imagery. These thermal products identified new archaeological features that were originally undocumented, including wall extensions, room block layouts and buried pit structures (Casana et al., 2014).

More recently, Hill et al. (2020) explored the utility of UAV-optimized radiometric thermal cameras for archaeological investigation, where in combination with VNIR multi-spectral sensors, they detect buried building foundations of several 18th century Shaker buildings in New Hampshire, US. By flying fifteen UAV surveys over the Enfield Shaker Village on seven different occasions in several different seasons, they could monitor the localised temperature fluctuations across the diurnal and seasonal cycle and optimise their choice of imagery for subsurface detection. Various detection techniques were employed, including the generation and interpretation of a multi-band false colour composite, comprising data values from twelve different thermal surveys and four bands of multi-spectral data. They also derived the first three principle components of the same multi-band image as a false colour composite and performed a temperature difference study (thermal image subtraction) between thermal images recorded at different times of the day and/or the year (Table 2.6). A study over a suspected 18th century building foundation under flat grassland using 'oblique time-lapse recording' of high-resolution thermal imagery delineated the building foundations in various tonal visualizations, and demonstrated the fluctuations in temperature contrast and thermal inertia throughout the night (Figure 2.13).

Other subsurface structures susceptible to TIR imaging are caves and in particular, cave entrances. Cave entrances appear as warm features in night-time thermal imagery and cool features in daytime thermal imagery, explained by the stabilisation of deep interior cave temperatures (Thompson and Marvin, 2005; Wynne et al., 2008). Consequently, Wynne et al. (2021) explored thermal predawn, midday and image differenced airborne imagery for detecting caves and ascertained which image type was most effective. Using a thermal imagery dataset of the Pisgah Lava Field in the eastern Mojave Desert, California, US, they also examined the effectiveness of slope, TPI and curvature to detect lava tube caves across the study area using pixel level assessments. Pixels were grouped into spatial clusters to examine pixel aggregations of known caves and non-cave landscapes. Their

cluster analysis revealed that predawn and differenced imagery were more effective than midday imagery, and that cluster analysis is a necessary step for identifying and predicting cave locations in thermal imagery (Table 2.6).

Finally, numerical simulations have now been used to understand how TIR remote sensing can detect underground facilities like military installations in a mountainous body (Deng et al., 2022). By assuming the heat transfer law of a distributed underground target in a mountain follows the mathematical model of heat conduction, the temperature field distribution of the Yujiashan mountain and its various underground targets was determined in China (Deng et al., 2022; Shi et al., 2022). Deng et al. (2022) showed that the thermal field generated by the superposition of the mountain and subsurface target can be mathematically expressed and that ultimately, the position of underground targets may be located using multi-temporal TIR images of the mountain, a high precision DSM and some grid level modelling of the direct solar radiation, scattered radiation and radiation from surface vegetation (Table 2.6).

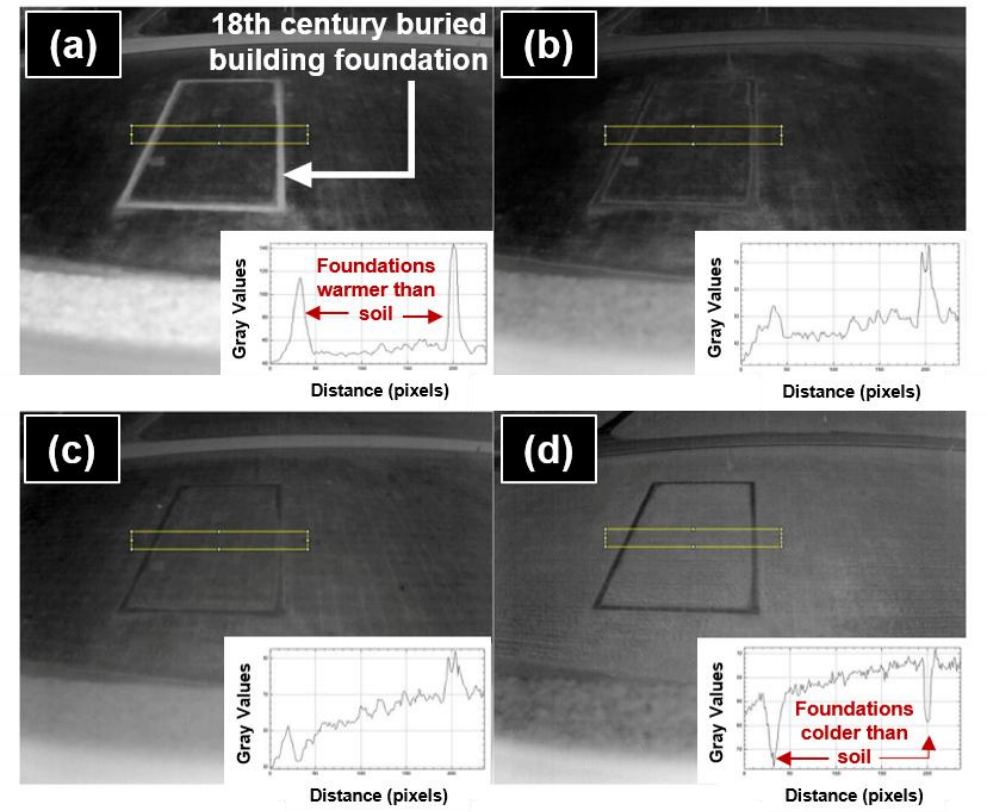



**Figure 2.13**. Four airborne thermal images of an 18th Century buried building foundation in the Enfield Shaker Village in New Hampshire, US. All four images (a – d) were taken using thermal oblique time-lapse recordings from different times in the night. Inside the yellow box, a temperature profile has been recorded across the buried building foundation, with results shown in the respective line graphs. a). Image taken just after sunset when foundation stones are warmer than surrounding soil matrix; b). A few hours after sunset when foundation stones have cooled; c). Dew appears in early morning and thermal contrast is further reduced; d). Taken after dawn when foundation stones are colder than surrounding soil matrix. Figure adapted from Hill et al. (2020).

### 2.9.2 Using hyperspectral imaging

In support of defence and security research, hyperspectral data has been used to detect the thermal signatures from several abandoned mine and cave entrances across the Skidoo Mining District in Death Valley National Park in California, US (Shen and Roettiger, 2012). Here, the thermal contrast between the mine or cave entrance and the ambient environment was regarded a discriminatory signature (Wynne et al., 2008), in conjunction with a water vapour absorption line at 12.55 µm wavelength and a quartz absorption feature at 9.25 µm (Table 2.6). Using LWIR hyperspectral data from a Twin Otter aircraft, a temperature and emissivity separation algorithm was applied to the LWIR data to generate a temperature map and an emissivity data cube of the scene. Second, by knowing that cave and mine entrances exhibit cooler thermal properties than their surroundings during the day (Thompson and Marvin, 2005), the thermal contrasts derived from the temperature map were used to delineate several prospective cave and mine entrances across the study area. Third, to increase confidence ratings, the emissivity of two absorption lines were used to reduce the number of false positives in the dataset. The first absorption line was 9.25 µm where quartz, an abundant mineral in many mining areas, typically exhibits strong absorption features. However, soils near mine and cave entrances present an absorption deficit due to the disturbed nature of the ground. The second absorption line was 12.55 µm, where water vapour (i.e. humidity) in the vicinity of caves and mine entrances is higher than the surrounding area, generating higher levels of absorption in this range. Subsequently, Shen and Roettiger (2012) observed new cave and mine entrances outside of their ground truth dataset.

**Table 2.6**
Airborne and spaceborne remote sensing techniques used to detect *heat retention anomalies*.

| Investigable Feature | Sensor Type | Remote Sensing Detection Technique | Example References |
|---|---|---|---|
| • Geothermal reservoirs<br>• Thermal plumes<br>• Underground coal fires<br>• Buried ditches and water channels<br>• Caves<br>• Buried archaeological features<br>• Tunnels / conduits<br>• Underground military facilities / civilian infrastructure | Thermal Infrared | 1. Collect thermal imagery when thermal inertia contrasts are high<br>2. Enhancement using TIR band ratios / edge enhancement filters<br>3. PCA on multi-band thermal images<br>4. Thermal image subtraction between different images in time<br>5. Oblique time-lapse recording<br>6. Empirical topographic temperature corrections<br>7. Slow and stable UAV collection platforms<br>8. Mission-planning software to program autonomous flights<br>9. Terrain analysis, terrain descriptors and pixel cluster analysis<br>10. Numerical simulation of heat transfer from distributed subsurface targets | 1. Del Grande (2009); Casana et al. (2017)<br>2. van der Meer et al. (2014); Du et al. (2022)<br>3. Hill et al. (2020)<br>4. Grande et al. (2013); Casana et al. (2017)<br>5. Hill et al. (2020)<br>6. Ulusoy et al. (2012)<br>7. Hill et al. (2020)<br>8. Casana et al. (2017)<br>9. Wynne et al. (2021)<br>10. Deng et al. (2022) |
| • Cave and mine entrances | Hyperspectral | 1. Thermal emissivity contrasts and absorption line analyses in LWIR hyperspectral data cubes<br>2. Increased water vapour content in air pixels | 1. Shen and Roettiger (2012) |

## 2.10 Detecting subsurface density anomalies

### 2.10.1 Using airborne gravity

Detecting subsurface density contrasts with airborne gravity is routine across academic and commercial applications. More recently, the use of airborne gravity was reviewed across the Jordan Dead Sea Transform (DST) Zone, where several potential field investigations of the Jordan DST were conducted to detect and evaluate the structural framework and lithologies across the region (El-Kelani, 2020). Airborne gravity data was collected to assist terrestrial gravity studies in revealing the geometry of the DST pull-apart basins, the depth of the basement and the dimensions of various magmatic intrusions and volcanic centres. Gravity data was also used to assess the spatial distribution of salt diapirism along the DST zone and the identification of underground salt structures in the Dead Sea basin (Choi et al., 2011). Additionally, gravity data was used to locate karst sinkholes and detect salt formations along the Dead Sea coast (Ezersky et al., 2013).

Most of this data was collected by the Natural Resources Authority in Jordan and in total, 100,000 gravity stations were deployed and augmented by airborne gravity (Götze et al., 2010), reinforcing data coverage on both sides of the Dead Sea basin (Götze et al., 2007). To enhance the various frequency components of the gravity fields, a variety of filtering techniques were employed (Table 2.7). Firstly, first and second derivatives of the residual Bouguer Anomaly (i.e. difference between observed and corrected gravity measurements and base station readings) were calculated to highlight the fault patterns around the Dead Sea basin and Lake Tabeires (Segev and Rybakov, 2011). Secondly, horizontal gradient analyses of the gravity field were applied to detect the discrete border of causative bodies at depth, revealing information about the deep structure of the Carmel fault zone (Achmon and Ben-Avraham, 1997). Thirdly, an isostatic regional gravity field of the southern transform region was produced, enhanced by the curvature analysis of local features in the isostatic residual gravity field (Götze et al., 2007). Finally, a wavelength filtering technique was used to separate the regional-residual gravity anomalies north of the Dead Sea basin. The residual field revealed a complex pattern of anomalies which were believed to correlate with the various geological structures associated with the origin of the Dead Sea (El-Kelani, 2020).

The importance of correcting observed gravity data before any further analysis and interpretation takes place cannot be overstated. Figure D5 (Appendix D) explains the importance of gravity data reduction (LeFehr, 2012) in some detail, where several corrections are applied to observed gravity measurements before subsurface density assessments are undertaken. Opportunistically, if airborne gravity and LiDAR are collected in tandem, the relevant tiles of LiDAR derived DEMs and DTMs can be used to calculate highly accurate terrain corrections (Table 2.7). This is particularly useful for low flying gravity surveys over complicated terrain like highway tunnel projects in mountainous terrain and environmental surveys over rugged karst environments (Zahorec et al., 2019).

Jamaludin et al. (2021) use airborne gravity techniques to understand the shallow and deep subsurface structures in Central Luconia Province off the coast of Sarawak, offshore Malaysia. The raw gravity data was acquired using airborne gravimeters mounted on a Basler turbo BT-67 aircraft operated by Bell Geospace Ltd. The survey used an Airborne 'Full Tensor Gradiometry' (Air-FTG) gravity technique which comprised a multiple accelerometer moving platform that measured accelerations in the inline and cross sections from three gravity gradient instruments (GGI). These GGIs were used to calculate the various directional gravity gradients which in turn, generate Tyx, Tyy, Tyz, Txz, and Tzz tensor components (Murphy, 2004), each representing a gravity gradient in an independent direction and each used to recognise and classify different lineaments associated with structural or stratigraphic changes below ground (Table 2.7). Subsequently, the different gravity gradient tensor components were analysed using contrasting frequency slicing, representing different scales and target depths across the province (Murphy and Brewster, 2007). This resulted in the detection and classification of several faults and structural lineaments, where each lineament was inferred as a structural and stratigraphic change across the Luconia Province. Further, strike directions of the interpreted structural trends using Air-FTG were measured and plotted as rose diagrams to distinguish the relevant subsurface structural orientations needed for future hydrocarbon exploration programmes (Jamaludin et al., 2021).

Subsurface exploration using airborne gravity can also assist with the exploration and evaluation of geothermal potentials, much like the geothermal potential in the Siwa Oasis in the Western Desert, Egypt (Abdel Zaher et al., 2018). In this study, a 3D inversion of airborne gravity data from the African Gravity Project was used to delineate the depths to Precambrian basement rocks, while a power spectrum method was used on some mutually supporting aeromagnetic data to estimate the Curie Point Depth and provide geothermal gradients and heat flow maps under the Siwa Oasis. The inverted airborne gravity data was used to generate a 3D density model of the sediment-basement topography which produced a theoretical gravity anomaly that aligned with the measured gravity anomaly. The 3D inversion results showed that the Precambrian basement surface across the study area had intensive irregular topography, with depths ranging from 2 km to 5 km (Abdel Zaher et al., 2018). Of note, a polynomial regression was used (Beltrão et al., 1991) to separate regions originating from long wavelength, deep-seated density sources and residual anomalies from shallow-seated density sources (Table 2.7).

### 2.10.2 Using SAR

Biondi (2022) detects subsurface density change using spaceborne SAR. By acknowledging the presence of several notable density changes inside a volcano, Biondi (2022) employs a SAR echography tomographic doppler imaging technique. This technique uses the micro-acoustic motions present in a volcano, and those generated from the Earth's underground heat, to process and analyse the coherent vibrational information embedded in a single SAR image. The sound information in the SAR image is used to generate a series of tomographic maps that reveal the

presence and location of the magma chamber and major volcanic conduits in Mount Vesuvius (Figure 2.14).

Similar techniques (noted in Table 2.7) are also used by Biondi and Malanga (2022) to reveal the internal structure of the Great Pyramid of Giza. Much like the study of Mount Vesuvius, SAR data from the COSMO-SkyMed Second Generation satellite constellation in the single-look complex configuration is used with background seismic waves from the natural environment (e.g., wind, River Nile etc) and the nearby city of Cairo to produce high-resolution 3D tomographic imaging of the Khnum-Khufu pyramid's interior.

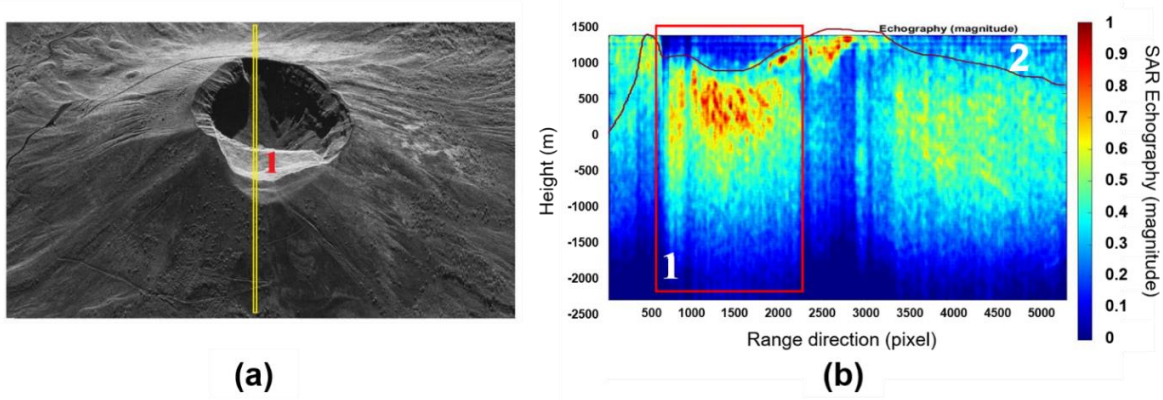



**Figure 2.14**. Range-line SAR echographic tomography profile of Somma Vesuvius. a). Single-look complex SAR image (magnitude only) with location of tomography profile (yellow line). b). Tomographic image along tomography profile using magnitude information from SAR data. Area 1 (red box) contains the magma chamber under the crater and Area 2 is the tomography result under the western slope of Mount Vesuvius. Figure adapted from Biondi (2022).

**Table 2.7**
Airborne and spaceborne remote sensing techniques used to detect *subsurface density anomalies*.

| Investigable Feature | Sensor Type | Remote Sensing Detection Technique | Example References |
|---|---|---|---|
| • Mineral ore deposits<br>• Structural geology / faults<br>• Sediment-Basement depths & topography<br>• Magmatic intrusions<br>• Geothermal potentials<br>• Salt diapirs<br>• Subsurface voids / karst cavities | Airborne Gravity | 1. First and second derivatives of the residual bouguer anomaly (incl vertical and horizontal gravity gradients) and wavelength filtering<br>2. Airborne Full Tensor Gradiometry (Air-FTG)<br>3. Upward and Downward Continuation / Frequency Slicing<br>4. 3D Gravity Inversion<br>5. Polynomial Regression | 1. Achmon and Ben-Avraham (1997); Segev and Rybakov (2011); El-Kelani (2020)<br>2. Jamaludin et al. (2021)<br>3. Murphy and Brewster (2007); Braitenberg et al. (2016)<br>4. Abdel Zaher et al. (2018)<br>5. Beltrão et al. (1991) |
| • Lithological contacts<br>• Tectonic / karstic discontinuities | Airborne LiDAR | 1. LiDAR DEMs / DTMs used to calculate accurate terrain corrections for gravity surveys | 1. Zahorec et al. (2019) |
| • Magma chambers and volcanic conduits<br>• Chambers inside pyramids | SAR | 1. SAR doppler tomography | 1. Biondi (2022); Biondi and Malanga (2022) |

## 2.11 Detecting magnetic field variation

### 2.11.1 Using aeromagnetics

Aeromagnetic surveys have been used extensively in the search for metalliferous mineral deposits. In 1966, total field aeromagnetic anomalies over the Eyre Peninsula in South Australia delineated the location of a large magnetic iron ore body, where the ratio of magnetite (magnetic) to haematite (typically non-magnetic) was high enough to produce two pronounced anomalies (c.4000 nT) north of Warramboo (Webb, 1966). The fundamental principles used in this study, and the widely acknowledged benefits of aeromagnetic mineral exploration are still employed today, where airborne surveys are often used in conjunction with ground survey and geochemical data to map ore deposits (Kharbish et al., 2022).

El-Raouf et al. (2023) successfully mapped the subsurface structure and location of several gold-ore mineralization deposits in ophiolitic assemblage rocks around the Wadi El-Saqia region in the Central Eastern Desert of Egypt. The aeromagnetic data was enhanced and interpreted using several edge-detection and edge-enhancement techniques (spatial derivative filtering) including the first-order vertical derivative (FVD), the analytic signal (AS), the total horizontal derivative (THD), the tilt derivative (TD), the tilt angle (TA), the theta filter and the Centre for Exploration Targeting (CET) grid analysis technique (Table 2.8). By employing each of these methods in turn, the subsurface study located the main structural lineaments and contacts associated with the distribution of hydrothermal alteration zones (Figure 2.15), formed when ophiolitic-assemblage rocks contact meta-sediments and other rock units. Geochemical analyses were then undertaken using the mineral chemistry of pyroxene and plagioclase to describe the tectonic and magmatic evolution across the region. Subsequently, the airborne magnetic results reveal the prevalence of various structural orientations across the study area, with depths ranging from 50 m to 600 m. El-Raouf et al. (2023) then used geochemical sampling to reveal significant percentages of gold in pyrite, galena, pyrrhotite, and electrum. Therefore, the utility of various derivative filtering techniques with aeromagnetic data can significantly assist with the identification of hydrothermal alteration zones and in this specific case, locations for gold mineralization.

There are numerous examples showcasing the application of horizontal gradient filters on total-field aeromagnetic data, proving it an effective procedure for separating shallow and deep magnetic source anomalies while enhancing the visualisation of particular linear features (Table 2.8). Doing exactly this, Grauch (2002) enhanced the visualisation of basin-filled sedimentary structures in Nevada, US, where localized regions of high magnetic horizontal gradients revealed the location of several shallow buried faults. By design, this particular aeromagnetic survey was high resolution, guaranteeing the successful assessment of shallow faulting and the near subsurface flow of hot fluids. Seemingly most of the faults within the basin were extremely shallow and therefore difficult

to detect with alternative subsurface imaging techniques like seismic refraction and seismic reflection (Everett, 2013).

A similar approach was used in the North Sea where aeromagnetic data from the Geological Survey of Norway's Crustal Onshore/Offshore Project (COOP) was used with 3D seismic data to map over 2,200 buried tunnel valleys (Ottesen et al., 2020). To support this study and others, 82,000 km of aeromagnetic data was acquired across the Norwegian North Sea (in a regular line-tie-line configuration) by the COOP and merged with existing magnetic data. High-pass filtering was applied to the new magnetic data to extract the magnetic signal from shallow sources and in particular, to highlight the magnetic signatures from the shallow buried tunnel valleys (Table 2.8). In total, 139 cross-cutting channel systems from the magnetic data were identified, most of which were 0.5 - 10 km wide, 80 - 100 km in length and 10s to 100s of metres deep. In parallel, the 3D seismic data identified a further 2,158 tunnel valleys. This combination of aeromagnetic and seismic analysis was able to reveal information on the past configuration and dynamics of the Scandinavian and British ice sheets and the processes by which sediment and meltwater were transported at the base of the ice-sheet during the Quaternary glacial periods. Albeit only 6 % of buried tunnel valleys were detected using airborne magnetics, Ottesen et al. (2020) prove that aeromagnetic data can provide a clear detection regime for buried tunnel valleys.

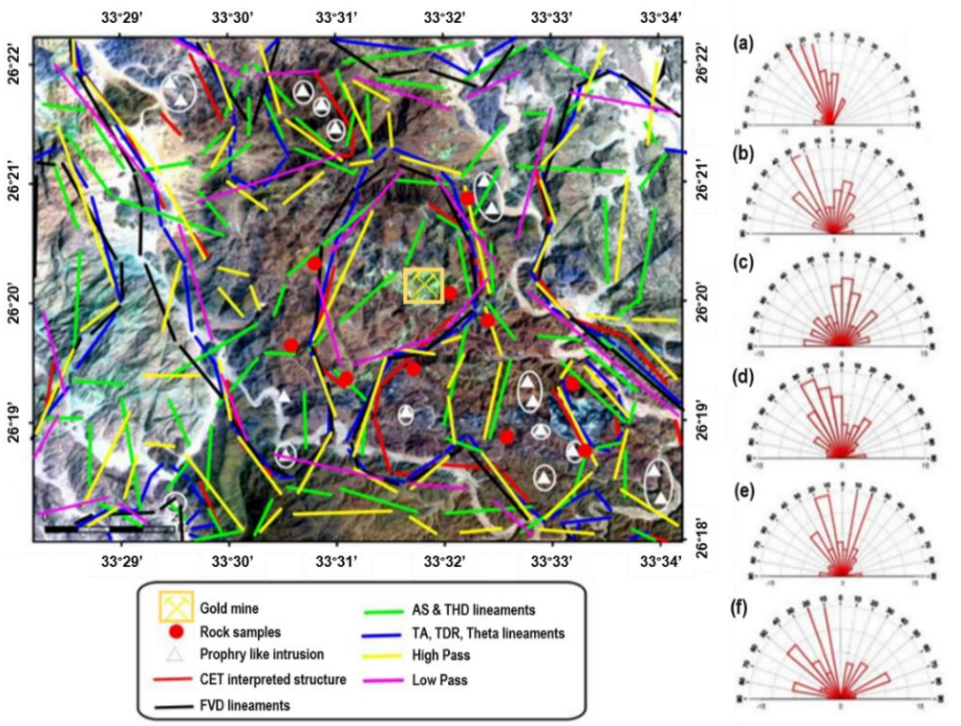



**Figure 2.15**. Image map showing the faults, contacts and dykes associated with gold mineralisation beneath the surface of the Wadi El-Saqia study region in the Central Eastern Desert, Egypt. The supporting rose diagrams display the primary and minor trends of subsurface lineaments for: a). the CET grid analysis; b). FVD; c). AS and THD; d). TA, Theta, and TD; e). high-pass filter; f). low-pass filter. The rose diagrams display the primary and minor trends of the subsurface lineaments. Figure adapted from El-Raouf et al. (2023).

### 2.11.2 Using airborne electromagnetics

Very much reliant on magnetic behaviour, the utility of airborne electromagnetic (EM) surveying also warrants some consideration, although this survey technique is not a standalone airborne remote sensing method in this review.

Using the principles of EM induction in the subsurface, airborne EM is able to detect variations in electrical conductivity and resistivity across the subsurface (Milsom, 2003). Airborne EM methods are therefore sensitive to detecting subsurface structures which contain different fluid types, clay content and porosity. Subterranean targets responsive to EM induction are similar to those susceptible to aeromagnetic investigation and typically comprise buried trenches, pipelines, tunnels, caves, shallow faults and inorganic plumes (Reynolds, 1997).

During operation, the primary EM signal is already known and so, by employing a spatially constrained inversion (Table 2.8), the primary signal can be removed from the observed EM response in the receiver, leaving only the residual unknown target response from the subsurface (Viezzoli et al., 2008).

Airborne EM was recently used across the Huola Mountain Tunnel site in the Luntai County of the Mongolian Autonomous Prefecture of Bayingolin, central China (Zhang et al., 2023). This extremely large tunnel is part of the Cedaya-S340 Holgutu Highway Construction Project, where the tunnel is built inside a high mountain landform, creating a highway tunnel 8.5 km long and 1.3 km below ground. Prior to excavation and construction, an airborne EM survey was conducted using a ground-airborne frequency domain electromagnetic method (GAFEM) and a helicopter-borne time-domain electromagnetic method (HTEM). The EM survey identified the major stratigraphic boundaries and fault fracture zones across the mountainous tunnel site (Table 2.8). Subsequently, the survey was able to evaluate the site for structural weakness, water content and karst development. The GAFEM revealed clear apparent resistivity profiles of deep sections across the tunnel site (200 – 2200 m in depth) whereas the HTEM generated high-resolution apparent resistivity images of shallow sections, ranging from 0 – 300 m in depth. The results were used to inform several geotechnical risk assessments needed prior to tunnel construction (Zhang et al., 2023).

An airborne EM survey was also conducted over the Damo Tunnel in Guangxi, southern China, where the tunnel site is known for its karst landforms. Here, Sun et al (2023) use a UAV and a semi-airborne transient electromagnetic method (SATEM) for tunnel investigation (Sun et al., 2023). The SATEM requires a grounded-wire source to be placed along the ground surface above the tunnel, which transmits an electromagnetic field into the subsurface. Low resistivity targets near the tunnel are induced by the transmitter which produce secondary fields that are proportional to the size and location of the subterranean target. From above, an induction coil is carried by the UAV which acquires the first derivative of the secondary magnetic field with respect to time $(\partial B/\partial t)$.

The information collected by the airborne induction coil is then inverted and transformed into a series of 3D resistivity images across the tunnel site, depicting various underground electrical structures and the size and location of various subsurface conductors (Sun et al., 2023).

**Table 2.8**
Airborne and spaceborne remote sensing techniques used to detect *magnetic field variation*.

| Investigable Feature | Sensor Type | Remote Sensing Detection Technique | Example References |
|---|---|---|---|
| • Ore mineralization deposits<br>• Faults and fracture zones<br>• Buried tunnel valleys<br>• Geothermal Potentials | Aeromagnetic | 1. Image enhancement filtering / spatial derivatives of total magnetic field anomalies: First-order Vertical Derivative (FVD); Analytic Signal (AS); Total Horizontal Derivative (THD); Tilt Derivative (TD); Tilt Angle (TA); Theta filter; Centre for Exploration Targeting (CET) Grid Analysis<br>2. Upward continuation and low pass filtering / Downward continuation and high pass filtering<br>3. Power Spectrum Method | 1. El-Raouf et al. (2023)<br>2. Everett (2013); Ottesen et al. (2020)<br>3. Abdel Zaher et al. (2018) |
| • Stratigraphic boundaries<br>• Fault zones<br>• Karst development / sinkholes<br>• Underground utility pipes | Airborne Electromagnetic | 1. Spatially Constrained Inversion (SCI)<br>2. Ground-airborne frequency domain electromagnetic method (GAFEM), helicopter-borne time-domain electromagnetic method (HTEM) and semi-airborne transient electromagnetic method (SATEM) | 1. Viezzoli et al. (2008)<br>2. Hartshorn et al. (2022); Sun et al. (2023); Zhang et al. (2023) |

## 2.12 Verifying remote sensing observations of the subsurface

Subsurface detection from air and space needs validating, otherwise the techniques used to reveal subsurface irregularities from above the ground cannot be assured. This ‘underground truthing’ may constitute a number of forms, each with their own merits and each dependent on localised ground conditions, weather, time of year and the nature of the subterranean target being explored. In this appraisal, four verification practices are discussed, with one or more methods appearing in multiple papers from several authors.

### 2.12.1 Ground reconnaissance

The first technique in which to ground truth air and space remote sensing anomalies of the subsurface is ground reconnaissance. Often coined ‘pedestrian survey’, this technique requires GPS positioning on the site, a simple visual inspection and, on occasion, specialist cameras (Thompson and Marvin, 2005) and/or 3D modelling applications (Ekaran, 2022). Measurements can often accompany a pedestrian survey to validate any geometrical relationships and anomalous surface elevation configurations seen from air and space. Terrestrial laser scanning is also a useful ground survey technique, especially when there is a requirement to accurately model the above and below ground spatial characteristics of a subterranean site in three dimensions (Konsolaki et al., 2022; Wang et al., 2014).

Moyes and Montgomery (2019) undertook pedestrian surveys to validate the identification of several potential cave openings in the Chiquibul Forest Reserve in Belize, where local relief modelling from lidar-derived images was used to identify vertical and horizontal cave openings in valleys, depressions and side slopes. The LiDAR results steered their pedestrian survey efforts, reducing the time spent on the ground searching for particular cave sites in dense forest. The location of 14 ancient Mayan caves were confirmed in-person and a further 26 non-Mayan cave openings were proven to align with their airborne LiDAR analysis (Figure 2.16), resulting in an 86% success rate. Furthermore, by visiting the caves in-person, the accuracy of their LiDAR detection routines could be evaluated. Similarly, Pisani and De Waele (2021) used a pre-existing cave register from the Atacama Desert and pedestrian survey to confirm the location of several candidate cave entrances across the Cordillera de la Sal in Chile. These ground truthing methods verified the quality and reliability of their remote sensing detection regimes, where they used 600 $km^2$ of Pléiades imagery and several DTMs from stereographic couples to map the lithological units, the drainage network and the cave entrance points.

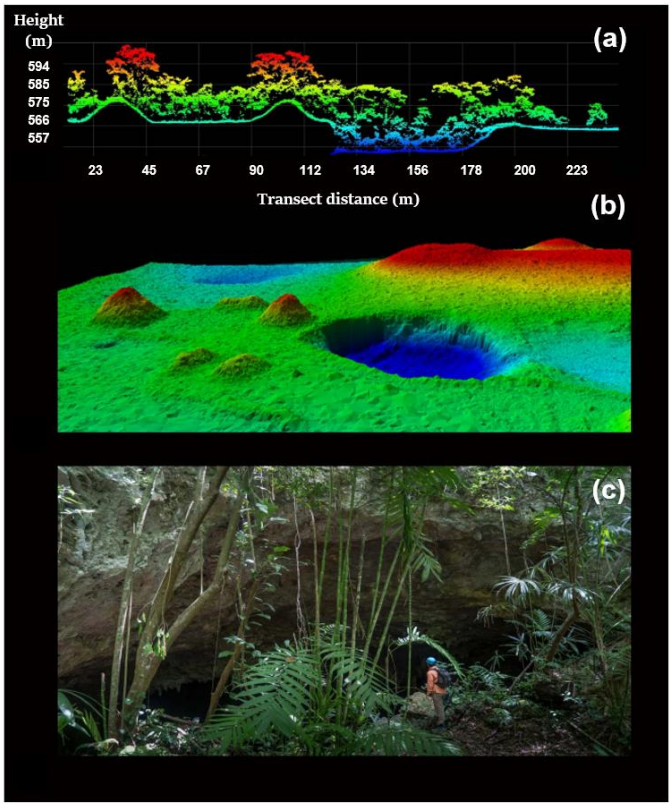



**Figure 2.16**. A cave opening inside a sinkhole in the Las Cuevas study site in Belize (Moyes and Montgomery, 2019): a). Transect of an airborne LiDAR point cloud across a cave opening and sinkhole (in blue); colours represent surface elevation in metres. b). 3D DEM of sinkhole (in blue) and surrounding surface structures. c). Photo of a Las Cuevas cave entrance found at the base of the sinkhole during site reconnaissance.

### 2.12.2 Field spectroscopy

Field spectroscopy is a terrestrial technique used to measure the reflectance properties of vegetation, soil, rock and water bodies in the natural environment, generally under solar illumination (Milton et al., 2009). In terms of verifying subsurface anomalies from airborne and spaceborne remote sensing, field spectroscopy can be used to calibrate and validate the spectral observations recorded by an airborne or spaceborne multispectral or hyperspectral imaging system (Themistocleous et al., 2018). Typically, a field spectrometer will accurately record the intensity of reflected solar light at many different wavelengths in the EM spectrum, generating spectral reflectance profiles for specific objects with percentage reflectance values typically recorded from 300 nm to 2500 nm wavelengths (Milton et al., 2009). Therefore, pending the depth of the subterranean anomaly, reflectance spectrums of the ground matrix (soil/sand and overlying vegetation) above a subsurface structure are expected to yield different reflectance spectra to the surrounding landscape. These in situ reflectance spectrums are then compared with reflectance spectra from the airborne and spaceborne multispectral and hyperspectral imagery, calibrating the spectral resolution of the remote imaging sensor and validating the presence of a subsurface anomaly.

As an example, Agapiou et al. (2010) compare field spectroscopy observations over the Kouklia Palaepaphos archaeological site in Cyprus with magnetic anomalies in a previous geophysical survey. They used a GER 1500 field spectrometer to produce several spectral reflectance profiles across the site and in turn, observe multiple spectral vegetation anomalies over the buried archaeological features. They witnessed real benefits in incorporating field spectroscopy measurements with a multispectral time series analysis, where optimal time windows for vegetation reflectance anomalies could be determined using field spectroscopy prior to undertaking any imagery analysis of the subsurface across larger regions of the study site. Similar observations were also noticed by Melillos et al. (2019), who use a similar field spectroscopy method to verify and augment Sentinel-2A anomalies above underground military structures in Cyprus.

### 2.12.3 Geophysical survey

To guarantee the presence of subsurface anomalies below ground, geophysical surveys are recommended. Many applied geophysical techniques exist, all responding to particular physical properties in the subsurface (Figure 2.17). Much like air and space remote sensing, both active and passive methods exist. Active methods transmit artificially generated signals into the ground which are then modified in response to the characteristics of the materials in which they travel (Everett, 2013). Passive methods are those that detect variations in the Earth's natural fields (e.g., gravity and magnetics). All methods rely on specific physical properties in the subsurface, indicating that the optimal geophysical technique is very much dependent on the type of subsurface structure being investigated and the local ground conditions in which it rests (Butler, 2008). According to Figure 2.17 (adapted from Reynolds (1997) and Morley (2011)), electromagnetics, resistivity, GPR

and magnetic survey are the most versatile geophysical methods for subsurface detection, where each method is classified as a primary survey technique for at least 50% of the applications illustrated. Moreover, terrestrial gravity survey is also considered the most versatile augmentation (i.e., secondary) technique in any geophysical survey.

Butcher et al. (2006) made full use of gravity augmentation when they imaged the Lamb Leer cave system in the Mendip Hills in Somerset, UK. During the summers of 2004 and 2006 a series of resistivity and microgravity profiles were performed across the cave system, where the resulting gravity data disproved the presence of a significant mass deficiency in the vicinity of a resistivity "high" that was previously believed to be a large subsurface chamber. Instead, the combined resistivity and gravity data revealed this area as an isolated section of highly resistive limestone which, some time ago, had been re-positioned by a local fault.

By undertaking different geophysical techniques over the same subsurface target, confidence levels in the subsurface anomaly's location and character are enhanced, although these increased assurances must be carefully balanced with time, funding and resources (Berezowski et al., 2021). Several studies in this review use a multi-geophysical approach to verify subsurface observations (Berezowski et al., 2021; Ghezzi et al., 2019) although, as best practice, the pairing or grouping of such techniques should exploit different properties in the subsurface, thereby optimising detection and contextualising interpretation (Křivánek, 2017).

| | | Subsurface Application (see key) | | | | | | | | | |
|---|---|---|---|---|---|---|---|---|---|---|---|
| Geophysical Method | Physical Property | 1 | 2 | 3 | 4 | 5 | 6 | 7 | 8 | 9 | 10 |
| Gravity/Microgravity | Density | P | P | S | S | S | S | ! | ! | S | ! |
| Magnetic Surveying | Susceptibility | P | P | P | S | ! | M | ! | P | P | ! |
| Seismic Reflection | Elastic moduli; Density | P | P | M | P | S | S | ! | ! | ! | ! |
| Seismic Refraction | Elastic moduli; Density | P | P | M | S | S | M | ! | ! | ! | ! |
| Electrical Resistivity | Resistivity | M | M | P | P | P | P | P | S | P | M |
| Spontaneous Potential | Potential Differences | ! | ! | P | M | P | M | M | M | ! | ! |
| Induced Polarization | Resistivity; Capacitance | M | M | P | M | S | M | M | M | M | M |
| Electromagnetic Induction | Conductance; Inductance | S | P | P | P | P | P | P | P | P | M |
| Ground Penetrating Radar (GPR) | Permitivity; Conductivity | ! | ! | M | P | P | P | S | P | P | P |
| Magneto-telluric | Resistivity | S | P | P | M | M | ! | ! | ! | ! | ! |

**Subsurface Application:**

1 = Hydrocarbon Exploration
2 = Regional Geological Study
3 = Mineral Exploration
4 = Engineering Site Investigation
5 = Hydrogeological Investigation
6 = Subsurface Cavity Detection
7 = Leachate and Continental Plume Mapping
8 = Buried metal object detection
9 = Archaeogeophysics
10 = Forensic Geophysics

**Key:**

**P** = Primary Method
**S** = Secondary Method
**M** = May be used but not recommended
**!** = Unsuitable

**Figure 2.17**. Principal geophysical methods and the subsurface properties they exploit. Each geophysical method is graded as either a primary (P), secondary (S), not recommended (M) or unsuitable (!) survey technique for ten subsurface exploration programmes listed on the right. Adapted from Reynolds (1997) and Morley (2011).

### 2.12.4 Integrated approach

A multi-sensor approach will increase subsurface detection assurances and evidently much work has been done to demonstrate this. For example, Lin et al. (2011) use high resolution GeoEye-1 satellite imaging, UAV photography and sub-surface geophysical investigation to detect ancient

subsurface features at a Bronze Age burial mound, a Turkish period tomb and a steppe city fortification in northern Mongolia. Aerial photographs of the sites were obtained with two customized electric-powered UAVs (one fixed wing and one rotary) and geophysical investigation was conducted with a GSM-19 Overhouser gradiometer, an EM38 electro-magnetometer and an IDS Opera Duo GPR. The satellite imagery and aerial photographs were combined with the geophysical survey results and on-site reconnaissance to provide significant information on the ancient anomalies, all of which were depicted in multiple layers of data.

Similar sensor fusion techniques were also employed by Kalayci et al. (2017), who integrated electromagnetic induction, magnetic survey and GPR with historical aerial photography, multispectral imagery analysis (from high-resolution WV2 and GeoEye-1 commercial satellite sensors) and a high resolution DTM from imagery taken by a UAV. Subsequently, this sensor rich and data heavy approach resulted in several comprehensive subsurface pictures of Neolithic settlements in Thessaly, Central Greece, revealing the dynamic character and structure of Neolithic enclosures, communal spaces and economic centres. More recently, Gaber et al. (2020) mapped groundwater potentials across the West Qena Area in Egypt by integrating an SRTM DEM with Landsat-8, ALOS/PALSAR-1 and Sentinel-1 imagery, geological data and soil maps. Furthermore, aeromagnetic data was processed to map the deep-seated structures across the same region, estimating the depth to the basement rocks that were believed to control the groundwater occurrence. Finally, vertical electrical sounding (VES) measurements were applied and calibrated with borehole data to delineate the subsurface geological and hydrogeological setting as well as the groundwater aquifers. Different geoelectric cross-sections and hydro-geophysical maps were then constructed using the borehole information and VES measurements to illustrate the lateral extension of the different lithological units, groundwater-bearing zones, water table and saturated thickness of the aquifer.

## 2.13 Future perspectives

This review identifies several promising research opportunities for the future. In particular, the spatial, spectral, radiometric and temporal integrity of high-quality airborne and spaceborne imagery now provides the data needed to perform VHR investigations of anomalous reflectance behaviour from vegetation and soil overlying near subsurface anomalies. Improved open access to high-resolution and VHR airborne and spaceborne remote sensing datasets is also encouraging, where the supremacy of deep learning techniques like multi-branch CNNs must continue to be employed on multi-sensor datasets, improving the likelihood and reliability of subsurface detection. We also identify the need to explore the detection sensitivities of active remote sensing techniques in variable potential fields. Revealing the subsurface density structure of semi-rigid structures using SAR tomography is of particular interest. Grouping these future research perspectives into three distinct study fields, we consider the detail of each.

### 2.13.1 Very-high-resolution (VHR) time series analyses

The ground conditions above and around subsurface structures continually change with time, and ground signatures from soil composition, heat retention, groundwater behaviour and surface elevation may be transformed and accentuated by natural and human processes. As we have demonstrated, airborne and spaceborne remote sensing applications may exploit such anomalous temporal behaviours, but are often limited by the spatial, temporal, radiometric and spectral resolutions of the sensor. Given recent advances in sensor technology and platform revisit times, we identify a need to further develop an understanding of the temporal behaviour of subsurface anomaly characteristics; with an emphasis on understanding how time affects the prominence of remotely sensed subsurface anomalies in contrast to the surrounding landscape. In the future, investigations could entail a VHR multispectral, hyperspectral, TIR and/or LiDAR time series analysis of ground reflectance characteristics, soil matrix irregularity, thermal emissivity and land subsidence over near-surface tunnels and caves. Very high spatial, spectral and temporal resolution datasets are needed to achieve this, a demand which, for example, could be accomplished with high performing UAV-optimised imaging sensors and very-high-resolution commercial satellites like Pléiades Neo and SatVu (for thermal change). When considering spaceborne observation, image fusion techniques with temporally-rich Planet images will generate numerous high-resolution multispectral images over short time periods, allowing the advantages of time-series analyses to accentuate any spectral anomalies above subsurface features (c.f. Agapiou et al., 2013a). The validity of such anomalies can then be correlated statistically with field spectroscopy, geophysical survey or integrated multi-sensor data.

### 2.13.2 Multi-branch convolutional neural networks (CNNs) on multi-sensor data

The multi-sensor integrated approach (reviewed in Section 2.12.4) can still evolve, where semi-automatic to fully automated subsurface detection routines are forged to make full use of the various airborne and spaceborne remote sensing datasets now available. Many more of the detection techniques presented in our technique tables (Tables 2.2 – 2.8) could be employed concurrently to increase the accuracy and reliability of subsurface detection. Here, multi-sensor subsurface detection algorithms could be designed to systematically search for anomalies in the visual, spectral, thermal, spatial, gravitational and magnetic domains concurrently to assess the likelihood of subsurface anomalies existing in user designated locations. Object-based image analysis (OBIA) using multi-sensor datasets has already been well employed in archaeological prospecting (e.g., Davis, 2019; Freeland et al., 2016; Lasaponara and Masini, 2018) although much could still be done to incorporate this analysis with geophysical datasets, GIS analysis and machine learning. In the past, predictive models in GIS have been used, in conjunction with remote sensing datasets, to locate areas with high archaeological potential (Nsanziyera et al., 2018), high groundwater potential (Gaber et al., 2020) and high geothermal potential (Abuzied et al., 2020) but now, various machine learning techniques are well placed to forge a larger and more reliable integration platform (Shirmard et al., 2022). Xu et al. (2018) have already set a promising benchmark, successfully

training a two-branch convolutional neural network (CNN) to “feature fuse” hyperspectral imagery with LiDAR data and then classify specific ground features, including that of surface proxies for subsurface anomalies (e.g., stressed grassland). Therefore, if optimal detection parameters are defined by subsurface target type and landscape condition (for multiple different sensor types), a multi-branch CNN could strive to statistically detect composite subsurface anomalies from the seven subsurface anomaly characteristics discussed in this paper.

### 2.13.3 Active remote sensing in variable potential fields

This review has identified the need for new and innovative approaches to remotely detect subsurface density changes and magnetic field variations from near-surface structures. As seen in Figure 2.4, little airborne or spaceborne remote sensing methodology exists outside of traditional airborne gravity and magnetic survey to identify these subsurface characteristics. However, Biondi (2022) and Biondi and Malanga (2022) have begun to address this, showcasing SARs tomographic ability to image density variations inside volcanoes and ancient pyramids from space. We see potential in trialling similar techniques on semi-rigid structures like grass covered tors and caves, where SAR returns are typically less coherent. Such innovation uses photons as a carrier medium for phononic information, inviting readers to think about other ways in which photons could reveal the presence of subsurface anomalies, particularly when changes in the Earth’s gravitational and magnetic field are present.

## 2.14 Concluding remarks

Considering the use of eight different sensor types, this review identifies five principal motivations for remote sensing the subsurface from air and space. As illustrated in Figure 2.2, these are: archaeological prospecting, environmental risk mitigation, natural resource exploration, defence and security and speleological research. The distinct ground indicators and potential field characteristics of a subsurface anomaly have also been categorised (Table 2.1 and Figure 2.3), allowing the review to document all published use cases by sensor type, research motive and subsurface anomaly characteristic. By doing so, the review reveals that 78% of appraised photogrammetry papers exploit visible signatures across previously known archaeological sites; 43% of multispectral papers detect soil matrix irregularities over buried archaeological features; anomalous groundwater behaviour can be identified using all major sensor types less airborne gravity and aeromagnetics; heat retention anomalies are a suitable subsurface proxy for all research motives; changes in subsurface density are detected or assisted with airborne gravity, airborne LiDAR and SAR; and 57% of LiDAR papers and 50% of SAR papers exploit changes in surface elevation (Figure 2.4).

In total, over seventy air and space remote sensing techniques have been identified across the eight sensor types considered in this review (Tables 2.2 – 2.8); each designed to accentuate subsurface anomalies in the visible, spectral, thermal, spatial, gravitational or magnetic domains

through the exploitation of a subsurface anomaly's visual markings, surrounding soil matrix, groundwater regime, surface elevation, heat retention, density distribution and magnetic susceptibility. By pooling these techniques together in seven technique tables that differentiate the subsurface anomaly characteristic being pursued, the investigable feature being detected and the remote sensor type used (Tables 2.2 – 2.8), the review exposes an extensive suite of tools and techniques for channelling subsurface detection studies with multiple sensors in different landscapes.

The importance of verifying remotely sensed observations of the subsurface from air and space has also been emphasised, recommending ground reconnaissance, field spectroscopy, geophysical survey and a multi-sensor integrated approach as the preferred means to calibrate and validate any prospective anomalies. Finally, the review considers future steps in remote sensing the subsurface, recommending the need for more VHR time series analyses over subsurface anomalies and further technical exploitation of CNNs, multi-sensor classification and quantum information protocols.

# 3

# Using gravity, ground penetrating radar and vegetation indices to derive a multispectral recipe for subsurface detection

Under review as: *Morley, A.M., Mather, T.A., Pyle, D.M. and Kendall, J.M., 2025. Using gravity, ground penetrating radar and vegetation indices to derive a multispectral recipe for subsurface detection.* Manuscript under review, *International Journal of Applied Earth Observation and Geoinformation*

## Abstract

The remote detection of shallow, subsurface features can assist archaeological prospecting, environmental risk mitigation and national security. However, few subsurface detection studies have used geophysical methods to statistically validate the detection efficiency of broadband vegetation indices (VIs) in high-resolution multispectral satellite imagery. In this reset study, we use 37 broadband VIs on eight Maxar (now rebranded to Vantor) multispectral satellite images to remotely detect stressed meadow grass and anomalous soil characteristics over an Iron Age fogou (stone-walled underground passage) in Carn Euny, Cornwall, UK. Using Maxar's high spatial resolution, the highest performing VIs are identified using a two-tier approach. First, we correlate the VIs with gravity and then, for a best performing image subset, we perform structural similarity index measurements (SSIMs) and 2D cross-correlations with ground penetrating radar (GPR) data. In doing so, we reprioritise the most suitable VIs for shallow, subsurface detection in temperate, grass covered environments. In summer months, the Iron Oxide index, Soil Salinity Index 7 (SI7) and the Structure Insensitive Pigment Index (SIPI) are most responsive across the fogou; all of which are algebraic manifestations of the Red/Blue reflectance ratio. By analysing their spectral profiles, gradient magnitudes, false colour composites (FCCs) and edge effects, we review the fogou's effect on soil salinity, iron oxide concentration and chlorophyll production. Demonstrating

the broader utility of Red/Blue reflectance ratios, we then present a multispectral image processing workflow which is calibrated to detect, at scale, shallow subsurface features in temperate, vegetated terrain.

## 3.1 Introduction

Advances in satellite sensor technology offer improved ways to remotely sense the Earth's subsurface (e.g., Luo et al., 2019). Fast and frequent image acquisition and high spectral, spatial and radiometric resolution now allow multispectral imaging systems to detect, with reasonable levels of assurance, the unique ground characteristics of shallow subsurface anomalies (e.g., Calleja et al., 2018; Dana Negula et al., 2020). The merits of doing so are becoming ever more extensive, with archaeological prospecting (e.g., Zanni and De Rosa, 2019), environmental risk mitigation (e.g., Mi et al., 2019) and defence and security (e.g., Perez et al., 2017) all benefitting from high-resolution multispectral imaging over large areas, difficult terrain and hazardous environments.

Supporting archaeology, multispectral satellite remote sensing is used to detect, catalogue and classify ancient subsurface structures at scale and at speed (Luo et al., 2019). In particular, it assists archaeological field studies which are large-scale, difficult to access, or cross multiple land-uses (e.g., Powlesland et al., 2006). Multispectral imaging methods and image processing techniques are also non-invasive, thereby avoiding ground disturbance of protected archaeological sites (El-Behaedi, 2021). Quick and frequent spaceborne acquisition methods can allow archaeologists to locate, manage and preserve cultural heritage sites, especially in areas under threat from urbanisation, industrialisation, looting and rising water levels (Dana Negula et al., 2020; Trier et al., 2015). Further, top-down analyses using pansharpened imagery may reveal large-scale spatial characteristics and geometrical relationships that are unrecognisable from the ground, for example spatial relationships with surrounding archaeological sites and prominent features across a landscape (Zanni and De Rosa, 2019).

In support of environmental risk mitigation, the use of various satellite and airborne remote sensing techniques to locate sinkholes, soil pipes and land subsidence are also well-practiced (Barla et al., 2016; Bernatek-Jakiel and Jakiel, 2021; Hofierka et al., 2018; Zhang et al., 2023). Once detected, specialist techniques like synthetic aperture radar (SAR) Interferometry (InSAR), differential InSAR (DInSAR) and advanced DInSAR (A-DInSAR) can be used to monitor the rate and extent of ground subsidence, mitigating any adverse impacts on urban development projects, tunnel construction and agronomic productivity (Anantrasirichai et al., 2021; Ramirez et al., 2022; Scoular et al., 2020). Other remote sensing objectives include the detection and behaviour of underground coal fires and sand dune migration (Du et al., 2022; Grandjean et al., 2001; Wang et al., 2015), the internal monitoring of volcanoes (Biondi, 2022) and the identification of drilling hazards in shallow, oil and gas exploration programmes (Ottesen et al., 2020).

In support of defence and security, various satellite imaging techniques can locate illegal cross border tunnel exchanges using, for example, specialised change detection techniques (Kwan, 2019) and feature detection algorithms like the identification of excavated spoil heaps (Perez et al., 2017). Further, multispectral and hyperspectral imagery is now frequently used by various Defence and Government Intelligence experts to classify adversary vehicles, equipment and troops near tunnels, caves and camouflage constructs (Shimoni et al., 2019). Pending burial depth and specific ground conditions, buried landmine and improvised explosive device (IED) detection is also achieved using specialist air and space remote sensing techniques like thermal infrared detection and hyperspectral analyses of soil reflectance spectra (Shimoni et al., 2019).

All of these use cases rely on the detection of one or more ground indicators and/or potential field characteristics, typically generated above a subsurface anomaly (Figure 3.1). These unique ground indicators present numerous opportunities for the remote detection and classification of subsurface features. Illustrated in Figure 3.1, Morley et al. (2025a; Chapter 2) group these distinct ground characteristics into seven categories: 1) visible features; 2) soil matrix irregularities; 3) anomalous groundwater behaviour; 4) surface elevation change; 5) heat retention anomalies; 6) gravitational anomalies; 7) magnetic field variations. Across these characteristics, the spectral information in high-resolution multispectral satellite imagery is particularly useful in the detection of visible features (Kwan, 2019), soil matrix irregularity (Calleja et al., 2018) and anomalous groundwater behaviour (Saha, 2022). Therefore, an airborne or spaceborne detection regime which identifies multiple ground characteristics is expected to increase the detection efficiency and reduce the risk of false positives.

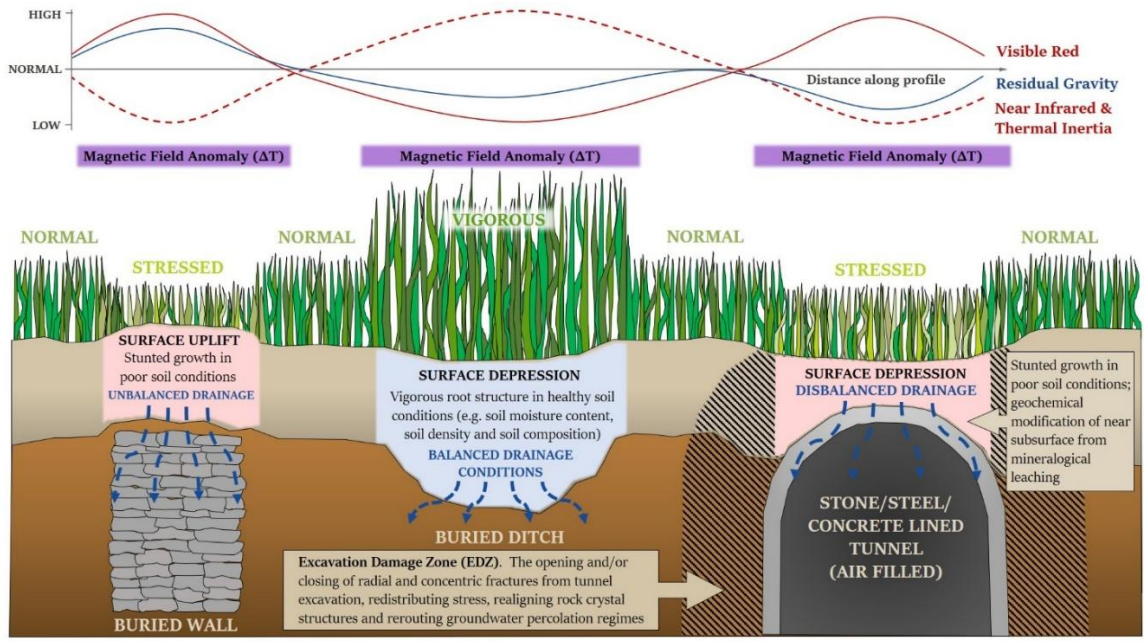



**Figure 3.1**. Anomalous ground characteristics generated by three *general* subsurface structures, detected using remote sensing and as illustrated by Morley at al. (2025a; Chapter 2). An underground wall (left), buried ditch (centre) and air-filled tunnel (right) are used as examples. Top diagram illustrates how red light, near infrared, thermal inertia and residual gravitational field strength vary across these structures. Purple bars denote locations of total magnetic field anomalies ($\Delta T$) and vegetation, topographic and drainage variations are shown pictorially, although some *or* all may not be present in every real-world scenario.

Object-based image analysis (OBIA) can use multi-sensor datasets of the ground characteristics in Figure 3.1 to assist archaeological prospecting (e.g., Davis, 2019; Thenkabail, 2024), and recent developments in the intelligent processing and deep learning of satellite video is now advancing OBIA even further (Chen et al., 2024). In particular, the classification and segmentation of subsurface objects in video scenes (Li et al., 2023) shows great potential. Machine learning techniques are also improving the general scale and reliability of remote sensing applications in subsurface exploration (Shirmard et al., 2022). For example, Xu et al. (2018) trained a two-branch convolutional neural network (CNN) to "feature fuse" hyperspectral imagery with LiDAR data, permitting the classification of specific subsurface indicators above ground, like stressed grassland over buried structures.

Stressed grassland is often the surface expression of a subsurface heterogeneity, explained by detrimental changes to the soil matrix above a shallow subsurface feature like a buried wall, ancient road or underground pipe (e.g., Agapiou et al., 2023). Often poor or imbalanced drainage regimes are introduced to the soil matrix above an anthropogenic structure, and geochemical alterations within the soil are intensified by the mineralogical leaching of a subsurface structure, which can exacerbate with time. This can result in detrimental modifications to the soil density, soil moisture content and soil composition above and around a buried anthropogenic structure (Rowlands and Sarris, 2007). Consequently, as illustrated in Figure 3.1, the health and growth of any vegetation at the surface is expected to deteriorate (Luo et al., 2019).

When applying vegetation indices (VIs) to high-resolution multispectral imagery, much can be understood about the behaviour and condition of grass, crops, plants and trees above subsurface features (Xue and Su, 2017). For example, VIs have been used to assess the chlorophyll concentration in crops overlying buried archaeological features (e.g., Agapiou et al. 2013) and tree growth near tunnel excavation programmes (Zeng et al., 2023). In such use cases, VIs are able to detect crop marks (Lasaponara and Masini, 2007), anomalous soil moisture and drainage (Dana Negula et al., 2020), vegetation stress (Sarris et al., 2013) and geochemical alterations in soil overlying subsurface anomalies (El-Behaedi, 2021).

By definition, VIs are algebraic combinations of spectral bands used to generate new unique pixel values which represent a particular behaviour or characteristic of vegetation in a scene (Basso et al., 2004). In previous research, VIs have been divided into broadband and narrowband indices (Agapiou et al., 2012a). Broadband VIs use broadband reflectance values (applicable to spaceborne multispectral imagery) and narrowband VIs use narrowband reflectance values (applicable to hyperspectral imagery and airborne multispectral imaging systems).

When applied, vegetation indexed images can enhance interpretation, revealing visual information about vegetation overlying subsurface incongruities that would otherwise go undetected in regular Red-Green-Blue (RGB) imagery (Bennett et al., 2013; Challis et al., 2009). However, the reliability

and accuracy of VIs in the detection of subsurface anomalies can be inconsistent, often depending on both biological *and* physical factors (Bannari et al., 1995). Biological factors comprise the landscape, soil characteristics, nutrient supply, climate, vegetation type and phenological cycle (Cerra et al., 2018; James et al., 2020; Moriarty et al., 2018). Conversely, physical factors include the size and depth of the subsurface feature being pursued, atmospheric effects, solar illumination geometry, sensor type, sensor calibration and sensor viewing conditions (Bannari et al., 1995). Moreover, VIs can be blindly used without due consideration of: 1) the biophysical properties on which they are formed (Agapiou et al., 2014); 2) the field instruments used in their derivation (Xue and Su, 2017); 3) the field and lab conditions in which they were created (Giovos et al., 2021). Moreover, they are rarely *quantitatively* examined and validated as "fit for purpose", although more recent numerical ground truthing methods show potential (e.g., Cerra et al., 2018; Roslan et al., 2020).

In this study, we revisit the utility of high-resolution multispectral VIs in their detection of changes in soil matrix irregularity and vegetation stress over structural anomalies below ground. Subsurface features of interest include tunnels, pipelines, drainage systems and culverts. Typical depths range from 1 – 10 m and structurally, these features are known to have linear form. Therefore, the anomalous ground behaviour generated by these features is expected to emulate similar geometrical form to their subterranean structures. Therefore, by shape alone, the risk of detecting a false positive at ground level is allayed (Morley et al., 2025a; Chapter 2).

To do this, we *quantitatively* validate and reprioritise the performance of 37 broadband VIs over an Iron Age underground passage (commonly termed a 'fogou') in Carn Euny Ancient Village, Cornwall, UK. By regarding this site as our control, we apply each VI to eight different Maxar (now rebranded to Vantor) high-resolution multispectral images of Carn Euny from different calendar months. Taking advantage of these high spatial resolutions, a novel two-tier geophysical approach is used to determine the highest performing VIs. First, we statistically correlate the VIs in 1D with a residual gravity profile and second, we correlate in 2D the best-performing VI subsets with GPR data. This geophysical examination of vegetation index performance is used to reprioritise those VIs most sensitive to change in soil and vegetation stress above the fogou. From this geophysical assessment, we analyse the detection efficiency of the highest performing VIs using spectral profiles, gradient magnitude operations, false colour composites (FCCs) and edge detection routines. As a proof of concept, this is the first use of gravity *and* GPR ground truthing in assessing the sensitivity and response of VIs in subsurface detection.

In a proposed workflow for detecting subsurface structures using VIs, we optimise the highest performing indices using gradient magnitude, pansharpening and clipping routines. We then assess the broader applicability of this image processing workflow on two different temperate, vegetated sites in Normandy, France. Both test sites feature shallow subsurface anomalies; the

first is a buried clay drainage pipe and the second is two buried ditches, once used as French drains.

## 3.2 Control Site

The control site for this study is located in the ancient village of Carn Euny, an Iron Age settlement in the civil parish of Sancreed in west Cornwall, UK (Figure 3.2). On the Penwith peninsula and approximately 7 km west of Penzance, Carn Euny encloses the foundations of several stone houses from the 2nd to 4th centuries AD, and Iron Age timber and turf round houses from 500 - 300 BC (English Heritage, 2024a). The ancient village is now managed by the Cornwall Heritage Trust (Cornwall Heritage Trust, 2020) and occupies an area of c.5,200 $m^2$, extending 80 m north to south and 65 m east to west. The site was occupied until the late Roman period and abandoned in c.400 AD (Historic Cornwall, 2020).

In the centre of the ancient village lies Carn Euny's most unique feature: a stone-walled underground passage called a 'fogou' (Figure 3.2a). Discovered by miners who were prospecting the area for tin in the 1840s, this underground passage is approximately 20 m long, 1.6 m wide, 0.5 m deep, 1.8 m high and capped with large stone slabs (Figures 3.2b, 3.2c and 3.2d). Fogous ('ogo' meaning 'cave' in Cornish) are a distinct type of late Iron Age monument (300 BC – 43 AD) only found in the west of Cornwall. They are considered a regional type of 'souterrain' (a generalised underground Iron Age structure) and their suggested purpose includes a place of refuge, a chamber for cold storage or a protected space for ritual practices (English Heritage, 2024b; Greaney, 2017). Near the south entrance of Carn Euny's fogou is a very small side-chamber and by the north entrance, as seen in Figure 3.2a, there is a side passage to a round stone chamber from the early Iron Age (500 – 300 BC). Again, the specific purpose of this large underground chamber is unknown but it closely resembles similar souterrain structures in Scotland (Wainwright, 1953), Ireland (Clarke, 1963) and more recently, those revealed by Hancock (2020) in New England, USA.

Given the physical dimensions and ease of access to these shallow subsurface voids, Carn Euny Ancient Village hosts several options for conducting a shallow subsurface detection study. In particular, the dimensions of the Iron Age fogou are well configured to examine the subsurface detection capabilities of Maxar's spaceborne, high-resolution multispectral imaging sensors.

Subsequently, a 13 m x 3.5 m rectangular control site was positioned over the fogou (Figure 3.2e), marked with corner flags and georeferenced with GPS coordinates. The control site was made deliberately small to accommodate the accurate, high-resolution recording of gravity, GPR information and multispectral reflectance ratios. The control site's central reference point is 50.1028491°N, 5.6340764°W and the site excludes steep slopes, significant ground undulations and rocky outcrops. The ground directly above the fogou is located in the eastern quadrant of the control site and the predominant grass type across the area is smooth stalked meadow grass (Poa

pratensis). By definition, this meadow grass is a cool-season grass that can grow in cooler temperatures, initiating and sustaining growth from the early spring to early autumn months in a temperate climate (Peterken, 2013). The soil beneath it is brown podzolic soil, a free-draining brown earth soil containing sand, silt and clay (Findlay et al., 1984).

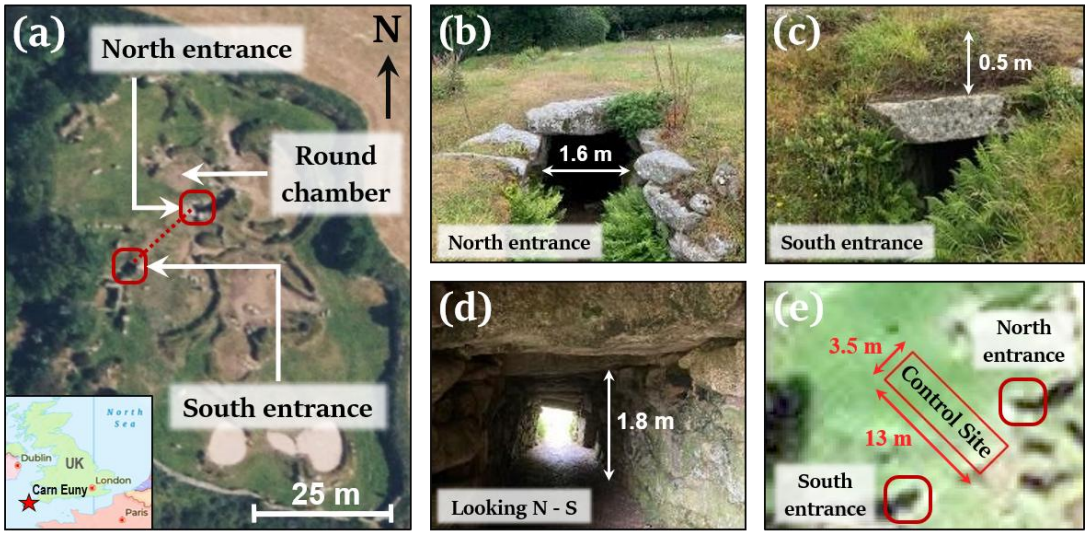



**Figure 3.2**. Carn Euny Ancient Village and Iron Age fogou. a). Maxar pansharpened RGB image of Carn Euny with location panel; red boxes denote north and south entrances to the fogou and red dotted line shows approximate direction of fogou. b) & c). North and south entrances to the fogou with approximate width and depth annotated. d). Looking north to south through the Iron Age fogou with approximate height annotated. e). Location of the control site (light red box) in relation to north and south entrances; site dimensions as shown.

## 3.3 Methodology

There are three stages to our analysis. The first is image acquisition, where high-resolution multispectral satellite imagery is acquired from Maxar's Analysis Ready Data (ARD) Dashboard. The second is a two-tier process for *quantitatively* prioritising and validating the most suitable vegetation indices (VIs) for subsurface detection across the fogou. To begin statistical correlations are performed between multispectral VIs and gravity in 1D, and then we correlate multispectral VIs and ground penetrating radar (GPR) data in 2D. In support of subsurface detection, the final stage uses the best performing VIs in gradient magnitude (Gmag) assessments, false colour composite (FCC) analysis and edge detection operations to identify the location of the fogou in the control site.

### 3.3.1 Image acquisition

We acquired all Maxar high-resolution satellite image files using the Maxar ARD Dashboard (Maxar, 2022a). The dashboard user interface allows the user to manually select or upload a geographical area of interest (AOI) in order to retrieve a visual catalogue of imagery tiles that suffice a predefined selection criterion. Selection parameters include the age of the imagery, cloud cover percentage and tolerances for off-nadir angle and sun elevation.

Maxar ARD are time-series stacks of imagery which have been atmospherically corrected, orthorectified and aligned pixel-by-pixel. This pixel-by-pixel alignment across all image tiles of the AOI is achieved by requesting a bundle block adjustment (BBA), Maxar's proprietary technique for aligning pixels within a stack of images where off-nadir angles are 30 degrees or less (Maxar, 2022a). The ARD service is available for Maxar's GeoEye-1, WorldView-1, WorldView-2, WorldView-3 and WorldView-4 satellite archives. Upon completion, the service delivers three cloud-optimized GeoTIFFs for each image tile selected: a 4 or 8-band multispectral image, a panchromatic image and a pansharpened RGB image (Maxar, 2022b). At the discretion of the user, a set of specialised vector and raster data masks are also supplied and the panchromatic and multispectral images are served at the resolution of the native ground sample distance.

For this study, eight Maxar ARD image bundles of the Carn Euny study area were selected, covering an observation period from January to November in an arbitrary calendar year. Within the image bundles, all images are bundle block adjusted, more than three years old, have less than 40% cloud cover, off-nadir angles no greater than 30 degrees and a minimum sun elevation of 5 degrees. The location of the control site was confirmed in all images and the resulting image bundles were delivered to a secure Amazon S3 cloud storage platform with supporting metadata (Appendix E).

### 3.3.2 Validating Vegetation Indices (VIs)

Vegetation indices (VIs) are algebraic combinations of spectral bands derived from multispectral and hyperspectral imaging data. They are used to generate new unique pixel values which represent a particular behaviour or characteristic of vegetation in a scene (Basso et al., 2004; Bennett et al., 2012) like: 1) chlorophyll activity; 2) vegetation density and biomass; 3) plant health and stress; 4) vegetation moisture (e.g., Agapiou et al., 2013a). To date, well over 150 VIs have been defined in the remote sensing literature (Moriarty et al., 2018). This is principally a reflection of the need and derivation of niche VIs for specific fields of research. The VIs are used to detect changes in vegetation stress, soil moisture, growth rates, structure (e.g., vegetation density, leaf orientation) and biochemical properties like the concentration of chlorophylls and carotenoids (Agapiou et al., 2012a).

Following Stagakis et al. (2010), VIs are categorised into five types: (a) broadband VIs used to study broadband reflectance (multispectral imaging); (b) narrowband VIs used to study narrowband reflectance (hyperspectral imaging); (c) leaf pigment indices; (d) vegetation stress indices; (e) water stress indices. There is subsequently a full suite of vegetation indices available to detect anomalous changes in the reflection and biophysical condition of vegetation overlying subsurface features. However, their utility in detecting subsurface anomalies can sometimes be unreliable, where there is often a dependency on biological and physical factors like the landscape, soil characteristics, nutrient supply, climate, vegetation type, atmospheric effects, solar illumination geometry, sensor type, sensor calibration and sensor viewing conditions (Bannari et al., 1995; Solymosi et al., 2019).

Moreover, relatively few multi-temporal studies have explored how VIs perform over extended observation periods and even fewer have attempted to use VIs for the detection of subsurface anomalies in temperate climates (Agapiou et al., 2012a, 2013; Bennett et al., 2013; Moriarty et al., 2018).

When VIs are used for subsurface detection (mostly archaeological applications), research efforts have been criticised for using VIs without due consideration of the biophysical properties on which they are formed (Agapiou et al., 2014) and the field instruments used during their derivation (Xue and Su, 2017). Furthermore, a detailed assessment of the numerical performance of VIs in subsurface detection is vague, though valued attempts have been undertaken using spectral separability indices (Agapiou et al., 2012b), statistical mutual dependencies with archaeological mapping (Cerra et al., 2018), statistical correlations with earth resistivity data (Roslan et al., 2020) and various information extraction techniques (Abate et al., 2020).

Here, we propose a new two-tier approach for determining the highest performing VIs over the fogou in Carn Euny, statistically correlating VIs with residual gravity profiles and then GPR data. This VI prioritisation, selection and validation process identifies those VIs most sensitive to change in soil and vegetation stress above the fogou and more broadly, those VIs most sensitive to shallow subsurface detection in temperate, vegetated landscapes. In total, we source 37 broadband VIs from referenced literature (Appendix F) and apply them to Maxar high-resolution multispectral imagery in Table E1, Appendix E. Each VI used in this study is in Table F1, Appendix F, complete with abbreviations, equations and example references.

#### 3.3.2.1 Correlation with gravity

A 24 m gravity profile was established across the fogou at Carn Euny, bisecting the control site. This gravity profile, A-A', trends NW-SE and deliberately orientated perpendicular to the central tunnel axis of the fogou (Figure 3.3a). The tunnel axis of the fogou is aligned with the gravity station at 12 m along A-A', ensuring the fogou is midway along the gravity profile. The profile is marked with survey flags and field tape and logged using GPS coordinates where A: 50.1028956°N, 5.6341695°W and A': 50.1027488°N, 5.6339236°W.

A gravity base station was then established 25 m northwest of the fogou, where base station readings were collected prior to, midway and after the survey. Temporal variations in gravitational field strength (e.g., instrumental drift) were recorded and used to correct the observed gravity readings during the survey. Using a Scintrex CG-5 AutoGrav Gravimeter (Scintrex, 2018), gravity measurements along profile A-A' were taken from 0 to 24 m at two metre station intervals, and the relative height of the levelled gravimeter was recorded at each station using a Trimble 4500 Theodolite. Residual bouguer gravity values were compiled using standard gravity reduction procedures (LaFehr and Nabighian, 2012), assuming a value of 0.3086 mGal/m for the free air correction and a bouguer correction reduction density of 1.7 g/cm$^3$. Given the very short profile

length and the level ground in and around the control site, latitude and terrain corrections were unnecessary and tidal corrections were made using the gravimeter's in-built tide correction program. After removing any regional trends in gravity from deeper basement and crustal variations, these reduction procedures reveal changes in gravitational field strength along A-A' from lateral density variations in the near subsurface. These results were then analysed graphically as a residual 'bouguer anomaly' along A-A', prior to further assessment.

In parallel, and by using the 'Spatial Profile' tool in Hexagon's Earth Resources Data Analysis System (ERDAS) Imagine software, VI profiles along A-A' for all 37 broadband VIs (Appendix F) were generated from each of the eight different Maxar high-resolution multispectral images at Appendix E. Correlation coefficients, *R*, were then determined for the residual bouguer anomaly along A-A' and each VI profile. Noting the relevant imaging sensor and acquisition date, all VIs with correlation coefficients greater than |0.7| were then selected for further ground validation with GPR.

### 3.3.2.2 Correlation with Ground Penetrating Radar (GPR)

Using survey flags, the 13 m x 3.5 m control site was transformed into a grid at 0.5 m intervals, generating line markers for 8 x longitudinal GPR swathes and 27 x transversal GPR swathes (Figure 3.3b). After calibrating the GPR distance sensor, a gridded GPR survey was performed across the control site using a four-wheel IDS Opera Duo / Leica DS2000 GPR (IDS GeoRadar, 2023a). Changes in subsurface permittivity, conductivity and permeability were then recorded using both 250 and 700 MHz radio waves from the GPR's dual frequency antenna (IDS GeoRadar, 2021). The survey data was imported to IQMaps, a GPR software package designed by IDS GeoRadar, for processing, visualising and interpreting the GPR data (IDS GeoRadar, 2023b).

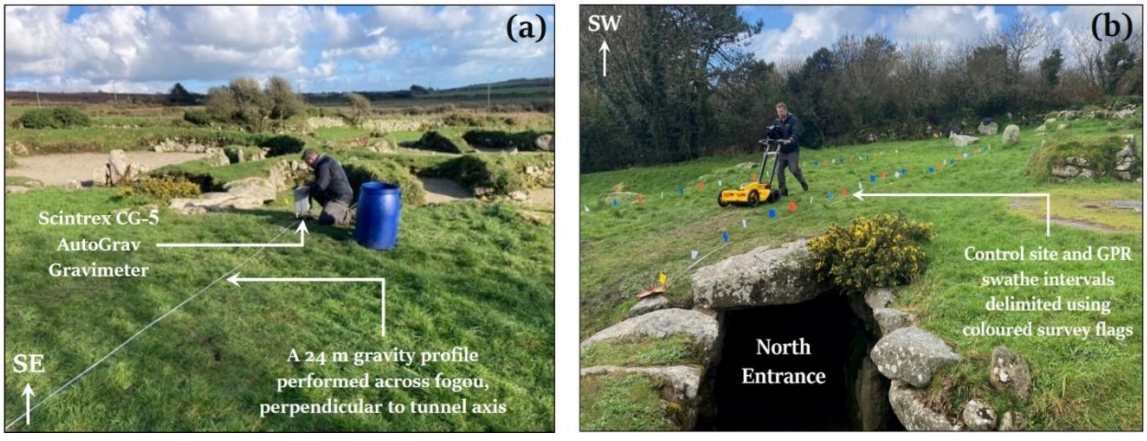



**Figure 3.3**. A residual gravity survey and gridded ground penetrating radar (GPR) survey of the control site above the Iron Age fogou in Carn Euny Ancient Village near Penzance, Cornwall, UK. a). A 24 m gravity profile is orientated perpendicular to the fogou's tunnel axis and the gravitational field strength is recorded every 2 m using a Scintrex CG-5 AutoGrav Gravimeter. b). The GPR survey is performed in a 13 m x 3.5 m grid and at 0.5 m swathe intervals. The survey is conducted using a four-wheel, dual frequency IDS Opera Duo / Leica DS2000 GPR (IDS GeoRadar, 2023a). The north entrance to the fogou and the location of the control site is as shown.

Within IQMaps, the GPR data swathes were extrapolated (merged) across the 0.5 m grid intervals to generate a series of GPR C-scans, defined as 2D plots of the relative change in dielectric permittivity, conductivity and permeability in the subsurface as a function of depth (Bigman, 2018). In 0.01 m depth increments, each GPR C-scan of the control site was visually inspected for the identification of significant and persistent subsurface anomalies over the fogou. Any credible anomalies were cross-referenced with the relevant B-scan, where GPR data is presented as a function of distance and depth for each swathe.

The GPR C-scans of the control site were also filtered using high and low-cut bandpass frequency filters (MHz) and signal smoothing techniques to enhance the GPR anomaly over the fogou (IDS GeoRadar, 2023b). The filtered C-scan best revealing subsurface anomalies in permittivity, conductivity and permeability above the fogou was imported into ESRI's ArcGIS Pro GIS software package as a GeoTIFF, where the processed C-scan could be compared to Maxar satellite imagery from Table E1.

Separately, all VIs with correlation coefficients greater than |0.7| (from Section 3.3.2.1) were applied to the Maxar high-resolution multispectral TIFF files to generate specific VI image layers. These optimal VI image layers were then pansharpened using a 'NNDiffuse Resolution Merge' or 'HPF Resolution Merge' (Amro et al., 2011; He et al., 2004; Zhao et al., 2016) before clipping with a shapefile of the control site. The result is a series of pansharpened spectral image subsets of the control site, each featuring pixel values of a particular vegetation index from a specific multispectral image that correlated above |0.7| with residual gravity.

The final processing stage required a quantitative means to assess and grade the similarity between the pansharpened VI image subsets and a GPR C-scan of clear subsurface anomalies from the fogou. Therefore, the most content-rich band showing these GPR anomalies was extracted from the GPR C-scan and exported to MATLAB. Similarly, the pixel values from the pansharpened VI image subsets of the control site were re-stretched from 0-255 before exporting to MATLAB as TIFF files with identical image and cell sizes as the GPR C-scan.

In MATLAB, the image similarity between the VI image subsets and the GPR C-scan (ground truth) were quantitatively assessed (and graded) using MATLAB's Structural Similarity Index Measure (SSIM) and a 2D cross-correlation. The former, using MATLAB function SSIM, compares the luminance, contrast and structural information between two images (Brunet et al., 2012; Dosselmann and Yang, 2011) and then calculates a structural similarity index value (*SSIMVAL)* between 0 and 1. The latter, using MATLAB function CORR2, returns the 2D correlation coefficient, *R*, between the two image arrays, again grading between 0 and 1. A similarity average (*SIMAV*) was calculated for each VI image subset where *SIMAV* = (*R*+*SSIMVAL*)/2. This similarity average was used to identify those VI image subsets of the control site which best represent the near subsurface and its material irregularities.

### 3.3.3 Subsurface detection

The three VI image subsets with the highest scoring similarity averages from Section 3.3.2.2 were selected for further analysis, beginning with a visual inspection of the rate of change in VI across the control site. By calculating a magnitude of the rate of change in VI (in both the '*x*' and '*y*' direction) for every pixel in a VI image subset, strong edge effects around substantial subsurface anomalies were identified. High and low pixel value "edge effects" depict significant *changes* in vegetation health from soil matrix irregularities over subsurface features like the fogou (Gao et al., 2024; Susantoro et al., 2018).

Subsequently, the three VI images with the highest scoring similarity averages were exported to MATLAB for a gradient magnitude (Gmag) computation[1] (ElBedwehy et al., 2020; Xue et al., 2014). We then applied the MATLAB function GRADIENTWEIGHT to each of the three VI images of Carn Euny before pansharpening and clipping to the extent of the control site. As a result, six VI image subsets were made available for further analysis; three original VI image subsets of the control site and their Gmag equivalent.

#### 3.3.3.1 Using False Colour Composites (FCCs)

The final six VI image subsets of the control site from Section 3.3.3 are visually examined and quantitatively assessed as a series of false colour composites (FCCs) through colour channels RGB. Here, each VI image is stacked to form a six-layer multiband raster using the COMPOSITE BANDS raster function in ArcGIS Pro. Each three-band combination from this six-layer image stack is systematically inspected in RGB, producing 20 different band combinations for review; *noting unique combinations of three bands is essential, but band order is not*. For quantitative assessment, each three-layer multiband raster (i.e., FCC) was transformed into a single greyscale layer (with equal weighting) using the ArcGIS Pro GREYSCALE raster function, and then pixel values were re-stretched from 0-255. Finally, we export each greyscale FCC to MATLAB for a structural similarity index measurement (SSIM) and a 2D cross-correlation with a suitable GPR C-scan of the control site. Similarity averages (*SIMAVs*), were calculated for each FCC and we grade accordingly.

#### 3.3.3.2 Using Edge Detection

Each of the six VI image subsets from Section 3.3.3 are filtered with a 5 x 5 low-pass filter, a smoothing operation that calculates the mean pixel value in a 5 x 5 neighbourhood across the extent of the image. After smoothing, a 'Sobel horizontal' and a 'Sobel vertical' edge detection filter (Gao et al., 2010; Vinesta and Milton-Joe, 2019) were applied to each smoothed image subset. The two filtered image subsets for each VI are then stacked to produce a two-layer multiband raster; band

[1] The gradient magnitude (*Gmag*) of image pixel *f* is: $Gmag = [(\partial f/\partial x)^2 + (\partial f/\partial y)^2]^{0.5}$

1 is the vegetation indexed image subset after applying a 'Sobel horizontal' edge detection filter and band 2 is the image subset after applying a 'Sobel vertical' edge detection filter. The two-layer multiband raster is visually inspected in RGB using band combination 1-1-2 and then converted into a single layer greyscale equivalent, ensuring both bands are equally weighted in the conversion. After re-stretching pixel values from 0-255, each Sobel filtered greyscale raster image is exported to MATLAB for a SSIM and a 2D cross-correlation with the GPR C-scan. Similarity averages were once again calculated for each 'Sobel' filtered image subset and then graded.

## 3.4 Results

Results are presented in four subsections, each containing observations and statistical analysis from the gravity, GPR, FCC and edge detection methods in Sections 3.3.2 and 3.3.3. In order, they are: 1) VI selection using gravity; 2) VI validation using GPR data; 3) subsurface detection using the best performing VIs in FCCs; 4) subsurface detection using the best performing VIs in edge detection analysis.

### 3.4.1 Vegetation Index (VI) selection using gravity

The residual bouguer anomaly in Figure 3.4 is representative of lateral changes in density in the near subsurface along profile A-A'. This residual bouguer anomaly, represented by a dark blue line and triangles, displays a prominent gravity 'low' over the fogou at 12 m. Prior to normalising the bouguer anomaly, this negative gravity anomaly (termed A1) exhibited a 0.06 mGal ($6 \times 10^{-5}$ cm/s$^2$) reduction in gravity, caused by a mass deficit inside the fogou where soil and rock is substituted with air.

To verify this observation, a simple density model of the fogou was generated in 'Grav2dc' (Cooper, 1998), a gravity modelling program which calculates theoretical gravity anomalies over 2D subsurface bodies with ascribed density contrasts. By approximating the fogou as a 20 m long rectangular column of air with a density contrast of -2.072 g/cm$^3$ and dimensions as per Figure 3.2, a theoretical gravity anomaly of -0.055 mGal is produced (Figure G1, Appendix G). Using this theoretical gravity anomaly, we successfully verify the observed magnitude and width of bouguer anomaly A1 along A-A'. Away from the fogou, 0.03 mGal gravity 'highs' are seen at 4 m and 22 m along the profile (Figure G1). These positive gravity anomalies are approximately 50% less influential than the gravity 'low' generated by the fogou (anomaly A1) and expected to reveal shallow rock formations from the original Iron Age settlement.

In parallel, and using the VIs in Table F1, 37 VI profiles are obtained from each of the eight high-resolution multispectral image files of Carn Euny - catalogued as image bundles in Appendix E. Subsequently, we compile 296 VI profiles along A-A', each of which are then correlated with the residual bouguer anomaly to determine which VI, sensor type and image date combination produce the strongest correlation (Appendix F). Conveniently, the approximate equivalence in spatial

resolution of Maxar multispectral imaging sensors (Table E1) and gravity station intervals along A-A' ensure the x,y pairs, to the nearest metre, align as observations along the profile.

By acknowledging that variables with correlation coefficients, *R*, above |0.7| are highly correlated (Ratner, 2009), only 6 of the 296 VI profiles (approx. 2%) qualify for further analysis (Appendix F). These are listed in Figure 3.4 and shown graphically as normalised spectral profiles, where the negatively correlated VI profiles are made positive and then all VI profiles are stacked to the maximum amplitude of the bouguer anomaly with mean values removed. Of note, when R > |0.7|, Soil Salinity Index 5 (SI5), Soil Salinity Index 6 (SI6) and the Enhanced Vegetation Index (EVI) are the only positively correlated VIs and Iron Oxide, Soil Salinity Index 7 (SI7) and the Structure Insensitive Pigment Index (SIPI) are the only negatively correlated VIs (Table F1). Given their alignment with the normalised bouguer anomaly in Figure 3.4, and their associated VI definitions, the VI anomalies directly over the fogou suggest low vegetation greenness and chlorophyll levels in the meadow grass (Huete et al., 2002, 1997; Penuelas et al., 1995) and high iron oxide and salt concentrations in the soil column below (Abbas and Khan, 2007; Allbed and Kumar, 2013; Al-Quraishi et al., 2022; Segal, 1982).

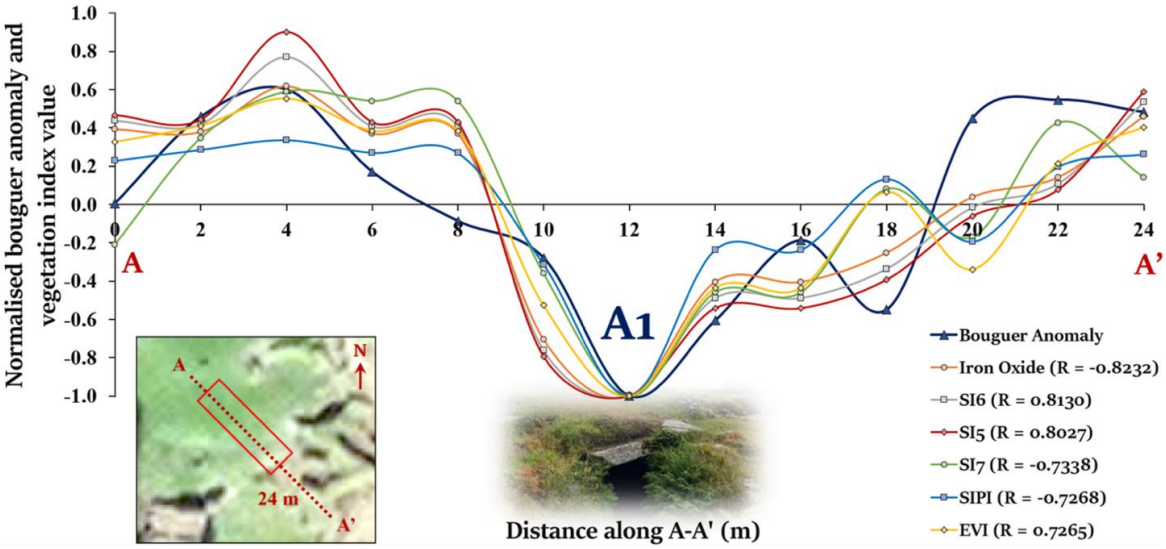



**Figure 3.4**. Normalised bouguer anomaly (dark blue line) and normalised vegetation index profiles along A-A' for all vegetation indices with residual gravity correlation coefficients > |0.7|; derived from Maxar's GeoEye-01 image dated 16 August 2013 and listed in descending order of magnitude. Negatively correlated vegetation indices are made positive and each vegetation index profile is stacked to the maximum amplitude of the bouguer anomaly, with mean values removed. The red dashed line in left inset image denotes orientation of 24 m long profile (A-A') through the control site, and central inset image of fogou entrance represents fogou location at 12 m.

In Figure 3.4 and according to Table F1, each of the VIs is also an algebraic manifestation of Red/Blue. Therefore numerically, the ratio of Red and Blue reflectance from the meadow grass and underlying soil appears to be the most sensitive *and* responsive spectral relationship along A-A'. Furthermore, all six VI profiles originated from Maxar's GeoEye-01 multispectral image of Carn Euny dated 16 August 2013 which, in any temperate region, is a warm month and an active

flowering month for smooth stalked meadow grass. It therefore seems apparent that the reflectance information from these six Red/Blue themed VIs is most representative of shallow subsurface irregularities when numerically analysed in the warmer months of a temperate climate. During these active growing months, the roots and shoots of cool-season grass are longer (Peterken, 2013), thereby becoming a more effective proxy for detecting irregularities in soil condition from underlying anomalies (Bennett et al., 2013; James et al., 2020).

### 3.4.2 VI validation using GPR

We use a 0.48 m deep 250 MHz GPR C-scan of the control site for VI validation. This GPR C-scan best represents the contrasts in dielectric permittivity, conductivity and permeability from the stone slabs across the roof of the fogou. To accentuate these subsurface material contrasts, the C-scan is visualised using traverse swathes only, and enhanced using a 1000 MHz high cut bandpass filter, a 100 MHz low cut bandpass filter, a 2 m background removal sliding window, a 10 m sensitive time control (STC) smoothed gain sliding window and a 10 ns STC smoothing time.

The most content-rich band in this filtered multiband GPR TIFF file is extracted from IQMaps and exported to MATLAB as a reference image for quantitative image comparisons with the six clipped and pansharpened VI image subsets. The six VIs used to generate these image subsets are those selected using the gravity observations along A-A' in Section 3.4.1. An example of this statistical 2D image comparison between the enhanced 0.48 m deep GPR C-scan and the EVI image subset is seen in Figure 3.5, showing both TIFF files staged in MATLAB after performing a 2D cross-correlation and SSIM calculation.

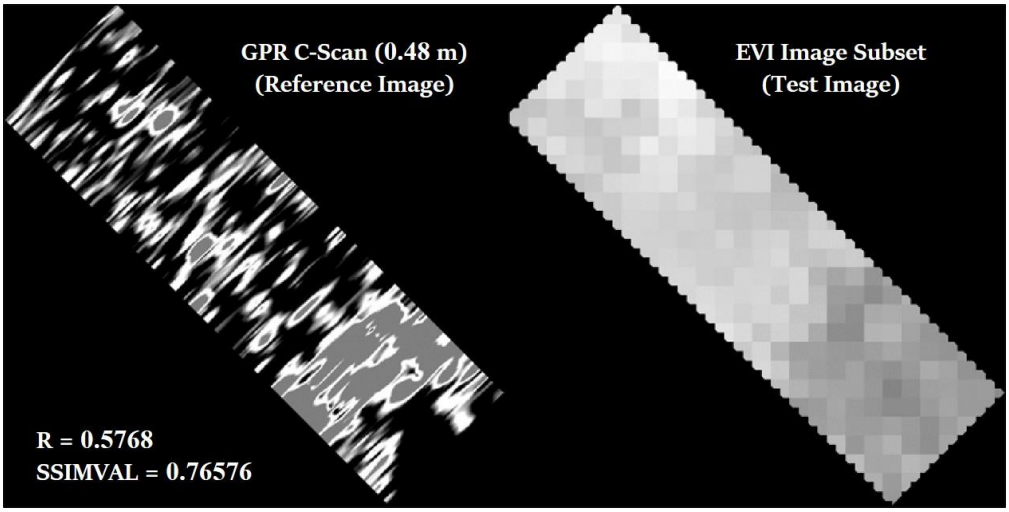



**Figure 3.5**. Image similarity assessment using the Enhanced Vegetation Index (EVI) image subset, staged in MATLAB for a 2D cross-correlation and structural similarity comparison using a ground penetrating radar (GPR) C-scan of the control site with dimensions 13 m x 3.5 m. **Left**: The reference image is a 0.48 m deep GPR C-scan of the control site in greyscale, acquired using an IDS Opera Duo GPR at 250 MHz. **Right**: The test image is a pansharpened EVI image subset of the control site, identical in size to the reference image. *R* is the 2D correlation coefficient and *SSIMVAL* is the structural similarity index value of the image pair; both scores range from 0 (no correlation) to 1 (identical images).

All image similarity results for VI validation using GPR are presented in Table 3.1. Image *SIMAVs* are recorded using the mean value from the SSIM and 2D cross-correlation coefficients. Compared to the *SSIMVALs*, a greater range in 2D correlation coefficient, *R*, can be seen, where the range in *R* is 0.0704 and the range in *SSIMVAL* is 0.004. This is explained by the lighter weighting of the 'pixel value' in SSIM calculations. Moreover, reducing the image subset pixel depth to 8-bit for MATLAB assessment will, to an extent, tone down and therefore standardise the original spectral variations in the image subset.

All *SIMAVs* are therefore very close in value, with a low standard deviation of 0.014 and a range of +/- 0.035. The VIs with the three highest *SIMAVs* in descending order are Iron Oxide, SI7 and SIPI, favouring the negatively correlated VIs from Section 3.4.1.

**Table 3.1**
Image similarity results for the pansharpened image subsets of the vegetation indices (with residual gravity correlation coefficients > |0.7|) and the 0.48 m deep GPR C-scan of the control site (reference image). The similarity average, *SIMAV*, for each vegetation indexed image subset (last column) is the mean value of the 2D correlation coefficient, *R*, and the structural similarity index value, *SSIMVAL*. Using similarity average (*SIMAV*), results are presented in descending order.

| Vegetation Index (VI) | 2D Correlation Coefficient (R)[1] | Structural Similarity Index Value (SSIMVAL)[2] | Similarity Average (SIMAV = [R + SSIMVAL] / 2) |
|---|---|---|---|
| Iron Oxide | 0.6371 | 0.76604 | 0.70157 |
| SI7 | 0.6359 | 0.76639 | 0.70115 |
| SIPI | 0.6264 | 0.76633 | 0.69637 |
| SI6 | 0.6040 | 0.76244 | 0.68322 |
| EVI | 0.5768 | 0.76576 | 0.67128 |
| SI5 | 0.5667 | 0.76626 | 0.66648 |

[1] Generated using MATLAB function CORR2; [2] Generated using MATLAB function SSIM

### 3.4.3 Subsurface detection - FCC analysis

A six-layer multiband raster is built for subsurface detection using the top three scoring VIs in Section 3.4.2 and Table 3.1, and their Gmag equivalents. Therefore, the six-layer multiband raster is: band 1 = Iron Oxide, band 2 = SI7, band 3 = SIPI, band 4 = Gmag Iron Oxide, band 5 = Gmag SI7 and band 6 = Gmag SIPI.

Using the method in Section 3.3.3.1, similarity averages for each FCC from the six-layer multiband raster can be seen in Table 3.2, noting there are a total of 20 different 3-band FCC combinations from a six-layer multiband raster. Similar to the image comparisons in Table 3.1, the 2D correlation coefficients, *R*, and the *SSIMVALs* are very close together. Again, compared to the *SSIMVALs*, a greater range in *R* is seen across the FCCs, where the range in *R* is 0.0187 and the range in *SSIMVAL* is 0.0016. Similarity averages, *SIMAVs*, once again have a low standard deviation of 0.003 and all *SIMAVs* are within +/- 0.011.

Regardless of the small range in *SIMAVs* across the 20 FCCs, a group of high scoring FCCs where *SIMAV* = 0.7012 are readily identified in Table 3.2. This group of FCC band combinations include:

2-3-5, 2-3-6, 2-4-5, 2-4-6 and 2-5-6; noting band 2 (SI7) is in each FCC and band 1 (Iron Oxide) is not. Within this group, all image comparison statistics are the same, suggesting that the superimposition of additional bands in support of SI7 has little effect on the resulting comparison with GPR data.

**Table 3.2**
Image similarity results for the 20 FCCs (test images) and the 0.48 m deep GPR C-scan of the control site (reference image). All 20 FCCs are derived from the six-layer multiband raster where: band 1 = Iron Oxide, band 2 = SI7, band 3 = SIPI, band 4 = Gmag Iron Oxide, band 5 = Gmag SI7 and band 6 = Gmag SIPI. There is a total of 20 combinations of three-band FCCs from a six-layer multiband raster. The group of FCCs with the highest scoring similarity averages, *SIMAVs*, are highlighted green.

| FCC Band Combination (Bands) | 2D Correlation Coefficient (R)[1] | Structural Similarity Index Value (SSIMVAL)[2] | Similarity Average (SIMAV = [R + SSIMVAL] / 2) |
|---|---|---|---|
| 1-2-3 | 0.6359 | 0.76639 | 0.70115 |
| 1-2-4 | 0.6359 | 0.76639 | 0.70115 |
| 1-2-5 | 0.6359 | 0.76639 | 0.70115 |
| 1-2-6 | 0.6359 | 0.76639 | 0.70115 |
| 1-3-4 | 0.6318 | 0.76624 | 0.69902 |
| 1-3-5 | 0.6319 | 0.76628 | 0.69909 |
| 1-3-6 | 0.6300 | 0.76612 | 0.69806 |
| 1-4-5 | 0.6327 | 0.76602 | 0.69936 |
| 1-4-6 | 0.6303 | 0.76588 | 0.69809 |
| 1-5-6 | 0.6302 | 0.76589 | 0.69805 |
| 2-3-4 | 0.6359 | 0.76640 | 0.70115 |
| 2-3-5 | 0.6360 | 0.76640 | 0.70120 |
| 2-3-6 | 0.6360 | 0.76640 | 0.70120 |
| 2-4-5 | 0.6360 | 0.76640 | 0.70120 |
| 2-4-6 | 0.6360 | 0.76640 | 0.70120 |
| 2-5-6 | 0.6360 | 0.76640 | 0.70120 |
| 3-4-5 | 0.6238 | 0.76591 | 0.69486 |
| 3-4-6 | 0.6227 | 0.76573 | 0.69422 |
| 3-5-6 | 0.6224 | 0.76572 | 0.69406 |
| 4-5-6 | 0.6173 | 0.76477 | 0.69104 |

[1] Generated using MATLAB function CORR2; [2] Generated using MATLAB function SSIM

In Figure 3.6, a visible differentiation between the regular VI image subsets and the Gmag VI image subsets is apparent. The FCC 1-2-3 (Iron Oxide – SI7 – SIPI) in Figure 3.6b and 3.6f shows lighter pixel values and therefore, according to VI definitions, higher levels of iron oxide, soil salinity and chlorophyll degradation over the fogou. These observations are well aligned with the material contrasts from the stone ceiling of the fogou, as detected by the GPR in Figure 3.6a and 3.6e. Conversely, FCC 4-5-6 (Gmag Iron Oxide – Gmag SI7 – Gmag SIPI) in Figures 3.6c and 3.6g presents a band of darker coloured pixel values handrailing the northwestern edge of the fogou, separating the meadow grass overlying the fogou from the meadow grass off the fogou. This band of darker pixels represents the zone in the control site where the *rates of change* in iron oxide, soil salinity and chlorophyll concentration are greatest. As expected, this pixel band delineates the edge of the fogou where, according to VI definitions, the rate of change in vegetation stress in the smooth stalked meadow grass is at its greatest. Figure 3.6d and 3.6h is FCC 2-3-6 (SI7 – SIPI – Gmag SIPI) from the highest scoring FCC group in Table 3.2, generating a *SIMAV* of 0.7012 with

the GPR C-scan. Here, the benefits of combining regular VI image subsets (SI7 and SIPI) with a Gmag VI image subset (Gmag SIPI) can be seen. The lighter coloured pixel values represent, by VI definition, higher levels of soil salinity and chlorophyll degradation over the fogou and the darker band of image pixels along the northwestern edge of the fogou signifies very high rates of change in chlorophyll concentration and vegetation stress in the meadow grass.

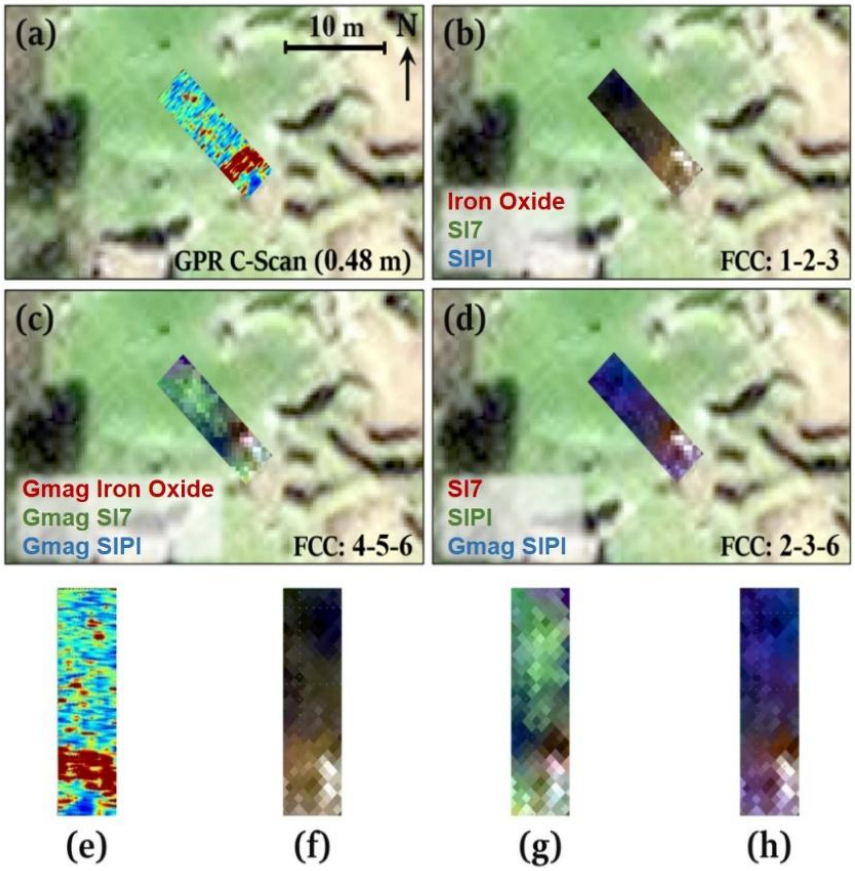



**Figure 3.6**. Ground penetrating radar **(**GPR) reference image and example false colour composites (FCCs) from the six-layer multiband raster. a) & e). Reference image of the control site is a 0.48 m deep GPR C-scan. b) & f). FCC of the control site with Iron Oxide observed through the red channel, Soil Salinity Index 7 (SI7) through green and the Structure Insensitive Pigment Index (SIPI) through blue. c) & g). FCC of the control site using gradient magnitude (Gmag) layers, with Gmag Iron Oxide through red, SI7 through green and Gmag SIPI through blue. d) & h). Regular vegetation index (VI) and Gmag FCC hybrid with joint top scoring similarity average, where SI7 is viewed through red, SIPI through green and Gmag SIPI through blue.

### 3.4.4 Subsurface detection - Edge Detection analysis

Edge detection *SIMAVs* for each VI image subset from the six-layer multiband raster in Section 3.4.3 are found in Table 3.3. Very closely scoring, the range in *R* is 0.0131 and the range in *SSIMVAL* is 0.0061. Similar to the FCC results, the *SIMAVs* have another low standard deviation of 0.003 and all *SIMAVs* are within +/- 0.01. The highest scoring VI is Gmag SI7, where *SIMAV* = 0.68151, followed by SIPI, where SIMAV = 0.67876. Following VI definitions, this implies that the 'Sobel horizontal' and the 'Sobel vertical' edge detection filters are most effective at detecting the

edges of the zone where there is: 1) the greatest rate of change in soil salinity (using Gmag SI7); 2) the lowest concentrations of chlorophyll (using SIPI).

**Table 3.3**
Using the 0.48 m deep GPR C-scan of the control site as the reference image, below are the image similarity results for each greyscale vegetation indexed image subset after applying a 'Sobel horizontal' and a 'Sobel vertical' edge detection filter and then stacking as a two-layer multiband raster. Using similarity average (*SIMAV*), results are presented in descending order.

| Vegetation Index (VI) | 2D Correlation Coefficient (R)[1] | Structural Similarity Index Value (SSIMVAL)[2] | Similarity Average (SIMAV = [R + SSIMVAL] / 2) |
|---|---|---|---|
| Gmag SI7 | 0.5949 | 0.76811 | 0.68151 |
| SIPI | 0.5905 | 0.76701 | 0.67876 |
| Gmag Iron Oxide | 0.5916 | 0.76250 | 0.67705 |
| Iron Oxide | 0.5869 | 0.76702 | 0.67696 |
| SI7 | 0.5850 | 0.76720 | 0.67610 |
| Gmag SIPI | 0.5818 | 0.76201 | 0.67191 |

[1] Generated using MATLAB function CORR2; [2] Generated using MATLAB function SSIM

An example of the edge detection process is shown in Figure 3.7 using the Gmag SI7 image subset. Viewed at a scale of 1:200 and after smoothing with a 5 x 5 low-pass filter, Figure 3.7a and 3.7e delineate the zone where the rate of change in SI7 is greatest, represented by a band of darker coloured pixels along the edge of the fogou. Figure 3.7b and 3.7f is the result after layer stacking the filtered Gmag SI7 image subset with a 'Sobel horizontal' edge detection filter (band 1) and a 'Sobel vertical' edge detection filter (band 2). At a scale of 1:200, this two-layer multiband raster is viewed in RGB as a FCC with layers 1-1-2. However, the edges depicting the zone of greatest rate of change in SI7 are not clear, because the viewing scale is too large (1:200).

Conversely, when viewed at 1:500 in Figures 3.7c and 3.7g, the edges of this zone become apparent, expressing the zone of increased soil salinity as a smoother patch than those regions where the rate of change in SI7 is much less. We then remove this scale dependency on the visual interpretation of edges by converting the two-layer multiband raster to a single greyscale layer (Figure 3.7d and 3.7h). This allows the user to explore the image subset for edges of significant change in VI much more easily.

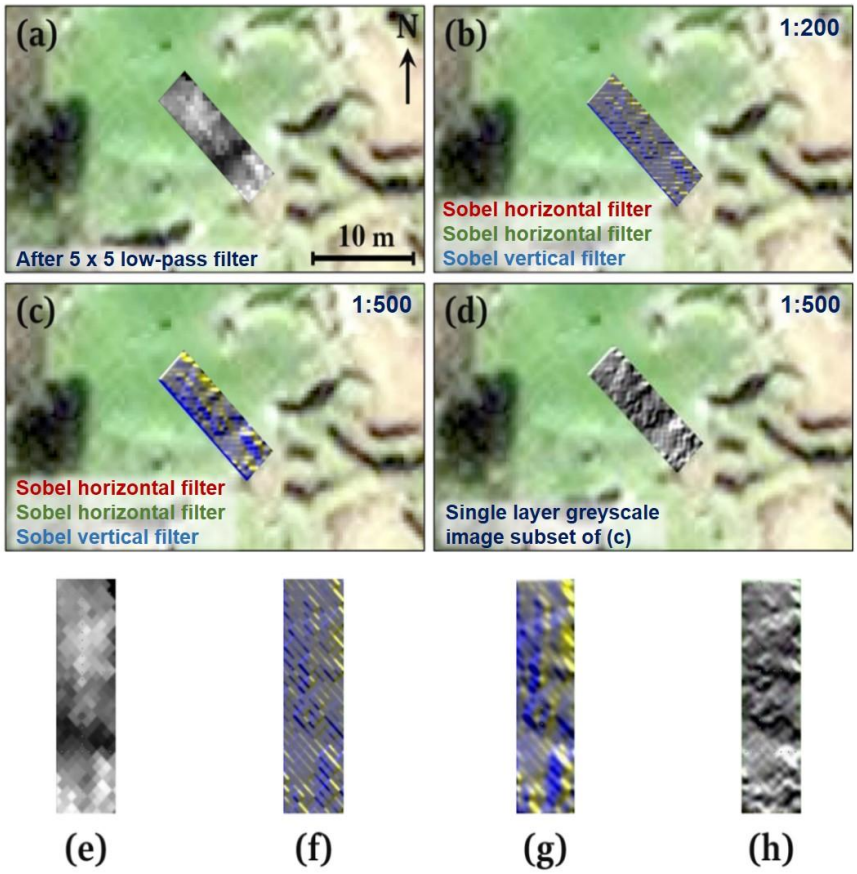



**Figure 3.7**. Edge detection analysis of the gradient magnitude (Gmag) Soil Salinity Index 7 (SI7) image subset. a) & e). Gmag SI7 image subset of the control site after smoothing with a 5 x 5 low-pass filter. b) & f). A two-layer multiband image subset of Gmag SI7 viewed at scale 1:200; layer 1 is the Gmag SI7 image subset filtered with a 'Sobel horizontal' edge detection filter and layer 2 is Gmag SI7 image subset filtered with a 'Sobel vertical' edge detection filter, observed in Red-Green-Blue (RGB) as layers 1-1-2 respectively. c) & g). Same as Figure 3.7b but observed at a scale of 1:500. d) & h). The two-layer multiband Gmag SI7 image subset from Figures 3.7b and 3.7c, converted into a single layer greyscale image subset and viewed at 1:500.

## 3.5 Discussion

The advantages of using high-resolution or very-high-resolution (VHR) multispectral imagery in subsurface detection are considerable, especially when searching for subsurface features less than c.2 m in width. By analysing multispectral pixels less than 2 m x 2 m, the option of conducting a statistical and graphical comparison of spectral profiles with geophysical field observations (like residual gravity) is unlocked. In doing so, VIs can be prioritised, validated and correctly calibrated for broader subsurface applications in similar environmental settings. Spectral comparisons with geophysical data are rarely undertaken numerically, other than some early attempts with microgravity (Morley and Ekpenyong, 2012) and more recently, electrical resistivity data (Roslan et al., 2020). Usually, remotely sensed observations of the subsurface are performed using open-access and freely distributed medium-resolution (5 - 10 m) multispectral imagery and then *visually* compared with survey data from geophysical campaigns (e.g., Agapiou et al., 2023).

By *numerically* identifying optimal vegetation indices for subsurface detection with geophysics and correlation statistics alone, any biases associated with the definition and application of each VI are alleviated. Given their vulnerability to physical factors like: 1) the size and depth of the buried feature; 2) atmospheric effects; 3) solar illumination geometry; 4) sensor type; 5) sensor calibration; 6) sensor viewing conditions (Bannari et al., 1995; Jackson et al., 1983; Solymosi et al., 2019), we deem it prudent to remove any application bias of VI's in subsurface detection. Proving this concept, the VIs we assess to be most responsive to buried anthropogenic features are determined purely by algebra; initially by their spectral response along a specified *distance* (correlation with gravity – Section 3.3.2.1) and then by their spectral response across a specified *area* (correlation with GPR – Section 3.3.2.2).

Our second observation relates the subsurface detection efficiency of each VI with the image acquisition date and therefore, time of year. As seen in Table F1, Appendix F, few of the VIs used in this study correlate with residual gravity over the fogou in the cooler winter months. However, in the warmer month of August, six VIs correlate significantly well with residual gravity, generating correlation coefficients > |0.7| (Figure 3.4). These are: Iron Oxide, EVI, SIPI, SI5, SI6 and SI7, each statistically identified and verified as a successful spectral index for subsurface detection when ambient temperatures are sufficiently high. We therefore suggest summer temperatures in a temperate, vegetated environment are crucial for the successful detection of subsurface features with multispectral remote sensing.

Our third observation resides with their algebraic similarity, where each of the six VIs identified using gravity are algebraic manifestations of Red/Blue (see VI equations in Table F1). This is explained by a notable separation in Red and Blue reflectance values over the fogou in warm temperatures (Figure 3.8). We exaggerate this separation by plotting the difference in Red and Blue reflectance along A-A' at a different scale to the raw spectral band reflectance values (Figure 3.8 - pink dashed line). Along with an observed increase in NIR absorption from the meadow grass directly above the fogou (Figure 3.8 – red dashed line), it is clear from our controlled study that a significant change in the Red/Blue reflectance ratio is a convincing indicator of soil matrix irregularity and anomalous vegetative behaviour above a subsurface incongruity.

From a *qualitative* perspective, and by using VI definitions, it is also worth considering the context and application of those VIs we identified using gravity. First, we consider the Iron Oxide index where, by definition, a significant increase in the Red/Blue reflectance ratio over the fogou could be indicating an increase in the rate of thermal transformation of free iron to iron oxides in the soil during warm, summer months (Mendes et al., 2022). Furthermore, during warmer months, increased chemical weathering of the fogou's 0.5 m deep granite capstones is probable, contributing to the increased concentration of iron (III) oxide (Oliva et al., 2003). This chemical transformation can reduce the concentration of soluble iron left in the soil, thereby triggering a

degradation in chlorophyll production (and potentially chlorosis) in the meadow grass above (Chaney and Bell, 1987; Rout and Sahoo, 2015).

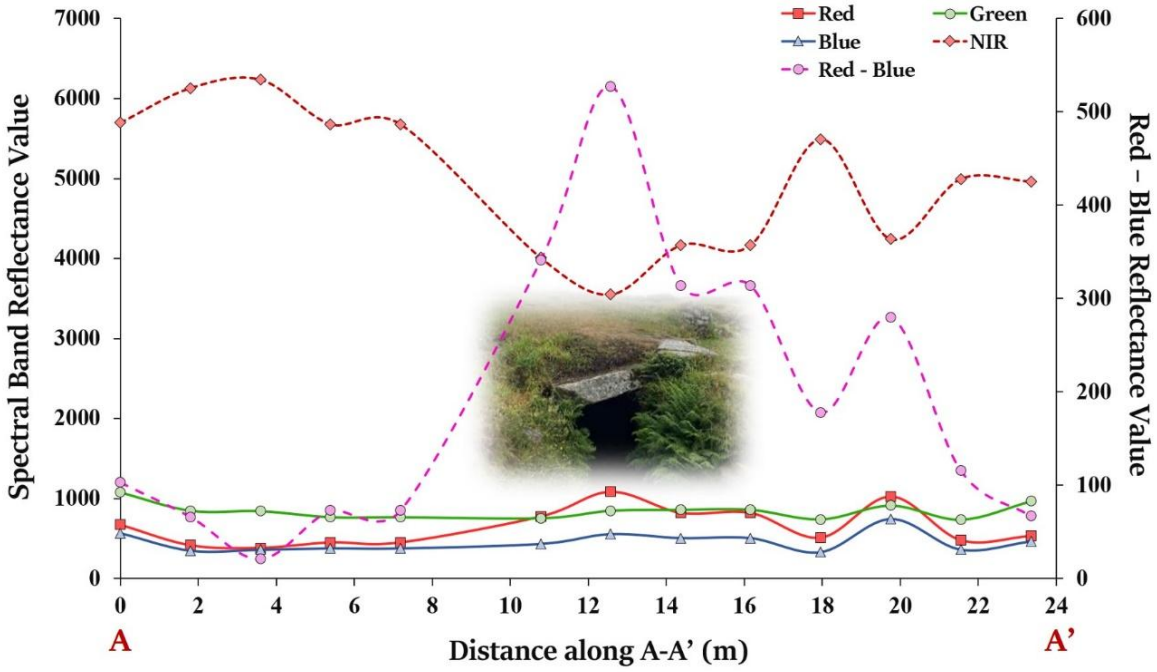



**Figure 3.8**. Variation in Red, Green, Blue, Near Infrared (NIR) and [Red – Blue] reflectance values from smooth stalked meadow grass above Carn Euny's fogou; observed along profile A-A' on 16 August 2013 from Maxar's GeoEye-01 Earth-imaging satellite. Central inset image of fogou entrance represents fogou location at 12 m.

Typical by-products from the subsurface weathering of granite are soluble salts (Migon, 2006). From using the definition of soil salinity indices SI5, SI6 and SI7 in this study (Abbas and Khan, 2007), we could be using manifestations of Red/Blue to identify the presence of ground salts over the fogou which again, could partially originate from the subsurface weathering of the underlying capstones. Ground salts like these can generate considerable osmotic stress in vegetation, which in this case, could be depriving the overlying meadow grass of sufficient water uptake, essential nutrients and reproductive development (Allbed and Kumar, 2013).

Soil salinity concentrations are also intensified in times of drier weather, especially in small soil profiles above voids like a fogou. Here, we expect the stone-walled fogou is behaving like a drain, accelerating soil drainage rates (Lv et al., 2020), reducing soil water storage levels (Zeng et al., 2023) and consequently, increasing soil salinity levels in the ground above (Allbed and Kumar, 2013). This soil profile can also become warmer than the soil columns either side of the fogou, triggered by: 1) the insulation from the air-filled fogou; 2) comparably less soil to heat; 3) a higher bulk density and heat dissipation rate from overlying soil compaction (Onwuka, 2016). These heating conditions could be reducing soil moisture levels and water viscosity above the fogou, allowing more water (at greater rates) to percolate through the soil profile above. Therefore, in times of warm and dry weather, we anticipate soil water retention above the fogou is much lower,

thereby increasing soil salinity levels and reducing the availability of water for overlying vegetation (Douaoui et al., 2006).

The spectral response we observe from the algebraic manifestations of Red/Blue in the EVI and the SIPI also seem to support these observations (Figure 3.4 and Table F1). The EVI signifies stress over the fogou because there are much higher levels of absorption in the NIR (Huete et al., 2002). The SIPI also signifies vegetation stress because, according to Penuelas et al. (1995), SIPI is designed to reveal a reduction in chlorophyll production from higher levels of reflection in Red, whilst sustaining reflectance and absorption levels in Blue from the resilience and unaffected behaviour of the original carotenoids in the meadow grass (Figure 3.8). During times of vegetation stress, carotenoids can also increase in concentration to protect the photosynthetic reaction centres from excess radiant energy (Penuelas et al., 1995), thereby further stabilising the reflection values in Blue (Figure 3.8).

Therefore, according to the *qualitative* descriptions of Iron Oxide, EVI, SIPI, SI5, SI6 and SI7, the Red/Blue reflectance ratio in each index is either wholly or partially representative of: 1) iron oxide concentrations in the soil; 2) ground salt concentrations; 3) vegetation stress. Subsequently, in warm summer months, the result we see remotely above the fogou in Carn Euny is: stressed meadow grass with reduced chlorophyll production, and a soil with relatively high concentrations of iron oxide (III) and ground salt.

A temporal study of these high performing VIs also supports our qualitative explanation. Figure 3.9a shows the behaviour of iron oxide reflectance levels “on” and “off” the fogou during an arbitrary calendar year. Iron Oxide index values are recorded at three specific points along A-A’ from each of the eight high-resolution multispectral images listed in Table E1. Iron oxide levels along A-A’ are similar until July, when concentrations increase above the fogou. From July to October, iron oxide levels in the soil profile above the fogou are notably higher than the soil profiles away from the fogou, almost doubling in reflection value. These observations align with the increased weathering of granite capstones across the fogou during higher temperatures (Migon, 2006), where greater concentrations of iron oxide are released into the soil above the fogou. To then reset the free iron/iron (III) oxide ratio in temperate soil takes time (Mendes et al., 2022) where, in this study, Figure 3.9a suggests iron levels along A-A’ are rebalanced (and much lower) by November.

Conversely, as seen in Figure 3.9b, SIPI reflection values from the meadow grass along A-A’ only meaningfully change above the fogou in July and August. This implies a deterioration in the physiology and phenology of the meadow grass above the fogou in the summer, where SIPI values are known to rise in senescing and unhealthy vegetation (Penuelas et al., 1995). Compared to iron oxide (Figure 3.9a), this is a far shorter interlude in typical reflectance behaviour, potentially signifying the stress weighting of the grass is less dependent on iron oxide concentration and more dependent on the soil’s water and salinity levels. This aligns with observations made by Gris (1844)

in Dogan (2008), who caveat iron's crucial role in chlorophyll synthesis with realistically low iron consumption rates.

Therefore, the temporal evidence in Figure 3.9 suggests that higher ambient temperatures in vegetated, temperate terrain will almost certainly foster the best conditions for shallow subsurface detection. Warmer months, especially between May and September, are active growing months for most temperate, cool-season vegetation types (Belesky and Fedders, 1995) and therefore the reflectance behaviour of overlying vegetation is much more sensitive to subsurface irregularity.

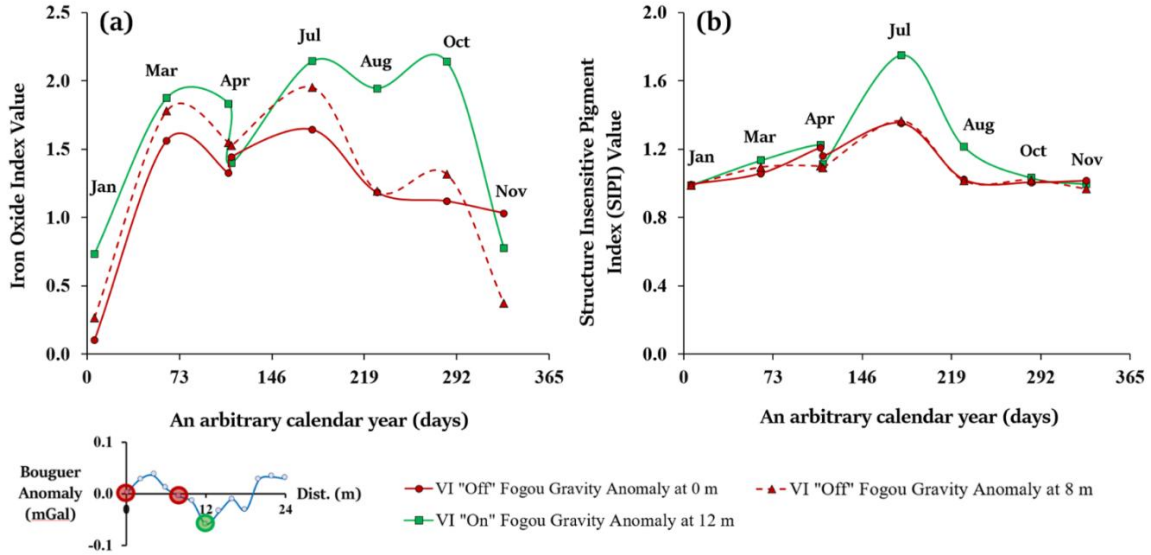



**Figure 3.9**. A temporal spectral analysis of Iron Oxide and the Structure Insensitive Pigment Index (SIPI) "on" and "off" the fogou gravity anomaly in Carn Euny. a). Temporal spectral analysis of Iron Oxide Index "on" the fogou gravity anomaly at 12 m (green line) and "off" the fogou gravity anomaly at 0 and 8 m (red bold and red dashed lines) along residual bouguer anomaly A-A' in Figure 3.4. b). Temporal spectral analysis of SIPI "on" and "off" the fogou gravity anomaly using the same distance observation markers as Figure 3.9a.

According to our *qualitative* interpretation of the most sensitive VIs in this study, the fogou in Carn Euny Ancient Village is thought to affect drainage rates, temperature profiles and chemical weathering, all of which are naturally accentuated in the summer months. However, from a *quantitative* perspective, we see greater levels of NIR absorption and a higher Red/Blue reflectance ratio above the fogou in warm, summer months (Figure 3.8). When we then consider these raw spectral observations with the physical factors that affect VI interpretation (Bannari et al., 1995), we deem it both prudent and pragmatic to propose that buried anthropogenic structures influence *numerous* soil properties, in which the behaviour of overlying vegetation becomes a proxy. During the warm, summer months in a temperate environment, anomalous reflectance behaviour in NIR and Red/Blue showcase a strong potential to expose these subsurface incongruities.

Finally, only one control site and one subsurface target site have been explored. This could bias our interpretation, particularly to GeoEye-01 multispectral imagery, meadow grass and subsurface

granite anomalies. Therefore, to assess the general detection efficiency of our highest performing VIs in a broader context (i.e., subsurface anomalies under cool-season vegetation), we consider their broader application on other temperate, grass covered sites at similar times of year. Only then can we progress our assurances of the Red/Blue reflectance ratio in the detection of buried subsurface features.

### 3.5.1 Subsurface detection workflow

Using airborne and spaceborne remote sensing, we present a subsurface detection workflow (Figure 3.10) which adopts the image processing methodology used in our controlled study. Underpinning this workflow is the application of the best performing VIs as evidenced from our results in Section 3.4. However, from a quantitative perspective, we anticipate our workflow will have broader utility in subsurface detection across all temperate, vegetated landscapes. As a minimum, we thereby recommend the algebraic definition of these VIs, and their Gmag equivalents, in any temperate, cool-season vegetated site with brown earth soil.

#### 3.5.1.1 Design

Incorporating SI7 and SIPI in the workflow (Figure 3.10) are obvious choices given their performance in depicting the stressed soil and meadow grass over the fogou in FCCs (Table 3.2 and Figure 3.6) and edge detection (Table 3.3 and Figure 3.7). Within the highest scoring group of FCCs (Table 3.2), all five FCCs contained variables of SI7, SIPI and their Gmag equivalents - less two FCCs which contained Gmag Iron Oxide as one of the three bands. Moreover, SI7 and SIPI (and the Red/Blue reflectance ratio therein), have already shown resilience and reliability outside of this study, celebrated respectively as the best performing indices in an appraisal of irrigated soil salinity in Pakistan (Abbas and Khan, 2007) and during an assessment of the carotenoids/chlorophyll *a* ratio in leaves (Penuelas et al., 1995).

The iron oxide ratio (Red/Blue) performed less well during the FCC and edge detection analysis although the SIMAV scores across all image similarity assessments are incredibly close. From an application perspective, detecting high levels of iron alteration is not always characteristic of a subsurface anomaly because some buried structures are purely soil based e.g., buried ditches, foundation trenches, moats, postholes and storage pits (Huisman, 2009). However, in the GeoEye-01 image dated 16 Aug 13, the spectral profile for the Iron Oxide index along A-A' produced the strongest correlation with residual gravity (Figure 3.4). Therefore, numerically, the VI equation for Iron Oxide (merely Red/Blue) is an essential spectral computation in our workflow.

Given our numerical selection process for best performing VIs, the VI image subsets produced in our image processing workflow adopt algebraic labels as opposed to VI names (Figure 3.10). This way, any application bias is removed, recognising the VI's conditional dependency on the instrument(s) used in their formation (Xue and Su, 2017), the conditions in which they were derived

(Giovos et al., 2021) and the physical factors that affect their reliability (Bannari et al., 1995; Jackson et al., 1983). In our workflow, these spectral indices are collectively termed 'subsurface detection indices'.

The Gmag equivalents are also produced in our image processing workflow (Figure 3.10), and then all six image tiles are pansharpened and clipped to the study area. An optimised six-layer image stack is then built using the clipped subsurface detection indices (Figure 3.10), before detecting subsurface anomalies using FCCs and edge detection analysis. To maximise the workflow's utility with various multispectral sensor types, only the four conventional spectral bands are needed: Red, Green, Blue and NIR. Similarly, to maximise the workflow's detection efficiency and to align with our observations from the controlled study, the use of multispectral images from summer months is also advised.

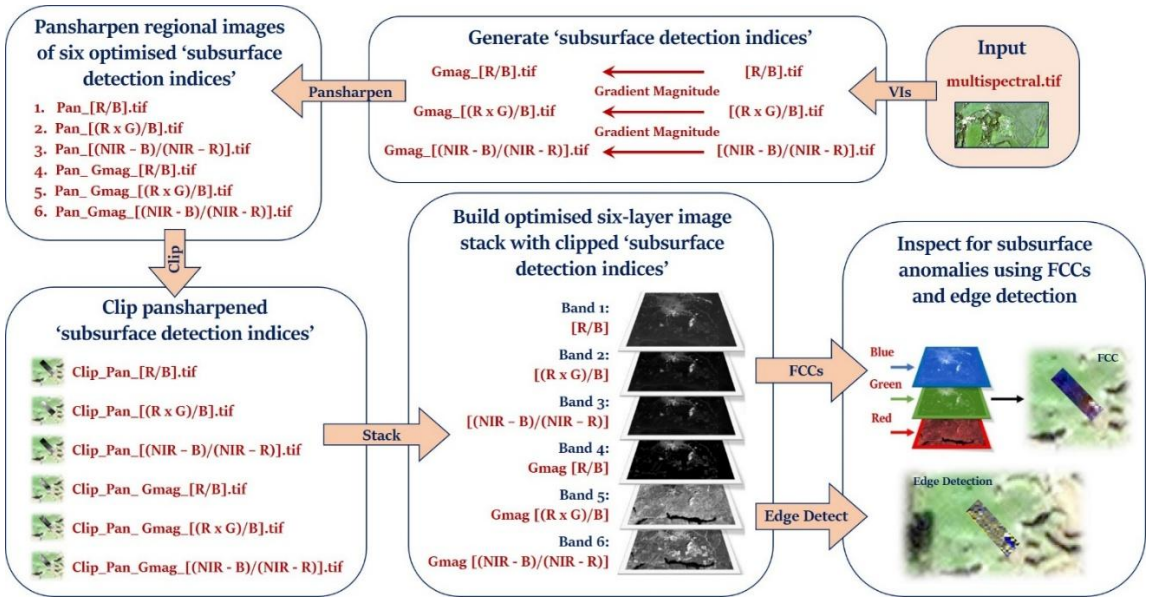



**Figure 3.10**. A multispectral image processing workflow for shallow subsurface detection in a temperate landscape with cool-season vegetation, optimised for detection during summer months.

### 3.5.1.2 Test

To test the detection efficiency of the multispectral image processing workflow in Figure 3.10, two experimental sites with similar agronomic conditions were inspected (Figure 3.11). Both sites are located in flat fields with cool-season grass, secured within a private estate south of Villers-Bocage in Normandy, France. The climate is temperate and the soils are free-draining composites of sand, silt and clay.

The first site, 'Experimental Site A', is a 0.4 m deep clay drainage pipe trending approximately 45 m E-W under a field of cool-season grass, predominantly covered by festuca, couch and meadow

grass (Figures 3.11a and 3.11b). The clay pipe is 0.23 m in diameter, built in sections and partially defective, reducing its effectiveness at syphoning water away from a nearby rill and moat.

The second site, 'Experimental Site B', consists of two buried ditches which upon close inspection, are legacy French drains now covered in a brown earth soil and cool-season grass. From using and interpreting GPR data[2], the buried ditches are approximately 2.1 m – 3.3 m wide, 0.1 – 0.4 m deep and extend across a flat open field to a catchment ditch in the east (Figures 3.11e and 3.11f).

The subsurface detection workflow successfully generates FCCs and greyscale edge detection image subsets which accentuate the stressed soil and vegetation anomalies over the clay drainage pipe and buried ditches (Figures 3.11c, 3.11d, 3.11g and 3.11h). Of note, band 5 (Gmag SI7) and band 6 (Gmag SIPI) from the workflow's optimised six-layer image stack in Figure 3.10 are used in the FCCs that best accentuate the subsurface anomalies (Figures 3.11c and 3.11g). Similarly, band 6 (Gmag SIPI) and band 2 (SI7) are, from visual inspection, the best performing subsurface detection indices with edge detection (Figures 3.11d and 3.11h). To understand the statistical significance of the spatial transitions in our FCCs and edge enhanced image subsets, local indicators of spatial association (LISA) could be employed to detect the *meaningful* boundaries of prospective subsurface anomalies (Anselin, 1995). The most common LISA statistic is Local Moran's I, which could be employed to standardise the pixel values along the edge of an anomaly (relative to an image mean), and then compare the pixel values to a weighted average of neighbouring pixels to determine which edges are similar to their neighbours and which are not (e.g., Song and Song, 2022).

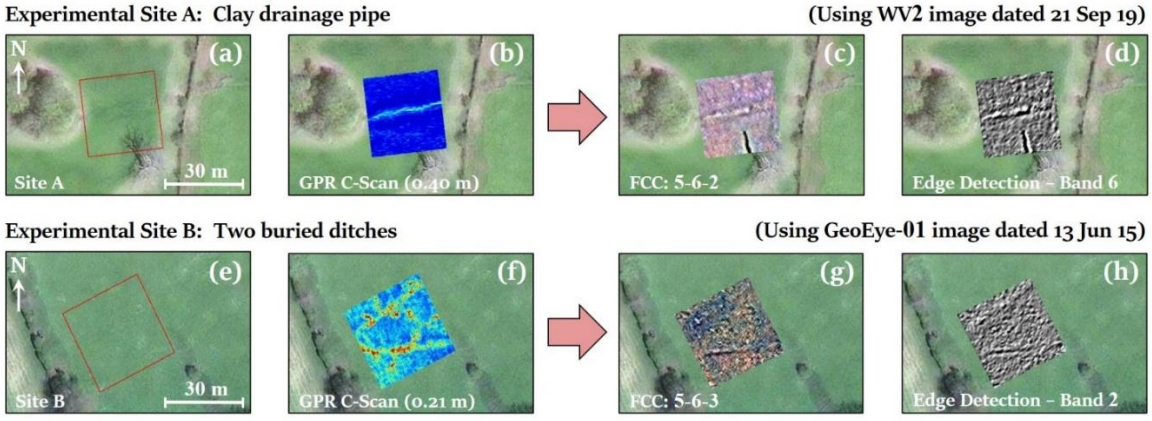



**Figure 3.11**. Applying the high-resolution multispectral subsurface detection workflow on two experimental sites; a clay drainage pipe (Site A) and two buried ditches (Site B). a) & e). Perimeter of experimental sites depicted by red lines. Site A is 30 m x 30 m and Site B is 34 m x 34 m. b) & f). Ground penetrating radar (GPR) C-scans of experimental sites A and B with depth slice annotated. c) & g). Example false colour composite (FCC) from each experimental site with Red-Green-Blue (RGB) band combination annotated. d) & h). Edge detection results from each experimental site in greyscale. All data has been acquired with the landowner's permission; site locations available on request to the authors.

[2] All geophysical data has been acquired with the landowner's permission.

Alternatively, advanced computer vision techniques could be used to enhance the visibility of the subsurface features in Figures 3.11c, 3.11d, 3.11g and 3.11h. For example, deep learning and in particular, CNNs, could be used for the recognition and detection of subsurface anomalies in FCCs and edge filtered rasters (Aslan and Özüpak, 2025; Yuan et al., 2025). To support archaeological prospecting, the utility of graph neural networks (GNNs) could also be explored, especially across large archaeological sites or several sites with similar heritage (Dilena, 2024). Here, relationships between the location and depth of suspected subsurface objects (positional), buried artefacts (relational) and the surrounding landscape could be modelled using the location of existing artefacts and anomalies pronounced by multispectral, hyperspectral, thermal and LiDAR imagery. Similarly, comparing Figures 3.11c, 3.11d, 3.11g and 3.11h with an airborne thermal change detection study (Casana et al., 2017; Casana and Ferwerda, 2024) or a LiDAR micro-relief assessment (Kokalj and Hesse, 2017) could visually enhance different sections of the clay drainage pipe and buried ditch system. Rasters of each could be resampled, normalised and combined to form a composite subsurface detection raster which depicts the drainage pipe and buried ditches more clearly. These anomalous image objects would then, by definition, represent a mathematical product of anomalous heat retention, micro-relief and solar reflection of the ground above the subsurface structure.

The time of year also appears to be crucial in these tests, where we observe distinct multispectral anomalies over the drainage pipe and buried ditches in French summer months, using a WorldView-2 image dated 21 September 2019 and a GeoEye-01 image dated 13 June 2015.

From following the multispectral image processing workflow (Figure 3.10), the importance of clipping a vegetation indexed image is apparent. After clipping, we witness clear advantages in *resetting* the pixel values across a smaller sized image subset, resulting in spectral anomalies which are far more accentuated.

When incorporating and analysing the gradient magnitude of subsurface detection indices (in this case VIs) as image subsets, we also witness considerable utility where, in this study, we appear to detect pronounced edge effects around zones of stressed soil and vegetation (Figures 3.6 and 3.7). To date, the gradient magnitude of a VI has never been considered, but this study successfully demonstrates the merits of analysing the rate of change in vegetation and soil property for any given VI. However, interpreting multispectral imagery after using gradient magnitude detection techniques will become much more complicated if detecting irregular shaped subsurface anomalies - as opposed to the linear, anthropogenic features used here. Moreover, when detecting irregular shaped structures, we expect the false positive rate to rise. However, in this study, and broadly aligning with the characteristics of buried anthropogenic structures, the pursuit and detection of *linear* subsurface anomalies will reduce the risk of false positives.

Target depth is also worth due consideration. Here, it is difficult to ascertain a clear depth constraint, especially when we solely manipulate multispectral vegetation indices to detect buried

anthropogenic structures. However, we expect detection depth to be a function of both target type *and* target size. Therefore, a larger subsurface feature is expected to increase the 'extent of influence' on overlying soil which, in turn, is emulated by the 'scale of impact' on overlying vegetation.

Finally, pansharpening must continue to be treated with caution. By increasing the spatial resolution of an image subset, pansharpening has benefits, especially when dealing with small areas of interest. However, some radiometric information can be lost during the process, so it is essential to select a pansharpening technique that best preserves the spectral integrity of an image (e.g., NNDiffuse Resolution Merge). Moreover, if the site of interest is greater than 50 m x 50 m, we would recommend bypassing this stage of our workflow, particularly if the subsurface anomaly under investigation is thought to be linear, and especially if the multispectral image is already VHR.

## 3.6 Concluding remarks

This study revisits the use and manipulation of vegetation indices (VIs) in their detection of shallow subsurface features in temperate, vegetated terrain. Using geophysical observations as a proof of concept, high performing broadband VIs from Maxar high-resolution multispectral satellite imagery are statistically reprioritised, numerically validated and then assigned with respective gradient magnitudes. The best performing VIs successfully detect stressed soil and deprived meadow grass over an Iron Age fogou in Carn Euny Ancient Village, Cornwall, UK, and more broadly, they reveal a clay drainage pipe and a buried ditch system beneath cool-season grass in Normandy, France.

When remotely searching for buried linear structures less than c.2 m in width, high-resolution or VHR multispectral imagery is crucial. At pixel level, this permits the use of statistical and graphical spectral analyses as a function of *distance* and *area* above a subsurface anomaly. High spatial resolution can also offer a subsurface detection regime the option of exploring 'the rate of change' in VI (Gmag assessment), a technique we highly recommend for depicting linear edge effects along zones of deprived soil and stressed vegetation from a buried geologic or anthropogenic structure.

By using geophysics and correlation statistics to select the best performing VIs, sensor type and image date, we reprioritise the indices that are most responsive to buried features in temperate, vegetated landscapes. In 1D, we compare VI spectral profiles to changes in gravity along a specified *distance* and then in 2D, we compare their spectral response to GPR data across a specified *area*.

Consequently, the three most sensitive VIs are the Iron Oxide index, Soil Salinity Index 7 (SI7) and the Structure Insensitive Pigment Index (SIPI), each responding exceptionally well to changes in the physiological and biophysical condition of overlying brown earth soil and smooth stalked meadow grass in warm, summer months. By analysing the behaviour of these VIs as spectral

profiles, false colour composites (FCCs) and edge detection image subsets, we identify high levels of soil salinity, greater concentrations of iron (III) oxide and a reduction in chlorophyll production above the fogou. These observations, according to VI definitions, are expected to demonstrate the fogou's notable effect on drainage rates, temperature profile and chemical weathering in the summer months of a temperate environment.

However, from a numerical perspective, we simply see greater levels of NIR absorption and a higher Red/Blue reflectance ratio above subsurface features (like the fogou) in warm, summer months (Figure 3.8). When we consider these raw spectral observations with a VI's dependency on the instrument(s) used in their creation (Xue and Su, 2017), the conditions in which the VI was derived (Giovos et al., 2021; Solymosi et al., 2019) and the physical factors that affect a VI's reliability (Bannari et al., 1995; Jackson et al., 1983), we propose that buried structures more generally influence *numerous* soil properties, in which the behaviour of overlying vegetation becomes a proxy. Therefore, during the warm, summer months in a temperate environment, anomalous reflectance behaviour in NIR and in particular, Red/Blue, showcase the greatest detection potential.

False positives are of course a risk, but these are generally mitigated in the detection of *linear* features like buried anthropogenic structures. Moreover, we expect the false positive rate to diminish when integrating remotely sensed observations from different sensor types, especially when different characteristics from subsurface anomalies are pursued (Figure 3.1).

To reinforce the observations from our controlled study, the algebraic forms of the Iron Oxide index, SI7 and the SIPI are woven into a subsurface detection workflow which exploits the sensitivities of the Red/Blue reflectance ratio and NIR reflectance from cool-season vegetation. Here, we use gradient magnitude, pansharpening and clipping routines to optimise the Iron Oxide index, SI7 and SIPI vegetation indices for shallow subsurface detection in temperate, vegetated landscapes. We test the subsurface detection workflow using two temperate, cool-season grass covered sites in Normandy, France, where the workflow is seen to generate FCCs and edge detection image subsets that reveal the location of other subsurface features like an underground drainage pipe and two buried ditches.

To further strengthen the resilience of these concepts and techniques, we recommend similar geophysical methods and numerical ground truthing procedures for spectral index selection in similar *and* different environments, especially arid landscapes and forested terrain. Similar methods could also be employed with airborne hyperspectral data and narrowband VIs, where a subsurface detection workflow is engineered using a blend of optimised VIs from geophysical survey and deep learning algorithms. The use of convolutional neural networks (CNNs) to detect and extract subsurface objects from imagery could also be explored, along with 'object and landscape' relationship modelling using graph neural networks (GNNs).

To conclude, this study reprioritises the most suitable multispectral VIs for shallow, subsurface detection by correlating their response with ground-based geophysical observations. The subsurface detection efficiency of the Red/Blue reflectance ratio is, from our research, considerably effective in vegetated terrain, especially when using Maxar imaging sensors in the warm summer months of a temperate environment. The detection efficiency of this reflectance ratio is already proven in mapping iron oxides, identifying soil salinity levels and assessing chlorophyll *a* and carotenoid ratios, but its utility in subsurface detection has been, until now, masked by high profile VIs (e.g., Normalised Difference Vegetation Index (NDVI), Green NDVI, Soil Adjusted Vegetation Index (SAVI)). Putting aside VI definitions and their prescribed application, we strongly encourage the use of our image processing workflow and in particular, algebraic manifestations of Red/Blue in any future temperate, vegetated subsurface detection study. Only then will imagery analysis be *correctly calibrated* for broad scale subsurface detection and deep learning.

# 4

# Remote sensing of the subsurface between a Cistercian abbey and a medieval grange

In preparation for publication as: *Morley, A.M., Allen, R., Mather, T.A., Pyle, D.M. and Kendall, J.M., 2026. Remote sensing of the subsurface between a Cistercian abbey and a medieval grange.* Manuscript in preparation for submission to *Journal of Archaeological Science: Reports*

## Abstract

Cistercian abbeys are associated with complex, subterranean networks of pipes, drains and tunnels. While much of this infrastructure would have been for the transport of water, and removal of waste, tunnels could have been used for other purposes – including concealment, evasion or escape. In this paper, we explore the use of remote sensing to detect linear and geometric subsurface features between the abbey of Aunay and La Garenne, a Cistercian abbey and a medieval grange in Normandy, France. By analysing, with statistical thresholds, anomalous multispectral reflectance behaviour from vegetation along a shared abbey-grange boundary wall, we reveal the location of a previously unknown, underground passage from La Garenne. We then combine our two-dimensional subsurface anomalies from high-resolution, vegetation indexed satellite imagery with elevation anomalies in a very-high-resolution (VHR) hillshaded digital surface model (DSM). In doing so, we reveal several high-resolution reflection and micro-relief anomalies in the abbey's largest field enclosure. When we compare these regular shaped anomalies with an eighteenth-century garden plan, we see several distinct similarities. We deem these remote sensing observations to be the surface expressions of several near-surface, structural features from a large, formal, baroque garden, reinstated by the Cistercians during their seventeenth-century restoration of the abbey.

## 4.1 Introduction

According to Urwin (1936), Cistercian monasteries were a point of origin for subterranean passages. Eyewitness reports, local beliefs and tradition suggest there are underground passages from Fountains Abbey, Dieulacres Abbey, Whalley Abbey, Kirkstead Abbey and Netley Abbey, all Cistercian abbeys in the UK (Errand, 1974; Urwin, 1936). Similar observations have also been documented by Ross (1991), who discusses subterranean passages from the Cistercian abbeys of Stoneleigh in Warwickshire, Buckland Abbey in Devon and Beaulieu in Hampshire, UK.

In most cases, these passageways were used for water provision, drainage and sewage (Kinder, 2002). Direct access to fresh water was essential, as was the need for a strong current to remove waste, control flooding and power Cistercian industry (Burton and Kerr, 2011). The end result was usually an elaborate system of stone-lined channels and underground passages, typically originating from the abbey's kitchen, the abbey's dormitories and the infirmary (Tobin, 1995).

However, recent reports of Cistercian tunnels found away from water sources suggest that some may have been used for other purposes. In 2021, a medieval tunnel was found near Tintern Abbey in Wales, UK (Figure 4.1a). Extending away from the Cistercian monastery, the rubble stone tunnel (Figure 4.1b) was a considerable distance from the River Wye, the abbey's principal water source (Robinson, 2006; Wright, 2021). Similarly, Burns (2023) reports evidence for several Cistercian tunnels beneath Faringdon, a historic market town in Oxfordshire, UK. It is believed that one of these tunnels connects All Saints' Church, a Cistercian church from the Middle Ages, with Gloucester House, a nearby Cistercian priory.

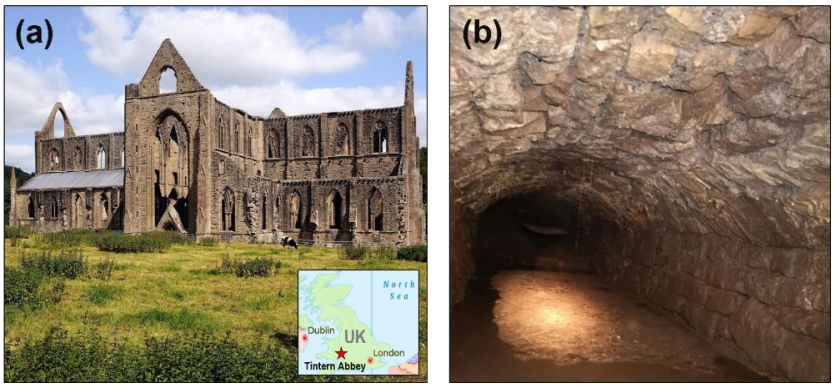



**Figure 4.1**. Tintern Abbey's gothic church in Wales, UK, and a nearby tunnel discovered in 2021 (Wright, 2021). a). A present-day view from the south of Tintern Abbey's gothic church in Monmouthshire, Wales, with inset map showing location in UK. b). An interior view of the rubble stone tunnel accidentally found by engineers several hundred metres from Tintern Abbey in March 2021 (Wright, 2021). The tunnel is approximately 1.2 m high, dated as medieval and believed to extend to the monastery.

In Dorset, UK, a Cistercian escape tunnel is thought to exist between Forde Abbey and Hay Farm, a cluster of nearby buildings once thought to be a medieval grange. This tunnel was reportedly used by priests and monks to escape the abbey and hide in the neighbouring

farmhouse during times of persecution (Clayton, 2015). Underground passages could have also been used for: the storage of religious artefacts, coinage and other valuables (e.g., Errand, 1974; Ross, 1991; Stray, 2012); isolating the sick (Burns, 2023); and imprisonment (e.g., Burton and Kerr, 2011; Le Hardy, 1897).

In France, similar Cistercian underground passages have also been reported (Jamroziak, 2013). In this study, we use high-resolution multispectral satellite imagery and airborne light detection and ranging (LiDAR) to inspect the subsurface between the Cistercian abbey of Aunay and a nearby medieval grange in Normandy, France. In the twelfth and thirteenth century, Aunay Abbey was a major establishment with royal affiliations (e.g., Le Hête, 2009; Vincent, 2021).

To remotely sense the subsurface, we use three vegetation indices (VIs), recently shown by Morley et al. (2025b; Chapter 3) to be effective 'subsurface detection indices', on six high-resolution multispectral satellite images of Aunay Abbey and a nearby grange called La Garenne[3]. We use these indices to inspect for soil matrix irregularities from tunnels and drains under the abbey-grange boundary wall and beneath the abbey's largest field enclosure. We then look for anomalous reflectance behaviour in a series of graphical and statistical analyses of reflectance values from cool-season vegetation near and along the abbey-grange boundary wall. We explore any anomalous observations with a pedestrian survey of the boundary wall, checking for evidence of tunnelling between the abbey of Aunay and La Garenne.

We also inspect the largest field enclosure in Aunay Abbey with the same high-resolution multispectral satellite imagery. Here, we searched the abbey field for heterogeneities in soil condition and vegetation health using the same three subsurface detection indices (from Morley et al., 2025b; Chapter 3) and their gradient magnitude equivalents. Once applied, we inspect for subsurface anomalies using false colour composites (FCCs) and edge detection filters. We then check for micro-relief signatures over subsurface anomalies in the same abbey field using a series of traditional hillshade analyses of a 50 cm LiDAR derived digital surface model (DSM) (e.g., Abate et al., 2023; Kokalj and Hesse, 2017; Luo et al., 2019). All geometrically shaped reflectance and topography anomalies in the abbey field are then annotated and combined, assisting our interpretation of the subsurface between the abbey and the grange.

By conducting this analysis from an aerial perspective, we reveal near-surface spatial characteristics and geometrical relationships beneath the abbey field, which are unrecognisable from within the abbey and the grange. We also overcome the need for invasive technology and direct ground access to the abbey. To close, we consider the function and purpose of any significant near-surface observations, in the hope of learning more about Cistercian abbeys, their infrastructure, and their subsurface relationship with neighbouring sites.

[3] La Garenne is French for 'The Warren'.

## 4.2 Aunay Abbey

Jordan de Say founded the abbey of Notre-Dame d'Aunay with his wife, Lucy d'Aunay, on 15 July 1131 (Power, 2013). As part of the monastic Congregation of Savigny, the abbey was dedicated to the Virgin Mary and established as the ninth daughter house of Savigny Abbey in Manche, Normandy (Le Hardy, 1897). The monastery stood on the northern slope of Mont des Lenques in Normandy, approximately 1 km west of Aunay-sur-Odon. Once established, it began to receive considerable donations from several benefactors including French nobleman, Richard du Hommet (Dugdale, 1846). From his marriage to Agnes de Beaumont (daughter of Jordan de Say), Richard du Hommet then became the Lord of Aunay, inheriting great influence and power over the abbey of Notre-Dame d'Aunay.

During the Anarchy[4], Richard du Hommet relocated the abbey of Notre-Dame d'Aunay to the banks of the River Odon, moving a thousand paces from the original site and remaining west of Aunay-sur-Odon (Le Hardy, 1897). In 1147, the monastic Congregation of Savigny was formally affiliated with Cîteaux, merging the congregation with the Cistercians (Allen, 2021). Subsequently, the abbey of Notre-Dame d'Aunay became part of the Clairvaux lineage and was renamed the abbey of Aunay (Dugdale, 1846). Significant donations were made to the abbey, including those from Richard, Lord of Creully, who was the son of Robert of Caen, an illegitimate grandchild of King Henry I (Le Hête, 2009).

After the administrative merger with the Cistercians, Aunay Abbey raised much support, increasing in popularity across Normandy (Le Hardy, 1897). The Lord of Aunay, Richard du Hommet, had also increased in status, winning the favour of Duke Henry of Normandy during the siege of Stamford in 1153. Soon after King Henry II's coronation in 1154, Richard du Hommet was officially appointed Constable of Normandy, High Sheriff of Rutland and more extensively, Constable of the Lord King[5] (Power, 2013). The abbey looked impressive, influencing familiares of King Henry II like Bertran III de Verdun to commission similar looking Cistercian foundations in England (Dace, 1999). In 1176, Croxden Abbey near Alton, Staffordshire, was founded by Bertram III de Verdun, officially becoming Aunay's daughter house (Hall, 2007).

During the closing years of King Henry II's reign, special protection was granted to Aunay Abbey in the form of a royal safeguard, declaring the royal protection of Aunay's abbot, Aunay's monks and all of their holdings and possessions therein (Le Hardy, 1897; Vincent, 2021). Then in another royal mandate, King Henry II granted the monks of Aunay a complete quittance from toll, passage and

[4] The Anarchy was a civil war in England and Normandy, and primarily a war of succession, between King Henry I's daughter, Matilda, and her cousin, Stephen of Blois. It began in 1138 and finished in 1153, culminating in the Treaty of Wallingford (Burton and Kerr, 2011).

[5] Richard du Hommet was also the most frequent lay witness of King Henry II's *acta*, witnessing 331 royal deeds; a total surpassed only by Thomas Becket, who witnessed 421 attestations. Furthermore, from 1164 - 1174, King Henry II awarded Richard du Hommet's steadfast loyalty with several gifts including Stamford, Princes Risborough, Whaddon, Nether Winchendon, Sheringham (all towns in England) and Auppegard, a French commune in Normandy (Power, 2013).

pontage, and in equal measure, all custom in the King's fairs, markets and any part of his kingdom (Vincent, 2021).

By 1211, Aunay Abbey was rich, owing to the work and generosity of the de Say family, the du Hommet family, the Semilly family, the Lords of Creully and many more (Le Hardy, 1897; Le Hête, 2009). The Lords of Sant-Clair, which issue from the latter, also celebrated the abbey, continuing this support and significant donations of land through the 1200s (Le Hête, 2009). It was benefactors like these who, after much life investment, would finish their time in Aunay Abbey as a Cistercian and then after passing, celebrated with a distinguished burial under the abbey church or the cemetery[6] (Power, 2013). The Hundred Years' War then followed (1337 – 1453) and soon after, the French Wars of Religion (1562 – 1598). These were difficult times for Aunay Abbey, sustaining several pillages and significant damage (Le Hardy, 1897).

It was not until 29 July 1600 that the monastic reputation of Aunay Abbey was re-established. On this day, Denis Largentier, the abbot of Clairvaux *and* the attorney general of the Cistercian Order, made his first visit to the abbey of Aunay (Le Hardy, 1897). He proceeded to restore Cistercian rules and the reformation of the Strict Observance, where the Cistercian monks of Aunay would, once again, strictly adhere to The Rule of Saint Benedict (Roux-Perino et al., 2014). Despite their small numbers, the monks rebuilt the abbey buildings, the cloister, sections of the abbey church and the garden enclosures, thereby protecting and celebrating the abbey's final years as a Cistercian monastery. In 1791, the last monks were asked to leave the monastery and the abbey was privately sold (Le Hardy, 1897). Soon after, parts of the monastery became a large spinning mill and then from 1890 to 1976, the abbey became a cheese diary. Present day now sees the abbey site used for private car repairs and farming.

The site once occupied by Aunay Abbey is bound by the River Odon to the south; a metalled road in the north (*seen by the remains of the north transept of the abbey church*); a 100 m long wall and a farmer's field in the west; a 140 m long wall with a nearby grange to the east (Figure 4.2). Monasteries with boundary walls were common in the twelfth, thirteenth and fourteenth centuries; often built to control access, demarcate the extent of the monks' territory and protect the Order from sieges and pillages (Burton and Kerr, 2011).

North-east of Aunay Abbey is La Garenne, a privately-owned site that is walled to the north, east and west, and bound by the River Odon in the south (Figure 4.2). Dating back to the infancy of Aunay Abbey, La Garenne was always by its side, occupied and overseen by brother Cistercians who farmed the land and managed livestock (Le Hardy, 1897). The farm of La Garenne was therefore considered a Cistercian grange of Aunay Abbey, containing "meadow land of modest consequence", used only by fellow Cistercians for arable farming and produce (Le Hardy, 1897;

[6] Richard du Hommet retired as constable in 1178 to become a Cistercian monk in the abbey of Aunay. In 1180, and at c.70 years of age, he died; he was then buried under the abbey church of Aunay (Le Hardy, 1897).

Stout, 2015). Once their time in La Garenne had passed, these Cistercians were usually buried in the abbey cemetery (Le Hardy, 1897).

The sites of Aunay Abbey and La Garenne come with significant differences in land size (Figure 4.2). Outlined in yellow, the site of Aunay Abbey is approximately six hectares whereas the site of La Garenne (outlined in purple) is approximately twenty hectares. Between them, they share a 4 m high stone wall boundary (located within the white dashed box in Figure 4.2), which we term the abbey-grange boundary. The northern section of the abbey-grange boundary is approximately 60 m long and the eastern section of the abbey-grange boundary is approximately 140 m long.

Given our intent to explore the subsurface for tunnels and drains between Aunay Abbey and La Garenne, the abbey-grange boundary in Figure 4.2 becomes our first study area, and the abbey field situated between Aunay Abbey and La Garenne becomes our second. Outlined in red, the abbey field is bound to the north and east by the 4 m high stone wall and the River Odon to the south (Figure 4.2). The abbey field is approximately 190 m east-to-west, 120 m north-to-south, flat and predominantly covered by cool-season grass. The grass type is a blend of meadow grass, couch grass and fescue, and the soil type is primarily a free-draining brown earth soil containing sand, silt and clay.

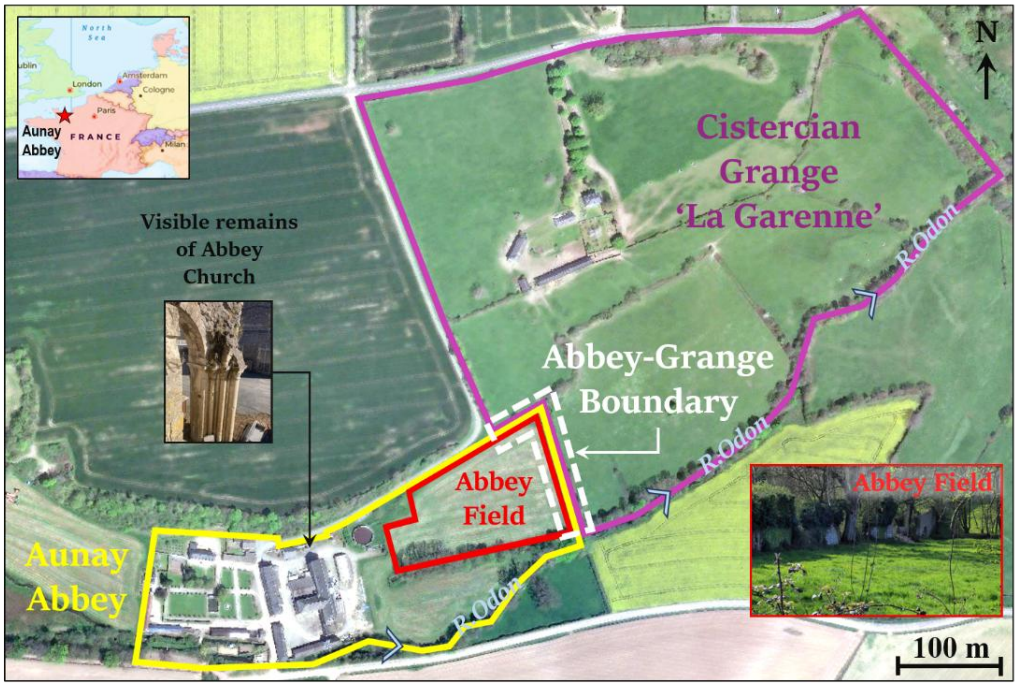



**Figure 4.2**. The location of Aunay Abbey, a Cistercian abbey from the High Middle Ages, and La Garenne, a medieval site once occupied by a Cistercian grange. Yellow line outlines the site perimeter of Aunay Abbey; purple line outlines the site perimeter of La Garenne; red line outlines the perimeter of the abbey field; white dashed line outlines the region of the shared abbey-grange boundary wall. The River Odon and flow direction are annotated in blue. From left to right, inset images show: location map of Aunay Abbey in Normandy, France; visible remains of Aunay's abbey church; east section of the abbey field and the east boundary wall.

## 4.3 Methodology

Our methodology has three stages. The first is image acquisition, where high-resolution multispectral satellite imagery is acquired from Maxar and a 50 cm LiDAR derived DSM is acquired from the Institut National de l'Information Géographique et Forestière (IGN)[7]. The second stage is to inspect the abbey-grange boundary using multispectral imagery. The third stage introduces the techniques used to inspect the abbey field, using both multispectral imagery and airborne LiDAR.

Underpinning our multispectral analysis in stages two and three is our application of three subsurface detection indices. These are specific vegetation indices (VIs) which Morley et al. (2025b; Chapter 3) statistically recognise to be the most sensitive to variations in vegetation stress from cool-season vegetation above shallow, subsurface features. These subsurface detection indices are the Iron Oxide index (Red/Blue), Soil Salinity Index 7 ([Red x Green] / Blue) and the Structure Insensitive Pigment Index ([NIR - Blue] / [NIR – Red]), where NIR is near-infrared. All three indices are algebraic manifestations of the Red/Blue reflectance ratio and by definition, they are able to generate new images of a scene which show variations in iron oxide concentration, (e.g., Al-Quraishi et al., 2022; Ducart et al., 2016; Mendes et al., 2022; Segal, 1982), soil salinity (e.g., Abbas and Khan, 2007; Allbed and Kumar, 2013; Metternicht and Zinck, 1997) and chlorophyll production (e.g., Kureel et al., 2022; Lees et al., 2020; Penuelas et al., 1995; Susantoro et al., 2018). To remotely explore the subsurface between Aunay Abbey and La Garenne, we analyse their reflectance profiles along the abbey-grange boundary wall and then we inspect the abbey field using their gradient magnitudes, their combined response in FCCs and their edge effects over subsurface anomalies.

### 4.3.1 Data acquisition

High-resolution multispectral satellite imagery was acquired from Maxar's Analysis Ready Data (ARD) Dashboard, with acquisition dates, sensor type, spatial resolutions and supporting meteorological information at Appendix H. In parallel, a 50-cm-resolution LiDAR derived DSM of Aunay Abbey and its environs was sourced from the IGN in France. Each data acquisition process is described respectively in subsections 4.3.1.1 and 4.3.1.2.

#### 4.3.1.1 Multispectral imagery

We acquired all Maxar high-resolution satellite image files using the Maxar ARD Dashboard (Maxar, 2022a). The dashboard user interface allowed the user to manually select or upload a geographical area of interest (AOI) in order to retrieve a visual catalogue of imagery tiles that suffice a predefined

[7] Translated, the Institut National de l'Information Géographique et Forestière (IGN) is the National Institute of Geographic and Forest Information. Located in Paris, it is France's national agency for creating and maintaining geographic information. This includes the production and dissemination of mapping, geospatial data and web services. Data is available and free to download via https://geoservices.ign.fr.

selection criterion. Selection parameters include the age of the imagery, cloud cover percentage and tolerances for off-nadir angle and sun elevation.

Maxar ARD are time-series stacks of imagery which have been atmospherically corrected, orthorectified and aligned pixel-by-pixel. This pixel-by-pixel alignment across all imagery tiles of the AOI is achieved by requesting a bundle block adjustment (BBA), Maxar's proprietary technique for aligning pixels within a stack of images where off-nadir angles are 30 degrees or less (Maxar, 2022a). The ARD service was available for Maxar's GeoEye-1, WorldView-1, WorldView-2, WorldView-3 and WorldView-4 satellite archives. Upon completion, the service delivers three cloud-optimized GeoTIFFs for each image tile selected: a 4 or 8-band multispectral image, a panchromatic image and a pansharpened Red-Green-Blue (RGB) image (Maxar, 2022b).

For this study, six Maxar ARD image bundles of Aunay Abbey were selected, covering an observation period from February to September in an arbitrary calendar year. Within the image bundles, all images were bundle block adjusted, more than three years old, have less than 40% cloud cover, off-nadir angles no greater than 30 degrees and a minimum sun elevation of 5 degrees. The location of the abbey field and the abbey-grange boundary were confirmed in all images and the resulting image bundles were delivered to a secure Amazon S3 cloud storage platform with supporting metadata (Appendix H).

#### 4.3.1.2 Light detection and ranging (LiDAR) digital surface model (DSM)

A LiDAR derived DSM of Aunay Abbey and the surrounding fields was sourced from the IGN in France. The DSM tile is 1487E2~1.tif; located and downloaded from the DSMs in Department 14 (Calvados) of IGN's 50 cm DSM data repository. This airborne LiDAR data was collected and processed by IGN in 2023, using the spatial reference RGF 1993 Lambert-93[8] and a 0.5 m x 0.5 m cell size.

### 4.3.2 Inspecting the Abbey-Grange Boundary

Where geology allows, tunnels prefer direct, straight line distances (Butler, 2008). Therefore, a subterranean passage connecting the site of Aunay Abbey to La Garenne is most likely to exist near the northeastern corner of the abbey field. Subsequently, our subsurface inspection of the shared boundary wall becomes a right-angled isolation of the abbey field in its northeastern corner (Figure 4.3). To do this, we position a series of equal length spatial profiles in the abbey field by the northeastern corner, ensuring they are close to the boundary wall and overlap by 90 degrees at the corner. Built as polylines in ESRI ArcGIS Pro GIS software, each spatial profile is 52 m long, parallel to successive spatial profiles and separated by an interval of 1.3 m. In total, four spatial

[8] RGF (Référentiel Géodésique Français) 1993 Lambert-93 is a regional projected coordinate system that uses a Lambert Conformal Conic projection. It is frequently used in aerial and engineering surveys across France, and commonly employed in LiDAR topographic mapping (Jaud et al., 2014).

profiles were positioned in parallel along the east wall and five spatial profiles were positioned in parallel along the north wall. For ease of reference, profile start and end markers E-E' and N-N' were used and arranged from a viewpoint of La Garenne (Figure 4.3). The number and length of spatial profiles along each wall section were dictated by the position of significant overhanging vegetation from the boundary wall and vegetation shadow. Using the MERGE geoprocessing tool in the ArcGIS Pro Data Management toolbox, all east and north wall spatial profiles (52 m long polylines) were subsequently grouped into two new output datasets named 'East_Wall_Profiles' and 'North_Wall_Profiles'.

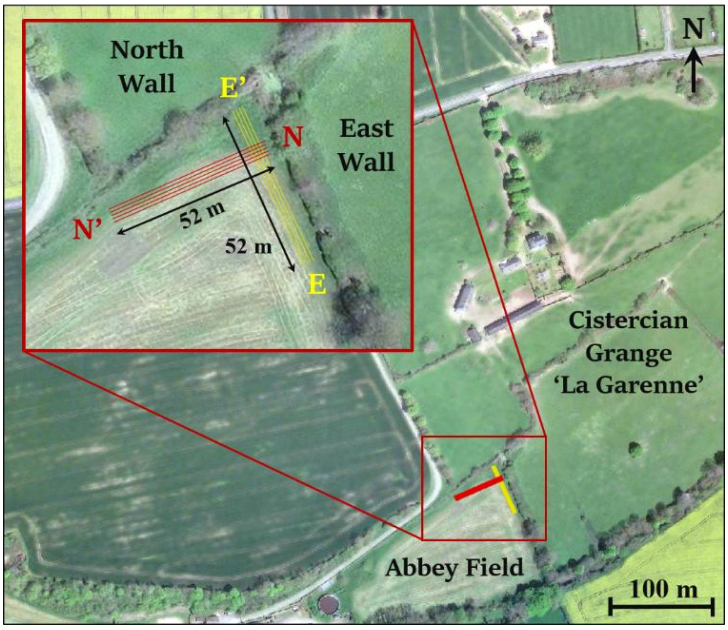



**Figure 4.3**. Location of spatial profiles along the shared abbey-grange boundary wall, positioned in the northeastern corner of the abbey field. Yellow lines denote the position and orientation of individual spatial profiles along the east wall; red lines denote the position and orientation of individual spatial profiles along the north wall. All spatial profiles are 52 m long, 1.3 m apart and parallel to adjacent profiles. All spatial profiles are orientated from a viewpoint in La Garenne, with profile start and end markers along the east and north wall labelled E-E' and N-N' respectively.

In parallel, the EXTRACT BANDS raster function was used in ArcGIS Pro to extract every single multispectral band (image layer) from each of the six high-resolution multispectral images catalogued in Appendix H. The STACK PROFILE geoprocessing tool in ArcGIS Pro was then used simultaneously on all extracted multispectral bands (*44 image layers in total*) using the 'East_Wall_Profiles' polyline dataset and then the 'North_Wall_Profiles' dataset. As a result, the tool generates east and north wall standalone tables in ArcGIS Pro, each containing the spectral band reflectance values as a function of distance along E-E' and N-N' for each multispectral image. These two tables were then exported as comma-separated value (CSV) text files and read by a bespoke MATLAB script. This script created individual CSV files with average spectral band reflectance profiles along E-E' and N-N' for each multispectral band in the multispectral images at Appendix H.

For each multispectral image, average Iron Oxide (IO), Soil Salinity Index 7 (SI7) and Structure Insensitive Pigment Index (SIPI) reflectance profiles were derived along E-E' and N-N', using the average spectral band reflectance values from the spatial profile information in the MATLAB generated CSVs. Of note, these three VIs were algebraically most responsive to buried anthropogenic features in Morley et al. (2025b; Chapter 3), who resultantly term them 'subsurface detection indices' after their successful correlation with gravity and ground penetrating radar (GPR) data above near-surface tunnels.

Given the success of these subsurface detection indices in Morley et al. (2025b; Chapter 3), the Iron Oxide index, SI7 and SIPI reflection profiles along E-E' and N-N' were subsequently inspected for anomalous reflection values. To do this, John Tukey's Interquartile Range (IQR) method was used to identify statistically significant outliers (Tukey, 1970), where IQR is the difference between the third quartile (Q3: 75th percentile of the data) and the first quartile (Q1: 25th percentile of the data). In Tukey's limited preliminary edition of Exploratory Data Analysis (1970), the IQR method defines "outside" observations as data points that fall below the first quartile (Q1) or above the third quartile (Q3) by *one* IQR. Similarly, "detached" observations are data points that fall below Q1 or above Q3 by *1.5 times* the IQR (Tukey, 1970). These clear definitions and statistical thresholds are also easily represented graphically, facilitating the identification of outliers along a profile and in return, demonstrate the effectiveness of Tukey's IQR thresholds.

Subsequently, these thresholds were applied to each average Iron Oxide index, SI7 and SIPI reflection profile along E-E' and N-N', acknowledging there are six index profiles for each VI along the two wall sections - one for each multispectral image. Any anomalous reflectance values will then show as "outside" or "detached" observations (*pending their VI value*) and if so, their distance along the relevant wall profile is recorded. For each wall section, "outside" and "detached" observations from each VI profile are combined in a stacked column chart to examine the quantity and distribution of "outside" and "detached" VI outliers along E-E' and N-N'. Significantly high quantities of VI outliers (anomalous reflectance values) at any given distance along the east and north wall profiles are then examined with a pedestrian survey, where specific sections of the abbey field's perimeter wall are closely inspected for tunnels and drains - *from within La Garenne.*

### 4.3.3 Inspecting the Abbey Field

First, we inspect the abbey field using multispectral imagery and our subsurface detection indices: Iron Oxide, SI7 and SIPI. Once applied, we look for subsurface anomalies using FCCs and edge detection filters (Section 4.3.3.1). Second, we inspect for micro-relief signatures using a procedural hillshade analysis of our 50 cm DSM (Section 4.3.3.2). All geometrically shaped reflectance and topography anomalies are annotated using a series of coloured polylines (vector data) in ArcGIS Pro and then combined over a single, pansharpened RGB image of the abbey field for interpretation and discussion.

#### 4.3.3.1 With multispectral imagery

We use an adapted version of the multispectral image processing workflow for shallow subsurface detection from Morley et al. (2025b; Chapter 3). However, our workflow seen in Figure 4.4 bypasses the requirement to pansharpen the subsurface detection indices, because the abbey field is sufficiently large enough to omit the need for enriched spatial resolution. This way, the spectral fidelity of the subsurface detection indices are preserved, guaranteeing higher levels of accuracy in FCC and edge detection analyses (Morley et al., 2025b; Chapter 3). Workflow input comprises all six high-resolution multispectral images at Appendix H and all images were analysed in ArcGIS Pro and MATLAB.

First, subsurface detection indices Iron Oxide, SI7 and SIPI were generated from each multispectral image. Next, their gradient magnitude equivalents were produced using MATLAB function GRADIENTWEIGHT. By calculating a magnitude of the rate of change in these subsurface detection indices (in the '*x*' *and* '*y*' direction), strong edge effects can appear around large subsurface features (Morley et al., 2025b; Chapter 3). Therefore, both high and low pixel value "edge effects" represent significant changes in vegetation health from soil matrix irregularities over subsurface features (Gao et al., 2024; Susantoro et al., 2018). As seen in Figure 4.4, the subsurface detection indices and their gradient magnitude equivalents were clipped to the extent of the abbey field. Once complete, they are stacked to form a six-layer image stack which, according to Morley et al. (2025b; Chapter 3), is correctly configured for subsurface detection in a temperate landscape (Figure 4.4).

Two different forms of multispectral analysis are exercised on the six-layer image stack of the abbey field. The first is a FCC analysis (Figure 4.4), where each three-band combination from the six-layer image stack is systematically inspected in RGB, producing 20 different band combinations for subsurface inspection (neglecting band order). The second is an edge detection analysis (Figure 4.4), where each of the six image layers in the image stack are filtered with a 5 x 5 low-pass smoothing filter and then operated on separately using a 'Sobel horizontal' and a 'Sobel vertical' edge detection filter (Gao et al., 2010; Vinesta and Milton-Joe, 2019). The two edge-filtered image layers are then stacked to produce a two-layer multiband raster image, where band 1 is the indexed image layer of the abbey field after applying a 'Sobel horizontal' edge detection filter and band 2 is the abbey field after applying a 'Sobel vertical' edge detection filter. Finally, this two-layer multiband raster image is visually inspected in RGB using band combination 1-2-2 and 1-1-2 and, if required, converted to a single layer greyscale equivalent for ease of interpretation.

During these FCC and edge detection analyses, any prospective subsurface anomalies with straight lines and regular geometric shapes are visually identified and recorded. Using a Black-Grey-White (BGW) tagging system, a three-tier subsurface anomaly detection rating is awarded to each FCC and edge detection layer. Here, black indicates the presence of distinct reflection anomalies from vegetation overlying underground features, grey signifies a vague representation

of subsurface discrepancy and white implies nothing found. Subsurface anomalies identified in black-rated FCCs and edge detection layers were annotated with coloured georeferenced polylines. *These polylines resemble the shape of the anomaly detected and their colour relates to the date of the multispectral image used in their detection*. Upon completion, all polylines representing the prospective location of a subsurface anomaly were combined and inspected over a pansharpened RGB image of the abbey field. Any repeated lines from FCCs and edge detection raster images of the same multispectral image were removed prior to combining the vector annotations, thereby mitigating the risk of clutter and reducing the risk of misinterpretation.

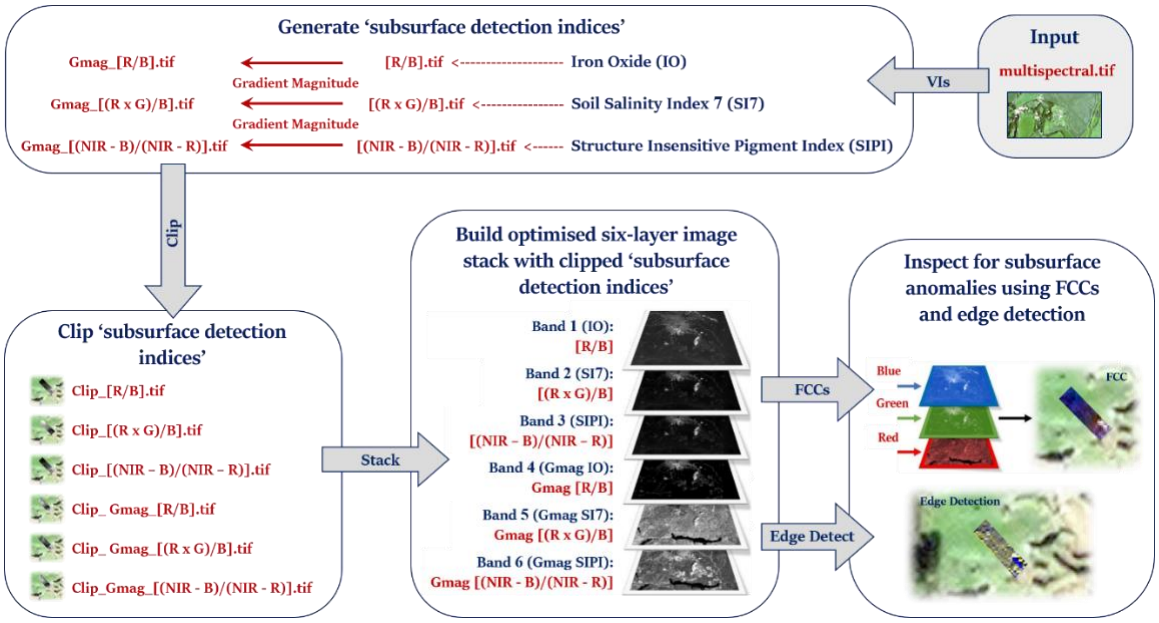



**Figure 4.4**. The image processing workflow used to inspect high-resolution multispectral satellite imagery of the abbey field. Adapted from Morley et al. (2025b; Chapter 3), this workflow is designed to detect anomalous reflectance behaviour from cool-season vegetation over shallow, subsurface features in temperate environments.

### 4.3.3.2 With airborne LiDAR

First, we clipped the 50 cm LiDAR DSM to the extent of the abbey field and then, using the traditional HILLSHADE raster function, we produced six hillshaded DSM layers with a sun altitude of 5 degrees and a sun azimuth every 60 degrees (Figure 4.5). We then used these six hillshaded DSMs to build a six-layer hillshaded DSM image stack, which we proceeded to inspect systematically in RGB as a series of three-band FCCs. This equated to 20 different band (sun azimuth) combinations, all of which were visually examined for geometrically shaped terrain anomalies. Using a BGW tagging system, a three-tier subsurface anomaly detection rating was then awarded to each hillshaded DSM FCC. As per our tagging system in Section 4.3.3.1, black indicated the presence of clear, geometrically shaped terrain anomalies, grey signified some evidence for micro-relief anomalies and white implied nothing found. This process was conducted for sun altitudes of 5 to 45 degrees, and repeated in 5-degree increments (Figure 4.5).

Three high performing hillshaded DSM layers were selected from those awarded a black subsurface anomaly detection rating and then converted to greyscale images with equal weighting. Finally, they were re-stacked to form a new optimised three-layer hillshaded DSM image stack and reinspected in RGB (Figure 4.5). Any clear and distinct micro-relief anomalies representing prospective subsurface irregularities were annotated with a georeferenced polyline and combined with the anomalous observations from our multispectral inspection.

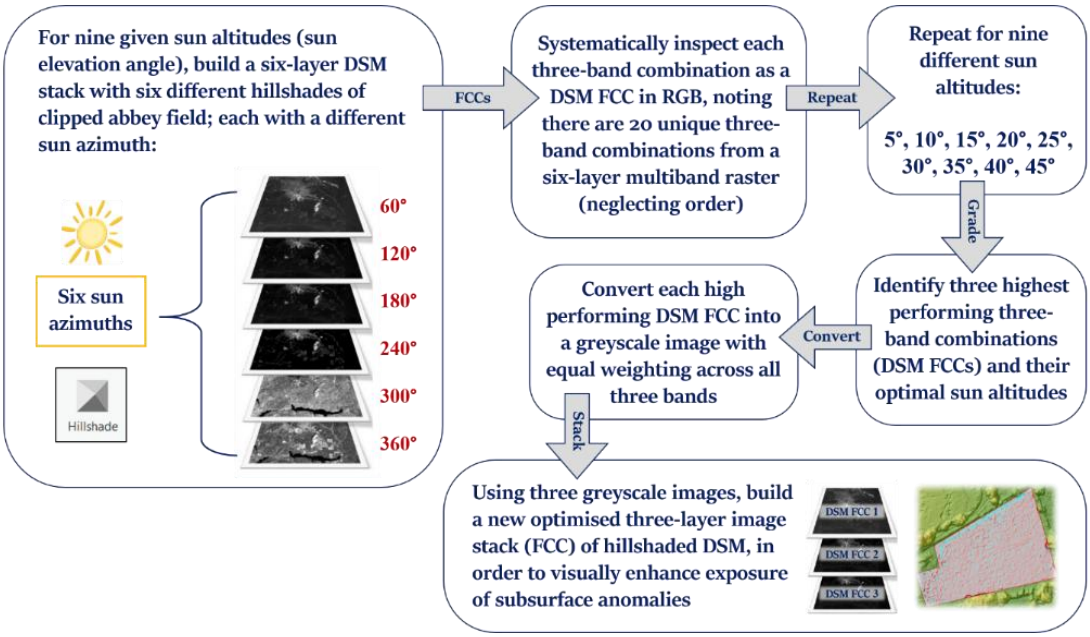



**Figure 4.5**. The multi-directional and multi-altitude hillshade sequence used to analyse a very-high-resolution (VHR) light detection and ranging (LiDAR) digital surface model (DSM) of the abbey field. The LiDAR elevation data was collected and processed by the Institut National de l'Information Géographique et Forestière (IGN). This workflow is designed to detect linear and regular shaped micro-relief anomalies over shallow, subsurface anomalies in flat and moderate terrain.

## 4.4 Results

Section 4.4.1 presents subsurface detection index profiles along the abbey-grange boundary, revealing the location of a near-surface anomaly under the shared boundary wall. Section 4.4.2 uses multispectral FCCs, multispectral edge detection and LiDAR hillshade analyses to reveal a series of linear and regular shaped reflection and micro-relief anomalies, exposing the location of several subsurface irregularities beneath the abbey field.

### 4.4.1 Abbey-Grange Boundary

For clear graphical representation, we use Tukey's IQR method (1970) to identify statistical outliers in our average subsurface detection index profiles along the east and north wall of the abbey field. These come in two types: "outside" observations and "detached" observations. Initially, we review the sensitivities of each subsurface detection index along E-E' and N-N', and then we discuss any temporal effects on the number of outliers along the wall profiles. We then combine these outside

and detached index values in a stacked column chart along E-E' and N-N'. Any specific distances along the two wall sections where the number of observed index outliers is notably high, are then checked for tunnels or drains with a pedestrian survey in La Garenne.

#### 4.4.1.1 East Wall

Using Tukey's IQR method (1970), the Iron Oxide subsurface detection index successfully identified 25% of the statistically anomalous reflectance values along the east wall of the abbey-grange boundary (Table 4.1 and Figure 4.6a). As defined by Tukey (1970), these are all outside observations. The SI7 and SIPI then proceed to identify the remaining anomalous reflectance values in equal measure (37.5%; Table 4.1), although 67% of those detected by SI7 are outside observations and 67% of those detected by SIPI are detached observations (Table 4.1 and Figures 4.6b and 4.6c). Compared to the Iron Oxide index and SI7, the SIPI appears well-configured to detect the *extremely* anomalous reflectance values from the cool-season vegetation in the abbey field, generating 67% of the detached reflectance values. We suspect this is explained by the incredibly sensitive nature of NIR and the high standard deviations routinely observed along NIR reflectance profiles, especially when they include reflections from stressed vegetation and poor soil (e.g., Cerra et al., 2018; Huete et al., 2014). In total, from the combined response of Iron Oxide, SI7 and SIPI, 62.5% of anomalous reflectance values along E-E' are outside observations and 37.5% are detached observations (Table 4.1 and Figures 4.6a, 4.6b and 4.6c).

**Table 4.1**
Percentage of reflection outliers from average subsurface detection index profiles along the east wall (E-E') of the shared abbey-grange boundary. Profiles were generated for each multispectral image in this study, and outside and detached observations were identified using Tukey's Interquartile Range (IQR) method (Tukey, 1970). Total reflection outlier percentages are as shown.

| Subsurface Detection Index | Percentage of all reflection outliers (%) | | TOTAL |
|---|---|---|---|
| | Outside Observation | Detached Observation | |
| Iron Oxide | 25.0 % | 0.0 % | 25.0 % |
| SI7 | 25.0 % | 12.5 % | 37.5 % |
| SIPI | 12.5 % | 25.0 % | 37.5 % |
| **TOTAL** | 62.5 % | 37.5 % | 100.0 % |

With regards to seasonal relationships in anomalous reflectance behaviour, Figures 4.6a, 4.6b and 4.6c show little trend. The images dated 23 March 2011 and 21 September 2019 reveal the greatest number of combined index outliers (37.5% each), suggesting these dates have the highest anomalous reflectance activity along the east wall. For the multispectral image dated 21 September 2019, this is less surprising because the weather was incredibly warm and dry during the time of image acquisition (Table H1, Appendix H). However, the same cannot be said for the multispectral image dated 23 March 2011, when ambient temperatures are much lower. Moreover, no anomalous reflectance outliers are seen along E-E' in the image dated 6 May 2016 (*taken during warm and dry conditions* - Table H1) yet the Iron Oxide and SIPI each detect a high outside reflectance value at 48 m along E-E' on 17 Feb 2020. At this time, ambient temperatures were

approx. 11°C and c.13 mm of rainfall had accumulated in three days (Table H1). According to Morley et al. (2025b; Chapter 3), these are not the typical weather conditions associated with high iron oxide and SIPI values above subsurface features. Instead, they suggest that excessive rainfall could be an alternative trigger for high levels of iron oxide and vegetation stress above a subsurface anomaly.

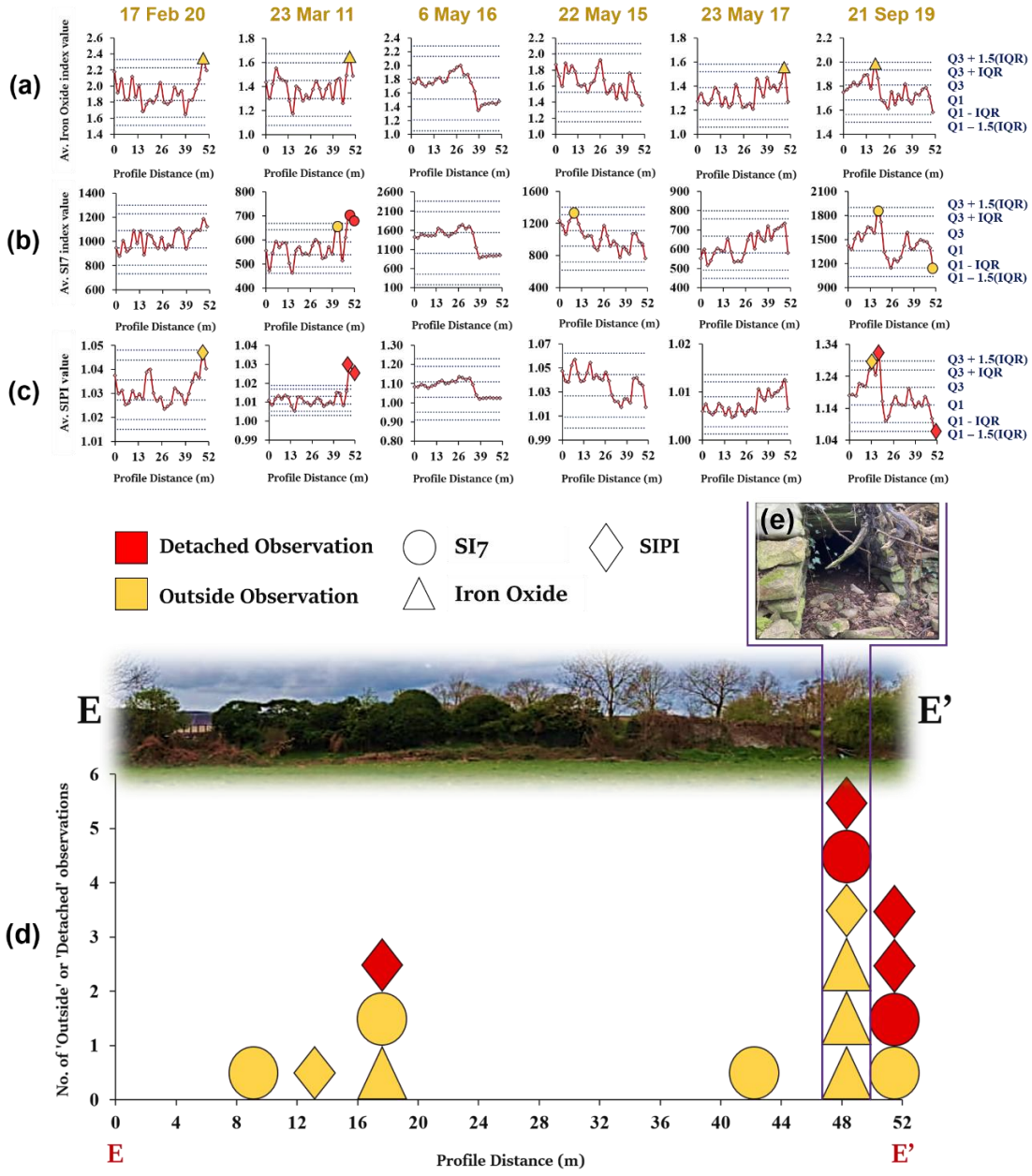



**Figure 4.6**. Average subsurface detection index profiles along the east wall (E-E' in Figure 4.3) for each multispectral image used in this study, and a stacked column chart revealing reflection outliers as a function of distance along E-E'. "Outside" reflectance values are yellow and "detached" reflectance values are red - classified using Tukey's Interquartile Range (IQR) method (Tukey, 1970). Blue dotted lines across all spatial profiles in Figures 4.6a, 4.6b and 4.6c are Tukey's IQR thresholds, unique to each subsurface detection index profile. a). Average Iron Oxide index reflectance profiles along E-E' with anomalous reflectance values shown as triangles. b). Average SI7 reflectance profiles along E-E' with anomalous reflectance values shown as circles. c). Average SIPI reflectance profiles along E-E' with anomalous reflectance values shown as diamonds. d). Anomalous reflection values from each subsurface detection index profile in 6a, 6b and 6c stacked in a column chart to examine the quantity of "outside" and "detached" reflection outliers along E-E'. Inset image shows east wall section from La Garenne. e). The tunnel entrance discovered 48 m along E-E', with picture taken at time of discovery. The tunnel entrance is approximately 0.8 m high, 0.6 m wide and 1.4 m below the abbey field.

All 16 outside and detached reflection outliers identified in Figures 4.6a, 4.6b and 4.6c were combined in a stacked column chart (Figure 4.6d), thereby permitting an assessment of the quantity and distribution of outside and detached index outliers along profile E-E' as a function of distance (Figure 4.6d). Of interest, and as seen in Figure 4.6d, 37.5% of the reflection outliers appear at 48 m along E-E'. These are all *high* outside or detached reflectance values from the multispectral images dated 17 February 2020, 23 March 2011 and 23 May 2017. At these times, our results indicate significantly high levels of iron oxide, soil salinity and vegetation stress from the cool-season grass in the abbey field at 48 m along E-E'. Given this convincing quantity of observations, a pedestrian survey was undertaken at 48 m along the wall section. From within La Garenne, much vegetation was cleared to allow sufficient space to inspect the abbey field's east perimeter wall. As a result, a tunnel entrance was identified at the foot of the east wall, 48 m along E-E' (Figure 4.6e). At the time of discovery, the tunnel entrance was approximately 0.8 m high, 0.6 m wide and 1.4 m below the abbey field. We assess the tunnel was filled with approximately 1 m of silt, although the tunnel's rubble stone lining and interior were dry and structurally intact. The tunnel axis follows a straight line under the east wall and the abbey field along a bearing of 235°.

#### 4.4.1.2 North Wall

Much like our inspection of the east wall, the Iron Oxide index identified 26.5% of the anomalous reflectance values along N-N' of the abbey-grange boundary (Table 4.2 and Figure 4.7a). The SI7 and SIPI also identified similar proportions of anomalous reflectance to those seen along E-E', detecting 35.3% and 38.2% of all reflection outliers along the north wall (Table 4.2 and Figures 4.7b and 4.7c). Most of these are outside observations, although akin to the east wall, SIPI was seen to detect 50% of the detached observations, all within the first 20 m of N-N' (Figure 4.7d). In total, from the combined response of Iron Oxide, SI7 and SIPI, 82.4% of anomalous reflectance values along the north wall are outside observations and 17.6% are detached observations (Table 4.2 and Figures 4.7a, 4.7b and 4.7c).

**Table 4.2**
Percentage of reflection outliers from average subsurface detection index profiles along the north wall (N-N') of the shared abbey-grange boundary. Profiles were generated for each multispectral image in this study and outside and detached observations were identified using Tukey's Interquartile Range (IQR) method (Tukey, 1970). Total reflection outlier percentages are as shown.

| Subsurface Detection Index | Percentage of all reflection outliers (%) | | TOTAL |
|---|---|---|---|
| | Outside Observation | Detached Observation | |
| Iron Oxide | 20.6 % | 5.9 % | 26.5 % |
| SI7 | 32.4 % | 2.9 % | 35.3 % |
| SIPI | 29.4 % | 8.8 % | 38.2 % |
| **TOTAL** | 82.4 % | 17.6 % | 100.0 % |

Temporally, the images dated 22 May 2015 and 23 May 2017 reveal the greatest number of combined index outliers (26.5% and 35.3% respectively), aligning with the temporal deductions

made by Morley et al. (2025b; Chapter 3). Similar to our observations along the east wall, the multispectral image dated 6 May 2016 also remains reasonably stable, revealing one outside observation with the Iron Oxide index at 6 m and one at 27 m. However, the multispectral images dated 23 March 2011 and 21 September 2019 are also reasonably stable; an observation which is very much in contrast to our results along the east wall.

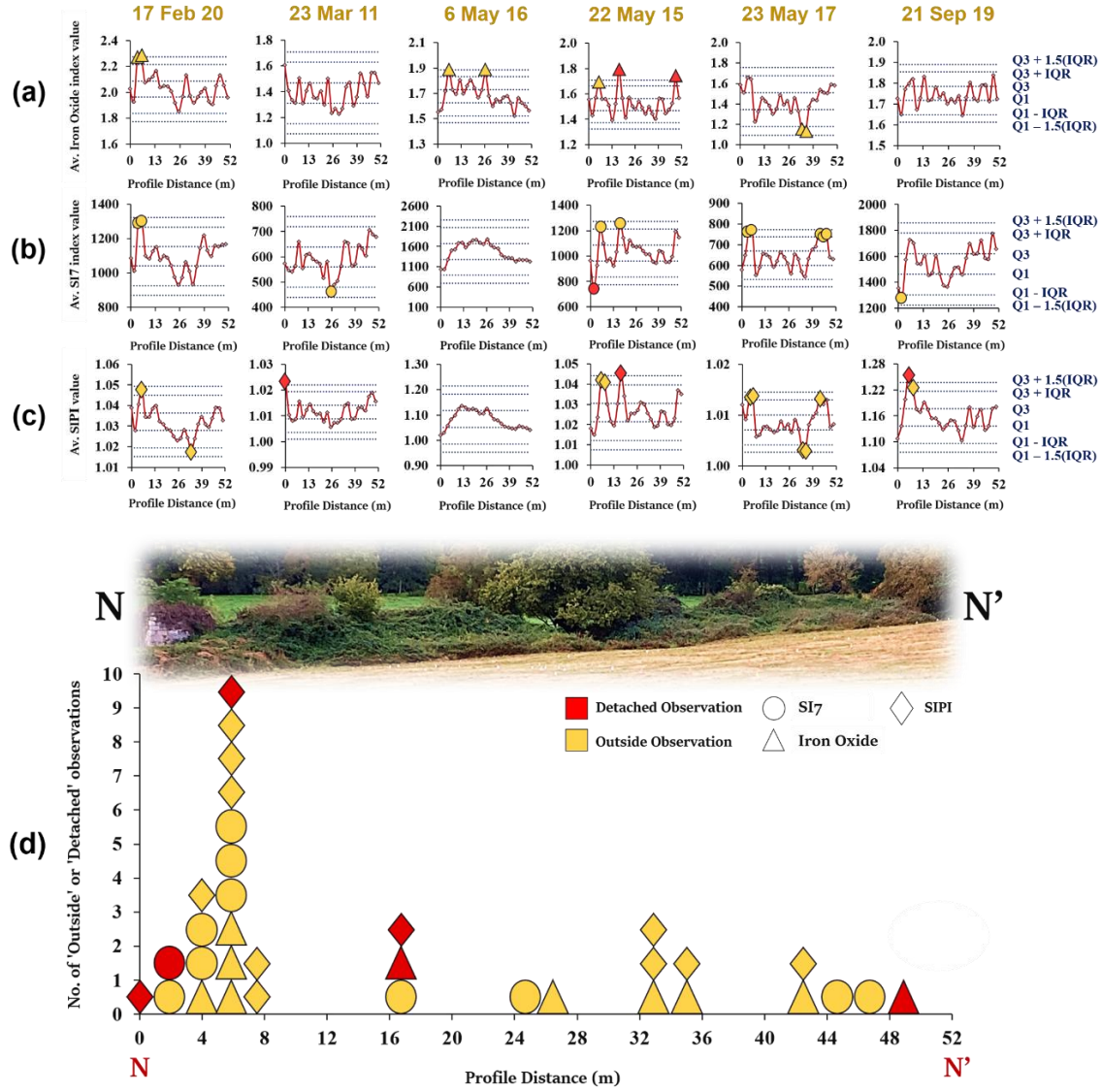



**Figure 4.7**. Average subsurface detection index profiles along the north wall (N-N' in Figure 4.3) for each multispectral image used in this study, and a stacked column chart revealing reflection outliers as a function of distance along N-N'. "Outside" reflectance values are yellow and "detached" reflectance values are red - classified using Tukey's Interquartile Range (IQR) method (Tukey, 1970). Blue dotted lines across all spatial profiles in Figures 4.7a, 4.7b and 4.7c are Tukey's IQR thresholds, unique to each subsurface detection index profile. a). Average Iron Oxide index reflectance profiles along N-N' with anomalous reflectance values shown as triangles. b). Average SI7 reflectance profiles along N-N' with anomalous reflectance values shown as circles. c). Average SIPI reflectance profiles along N-N' with anomalous reflectance values shown as diamonds. d). Anomalous reflection values from each subsurface detection index profile in 7a, 7b and 7c stacked in a column chart to examine the quantity of "outside" and "detached" reflection outliers along N-N'. Inset image shows north wall section from La Garenne.

All 34 reflection outliers revealed in Figures 4.7a, 4.7b and 4.7c were combined to form a stacked column chart (Figure 4.7d), thereby producing a visual assessment of the quantity and distribution

of outside and detached index outliers as a function of distance along N-N' (Figure 4.7d). This time, 29.4% of the reflection outliers appear at 6 m along N-N'. As per the reflection outliers at 48 m along the east wall, these reflection outliers are all *high* outside or detached reflectance values, which we observe in all multispectral images less the image dated 23 March 2011. This would again suggest the presence of significantly high levels of iron oxide, soil salinity and vegetation stress from the cool-season grass in the abbey field at 6 m along N-N' (less 23 March 2011).

Given the credible number of observations at 6 m along the north wall section, a pedestrian survey was undertaken. From within the grange, all vegetation was cleared to reveal a continuous wall with no obvious disturbance. No evidence of tunnelling, blocked entrances, ground subsidence or ground channelling were seen. However, these observations may signify the presence of a deeper tunnel, perhaps originating from the buildings of La Garenne in the north. Alternatively, these reoccurring reflection anomalies may signify the presence of a different subsurface feature unique to the abbey field, or a change in direction of the tunnel already identified under the east wall (Section 4.4.1.1).

### 4.4.2 Abbey Field

In sections 4.4.2.1 and 4.4.2.2, the observed results from all FCCs, edge detection rasters and image dates are tabulated, and we discuss the BGW detection ratings as a function of index performance and time of year. We then show examples of our subsurface anomaly annotations as a series of figures, acknowledging we only identify and annotate subsurface anomalies in an image with a black detection rating. Understanding why some FCCs and edge detection operations underperform is also important. We address this in the same two subsections and we provide examples of BGW FCCs and BGW edge detection raster images at Appendix J.

In Section 4.4.2.3, we reveal the BGW assessment of our LiDAR hillshaded DSM FCCs. These were generated with our controlled, multi-directional and multi-altitude hillshade workflow (Figure 4.5). Here, we discuss the detection efficiency of micro-relief anomalies above prospective subsurface features, both as a function of sun altitude and sun azimuth. We then introduce our optimised three-layer image stack of hillshaded DSMs, which we proceed to view and analyse in RGB as an optimised DSM FCC of the abbey field.

#### 4.4.2.1 Using multispectral False Colour Composites (FCCs)

The most distinct subsurface anomalies are seen in the WV2 multispectral image dated 21 September 2019 (Table 4.3 and Figure 4.8). As seen in Table 4.3, clear geometrical shaped anomalies appear in 85% of the FCCs generated by our six-layer image stack of the subsurface detection indices from this date. Performing less well were the FCCs from the six-layer image stacks dated 17 February 2020, 6 May 2016 and 23 May 2017, where only 10% - 20% of FCCs were seen to reveal distinct reflection anomalies from vegetation overlying prospective subsurface

anomalies (Table 4.3). Furthermore, multispectral images dated 23 March 2011 and 22 May 2015 were seen to underperform almost completely, producing a significant number of FCCs with little or no anomalous reflection behaviour from linear or geometrical entities below ground.

**Table 4.3**
Black, Grey and White (BGW) subsurface anomaly detection rating of six clipped multispectral images of the abbey field. For each multispectral image, the BGW detection rating is applied to 20 false colour composite (FCC) band combinations, taken from the six-layer image stack in Figure 4.4. Percentage of BGW images per FCC and percentage of BGW FCCs per multispectral image are shown, with BGW definitions found in table footnotes.

| FCC Band Combination (Bands) | BGW subsurface anomaly detection rating using multispectral image dated: | | | | | | For given FCC, percentage of images showing: | | |
|---|---|---|---|---|---|---|---|---|---|
| | 17 Feb 20 | 23 Mar 11 | 6 May 16 | 22 May 15 | 23 May 17 | 21 Sep 19 | Black[1] | Grey[2] | White[3] |
| 1-2-3 | | | | | | | 16.7 % | 50.0 % | 33.3 % |
| 1-2-4 | | | | | | | 16.7 % | 50.0 % | 33.3 % |
| 1-2-5 | | | | | | | 66.7 % | 33.3 % | 0.0 % |
| 1-2-6 | | | | | | | 33.3 % | 50.0 % | 16.7 % |
| 1-3-4 | | | | | | | 16.7 % | 0.0 % | 83.3 % |
| 1-3-5 | | | | | | | 16.7 % | 16.7 % | 66.7 % |
| 1-3-6 | | | | | | | 16.7 % | 16.7 % | 66.7 % |
| 1-4-5 | | | | | | | 0.0 % | 16.7 % | 83.3 % |
| 1-4-6 | | | | | | | 16.7 % | 16.7 % | 66.7 % |
| 1-5-6 | | | | | | | 16.7 % | 16.7 % | 66.7 % |
| 2-3-4 | | | | | | | 16.7 % | 16.7 % | 66.7 % |
| 2-3-5 | | | | | | | 66.7 % | 33.3 % | 0.0 % |
| 2-3-6 | | | | | | | 16.7 % | 50.0 % | 33.3 % |
| 2-4-5 | | | | | | | 0.0 % | 33.3 % | 66.7 % |
| 2-4-6 | | | | | | | 16.7 % | 16.7 % | 66.7 % |
| 2-5-6 | | | | | | | 33.3 % | 50.0 % | 16.7 % |
| 3-4-5 | | | | | | | 16.7 % | 16.7 % | 66.7 % |
| 3-4-6 | | | | | | | 16.7 % | 16.7 % | 66.7 % |
| 3-5-6 | | | | | | | 16.7 % | 33.3 % | 50 % |
| 4-5-6 | | | | | | | 16.7 % | 16.7 % | 66.7 % |
| **For given image date, percentage of FCCs showing:** **Black[1]** | 15.0 % | 0.0 % | 20.0 % | 0.0 % | 10.0 % | 85.0 % | | | |
| **Grey[2]** | 60.0 % | 30.0 % | 30.0 % | 15.0 % | 15.0 % | 15.0 % | | | |
| **White[3]** | 25.0 % | 70.0 % | 50.0 % | 85.0 % | 75.0 % | 0.0 % | | | |

[1] Black = Distinct anomaly(ies); [2] Grey = Vague representation; [3] White = Nothing seen

Given the maximum daily temperatures recorded in Caen during image acquisition (Table H1), the FCCs with a black subsurface detection rating in Table 4.3 broadly imply a higher likelihood of detecting subsurface anomalies (from anomalous vegetation reflections) when daily temperatures are above 20°C (Table H1). In particular, the FCCs of the subsurface detection indices from 21 September 2019 performed considerably well. At this time, ambient temperatures were close to c.30°C (Table H1) and ground conditions were exceptionally dry from prolonged drought, caused by the 2019 European heat wave (Sousa et al., 2020). However, 15% of FCCs from the subsurface detection indices dated 17 February 2020 *also* revealed clear linear reflection anomalies from cool-season vegetation in the abbey field (Table 4.3). At this time, the maximum daily temperature in nearby Caen was 11°C and 13 mm of rainfall had accumulated in three days. Therefore, these

observations may represent anomalous drainage patterns from subsurface anomalies under the abbey field, causing the reflectance behaviour of overlying vegetation to behave differently on-and-off the anomaly after significant rainfall (Lv et al., 2020; Waters et al., 2019).

We also observe two high performing FCC combinations. In 66.7% of the images, FCC 1-2-5 (Iron Oxide - SI7 - Gmag SI7) and FCC 2-3-5 (SI7 – SIPI - Gmag SI7) reveal very distinct reflectance anomalies, receiving 4/6 black subsurface anomaly detection ratings in Table 4.3. Bands SI7 and Gmag SI7 are shared in both FCCs, indicating this soil salinity index and its gradient magnitude are the most weather resilient when operating in tandem. Interestingly, when used in combination with another gradient magnitude index, this FCC performs less well, but when inspecting these two indices in concert with the Iron Oxide index or SIPI, the detection of any shallow, subsurface feature under cool-season vegetation seems likely. This also aligns with the results in Morley et al. (2025b; Chapter 3), who similarly show the subsurface detection efficiency of FCCs with SI7 and Gmag SI7. In equal and opposite measure, we notice that FCCs with band 1 (Iron Oxide) and band 4 (Gmag Iron Oxide) perform poorly, with the latter adding very little detection value in any of its FCCs (Table 4.3).

Some of the higher performing FCCs of the abbey field (with a black detection rating) can be found in Figure 4.8, with subsurface anomalies annotated as coloured lines. This allows comparisons to be made between each set of subsurface anomalies, thereby identifying those bespoke to particular images and those which reoccur and overlap from multiple image dates. As a result, overlapping reflection anomalies from different image dates increases the assurance and likelihood of a subsurface anomaly being present. Figures 4.8a, 4.8c, 4.8e, 4.8g and 4.8i show FCCs from multispectral images dated 17 February 2020, 6 May 2016, 23 May 2017 and 21 September 2019. Figures 4.8b, 4.8d, 4.8f, 4.8h and 4.8j are then their equivalent, with subsurface anomaly annotations overlaid as coloured lines. The colour of each polyline is representative of the date of image used to generate the line annotation. As seen in Table 4.3, several other black-rated FCCs were identified, but they offer no additional information to those FCCs in Figure 4.8. Those not shown feature the same subsurface anomalies as those in Figure 4.8, but with less pronounced colour schemes[9].

From inspecting the FCCs in Figure 4.8, it is clear that different image dates and different sensor types reveal different geometric anomalies in the FCCs of the abbey field (e.g., straight lines, regular shapes, closed loops, varying orientations and differing sizes etc). We suspect this is due to: 1) the type of subsurface feature under detection; 2) changes in vegetation and soil type; 3) variable drainage regimes across the abbey field. Of note, FCCs from the 21 September 2019 image are incredibly clear, showing several well-defined, linear reflections from overlying vegetation as bright yellow subsurface anomalies (Figures 4.8i and 4.8j). This particular FCC is 2-3-6 (SI7 – SIPI –

[9] An example Black-Grey-White (BGW) image catalogue from this study is at Appendix J.

Gmag SIPI), signifying (in yellow) the high levels of soil salinity and vegetation stress over underground facets.

Interestingly, some of the FCCs from the GeoEye-01 multispectral image dated 23 May 2017 reveal diagonal subsurface features across the abbey field; features which cannot be seen in any other multispectral image in this study (Figures 4.8f and 4.8h). Noting all other imagery is from a WorldView-2 sensor, this could be explained by different sensor capabilities in the GeoEye-01 multispectral sensor. Albeit subtle, and as seen in Table 4.3, FCCs 1-2-5 and 2-3-5 most clearly reveal these diagonal anomalies, with the former shown in Figure J1a (Appendix J) as an example FCC with a black subsurface anomaly detection rating. To accentuate these diagonal reflection anomalies, we present FCC 5-2-2 in Figure 4.8e and SI7 as a single band (FCC 2-2-2) in Figure 4.8g. In Figure 4.8g, the linear anomalies (including the diagonals) are white, denoting linear sections of high SI7 (high soil salinity) in the abbey field (e.g., Abbas and Khan, 2007; Allbed and Kumar, 2013).

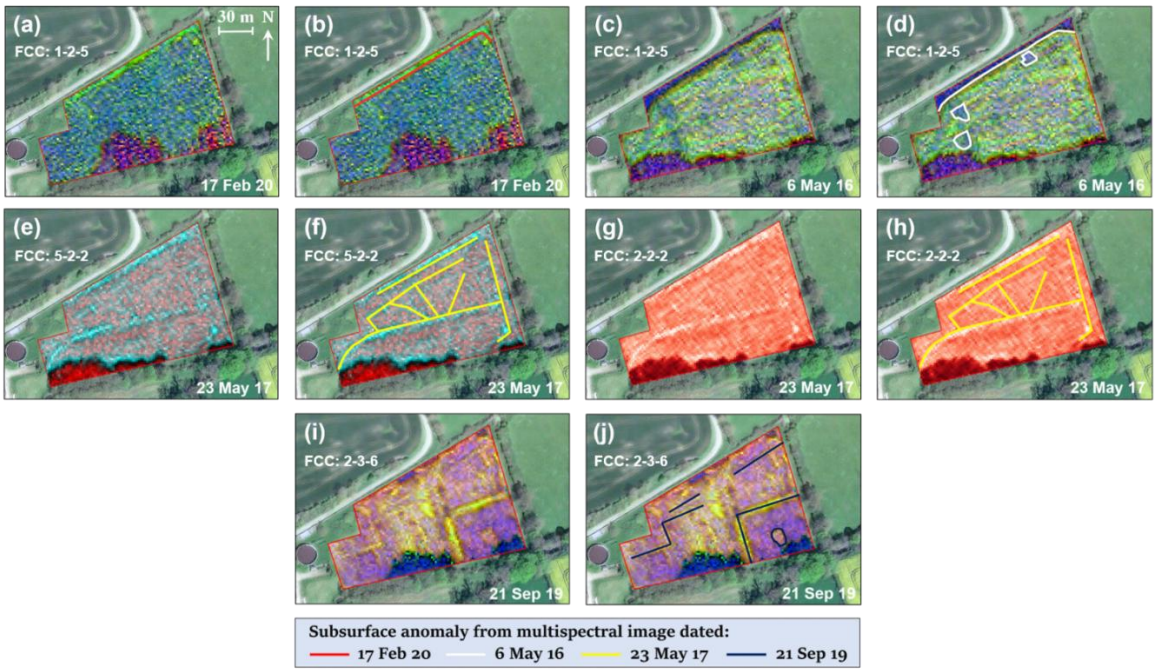



**Figure 4.8**. Coloured lines represent subsurface anomalies detected in the abbey field using false colour composites (FCCs) from the six-layer image stack in Figure 4.4. FCC band combinations are in a Red-Green-Blue (RGB) colour channel configuration and image dates are as shown. Figures 4.8a, 4.8c, 4.8e, 4.8g and 4.8i are example FCCs with black subsurface detection ratings from Table 4.3. Figures 4.8b, 4.8d, 4.8f and 4.8h are their respective equivalents, showing subsurface anomalies as coloured lines. Line colour corresponds to date of image used in their detection. a) & b). FCC 1-2-5 using multispectral image dated 17 February 2020. c) & d). FCC 1-2-5 using multispectral image dated 6 May 2016. e). & f). FCC 5-2-2 using multispectral image dated 23 May 2017. g). & h). FCC 2-2-2 using multispectral image dated 23 May 2017; after smoothing, sharpening and symbolising with a red-white colour ramp. i) & j). FCC 2-3-6 using multispectral image dated 21 September 2019.

### 4.4.2.2 Using multispectral Edge Detection

Aligning with our FCC observations in Section 4.4.2.1, the most prominent edges from prospective subsurface irregularities can be seen in the WV2 multispectral image dated 21 September 2019. Here, our subsurface detection indices and Sobel edge detection filters reveal clear, regular shaped anomalies from 50% of the indices, thereby scoring a black detection rating in Table 4.4. We also observe vague edge anomalies in the remaining indices, consequently receiving a grey subsurface detection rating. As seen in Figures 4.9g, 4.9h, 4.9i and 4.9j, the edges are clear, showcasing SIPI's ability to emphasise the boundaries of stressed vegetation over subsurface features. As discussed in Section 4.4.2.1 and as shown in FCC 2-3-6 (Figures 4.8i and 4.8j), the SIPI is extremely effective at accentuating stressed ground over subsurface features, especially when ground conditions are considerably dry and daily temperatures are significantly high. When this multispectral image was taken, the maximum temperature recorded in nearby Caen was 29°C (Table H1) and ground conditions were exceptionally dry from regional drought; instigated by the 2019 European heat wave (Błażejczyk et al., 2022).

Conversely, our edge detection filters were much less effective on the subsurface detection indices from the WV2 image dated 17 February 2020. Here, 50% of the indices failed to show any edge anomalies (receiving a white detection rating in Table 4.4) and 33.3% were awarded grey. However, the resilience of SI7 is notable, demonstrating weather agnostic behaviour in its efficiency to detect anomalous reflection behaviour from the vegetation above a subsurface anomaly. This can also be seen in our FCC results (Table 4.3), where FCCs containing SI7 (band 2) predominantly score black or grey ratings across all six multispectral images.

**Table 4.4**
Black, Grey and White (BGW) subsurface anomaly detection rating of six clipped multispectral images of the abbey field. For each subsurface detection index from each multispectral image, Sobel edge detection filters were applied. Percentage of BGW edge detection raster images per subsurface detection index and percentage of subsurface detection indices per multispectral image are shown, with BGW definitions found in table footnotes.

| Edge Detection Raster Image (subsurface detection index) | BGW subsurface anomaly detection rating using multispectral image dated: | | | | | | For given subsurface detection index, percentage of images showing: | | |
|---|---|---|---|---|---|---|---|---|---|
| | 17 Feb 20 | 23 Mar 11 | 6 May 16 | 22 May 15 | 23 May 17 | 21 Sep 19 | Black[1] | Grey[2] | White[3] |
| Iron Oxide | | | | | | | 0.0 % | 66.7 % | 33.3 % |
| SI7 | | | | | | | 66.7 % | 33.3 % | 0.0 % |
| SIPI | | | | | | | 50.0 % | 33.3 % | 16.7 % |
| Gmag Iron Oxide | | | | | | | 0.0 % | 50.0 % | 50.0 % |
| Gmag SI7 | | | | | | | 0.0 % | 83.3 % | 16.7 % |
| Gmag SIPI | | | | | | | 66.7 % | 16.7 % | 16.7 % |
| **For given image date, percentage of subsurface detection indices showing:** **Black[1]** | 16.7 % | 33.3 % | 33.3 % | 33.3 % | 16.7 % | 50.0 % | | | |
| **Grey[2]** | 33.3 % | 33.3 % | 66.7 % | 50.0 % | 50.0 % | 50.0 % | | | |
| **White[3]** | 50.0 % | 33.3 % | 0.0 % | 16.7 % | 33.3 % | 0.0 % | | | |

[1] Black = Distinct anomaly(ies); [2] Grey = Vague representation; [3] White = Nothing seen

In this study, applying our Sobel horizontal and vertical edge detection filters on SI7 reveal clear, anomalous edges in 66.7% of the images (Table 4.4 and Figures 4.9a, 4.9b and J1d). Also, equally effective is our Gmag SIPI subsurface detection index, which reveals well-defined edges in the abbey field in 66.7% of images (Table 4.4). Across these two subsurface detection indices alone, a black edge detection rating can be found in all images (Table 4.4). Similar success was shown by Morley et al. (2025b; Chapter 3) who, in a similar temperate, vegetated environment, reveal: 1) the location of a buried clay drainage pipe in a WV2 image using Sobel edge detection filters with Gmag SIPI (band 6); 2) the position of a buried ditch system in a GeoEye-01 image using Sobel edge detection filters with SI7 (band 2).

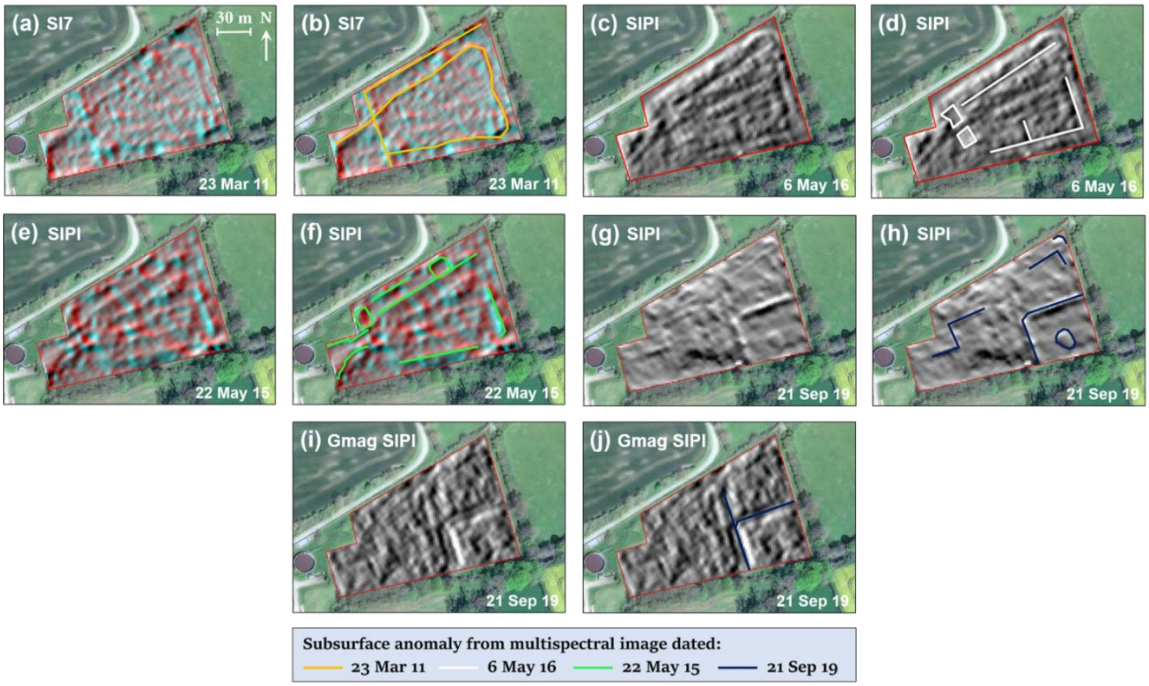



**Figure 4.9**. Coloured lines represent subsurface anomalies detected in the abbey field using Sobel edge detection filters on subsurface detection indices in the six-layer image stack in Figure 4.4. Figures 4.9a, 4.9c, 4.9e, 4.9g and 4.9i are example edge detection raster images with black subsurface detection ratings from Table 4.4. Figures 4.9b, 4.9d, 4.9f and 4.9h are their respective equivalents, showing subsurface anomalies as coloured lines. Line colour corresponds to date of image used in their detection. a) & b). Soil Salinity Index 7 (SI7) from multispectral image dated 23 March 2011, filtered with Sobel horizontal (layer 1) and Sobel vertical (layer 2) edge detection filters; stacked and observed in Red-Green-Blue (RGB) as layers 1-2-2. c) & d). Structure Insensitive Pigment Index (SIPI) from multispectral image dated 6 May 2016, filtered with Sobel horizontal and Sobel vertical edge detection filters; stacked and converted to a single greyscale image. e). & f). SIPI from multispectral image dated 22 May 2015, filtered with Sobel horizontal (layer 1) and Sobel vertical (layer 2) edge detection filters; stacked and observed in RGB as layers 1-2-2. g). & h). SIPI from multispectral image dated 21 September 2019, filtered with a Sobel horizontal edge detection filter. i) & j). Gradient magnitude (Gmag) of SIPI from multispectral image dated 21 September 2019, filtered with a Sobel vertical edge detection filter.

The edge detection efficiency of SI7 (band 2), SIPI (band 3) and Gmag SIPI (band 6) can also be seen in Figure 4.9, which display five examples of black-rated edge detection images from Table 4.4. Figure 4.9a shows the edges detected in the abbey field after layer stacking the smoothed SI7 image with a ‘Sobel horizontal’ edge detection filter (band 1) and then a ‘Sobel vertical’ edge detection filter (band 2), taken from multispectral image dated 23 March 2011. When viewed in RGB as a FCC with layers 1-2-2, Figure 4.9b reveals a series of straight and disjointed perimeter

lines around the abbey field, which we annotate as orange polylines. In Figures 4.9d, 4.9f and 4.9h, we also observe a series of closed polygons, signifying various regular and geometric shapes with closed edges. In turn, these were found by: layer stacking 'Sobel horizontal' and 'Sobel vertical' edge filtered images of SIPI from the multispectral image dated 6 May 2016 and then converting to greyscale (Figures 4.9c and 4.9d); layer stacking 'Sobel horizontal' and a 'Sobel vertical' edge filtered images of SIPI from the multispectral image dated 22 May 2015 (Figures 4.9e and 4.9f); filtering SIPI from multispectral image dated 21 September 2019 with a 'Sobel horizontal' edge detection filter (Figures 4.9g and 4.9h).

What is particularly clear from studying Figure 4.9g is the prominent right angle which we annotate in Figure 4.9h with dark blue lines, forming a square with the perimeter of the abbey field in the south-eastern corner. This anomalous feature is significant, occupying c.20% of the study area. It can also be identified when using a 'Sobel vertical' edge detection filter with Gmag SIPI from the same image (Figures 4.9i and 4.9j). Confidence ratings increase when overlapping polyline annotations of prospective underground features from different subsurface detection indices *and* different image processing techniques are observed. Even more so, overlapping annotations from different images (i.e. different coloured polylines) will significantly increase the likelihood of a subsurface anomaly being present. In Figure 4.9, such overlaps can be seen with the perimeter edge anomalies in Figures 4.9b, 4.9d and 4.9f.

Also, as seen in Table 4.3, several other black-rated edge detection rasters were identified in the study, but they offer no additional information to the edge detection raster images in Figure 4.9. Those black grade edge detection images not shown feature the same subsurface anomalies as those in Figure 4.9, but in lower contrast. An example BGW image catalogue from this study can be found at Appendix J.

#### 4.4.2.3 Using LiDAR hillshade analysis

Given the visual nature of our BGW subsurface anomaly detection rating in Table 4.5, it is evident that all black-rated DSM FCCs are when the altitude of the sun is between 20 degrees and 40 degrees. In particular, when the sun altitude is 30 and 35 degrees, 45% of all hillshaded DSM FCCs in Table 4.5 are rated black, thereby revealing distinct, geometric micro-relief patterns in the abbey field. This aligns with observations from several other LiDAR hillshade analyses (e.g., Kokalj and Hesse, 2017) where, in general terrain, the optimal sun elevation angle is 35 degrees. However, when the sun altitude is very low (less than 10 degrees) or too high (greater than 40 degrees), the hillshaded DSMs of the abbey field are too dark (e.g. Figure J9) or too light to determine changes in ground topography from subsurface features (Table 4.5).

We also notice trends in those hillshaded DSM FCCs which perform well and those which underperform. High performing DSM FCCs are those with successive or mutually supporting band

combinations (e.g. 1-2-3). For a given altitude, these FCCs contain shade information from sun azimuths that are positioned in similar broad, cardinal directions. However, those DSM FCC band combinations with sun azimuths opposing each other (e.g., 1-4-5) are seen to work against each other, rendering the DSM FCC unworkable across most *or* indeed all sun altitudes (Table 4.5). We also notice that hillshaded DSM FCCs with sun azimuths trending northwest – southeast (e.g., 4-5-6) are generally more effective at detecting micro-relief patterns than those FCCs with sun azimuths orientated northeast – southwest (e.g., 3-4-5). This suggests that the majority of linear elevation anomalies in the abbey field are trending northeast – southwest, and therefore orientated parallel to the north perimeter wall. Example BGW hillshaded DSM FCCs can be found at Appendix J.

**Table 4.5**
Black, Grey and White (BGW) subsurface anomaly detection rating of 20 hillshaded digital surface model (DSM) false colour composites (FCCs) from the six-layer DSM image stack in Figure 4.5. For each hillshaded DSM FCC, the BGW subsurface detection assessment is applied and repeated for nine different sun altitudes - as shown. Percentage of BGW elevation images (with sun altitude from 5 to 45 degrees) per DSM FCC, and percentage of BGW DSM FCCs per sun altitude are shown. Supporting BGW definitions can be found in table footnotes.

| Hillshaded DSM FCC (Bands) | BGW subsurface anomaly detection rating at sun altitude: | | | | | | | | | For given DSM FCC, percentage of sun altitudes showing: | | |
|---|---|---|---|---|---|---|---|---|---|---|---|---|
| | 5° | 10° | 15° | 20° | 25° | 30° | 35° | 40° | 45° | Black[1] | Grey[2] | White[3] |
| 1-2-3 | | | | | | | | | | 44.4 % | 55.6 % | 0.0 % |
| 1-2-4 | | | | | | | | | | 33.3 % | 66.7 % | 0.0 % |
| 1-2-5 | | | | | | | | | | 0.0 % | 66.7 % | 33.3 % |
| 1-2-6 | | | | | | | | | | 0.0 % | 66.7 % | 33.3 % |
| 1-3-4 | | | | | | | | | | 44.4 % | 55.6 % | 0.0 % |
| 1-3-5 | | | | | | | | | | 0.0 % | 88.9 % | 11.1 % |
| 1-3-6 | | | | | | | | | | 0.0 % | 66.7 % | 33.3 % |
| 1-4-5 | | | | | | | | | | 0.0 % | 0.0 % | 100.0 % |
| 1-4-6 | | | | | | | | | | 0.0 % | 33.3 % | 66.7 % |
| 1-5-6 | | | | | | | | | | 33.3 % | 55.6 % | 11.1 % |
| 2-3-4 | | | | | | | | | | 44.4 % | 55.6 % | 0.0 % |
| 2-3-5 | | | | | | | | | | 44.4 % | 55.6 % | 0.0 % |
| 2-3-6 | | | | | | | | | | 0.0 % | 100.0 % | 0.0 % |
| 2-4-5 | | | | | | | | | | 0.0 % | 0.0 % | 100.0 % |
| 2-4-6 | | | | | | | | | | 0.0 % | 0.0 % | 100.0 % |
| 2-5-6 | | | | | | | | | | 33.3 % | 44.4 % | 22.2 % |
| 3-4-5 | | | | | | | | | | 0.0 % | 44.4 % | 55.6 % |
| 3-4-6 | | | | | | | | | | 0.0 % | 44.4 % | 55.6 % |
| 3-5-6 | | | | | | | | | | 33.3 % | 44.4 % | 22.2 % |
| 4-5-6 | | | | | | | | | | 44.4 % | 55.6 % | 0.0 % |
| **For given sun altitude, percentage of DSM FCCs showing:** **Black[1]** | 0.0 % | 0.0 % | 0.0 % | 15.0 % | 30.0 % | 45.0 % | 45.0 % | 25.0 % | 0.0 % | | | |
| **Grey[2]** | 35.0 % | 50.0 % | 70.0 % | 65.0 % | 50.0 % | 40.0 % | 40.0 % | 45.0 % | 55.0 % | | | |
| **White[3]** | 65.0 % | 50.0 % | 30.0 % | 20.0 % | 20.0 % | 15.0 % | 15.0 % | 30.0 % | 45.0 % | | | |

[1] Black = Distinct anomaly(ies); [2] Grey = Vague representation; [3] White = Nothing seen

By observing and recording the most effective sun altitude and sun azimuth combinations, our optimised three-layer image stack of hillshaded DSMs becomes: band 1 = DSM FCC 2-3-4 at 25-degree sun altitude; band 2 = DSM FCC 1-2-3 at 30-degree sun altitude; band 3 = DSM FCC 4-5-

6 at 35-degree sun altitude. Each of these DSM FCCs are transformed to a single greyscale image (*with equal weighting across all three bands*), and then stacked as per Figure 4.10a, forming a series of optimised hillshaded DSM FCCs of the abbey field. The three hillshaded DSMs used in this optimised three-layer image stack subsequently contain varying sun azimuth combinations and different sun altitudes, introducing greater resilience in the final hillshaded DSM FCCs. Subsequently, we see an emphasised exposure of anomalous micro-relief variations near and above subsurface anomalies across the abbey field.

When viewing our optimised three-layer image stack as DSM FCC 3-2-1 in RGB (Figure 4.10b), several regular shaped micro-relief features can be seen, which we annotate as purple polylines (Figure 4.10c). Compared to our multispectral FCCs and our edge detection analyses (c.2 m pixel size), we initially notice the advantages of using a very-high-resolution (VHR) DSM (50 cm pixel size), where considerably more spatial detail can be seen and captured from the LiDAR micro-relief anomalies. As a result, Figure 4.10c shows parallel lines depicting corridor-type topographies, small circular features and irregular shaped polygons – all annotated as purple lines. At varying levels of definition, the same features can be seen in all six optimised DSM FCC permutations, proving the reliability of our systematic, multi-directional and multi-altitude hillshade approach. Our annotations (purple polylines) from the LiDAR elevation anomalies in Figure 4.10c were combined with our polyline annotations from the multispectral FCCs (Figure 4.8) and edge detection analyses (Figure 4.9) to shape our near-subsurface interpretation of the abbey field.

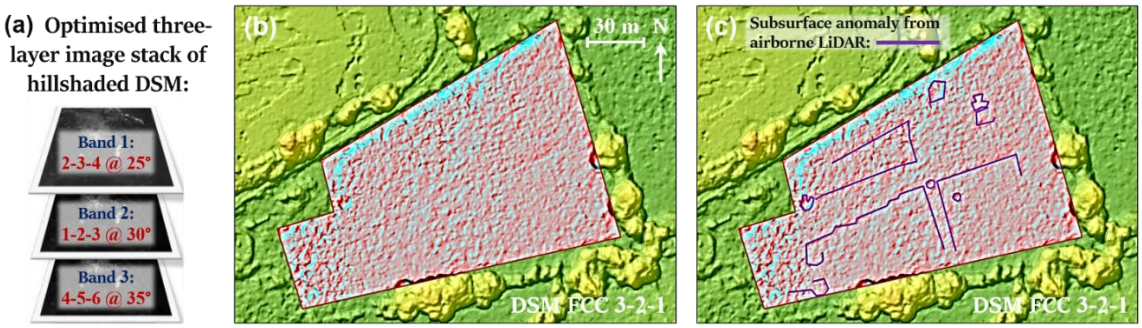



**Figure 4.10**. Light detection and ranging (LiDAR) hillshade analysis and micro-relief anomalies (purple lines) in the abbey field, and a regional hillshaded digital surface model (DSM) with a green-yellow-red colour ramp and 40% transparency. a). Optimised three-layer image stack of hillshaded DSMs. Each band is a single layer greyscale image of a DSM false colour composite (FCC) with a black subsurface detection rating in Table 4.5. b). Enhanced DSM FCC from the three-layer image stack of hillshaded DSMs in Figure 4.10a, observed in Red-Green-Blue (RGB) as bands 3-2-1 respectively. c). DSM FCC 3-2-1, showing subsurface anomalies as purple lines. All LiDAR elevation data was collected over Aunay in 2023 by the Institut National de l'Information Géographique et Forestière (IGN).

## 4.5 Interpreting the Abbey Field

To interpret the near-surface of the abbey field, we collectively study all black-rated subsurface anomalies from our results in Section 4.4, noting that polyline colour is representative of the sensor type and acquisition date used in their detection (Figure 4.11a). The tunnel entrance along the east

boundary wall (discovered in Section 4.4.1.1) is also shown in Figure 4.11a, where the tunnel axis is representative of the brown coloured arrow's orientation and direction.

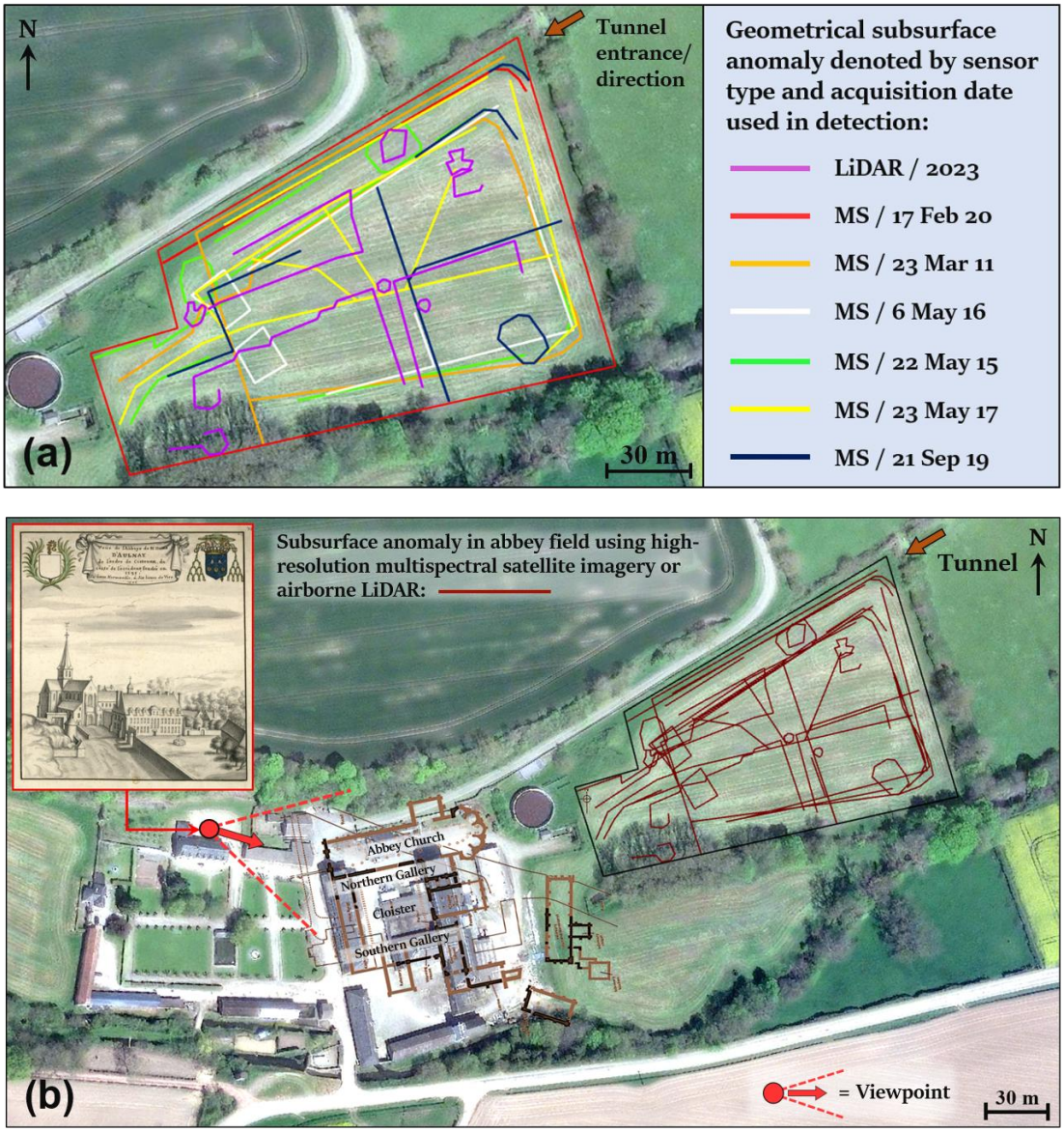



**Figure 4.11**. Subsurface anomalies identified in the abbey field of Aunay Abbey using multispectral satellite imagery and airborne light detection and ranging (LiDAR), and their position in relation to our reconstruction of Aunay Abbey. a). Coloured lines show linear and geometrical subsurface anomalies identified in the abbey field using multispectral (MS) false colour composites (FCCs), multispectral edge detection and LiDAR hillshade analysis. Line colour resembles sensor type and acquisition date used in their detection and red box outlines perimeter of abbey field. Brown arrow reveals location and direction of tunnel under east wall of abbey-grange boundary. b). The site once belonging to Aunay Abbey. Abbey buildings reconstructed using a scaled projection of Croxden Abbey site plan (English Heritage, 2015) over Aunay Abbey's legacy buildings in a recent Red-Green-Blue (RGB) image. Brown lines in abbey field reveal location of subsurface features disclosed in this study, and brown arrow reveals location and direction of tunnel under abbey-grange boundary wall. Inset image is illustration of Aunay Abbey by Louis Boudan in 1706 (Werner, 2021) and red dot, red arrow and red dashed lines represent presumed location of viewing point during the illustration.

Given the high quantity and mixed orientation of geometric anomalies in Figure 4.11a, the likelihood of each one representing anomalous ground expression from a Cistercian tunnel or drain is low. That said, we do observe several straight-line anomalies along the northern edge of the abbey field,

parallel with the north boundary wall and aligning with the tunnel entrance in the east (Figure 4.11a). Therefore, there is a possibility that these particular subsurface anomalies delineate the spatial extent of the tunnel found in Section 4.4.1.1 and interestingly, if these anomalies were to continue extending south-west, they would head directly to the abbey church (Figure 4.11b).

We are certain in the location of Aunay's abbey church because remains of the north transept and its pointed vaults are still visible today. Given these church remains, the configuration of the old abbey buildings that remain, and the fact that Cistercian monasteries followed the same general building plan (Coppack, 2000; Tobin, 1995), we are confident in our reconstruction of Aunay Abbey, which we achieve by superimposing a scaled plan of Croxden Abbey[10] over matching building features (Figure 4.11b).

Croxden Abbey was the daughter house of Aunay; built by a group of Cistercian monks who were sent from Aunay to the UK to build the daughter abbey under the direction of Bertran III de Verdun (Dace, 1999). Under his guidance, the monks of Aunay replicated the design of Aunay Abbey and in particular, the abbey church, in their construction of Croxden (Hall, 2007). The image inset in Figure 4.11b is a drawing of Aunay Abbey in 1706, illustrated by French artist Louis Boudan (Werner, 2021). It shows the grandeur and simplicity of Cistercian architecture, whilst affirming the location of the abbey church in relation to the buildings around the cloister. It was drawn from the west of the monastery in a position that, we suspect, closely aligns with the viewpoint in Figure 4.11b.

However, our projection of the tunnel running under the abbey field and towards the abbey church does not explain the remaining reflection and micro-relief anomalies within the abbey field in Figures 4.11a and 4.11b. These subsurface anomalies could reveal the location of building foundations, although in Figure 4.11b, all monastic buildings are accounted for using our projection of Croxden Abbey. Moreover, the layout of a Cistercian monastery rarely deviated from its blueprint (Kinder, 2002), although the abbey buildings may have been repositioned. Our observations in Figure 4.11 could therefore reveal an earlier location of Aunay Abbey prior to the Hundred Years' War and the French Wars of Religion. Cistercian site moves were not uncommon in the Middle Ages and they were often triggered by the need to upsize or remove themselves from environmental risks like flooding (Tobin, 1995). According to Le Hardy (1897), flooding was not unusual near the River Odon, with at least two episodes reported in the abbey in 1760. Also, some monastic sites were only intended as temporary locations, providing the monks with a place for accommodation and spiritual practice while a permanent site was being developed (Burton and Kerr, 2011). However, it is difficult to comprehend the type of buildings that require foundations shaped like those seen in Figure 4.11a and 4.11b, and they clearly don't emulate the typical building plan of a Cistercian monastery.

[10] A scaled plan of Croxden Abbey in Staffordshire, UK, was sourced from the English Heritage and available at: https://www.english-heritage.org.uk/visit/places/croxden-abbey/history.

If the abbey field did not contain buildings from the Middle Ages, it reduces the land use to that of farming and gardening. According to Le Hardy (1897), all farming was undertaken outside of the monastery in the various lands donated to the Cistercians, including that of La Garenne. There were however several garden enclosures inside the monastery. During the seventeenth-century restoration of the abbey, Le Hardy (1897) highlights some of the hardships handled by the Cistercians during their return to good order. In particular, he celebrates their tenacity to complete an elaborate garden with lawn canals, which the Cistercians finished in 1642.

We suggest that these garden references relate to the plan in Figure 4.12a which, when translated, is an eighteenth-century plan of the garden of the abbey of Aunay, including the line of the dormitory, the house, the courtyard, the fields and lands being worked (BnF, 2025). Sourced from the Bibliothèque nationale de France (BnF) catalogue général, this garden plan presents a series of structural features which closely resemble the reflection and micro-relief anomalies identified using our multispectral and LiDAR image processing workflows (Figures 4.4 and 4.5). Once we rotate the garden plan in Figure 4.12a 180 degrees (because north is orientated downwards) and then crop (Figure 4.12b), balanced comparisons can be made between the Cistercian's eighteenth-century garden plan and our regular shaped subsurface anomalies (Figure 4.12c).

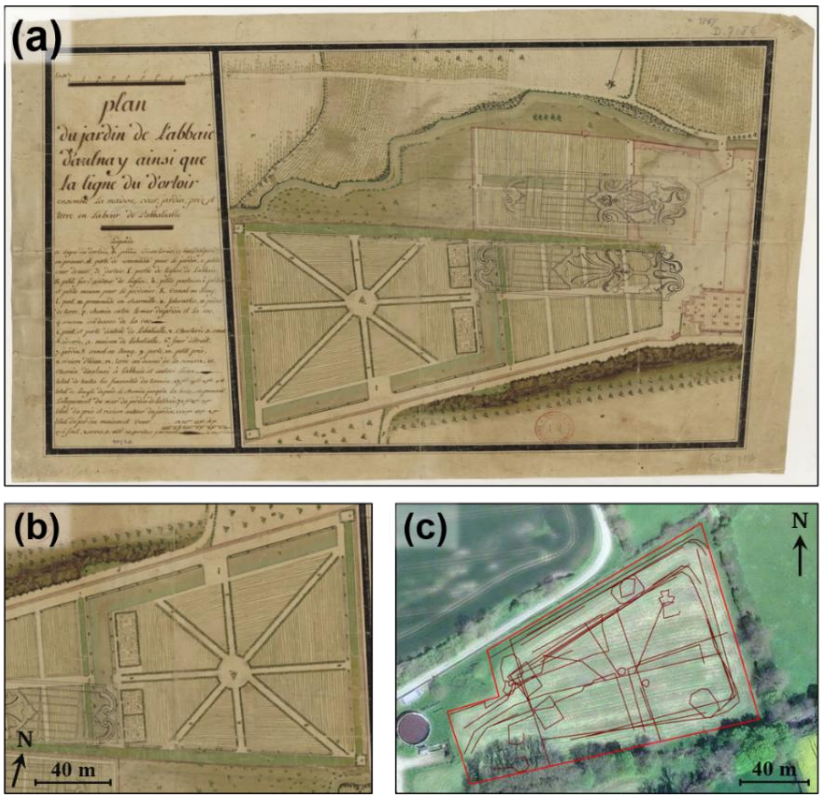



**Figure 4.12**. An eighteenth-century garden plan of the abbey field and the subsurface features found in this study using multispectral satellite imagery and airborne light detection and ranging (LiDAR). a). An eighteenth-century plan of the garden of the abbey of Aunay, including the line of the dormitory, the house, the courtyard, the fields and the lands being worked (BnF, 2025). The garden plan was found using the Bibliothèque nationale de France (BnF) catalogue general. b). The eighteenth-century garden plan cropped to the approximate extent of the abbey field and rotated 180 degrees, ensuring north is directed upwards. c). Brown lines depict location of buried garden features found in this study with high-resolution multispectral satellite imagery and a very-high-resolution (VHR) LiDAR derived digital surface model (DSM).

Allowing for uncertainties, we infer that our results reveal the edges, shape and structure of an elaborate, French formal (baroque) garden (e.g., Baridon, 1998). In particular, our remotely sensed anomalies reveal the spatial extent of the lawn canals and rectangular ponds, formal parterres, gravelled walkways, long avenues, a garden bridge and a central circular feature which, according to the garden plan, was reserved for a lone tree (Figures 4.12a, 4.12b and 4.12c). Therefore, our results imply the detection of, what is now, concealed edge work, various stone and gravel foundations and changes in ground composition, all retaining the geometric patterns and symmetry of a French baroque garden (Lyons, 2019). In present day, we suspect these subsurface characteristics to be variations in soil type and vegetation stress; all originating from the design of an elaborate, walled garden from over three hundred years ago.

## 4.6 Discussion

Section 4.6.1 reviews our tunnel detection techniques and the likely purpose of the tunnel under the east wall. Section 4.6.2 reviews our garden detection techniques, the likely sources of inaccuracy and the purpose of the eighteenth-century garden plan.

### 4.6.1 Tunnel detection

The detection of anomalous reflection behaviour from overlying vegetation is often ambiguous and subjective in 2D imagery. However, when attempting to locate shallow tunnels, the number of false positives is reduced by the linear surface expression a tunnel creates in the soil composition and vegetation stress above (e.g., Morley et al., 2025b; Chapter 3). A tunnel usually follows a straight line to its end destination, thereby keeping excavation efforts and building resource to a minimum. Moreover, straight line tunnel bearings will overcome most navigational difficulties underground, especially during the excavation phase (Butler, 2008). However, the tunnel's effect on overlying soil and vegetation diminishes with increased tunnel depth, reducing the likelihood of identifying persistent, linear reflectance anomalies in multispectral satellite imagery or, persistent, linear micro-relief anomalies in VHR DSMs.

In this study, we have shown other ways to detect statistically significant reflection anomalies from linear subsurface features like tunnels. When tunnels are thought to exist along predefined boundaries, we demonstrate the utility of calculating, stacking and averaging several spectral profiles along a boundary. Inspecting for statistical outliers is then undertaken using Tukey's IQR method (Tukey, 1970), which is readily visualised graphically and facilitates the detection of outliers, although alternative approaches such as Z-scores could also be considered (e.g., Senthamarai Kannan et al., 2015).

First, all reflection information in the corresponding spectral profiles must come from the same ground sections, and they must be free of temporal effects from trees or hedgerows like, for

example, shadow and seasonal leaf growth. If corresponding spectral profiles are then taken from different multispectral images, all images must be of a similar spatial resolution (+/- 0.2 m). Once complete, reflection outliers from our spectral indices can be quantitatively examined as a function of distance along our field boundaries, which we examine as stacked column charts. Of note, we only used 4-5 spectral profiles along each boundary wall, but a similar approach could be employed over any 2D linear anomaly, where multiple spectral profiles (traverses) could be taken along the length of a suspected subsurface anomaly and then stacked and averaged for the inspection of statistical outliers. This approach could easily be automated and delivered as a web service for archaeologists where, for example, a user declares the boundaries to be inspected for tunnels or, after generating a series of spectral indices, convolutional neural networks (CNNs) are used to recognise linear anomalies across a study area. Several spectral profiles could then be taken along the length of the suspected tunnel boundary or CNN anomaly to determine if a tunnel is present *or*, which linear anomalies detected by the CNN are statistically significant.

In this study, a graphical inspection of Iron Oxide, SI7 and SIPI subsurface detection indices along the east and north wall of the abbey-grange boundary reveal a tunnel entrance under the east wall (Figure 4.6 and Figure 4.11). Above the tunnel, all anomalous reflection values from these indices are high, suggesting the 1.4 m deep, rubble stone tunnel is, relative to the ground 'off' the tunnel, creating *higher* concentrations of ground salt and iron oxide and therefore, greater levels of stress in the cool-season grass above. Much aligned with the observations and deductions in Morley et al. (2025b; Chapter 3), we expect the higher concentrations of ground salt and iron oxide arise from the chemical weathering and active leaching of the significant volumes of tunnel stone below ground.

Given the design, we suspect the tunnel is medieval (e.g., Surmely and Chalin, 2019) and likely to predate the abbey-grange boundary wall above. The tunnel is approximately 0.6 m wide and, after some controlled hand-excavation, 1.4 m high (Figure 4.13a). From observation, we also know the tunnel extends approximately 9 m in a straight line under the boundary wall (Figure 4.13b), to a free-standing boulder which is unrelated to the tunnel structure and positioned in front of an archway filled with silt (Figure 4.13c). The tunnel is intricately built with numerous stone blocks layered to form its sides, and then wedged to form an arched roof. Along the length of the tunnel, there are a series of small recesses in the tunnel walls, alternately staggered every metre.

The purpose of this tunnel remains a mystery. Drainage is the most likely function, where water and/or sewage is channelled away from the buildings and the fields of La Garenne and towards the River Odon. However, the rationale for passing the water under the abbey's garden by a tunnel to a discharge point in the River Odon *upstream* from La Garenne makes little sense. If it were part of a drainage or sewage plan for La Garenne, it would be prudent to discharge the water into the river downstream. However, according to Errand (1974), there is logic in channelling water from the high ground to a tunnel that will lead to the monastery's water-mill. The water could then be

used in the abbey's kitchen for cooking, drinking and washing and then onwards to the latrines for drainage. If this were the case, and by assuming Aunay Abbey was never positioned any closer to La Garenne, we can expect the tunnel to extend at least 300 m under the walled garden before reaching the abbey's kitchen. Using Figure 4.11b as a guide, the Cistercian's kitchen is found along the southern gallery of the abbey's cloister (Coppack, 2000). Alternatively, the tunnel may have been used to manage and circulate pond water (e.g., Baridon, 1998) or irrigate the formal garden.




**Figure 4.13**. Rubble stone tunnel found under east wall of abbey-grange boundary in Section 4.4.1.1. a). Tunnel entrance after hand-excavation; tunnel entrance is approximately 0.6 m wide and 1.4 m high. b). Tunnel interior, following a straight-line tunnel axis to a free-standing boulder, found approximately 9 m from the tunnel entrance along a bearing of 235 degrees. c). Free-standing boulder at the end of the tunnel section, unrelated to tunnel structure and positioned in front of an archway filled with silt. Free-standing boulder seen to rest on a flat stone slab and underlying silt. The boulder is approximately 0.5 m wide, 0.25 m high and 0.2 m deep.

Rather than a point of ingress, we also consider the tunnel's utility as a point of egress, but this time for the Cistercians themselves. A Cistercian's need to escape and evade persecution is possible, especially if an abbot or a senior monk has been opposing royal authorities or seeks refuge from the riots and pillages of war, schism and rising nationalism (Burton and Kerr, 2011). Hiding in the farm of La Garenne is plausible, and aligns with reports of a Cistercian escape tunnel from Forde Abbey in Dorset, England, which is thought to be connected with Hay Farm, a nearby farmhouse (Clayton, 2015). In tandem, the tunnel could have been used by the Cistercian farmers of La Garenne as a direct means of access to the monastery and the abbey church; a useful convenience for daily mass and worship.

Alternatively, this tunnel could have been used for the safe movement and protection of monastic wealth and sacred possessions to-and-from the monastery. Many gifts were donated to Aunay Abbey in the High Middle Ages (e.g., Le Hête, 2009) and King Henry II chose to safeguard the abbey with a formal declaration of royal protection in the late 1100s (Le Hardy, 1897; Vincent, 2021). Evidence therefore suggests that the abbey of Aunay was of significant national importance and considerably wealthy during this time, exposing it as a high-reward target for looting and sabotage. Moreover, by using the process of elimination, little seems to be known about Aunay Abbey's production of historiographical texts (Allen, 2021), and even the first charter of Aunay Abbey's foundation disappeared many year ago (Le Hardy, 1897). This raises the question of the

abbey's need to protect such assets[11] somewhere safe and out-of-reach, versus their unfortunate apprehension in the years that followed King Henry II's reign.

The recesses along the tunnel sides could imply they were designed for positioning a light source like a candle or lantern. If so, this disqualifies the sewer and drainage concept, unless the recesses were solely built for positioning light during tunnel construction. If not, we suspect other pedestrian needs to include that of a passageway to a cool chamber for isolating the sick (Burns, 2023), or an underground passage to a dungeon or prison. The former makes little sense, because predominantly all Cistercian monasteries had a dedicated infirmary. The latter is therefore more likely, with several references documenting the need to confine disobedient monks in prisons in or near Cistercian monasteries (e.g., Burton and Kerr, 2011; Le Hardy, 1897). Without further exploration, we suspect any of the above functions are plausible, although water provision, drainage and sewage disposal are typically the norms (Errand, 1974; Ross, 1991; Urwin, 1936)

### 4.6.2 Garden detection

Our subsurface detection indices, FCCs, Sobel edge detection filters and multi-directional/multi-altitude LiDAR hillshade analyses have, in this study, proven successful in the detection of anomalous reflection behaviour and regular micro-relief arrangements in a grass-covered field enclosure in the abbey of Aunay. These anomalies arise from the now concealed and dilapidated stone foundations, edge work and changes in ground composition of an elaborate, French formal (baroque style) garden that was reinstated by the Cistercians during the seventeenth-century restoration of the abbey. A visual comparison with an eighteenth-century garden plan in Figure 4.12 (BnF, 2025) supports these remotely sensed observations of the subsurface. However, our remote detection of a Cistercian tunnel under the abbey's garden is, *in 2D imagery*, unresolved. The tunnel's course from the entrance along the east wall *could* be represented by one or more of the geometric anomalies in Figures 4.11 and 4.12c, but without geophysical validation, the trace of the tunnel remains unknown.

The surface expression from the tunnel could be masked by the considerable quantity of regular shaped anomalies in the abbey field. This number is testament to our use of several high-resolution Maxar multispectral images from different sensors[12] and different acquisition dates, along with our application of: 1) three different subsurface detection indices; 2) two very different manipulations of these indices (FCCs and edge detection); 3) our integration with VHR airborne LiDAR data.

All multispectral images reveal subsurface anomalies in the walled garden, demonstrating the advantage of analysing several multispectral images from different sensor types and at different

[11] Assets of Cistercian wealth are expected to include precious metals, various relics and reliquaries, altar vessels, gold and silver plates, manuscripts and coinage (Clayton, 2015).
[12] Different EO sensors have different spatial, spectral and radiometric capabilities, thereby hosting different potentials in their detection of subsurface features.

times of year. Warm, dry weather conditions are usually the most favourable for detecting reflectance anomalies from vegetation over shallow buried features (Morley et al., 2025; Chapter 3), although we propose any weather setting which *differentiates* ground conditions across a study area to be the most effective. Such differentiations are caused by localised alterations in drainage (e.g., Luo et al., 2019; Lv et al., 2020; Waters et al., 2019). This would suggest that studying multispectral images soon after excessive rainfall *or* during times of drought are optimal times for remotely detecting changes in ground condition and reflectance behaviour from subsurface features. In this case, variations in drainage across the walled garden is determined by changes in vegetation, soil type and the presence of stone structures below ground. In turn, these changes are defined by the remnants of formal parterres, water features, garden walkways, gravel avenues, edge work and the various stone structures from Aunay Abbey's eighteenth-century garden plan (Figures 4.12a and 4.12b).

To increase the likelihood of detecting subsurface features with reflectance values from cool-season vegetation, we recommend using a FCC that contains VIs SI7 and Gmag SI7. When combined with the Iron Oxide index or SIPI, these two indices are seen to perform very well in the walled garden - *across all seasons*. Therefore, if we assume VI definitions are precise, an examination of FCCs containing ground salt levels (SI7) and a rate of change in ground salt (Gmag SI7) to be the most reliable for exposing subsurface features, regardless of weather. The SI7 index also responds well to Sobel edge detection filtering, achieving black or grey subsurface detection ratings in all multispectral images used in this study. However, when the ambient weather is considerably hot and dry, and if groundwater is scarce, the SIPI and Gmag SIPI become much more competitive, utilising the reflection sensitivities in the NIR to delineate regions of significant vegetation stress over subsurface features.

Detecting likely garden facets with airborne LiDAR also allowed us to look for micro-relief patterns in the abbey field, thereby exploiting a second ground characteristic of subsurface features. Here, sun altitudes of 30 and 35 degrees were most effective, especially on hillshaded DSM FCCs with successive sun azimuths trending northwest – southeast. These sun azimuths were perpendicular to the general trend of the longest linear elevation anomalies in the walled garden (Figure 4.10c), which we now propose are the edges of garden walkways, parterres, lawn canals and rectangular ponds (Figure 4.12). The three hillshaded DSMs used in our optimised three-layer image stack contained various sun azimuth combinations and different sun altitudes (Figure 4.10a), therefore enhancing the resilience of our final hillshaded DSM FCCs. Our end result in Figures 4.10b and 4.10c saw the emphasised exposure of various micro-relief anomalies near and above the edges of garden walkways, gravel avenues, individual parterres and lawn canals, demonstrating sufficient reliability in our multi-directional and multi-altitude hillshaded DSM workflow (Figure 4.5).

However, it is evident that our interpretation of the multispectral FCCs, edge filtered raster images and hillshaded DSMs present *some* subjectivity. We use a visual depiction and a BGW grading

system to classify our processed imagery and DSMs, based on the premise that straight lines and regular shapes are rarely surface expressions from naturally occurring features. Without a quantitative means to grade our results (e.g. 2D image correlations with geophysical data), our BGW subsurface detection rating only offers a *qualitative* means in which to categorise our results. Visually searching for archaeological anomalies in 156 processed satellite images (FCCs and edge filtered rasters) and 180 hillshaded DSM FCCs also needs order, patience and discipline. In some cases, to increase the likelihood of visual detection, we observed the need to use different colour schemes, different viewing scales and on occasion, a 90 to 180-degree rotation of the image.

We must also address our likely sources of inaccuracy. In Figure 4.14, we superimpose our subsurface anomalies on the eighteenth-century garden plan for Aunay Abbey, where we have scaled-up our vector polylines and arranged them over the various garden features. In places, we see a close fit but in others (like the bridge over the lawn canal halfway along the north wall – labelled *'l'*), our positioning is out by almost 20 m (Figure 4.14). We offer several reasons for this inaccuracy: 1) the spatial resolution of our data; 2) sensor calibration and sensor viewing conditions; 3) pre-processing error; 4) atmospheric effects and solar illumination geometry in our multispectral data; 5) noise from dense vegetation and the garden wall in our LiDAR data; 6) spatial reference conversions; 7) cartographic skill and map scaling procedures in the eighteenth century[13]; 8) our visual interpretation; 9) our polyline digitisation skills. It is difficult to assess the weighting of each, but in equal measure, it is useful to appreciate the many contributing factors of our inaccuracy.

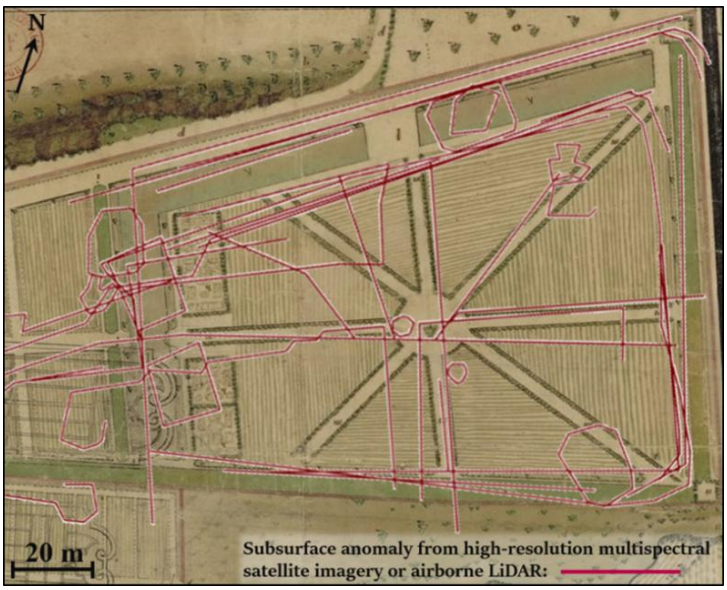



**Figure 4.14**. A comparison between the now concealed garden features of Aunay Abbey, identified using multispectral satellite imagery and airborne light detection and ranging (LiDAR), and the garden features mapped in the abbey of Aunay's eighteenth-century garden plan (BnF, 2025). Burgundy coloured lines denote garden features detected in this study using high-resolution multispectral satellite imagery and very-high-resolution (VHR) airborne LiDAR data.

[13] In the eighteenth century, scaled plans were created using hand-drafting techniques with instruments like rulers, compasses and protractors. Architects and surveyors would accurately measure distances and angles on site and then translate them to paper using a consistent ratio, known as 'the scale' (Pedley, 2005).

Finally, we consider the orientation of the garden plan and the reason for producing it. Given north is pointing downwards in Figure 4.12a, the eighteenth-century garden plan for Aunay Abbey is not conventional. Either it was produced by an individual who was well-accustomed to viewing the garden from La Garenne or, the abbey's access road from the north was the main approach to the abbey, thereby designating a northerly perspective as the front-facing perspective of the abbey. Also, given the listed description in the title (see caption for Figure 4.12a) and the itemised legend in the garden plan, we suspect the scaled drawing was used to augment a property inventory for the abbey. Property inventories were common in the eighteenth century, especially when an estate was for sale or due transfer to a nominated custodian (Nicholson, 2017). In 1791 the Cistercian monks were asked to leave the abbey, and on 25 May 1792, the abbey buildings and garden enclosure were purchased by Jean-François Bellissent for 44,600 livres (Le Hardy, 1897).

## 4.7 Concluding remarks

Using high-resolution multispectral satellite imagery and a very-high-resolution (VHR) LiDAR derived digital surface model (DSM), we detect a tunnel between the abbey of Aunay and La Garenne, a nearby medieval grange. We also detect various buried garden features, once delineating the shape, size and form of a formal Cistercian, baroque-style garden.

To find the tunnel, we used average Iron Oxide index, soil salinity index 7 (SI7) and structure insensitive pigment index (SIPI) reflection profiles along the east and north walls of the abbey-grange boundary. By thresholding these index reflection profiles with statistical limits, we exposed several anomalous reflection values from the cool-season grass along the north and east boundary wall of the abbey field (Figures 4.6 and 4.7). Within La Garenne, a quantitative inspection of these reflection values along the perimeter walls revealed a tunnel entrance, which we suspect is medieval (Figures 4.6e, 4.13a and 4.13b). This tunnel is 1.4 m below the abbey field and the direction of the tunnel is towards the abbey church, although it is currently blocked by a free-standing boulder c.9 m from the entrance.

In revealing the location of this tunnel from La Garenne, we demonstrate the tangible advantages of inspecting VI reflection profiles for anomalous reflection values. In the right landscape, we expect this technique to assist with the detection of near-surface tunnels, especially under borders and boundaries in vegetated terrain. We also see the same *type* of anomalous reflection behaviour from cool-season grass above the tunnel, where high Iron Oxide, SI7 and SIPI reflection values are recurrently observed, especially after adverse weather events. These high concentrations of iron oxide and ground salt are expected to be the secondary effects of: 1) a different drainage regime above the tunnel; 2) the chemical weathering and leaching of the tunnel stone below.

The subsurface detection indices of the abbey field, and their gradient magnitude equivalents, are analysed using false colour composites (FCCs) and Sobel edge detection filters. The resulting

imagery is graded black, grey or white (BGW), pending the opacity of the linear or regular shaped reflection anomalies inside the abbey field. Similarly, a 50 cm resolution DSM of the abbey field is analysed using a multi-azimuth and multi-altitude hillshade sequence. Again, the resultant DSMs are graded with a BGW subsurface detection rating, prescribed by the levels of accentuation of the micro-relief anomalies inside the field.

We combine all reflection and elevation anomalies from the black-graded imagery to reveal several linear and geometric shaped distinctions in soil type, drainage, vegetation stress and micro-relief across the abbey field (Figure 4.11). We compare these ground variations and biophysical alterations to an eighteenth-century garden plan of the abbey field (Figures 4.12 and 4.14). In doing so, we verify these anomalies to be the surface expression of stone foundations, edge work and changes in ground composition from a French formal, baroque style garden that was reinstated by the Cistercians during the seventeenth-century restoration of the abbey. We propose that our remotely sensed observations disclose the location of formal parterres, garden walkways, gravel avenues, rectangular ponds and a garden bridge, thereby reconstructing a landscape once celebrated by the Cistercians as a sanctuary for prayer, reading and meditation.

In unveiling the likely features of this formal, baroque garden, we demonstrate the advantage of using several multispectral images from different sensor types and different times of year. This approach broadens the detection range, where different sensor capabilities, drainage conditions, soil health and vegetation vigour from different scenes will increase the likelihood of detecting different subsurface anomalies (Figures 4.8 and 4.9). In doing so, we reveal evidence of several eighteenth-century boundaries of formal parterres, water features, garden walkways and gravel avenues (Figure 4.12). We also recommend inspecting a FCC with SI7 and its gradient magnitude (Gmag) equivalent. When combined with the Iron Oxide index or SIPI, these FCCs perform incredibly well in all aspects of subsurface detection in temperate, vegetated terrain (e.g., Figures 4.8c and 4.8d). The SI7 index is also seen to perform incredibly well in Sobel edge detection, expressing clear edge effects from changes in ground salt concentration on-and-off subsurface features at various times of year (e.g., Figures 4.9a and 4.9b). However, in considerably hot and dry weather conditions, the SIPI and Gmag SIPI become much more competitive, using reflection sensitivities in the NIR to locate regions of significant vegetation stress above subsurface features (e.g., Figures 4.8i and 4.8j).

Using airborne LiDAR, we demonstrate the credibility of systematically exploring a hillshaded DSM at various sun altitudes and at multiple sun azimuths. At a 30 to 35-degree sun altitude, and when using a combination of sun azimuths trending northwest – southeast, we show the location of several micro-relief anomalies from the edge of garden walkways, parterres, lawn canals and rectangular ponds (Figure 4.10). We also address the sources of our inaccuracy, documenting contributions from the spatial resolution of our datasets, the calibration of our sensors, their viewing conditions, pre-processing routines, atmospheric effects, solar illumination geometry, spatial

reference conversions, cartographic skills from the eighteenth century, and the subjectivity of our qualitative BGW assessment.

To close, the purpose and end destination of La Garenne's tunnel will remain unanswered. Water provision to and drainage from the abbey and its gardens is the obvious fit. However, in relation to the location and flow of the River Odon, the tunnel's setting for water management is dysfunctional. Further, the tunnel's craftsmanship is exemplary, it is large in size, there are small recesses for light, and there is a free-standing boulder in front of an arch, deliberately blocking access further into the tunnel. Subsequently, a subterranean passage for people is not unreasonable, especially given the elevated status and wealth of Aunay Abbey in the High Middle Ages. The rightful founder of Aunay Abbey's *second* site, Richard du Hommet, was the constable of Normandy and the chief constable to King Henry II. He protected and projected the profile of Aunay Abbey in all its splendour, inspiring the build of replica abbeys outside of Normandy, attracting countless donations, and winning the King's royal protection. If any Cistercian abbey and its grange were to accommodate subterranean passages for a function other than water, the abbey of Aunay and La Garenne seem likely. Given Aunay Abbey's once impressive and majestic reputation, the need for escape and evasion, imprisonment and the protection of monastic wealth seem credible. All abbeys need water, but maybe Aunay Abbey also needed something different.

# 5

# Remote detection of linear subsurface features around Glastonbury Tor: A multi-sensor approach

In preparation for publication as: *a technical report for the National Trust*

## Abstract

Glastonbury Tor in Somerset, UK, has fascinated people for centuries. The Tor and its surrounding landscape are steeped in legend and rich in mythology, yet little is known about the subsurface. To date, there are no official records of archaeological investigation in the fields bordering Glastonbury Tor, contrasting with several excavations on the Tor itself. The Tor is bordered to the north by nine grass covered fields which, given their location between the Tor, Chalice Hill and Glastonbury Abbey, are favourable sites for tunnels, pipes and drains. In this study, we remotely search for linear subsurface features in the border fields north of Glastonbury Tor using three different sensor types. First, we use high-resolution light detection and ranging (LiDAR) elevation differencing to find linear elevation-change anomalies. We apply statistical thresholds to average elevation-change profiles to ascertain which linear anomalies (LAs) show abnormal height change. Second, we inspect the ground above these abnormal LAs for atypical concentrations of iron oxide, ground salt and vegetation stress using a WorldView-2 multispectral satellite image. Third, we conduct an airborne thermal drone survey to examine the heat retention properties of each abnormal LA. In doing so, two distinct subsurface anomalies are observed. When augmented with 2D electrical resistivity tomography (ERT), one LA is interpreted as an underground spring and the other a utility pipe. A third ERT profile reveals a tunnel-like feature, coinciding with a deeper ground penetrating radar (GPR) anomaly and a previously dowsed tunnel observation. Further high-resolution remote

sensing, integrated with additional ERT, GPR and electromagnetism (EM) is advised to confirm this near-surface tunnel signature.

## 5.1 Introduction

Glastonbury Tor is a 158-m tall conical hill that dominates the landscape around Glastonbury town in Somerset, UK. Geologically, the Tor consists of layered Jurassic blue-limestone (Blue Lias) and a Midford Sandstone cap from the Bridport Sand Formation (Rahtz, 1970). A calcite rich spring is also known to rise beneath the Tor, forming water tunnels in the soft limestone that, on occasion, can render the Tor's limestone unstable (Mann, 1986). There is a major outlet of the Tor's spring at the bottom of Well House Lane (*named the White Spring*), approximately 500 m west of the Tor. Glastonbury Tor is Neolithic (10,000 BC – 2,200 BC), with human occupation on or near the Tor since 4,000 BC (Matthews, 1993). More recently, excavations on the top of the Tor revealed dark age occupation (5th – 7th centuries) through to late medieval (Rahtz, 1970). The Tor also features a series of distinct terraced slopes (Figure 5.1a) which, although still uncertain, are thought to be: 1) Iron Age defensive ramparts (e.g., Mann, 2001); 2) a processional pathway for ancient pagan rituals and/or medieval pilgrims (e.g., Wingfield, 2018); 3) terraces for agriculture and cultivation (e.g., Rahtz, 2002).

In contrast to the heritage and legacy of Glastonbury Tor, very little is known about the grass covered fields surrounding its perimeter (Figure 5.1a). The grass covering these fields is cool-season (Bunting, 2025) and the soils are Pennard[14] and Martock[15] (Figure 5.1b), both brown earth soils in Avery (1955). There are no records of any legitimate archaeological investigation in these fields. However, one *illegal* excavation has been recorded where, in 2016, a medieval "well house" was discovered near Lypyatt Lane (Stray, 2018). This "well house" featured a series of steps to a blocked passage, which reportedly extends below Well House Lane and towards Glastonbury Tor (Figure 5.1c and 5.1d; Stray, 2018).

Stray (2018) also presents a dowsing[16] survey of Glastonbury Tor and its surrounding fields, producing the results in Figure 5.1d. Although dowsing is a controversial and much debated technique (e.g., More, 2014), the yellow dashed lines denote the trace of suspected tunnels and the blue dashed lines depict the trace of underground springs, where groundwater travels away

[14] The Pennard series are from the Calcareous soil group. They are warm brown soils of variable depth, resting on rubbly limestones. Types include silty clay loam, silty clay and clay. They typically occur on shelf-like features around Glastonbury and generally demonstrate free natural drainage. In some places, a perched water-table can exist within the rock, held up by underlying bands of impervious marl or silt (Avery, 1955).

[15] Soft micaceous siltstones of the Middle and Upper Lias formations give rise to soils of the Martock series. These soils are from the Brown Earth soil group. Types include loam, silt loam and silty clay loam. They occupy undulating and elevated land close to the Junction Bed outcrop, and also appear at lower levels on the basal beds of the Middle Lias. Internal drainage is slow, and appreciable run-off takes place on sloping land under arable cultivation (Avery, 1955).

[16] "Dowsing" refers to the practice of using a forked stick, rod or pendulum to locate underground water, voids and minerals. The technique relies on subconscious information and a user's unconscious reaction to detect heterogeneities below ground (USGS, 1977).

from the Tor. In Stray (2018), these alleged tunnels are considered medieval; built by Benedictine monks during their occupancy of Glastonbury Abbey in the Middle Ages (e.g., Bond, 1924, 1918). Such tunnels were needed to: 1) control water supply from Glastonbury Tor to the Abbey (e.g., Gilchrist and Green, 2015); 2) safeguard monastic wealth (e.g., Mantle, 1911); 3). evade persecution (e.g., Bond, 1918). According to Wakefield (1814), at least one subterranean passage connected Glastonbury Abbey (approximately 1 km west of the Tor) to St Michael's Church, a daughter house of Glastonbury Abbey; founded on the Tor in the 9th century (Matthews, 1993).

In 1539, St Michael's Church was destroyed during the dissolution of the monasteries (Bond, 1924), leaving only a stone-built church tower that stands today (Figure 5.1a). During this time, the last abbot, the treasurer and the curator of vessels, vestments and relics from Glastonbury Abbey were hung, drawn and quartered as traitors on Glastonbury Tor, because they refused to hand over the Abbey and all its treasures to King Henry VIII (Stray, 2018). These treasures are still unaccounted for, even though Glastonbury Abbey was the second richest abbey in England after Westminster (Costen, 2005; Stray, 2018). The prophecy in Stray (2018) proclaims: "Before the closure of Glastonbury Abbey, monks hid the vast wealth of relics, manuscripts and other treasures within tunnels and caverns beneath Glastonbury Tor. Legends say these hidden treasures will one day be revealed, ushering an age of peace and enlightenment into the world."

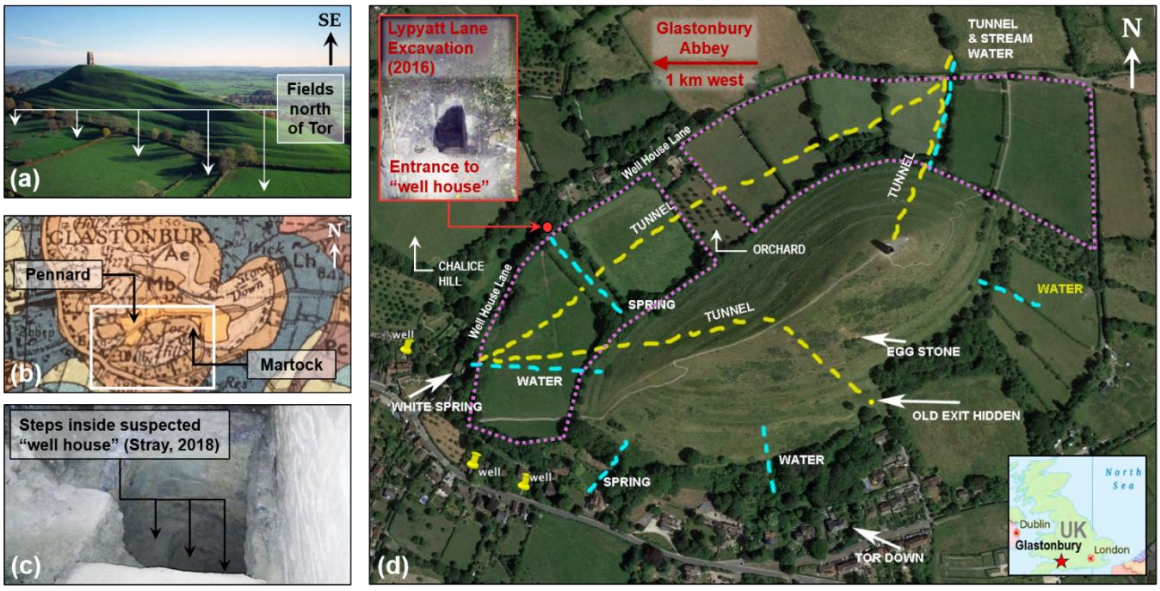



**Figure 5.1**. Glastonbury Tor and its environs, including the Tor's border fields, soil coverage and the 2016 Lypyatt Lane "well house" excavation. a). View of Glastonbury Tor from the north-west, showing the Tor's distinct terraced slopes, St Michael's Tower and five of the ten border fields north of the Tor. b). A soil map of Glastonbury, showing soil types in border fields north of Glastonbury Tor (Avery, 1955). White box denotes spatial extent of red-green-blue (RGB) aerial image in Figure 5.1d. c). Photograph of steps descending under Well House Lane from "well house" excavation near Lypyatt Lane in 2016 (Stray, 2018). d). RGB aerial image of Glastonbury Tor with dowsed results from Stray (2018). Location of dowsed tunnels are yellow dashed lines and location of dowsed underground water courses are blue dashed lines. Border fields investigated in this study are inside pink dashed lines. From left to right, inset images show: entrance to "well house" discovered in 2016 Lypyatt Lane excavation; location map of Glastonbury in Somerset, UK. Figure 5.1d was adapted from Stray (2018).

In this study, we use various remote sensing techniques to detect linear subsurface features beneath the grass covered border fields *north* of Glastonbury Tor. These border fields are located between the Tor, Chalice Hill[17] and Glastonbury Abbey (Figure 5.1d). Therefore, by proximity alone, they become the most plausible perimeter fields for Benedictine tunnels and drains between the Tor and Glastonbury Abbey. The fields used in this study are bound by pink dotted lines in Figure 5.1d. Of note, each border field north of the Tor is analysed, apart from the orchard, which is densely covered by trees.

To begin, we use high-resolution light detection and ranging (LiDAR) elevation differencing (e.g., Daehne and Corsini, 2013; James et al., 2012; Li et al., 2024; Morley et al., 2025a; Chapter 2) to detect linear elevation-change anomalies in the fields north of Glastonbury Tor (Figure 5.1d). Next, we apply statistical thresholds (Tukey, 1970) to average elevation-change profiles to ascertain which linear anomalies (LAs) are showing abnormal elevation change. These abnormal LAs are then inspected for anomalous reflectance behaviour in a high-resolution, multispectral satellite image, where ground conditions are exceptionally warm and dry. Here, the LAs are analysed as 1D reflectance profiles and 2D image subsets using three vegetation indices (VIs) from Morley et al. (2025b; Chapter 3). These VIs are: Iron Oxide; Soil Salinity Index 7 (SI7); Structure Insensitive Pigment Index (SIPI)[18]. We then study the thermal properties of these LAs by conducting two airborne thermal drone surveys; one during the day and one at dusk (e.g., Casana et al., 2017). We verify the LAs with 2D electrical resistivity tomography (ERT) profiles (e.g., White et al., 2023) and then, to close, we relate our observations to Glastonbury Tor's groundwater hydrology, utility provision and medieval heritage.

## 5.2 Methodology

We focus our remote detection regime on nine border fields north of Glastonbury Tor, located between the Tor, Chalice Hill and Glastonbury Abbey (Figure 5.1d). Given their proximity to Glastonbury Abbey and Glastonbury town, these are the most plausible fields around the Tor for near-surface tunnels, pipes and drains.

Using LiDAR elevation differencing (Section 5.2.1), we inspect each field north of the Tor for linear, elevation-change anomalies. However, the orchard (Figure 5.1d) is encumbered with trees, reducing the accuracy and reliability of any subsurface inferences from LiDAR, multispectral and thermal analyses. We therefore omitted the orchard from our study prior to inspecting each of the fields for linear elevation-change anomalies. All resultant LAs were numbered, and statistical thresholds were then enforced to determine which LAs are statistically significant elevation-change

[17] Chalice Hill is a small, 95-m high hill approximately 400 m north-west of Glastonbury Tor. It is co-located with Chalice Well, an ancient holy well with iron-rich water from the nearby Chalice Spring (Mann, 1986; Stray, 2018).
[18] These vegetation indices are termed 'subsurface detection indices' in Morley et al. (2025b; Chapter 3) after their successful correlation with gravity and ground penetrating radar (GPR) data over a near-surface tunnel.

anomalies. We compare these results with the local Bristol Water pipeline dataset and document any LAs which coincide with the pipeline.

In Section 5.2.2, we use a high-resolution multispectral satellite image and the adapted, multispectral image processing workflow from Morley et al. (2025b; Chapter 3); Appendix K. We use this workflow to further assess the anomalous behaviour of the abnormal LAs from our LiDAR elevation differencing. Here, the Iron Oxide index, SI7 and the SIPI are employed to examine iron oxide levels, soil salinity concentrations and vegetation stress from the ground overlying the LAs. We then inspect the heat retention properties of these LAs by conducting an airborne thermal survey (Section 5.2.3). We close with a section on electrical resistivity tomography (ERT); a geophysical ground-truthing technique used to verify the remote detection of subsurface features (Morley et al., 2025a; Chapter 2).

### 5.2.1 Light Detection and Ranging (LiDAR) elevation differencing

Two one-metre resolution LiDAR derived digital terrain models (DTMs) of Glastonbury (elevation tile: ST53nw_DTM_1m) were sourced from the UK's Environment Agency (EA). The EA's airborne LiDAR survey of elevation tile ST53nw_DTM_1m was flown in January 2015 and again in February 2021, in support of the EA's national LiDAR programme (UK Environment Agency, 2025a). This national LiDAR programme collects and processes elevation data across the UK in accordance with with the Royal Institution of Chartered Surveyors (RICS) height accuracy Band F. On soft detail like the grass fields around Glastonbury Tor, this height accuracy band is +/- 0.1 m (UK Environment Agency, 2025b).

Initially, within Esri's ArcGIS Pro, we snap together the LiDAR DTMs to ensure the elevation cells from each DTM are spatially aligned. This mitigates any systematic error in the subsequent DTM subtraction (Van Niel et al., 2008). We then subtract the 2015 DTM from the 2021 DTM using the raster function MINUS. The resulting elevation raster is a DTM showing elevation change around Glastonbury Tor over a six-year period, where negative elevation values represent regions of ground subsidence and positive elevation values represent areas of surface uplift. Abiding by the laws of error propagation (Lonseth, 1947), we annotate all elevation changes with an accumulated error of +/- 0.2 m.

Next, we clip the LiDAR differenced DTM using individual polygons of each border field north of Glastonbury Tor, and then we label each field from Field 1 (F1) to Field 9 (F9). We then re-symbolise the clipped elevation raster images of each field, standardising and representing elevation change in eight discrete *elevation-change* groups.

To detect linear subsurface features like tunnels, drains and pipes, the clipped LiDAR differenced DTMs for F1 to F9 were visually inspected for linear *subsidence* and linear *uplift* elevation anomalies. Each LA was assigned a number, and then a series of parallel polylines were generated

across and perpendicular to each LA. These parallel polylines, termed *elevation-change profiles*, formed a grid of individual profile lines along the length of the LA at 1.3 m intervals. For a given LA, each elevation-change profile was the same total distance, the same distance to the LA, and the same azimuth. We then used the STACK PROFILE geoprocessing tool in ArcGIS Pro to extract the elevation-change data along each elevation-change profile for each LA, and we export as comma-separated value (CSV) text files. Using a bespoke MATLAB script, we used the elevation data in the CSV text files to calculate an *average elevation-change profile* across each LA.

To determine which LAs had average elevation-change profiles with statistically significant elevation change, we used Tukey's Interquartile Range (IQR) method (Tukey, 1970). Here, the IQR is the difference between the third quartile (Q3: 75th percentile of a dataset) and the first quartile (Q1: 25th percentile of a dataset). In Tukey's limited preliminary edition of Exploratory Data Analysis (1970), the IQR method defines "outside" observations as data points below the first quartile (Q1) or above the third quartile (Q3) by *one* IQR. Similarly, "detached" observations are data points below Q1 or above Q3 by *1.5 times* the IQR (Tukey, 1970). These clear definitions and statistical thresholds are simple to visualise in graphical form, thereby easing the identification of outliers along a profile, whilst demonstrating the effectiveness of Tukey's IQR thresholds.

These IQR thresholds were applied to the average elevation-change profile of each LA identified from our LiDAR elevation differencing. Any LAs presenting outside or detached elevation change were deemed statistically significant, presenting themselves to be LAs with abnormal height change. These LAs were then selected for supplementary inspection using multispectral and thermal analyses.

### 5.2.2 Multispectral analysis

Any LAs in the fields north of Glastonbury Tor (F1-F9) with statistically significant (i.e., abnormal) elevation change were reinspected using a high-resolution, multispectral satellite image from Maxar. To do this, we used an eight-band WorldView-2 image dated 21 June 2017, with 2.25 m spatial resolution. The multispectral image file[19] was sourced from Maxar's Analysis Ready Data (ARD) Dashboard (Maxar, 2022b). The image was atmospherically corrected and orthorectified at source. The image was collected on a hot and dry day with no cloud cover, no precipitation for at least three days prior, and a maximum temperature of 32°C (Weather Online, 2025).

By following the adapted, multispectral image processing workflow in Appendix K, Maxar's high-resolution image was subsequently used to calculate the VIs Iron Oxide, SI7 and SIPI. Using the GRADIENTWEIGHT function in MATLAB, we then calculate their gradient magnitude (Gmag) equivalents. All six image indices were then clipped to the extent of the field polygons that contain

[19] Maxar multispectral image filename: 103001006D32C100-ms.tif.

statistically significant elevation anomalies. We then inspected the clipped image indices for the same LAs using false colour composites (FCCs) and Sobel edge detection filters (Appendix K).

### 5.2.3 Thermal analysis

In parallel to our multispectral analyses, we reinspected the same linear elevation anomalies with an airborne thermal survey. On 6 August 2025, a DJI[20] H20T thermal sensor was secured to a DJI M300 rotary drone and then, courtesy of AtkinsRéalis[21], it was flown above the relevant fields to detect the statistically significant LAs that we identify in Section 5.2.1 (Figure 5.2a). The drone followed a predefined flight path across all relevant fields and it was consistently flown within visual line of sight (VLOS) of the pilot or a spotter on Glastonbury Tor. The DJI H20T thermal sensor was calibrated to collect ground surface temperatures at 10 cm resolution, and the drone was calibrated to fly no more than 110 m above ground level. The drone operated from a single take off and land position (TOLP) in a private field north of Glastonbury Tor (Figure 5.2a).

Two flight blocks were conducted; the first was from 1245 – 1400 hours and the second was from 1915 – 2030 hours (local time). The former flight block was during the heat of the day with clear skies, minimal wind (less than 5 m/s) and temperatures reaching 24°C (Weather Online, 2025). The latter flight block was performed at dusk, when the air temperature was much cooler, ranging from 17-18°C (Weather Online, 2025). As a result, two thermal images of each field were produced; one image showing ground temperature variations from solar warming and the other showing ground temperature variations from cooling.

Using the MINUS raster function in ArcGIS Pro, the daytime image was subtracted from the dusk image for each field with an abnormal, linear elevation-change anomaly (identified in Section 5.2.1). The result, for each field of interest, was a heat retention image, showing variations in the rate of heat lost from the ground above and beside the LAs identified in our LiDAR elevation differencing. To assist interpretation, a 2 cm resolution Red-Green-Blue (RGB) image of each field was also collected by the drone. This airborne optical survey was flown between the two thermal survey flight blocks (1430 – 1515 hours) using a DJI P1 RGB camera.

### 5.2.4 Electrical Resistivity Tomography (ERT)

To assist with interpretation, ground-based ERT was performed across any statistically significant LAs identified in our LiDAR elevation differencing (Section 5.2.1). Where relevant, a single 71 m long resistivity profile was positioned perpendicular-to and across the centre of the LA using 72

[20] Da-Jiang Innovations (DJI) is a Chinese technology company and a leading manufacturer of drones and camera equipment worldwide - founded in 2006 (DJI, 2025).
[21] AtkinsRéalis is a design, engineering, project management and nuclear organisation who specialise in infrastructure and energy systems worldwide (AtkinsRéalis, 2025).

stainless-steel electrodes at 1 m intervals (Figure 5.2b). The Wenner-Schlumberger resistivity array, an ERT acquisition configuration (e.g., Supandi, 2021), was then used for all electrical resistivity measurements of the subsurface. Negating the need for a remote electrode, this type of array is compatible with our IRIS Syscal Junior multichannel resistivity meter (Figure 5.2b) and well-configured for high-lateral resolutions of localised objects (e.g., Prins et al., 2019).

The electrical resistivity data from each 71 m long resistivity profile was then processed using Prosys II[22] to generate an *apparent* (observed) ERT profile. Each *apparent* ERT profile was then inverted using RES2DINV (Loke, 1999) to produce an *absolute* (model) ERT profile across the LAs. In doing so, the root mean square error (RMSE) between the observed and model values was used to regulate the number of inversions. An accurate elevation profile was then taken along each resistivity line using a Hemisphere GPS S320 differential global positioning system (DGPS). Accurate coordinates and the height above mean sea level (in metres) were recorded at each electrode along the profile. This elevation data was then used to invert the ERT profiles once more, generating model ERT profiles across the LAs with the correct topography (e.g., Perrone et al., 2014). The resulting 2D ERT profiles became coloured cross-sections of the subsurface, depicting variations in electrical resistivity in ohm-meters (Ω.m). This allowed us to study the near-surface for changes in electrical resistivity as a function of *distance* along the resistivity profile and as a function of *elevation* above mean sea level (MSL).




**Figure 5.2**. Airborne thermal survey and electrical resistivity tomography (ERT) survey of border fields north of Glastonbury Tor. a). DJI M300 rotary drone in mid-air, immediately after take off from a border field north of Glastonbury Tor. Drone take off and land position (TOLP) is represented by the orange mat in the field and the background shows St Michael's Church Tower on top of Glastonbury Tor. Image inset shows the DJI M300 rotary drone with a DJI H20T thermal payload. b). A single 71 m long resistivity profile across a border field north of the Tor, comprising: resistivity cable; an IRIS Syscal Junior multichannel resistivity meter (grey box in foreground); stainless-steel electrodes at 1 m intervals.

## 5.3 Results

We present our remote sensing observations in three subsections. Our LiDAR elevation differencing in Section 5.3.1 reveals several linear elevation-change anomalies. We then inspect

[22] Prosys II is free utility software from IRIS Instruments. It is used for downloading, processing and analysing resistivity data from Syscal and Elrec instruments (IRIS Instruments, 2022).

these linear anomalies (LAs) as *average elevation-change profiles* to determine which LAs show anomalous elevation change. The LAs deemed anomalous are then reinspected with our multispectral image processing workflow at Appendix K. Here, vegetation indices Iron Oxide, SI7 and the SIPI are applied to a high-resolution multispectral satellite image, along with their Gmag equivalents. In the relevant fields, the LAs are then identified and accentuated using Sobel edge detection filters (Section 5.3.2). To close, Section 5.3.3 analyses the warming, cooling and heat retention properties of the same anomalous LAs using the thermal raster images from the airborne thermal survey.

### 5.3.1 LiDAR

The clipped elevation-change raster images in Figure 5.3 reveal varying amounts of uplift and subsidence across the nine border fields (F1-F9) north of Glastonbury Tor, ranging from 0.01 m/year uplift (dark red pixels) to -0.01 m/year subsidence (pure white pixels). In particular, the LiDAR elevation differencing revealed six LAs beneath the fields; three LAs in F1 (LA1 – LA3) and one LA in: F2 (LA4), F3 (LA5) and F9 (LA6).

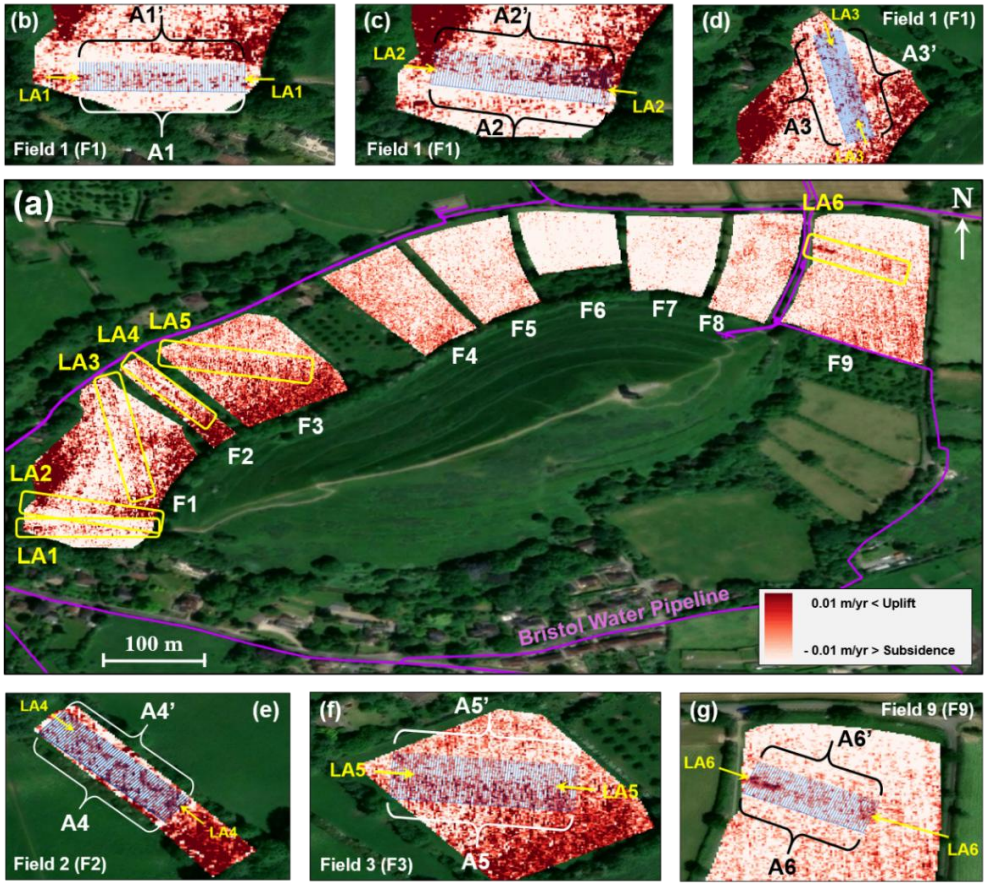



**Figure 5.3**. Results of light detection and ranging (LiDAR) elevation differencing in border fields north of Glastonbury Tor. a). Elevation-change rasters of the nine border fields, F1 to F9, used in this study. Dark red pixels denote 1 m x 1 m regions of uplift and pure white pixels denote 1 m x 1 m regions of subsidence. Linear elevation-change anomalies (LAs) are shown in yellow boxes and labelled LA1 to LA6. Purple lines are the Bristol Water pipeline around Glastonbury Tor. b). Linear anomaly 1 (LA1) in Field 1 (F1), shown by yellow arrows and superimposed with blue coloured elevation-change profiles at 1.3 m intervals. Beginning and end of each elevation-change profile collectively annotated as A1 and A1' respectively. c). Linear anomaly 2 (LA2) in F1. d). Linear anomaly 3 (LA3) in F1. e). Linear anomaly 4 (LA4) in Field 2 (F2). f). Linear anomaly 5 (LA5) in Field 3 (F3). g). Linear anomaly 6 (LA6) in Field 9 (F9).

Each of these linear elevation-change anomalies, at varying orientations, depict linear trends in *uplift* across one of the fields. These LAs can be seen within the yellow boxes in Figure 5.3a and they *do not* correspond to the water pipeline dataset from Bristol Water (purple lines in Figure 5.3a). Consequently, in ArcGIS Pro, a series of elevation-change profiles (GIS polylines) were positioned across the LAs at 1.3 m intervals, producing a grid of individual profile lines seen in *blue* in Figures 5.3b – 5.3g. The beginning and end of each profile were collectively annotated *A#* to *A#'* respectively, where *A* represents '*anomaly*' and # represents the LA '*number*'.

An average elevation-change profile across each LA was then calculated in MATLAB, producing six average elevation-change profiles in Figure 5.4. Tukey's IQR thresholds (Tukey, 1970) for each average elevation-change profile are displayed along each profile as dark blue lines, and mean elevation change[23] from 2015 to 2021 is shown in metres (Figures 5.4a – 5.4f). Of note, LA4 in Figure 5.4d reveals one outside observation which, according to Tukey's IQR method (Tukey, 1970), signifies anomalous elevation uplift. This outside observation is represented as a yellow-coloured outlier at 11 m along A4 – A4', where the mean uplift along LA4 from 2015 to 2021 is 0.031 m (0.5 cm/yr). Similarly, LA6 in Figure 5.4f reveals two *outside* elevation-change observations and one *detached* observation which again, signify anomalous elevation change (Tukey, 1970). The *outside* observations at 10 and 12 m along A6 - A6' are represented as yellow-coloured outliers and the *detached* observation at 11 m is a red outlier, where the mean uplift along LA6 from 2015 to 2021 is 0.025 m (0.4 cm/yr). These are the only two LAs that express *statistically anomalous* elevation change across their length. According to Tukey's IQR thresholds (1970), the mean elevation change across the remaining LAs (Figures 5.4a, 5.4b, 5.4c and 5.4e) show no credible elevation outliers, signifying these to be *natural* elevation changes. As a result, only LA4 and LA6 were selected for multispectral and thermal analyses, receiving green ticks in Figures 5.4d and 5.4f respectively.

### 5.3.2 Multispectral

Using a WorldView-2 multispectral image dated 21 June 2017, we generated the subsurface detection indices Iron Oxide, SI7 and SIPI. Using the GRADIENTWEIGHT function in MATLAB, we also calculated their Gmag equivalents, and then we clipped all six image indices to the extent of the field polygons for Field 2 (encompassing LA4) and Field 9 (encompassing LA6). As per the adapted, multispectral image processing workflow in Appendix K, we proceeded to detect LA4 and LA6 in select FCCs and edge detection raster images.

Both LAs were most prominent in the SIPI imagery, and even more so after smoothing and filtering with Sobel edge detection filters. Figure 5.5a shows Field 2 in situ in the month of November and Figure 5.5b shows LA4 after smoothing and filtering the SIPI with a Sobel vertical edge detection

[23] Elevation change is the change in ground height, in metres, above mean sea level (MSL). Elevation above MSL was officially recorded by the Newlyn Tidal Observatory (Ordnance Datum Newlyn – ODN) between 1915 and 1921 (Maritime Archaeology Trust, 2025).

filter. Figure 5.5c then shows the grass marking above LA4 in the month of May. Of note, Figure 5.5b reveals high SIPI values (in yellow) along the length of LA4 implying that, in extremely warm and dry weather conditions, the soil and cool-season grass above LA4 is considerably more stressed than the ground beside it.

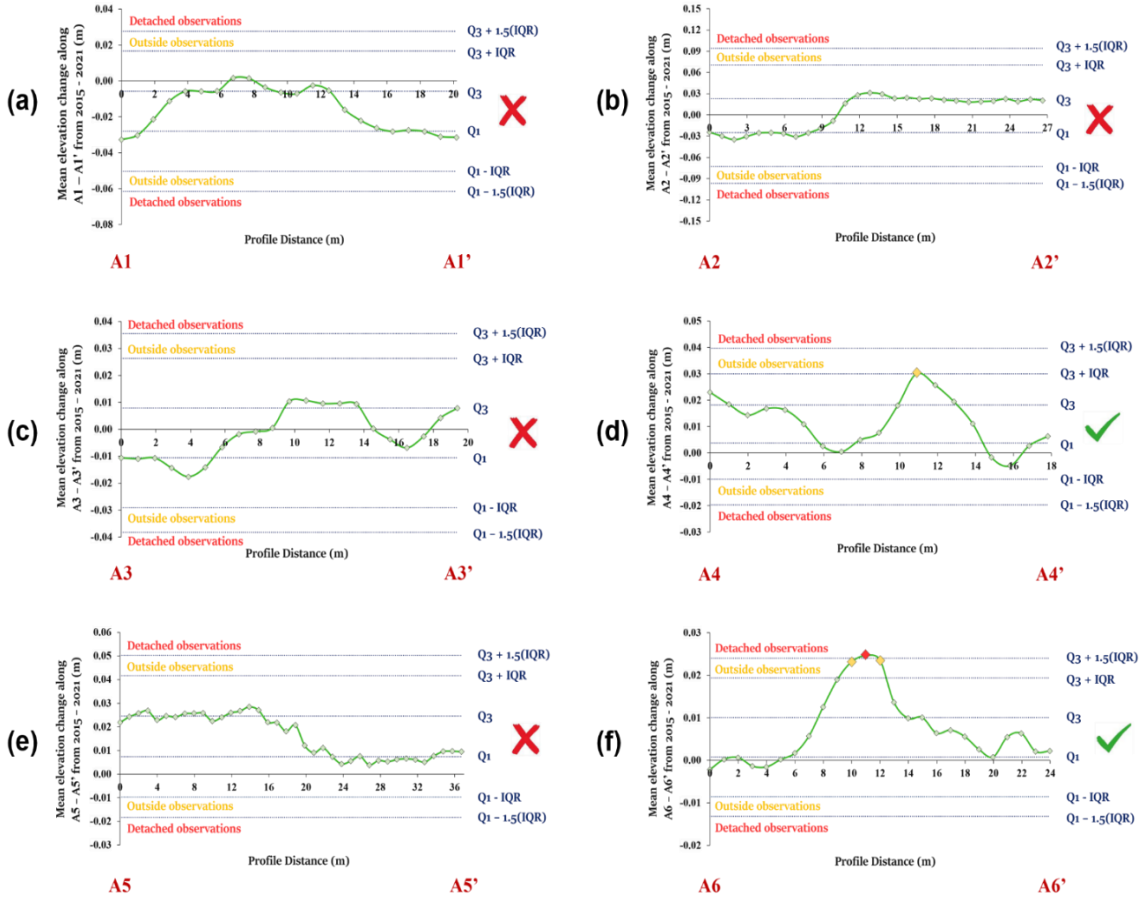



**Figure 5.4**. Average elevation-change profile (green line) across each linear anomaly (LA), showing elevation change from 2015 to 2021. Blue dotted lines along each profile are Tukey's upper and lower Interquartile Range (IQR) limits (Tukey, 1970), delineating anomalous elevation-change thresholds for outside observations (represented by amber data points) and detached observations (represented by red data points). Profile markers are annotated in red under each profile. Average elevation-change profiles showing anomalous elevation change receive green ticks and average elevation-change profiles showing no anomalous elevation change receive red crosses. a). Mean elevation change from A1 to A1' across linear anomaly 1 (LA1). b). Mean elevation change from A2 to A2' across linear anomaly 2 (LA2). c). Mean elevation change from A3 to A3' across linear anomaly 3 (LA3). d). Mean elevation change from A4 to A4' across linear anomaly 4 (LA4), showing anomalous uplift 11 m along profile. e). Mean elevation change from A5 to A5' across linear anomaly 5 (LA5). f). Mean elevation change from A6 to A6' across linear anomaly 6 (LA6), showing anomalous uplift 10 – 12 m along profile.

LA6 shows similar characteristics after the SIPI of Field 9 was filtered with a Sobel horizontal edge detection filter. In comparison to the photo of Field 9 in May 2023 (Figure 5.5d), the SIPI results in Figure 5.5e distinctly accentuate the stressed grass column above LA6 as a linear section of SIPI with slightly higher reflection values than its surroundings. This would again imply that, during significantly warm weather conditions, the soil and cool-season grass above LA6 is considerably

more stressed. We verified this observation in May 2025, where warm and dry weather conditions revealed a linear section of early-stage chlorosis[24] in the grass directly above LA6 (Figure 5.5f).

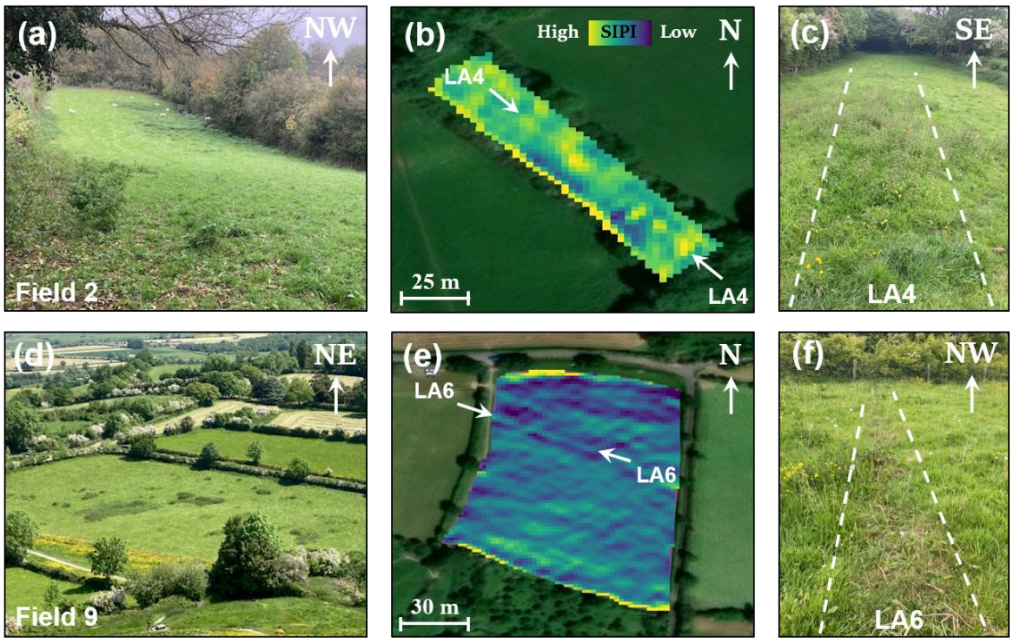



**Figure 5.5**. Photographs of anomalous linear elevation-change anomalies (LAs) in their respective fields north of Glastonbury Tor and high-resolution multispectral observations of the same LAs. a). Looking north-west along Field 2; a border field containing linear anomaly 4 (LA4) north-west of Glastonbury Tor. b). Stressed soil and vegetation above LA4 shown, in yellow, as a series of *high* structure insensitive pigment index (SIPI) values in Maxar's high-resolution multispectral satellite imaged dated 21 June 2017. Extent of SIPI anomaly annotated using white arrows. c). Looking south-east along LA4 in Field 2; photo taken in May 2025. d). Looking north-east across Field 9, a border field containing linear anomaly 6 (LA6) north-east of Glastonbury Tor. e). Stressed soil and vegetation above LA6 shown, in light blue, as a linear series of *high* SIPI values in Maxar's high-resolution multispectral satellite imaged dated 21 June 2017. Extent of SIPI anomaly annotated using white arrows. f). Looking north-west along LA6 in Field 9; photo taken in May 2025.

### 5.3.3 Thermal

The optical and thermal properties of the ground above LA4 and LA6 were examined using a DJI P1 RGB camera and a DJI H20T thermal sensor, mounted consecutively on a DJI M300 rotary drone. The airborne survey was conducted on 6 August 2025; a warm and dry day in Glastonbury, with maximum temperatures reaching 24°C (Weather Online, 2025). Figures 5.6a and 5.6e show the airborne RGB image of Field 2 and Field 9 respectively.

Despite the warm and dry weather conditions, and the very-high-resolution image acquisition (2 cm resolution), LA4 and LA6 are unnoticeable in the RGB imagery (Figures 5.6a and 5.6e). However, at 10 cm resolution, the daytime thermal image of Field 2 reveals a series of linear, parallel temperature highs (in yellow), extending northwest – southeast along the centre of the field (Figure 5.6b). Collectively, these linear anomalies constitute LA4. Albeit subtle, the daytime thermal image

[24] In botany, chlorosis is a condition in which grass and leaves produce insufficient chlorophyll due to: 1) nutrient deficiencies (especially iron, nitrogen, magnesium and manganese); 2) high soil pH - *making iron unavailable*; 3) poor soil drainage; 4) environmental stress - (Brown, 1961).

of Field 9 also shows a single line of higher ground temperature from east to west, coinciding with LA6 from Sections 5.3.1 and 5.3.2 (Figure 5.6f).

The thermal image of LA4 at dusk is less clear (Figure 5.6c), although the very dark coloured parallel lines in Field 2 suggest that the linear, parallel temperature highs in Figure 5.6b have cooled significantly. Conversely, LA6 is much more pronounced in the dusk image of Field 9, where the ground above the LA remains warmer than its cooler surroundings; denoted by the pink thermal anomaly in Figure 5.6g. The heat retention image of Field 2 in Figure 5.6d is the most distinct thermal image of LA4. Here, the same group of parallel striations and a semi-circular feature are prominent (depicted in bright yellow). These thermal anomalies have been accentuated by the low heat retention properties of the ground above the striations. This indicates that the ground above the striations in LA4 warm quickly and cool quickly. In contrast, the heat retention image of LA6 in Field 9 (Figure 5.6h) is ambiguous. The ground above this LA is much more effective at retaining heat, so we suspect the ground here takes longer to warm and longer to cool. As a result, the temperature change of the ground surface above LA6 between day and dusk is comparatively slight, and consequently less exaggerated in the heat retention image (Figure 5.6h).

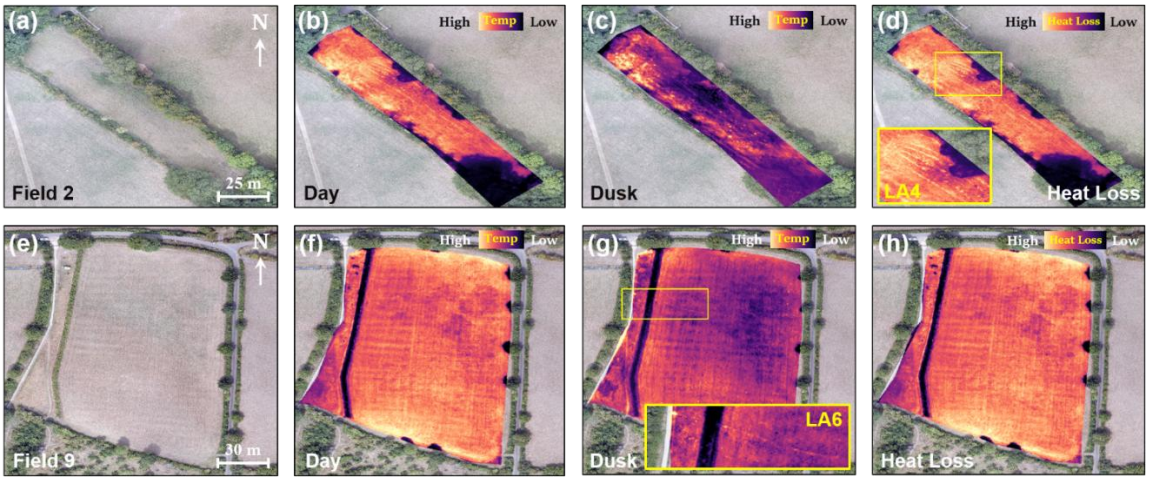



**Figure 5.6**. Red-Green-Blue (RGB) and thermal imagery of linear anomaly 4 (LA4) in Field 2 and linear anomaly 6 (LA6) in Field 9; taken with a DJI M300 rotary drone. a). RGB image of Field 2 at two-centimetre resolution. b). Daytime thermal image of LA4 in Field 2, when solar warming of ground is prevalent. c). Thermal image of LA4 in Field 2 at dusk, when ground cooling is prevalent. d). Heat retention image of LA4 in Field 2; high heat loss shown in yellow and low heat loss shown in black. Image inset of LA4 shows high heat-loss striations and a semi-circular thermal anomaly. e). RGB image of Field 9 at two-centimetre resolution. f). Daytime thermal image of LA6 in Field 9 (ground warming). g). Thermal image of LA6 in Field 9 at dusk (ground cooling). Image inset of LA6 shows marginally warmer temperatures along complete length of anomaly. h). Heat retention image of LA6 in Field 9; high heat loss shown in yellow and low heat loss shown in black.

## 5.4 Interpretation

In order to verify our remotely sensed observations, Section 5.4.1 presents a 2D ERT profile across LA4, with a normalised and centred: 1) average elevation-change profile; 2) average Iron Oxide, SI7 and SIPI reflection profile; 3). average relative heat loss profile. We combine this information to interpret LA4 and then in Section 5.4.2, we repeat the process for LA6. For reference, complete 2D ERT profiles for LA4 and LA6 (in bold colour) are found at Appendix M.

### 5.4.1 Linear Anomaly 4 (LA4)

In Section 5.3.1, we see credible uplift across LA4. If this uplift is constant and steady, our results suggest the ground above LA4 is rising by 0.5 cm every year. However, we cannot determine whether this uplift is constant *or* steady. Instead, seasonal or climatic variations may explain the swelling of the ground along LA4.

In warm and dry conditions, the high SIPI values along the length of LA4 suggest the overlying soil and vegetation is stressed. Therefore, the ground above LA4 appears vulnerable to high temperatures and low precipitation, suggesting there could be an *excessive* drainage regime along its length.

In our heat retention study (Section 5.3.3), we observe several anomalous thermal striations along the length of LA4 (Figures 5.6b, 5.6c and 5.6d). The ground along these striations is seen to heat and cool quickly, implying the ground above LA4 has a lower specific heat capacity than its surroundings. Compared to the surrounding ground matrix, these observations may indicate a groundwater deficit along the striations; noting groundwater would increase the specific heat capacity of a soil column (Ren et al., 2003).

To assist our interpretation of LA4, we inspect the relevant section of a 2D ERT profile across LA4. To achieve this, a 71 m long resistivity profile, X-X', was positioned perpendicular-to and across the centre of LA4, as per the layout in Figure M1a. A Wenner-Schlumberger resistivity array with 1-m-electrode spacings was used to produce an apparent resistivity profile. After recording the ground elevation at each electrode, we inverted the apparent resistivity profile in an iterative process to produce the model ERT profile in Figure M2a. Four iterations were used in this inversion process, generating a reliable, model ERT profile with a low RMSE of 0.73.

Figure 5.7 aligns the relevant section of 2D ERT profile X–X' from Figures M1a and M2a with the normalised and centred average elevation-change profile along A4 – A4' (from Figure 5.4d). We also include normalised and centred average Iron Oxide index, SI7 and SIPI profiles along A4 – A4', and an average relative heat loss profile. The former is calculated from the vegetation indexed imagery of our multispectral image dated 21 June 2017 and the individual profile lines used in our average elevation-change profiles (seen in blue in Figure 5.3e). The latter is calculated from the heat loss raster image of Field 2 in Figure 5.6d and the individual profile lines from our average elevation-change profiles in Figure 5.3e.

Interestingly, the clear elevation uplift 11 m along A4 – A4' (from LA4) coincides with a comparable increase in Iron Oxide index, SI7 and SIPI (Figure 5.7). This would suggest that the ground above LA4, when stressed from warm and dry weather, produces greater concentrations of iron oxide and ground salt. Also, between 13 and 18 m, small peaks of relatively high heat loss are observed from the thermal striations in Figure 5.6d. These thermal anomalies could be more pronounced, but

instead they are masked by regions of low heat loss from the cool air and shaded ground by the nearby hedgerow.

The anomalous remote sensing observations between 10 and 14 m coincide with a distinct change in electrical resistivity within the first 0.5 m of the subsurface. Here, resistivity is approximately 40 – 45 Ω.m (dark green and light green ERT anomalies in Figures 5.7 and M2a) and approximately 10 Ω.m higher than the near-surface ground matrix beside LA4. Also, below this high resistivity anomaly (c.0.5 – 1 m depth) sits a significant wedge of comparably lower resistivity material, which is closer to 30 Ω.m (light blue ERT wedge in Figures 5.7 and M2a).

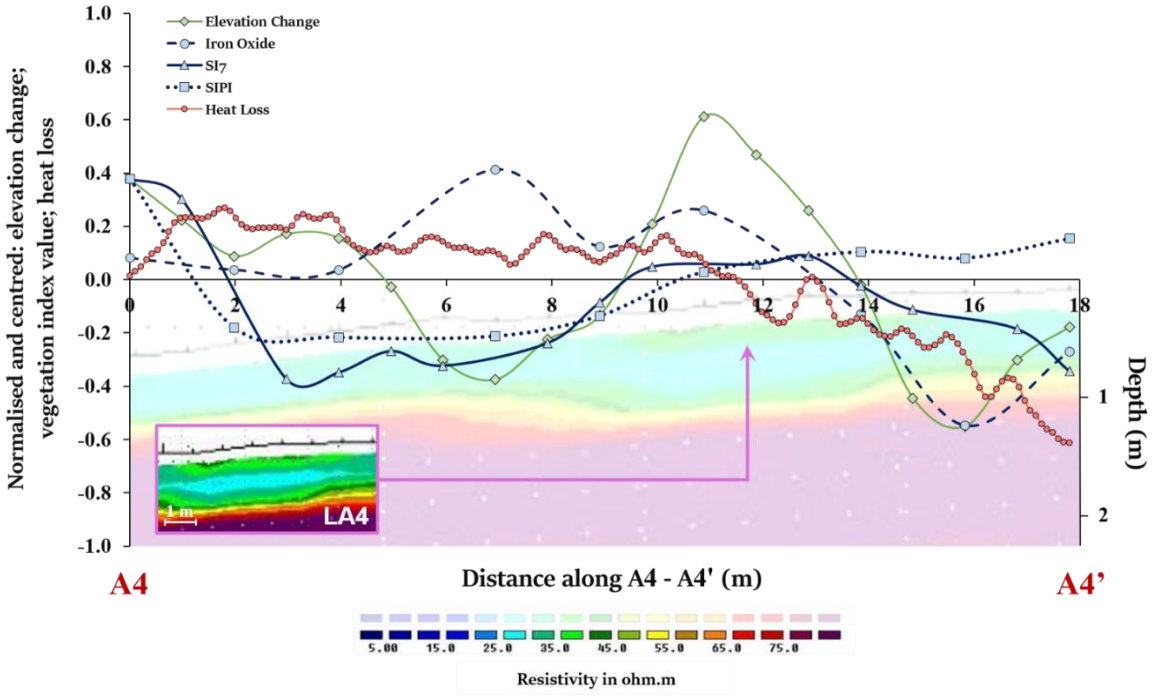



**Figure 5.7**. Averaged and normalised elevation-change profile across linear anomaly 4 (LA4) using collective profile markers A4 - A4' from Figure 5.3e. Averaged and normalised Iron Oxide index, Soil Salinity Index 7 (SI7) and Structure Insensitive Pigment Index (SIPI) reflection values from Maxar multispectral imaged dated 21 June 2017 are also shown, along with an averaged and normalised relative heat loss profile from the airborne thermal survey. All remotely sensed profiles are aligned with the relevant section of a 2D electrical resistivity tomography (ERT) profile across LA4. The full ERT profile X-X' (a single resistivity profile) in bold colour, and its location, can be found in Appendix M (Figures M1a and M2a). Image inset shows resistivity anomaly beneath LA4 between 10 and 14 m along A4 - A4'; resistivity values relate to colour bar under profile in ohm.metres (Ω.m).

By combining all of these observations, we infer that LA4 is a series of shallow, hydrological anomalies, where groundwater is carried away from the Tor. Collectively, we describe this LA as a shallow, underground spring that is no deeper than 1.5 m below the surface. This would explain the *overactive* drainage regime and the comparably dry ground striations during regions of warm weather and low precipitation. This would also account for the higher concentrations of ground salt and the lower specific heat capacity along the LA (Ren et al., 2003). We also believe the ground uplift identified in our LiDAR elevation differencing to fluctuate over time, depending on the activity and water pressure from the underground spring and the softening and expansion of the surrounding ground matrix (Gaber et al., 2020).

### 5.4.2 Linear Anomaly 6 (LA6)

Similar to LA4, we also see very clear uplift above LA6. If constant and steady, the LiDAR elevation differencing indicates the ground is rising by 0.4 cm every year. However, like LA4 in Field 2, we cannot categorically determine whether this uplift is constant, steady, seasonal or climatic.

In warm and dry weather conditions, the higher SIPI values along LA6 indicate the presence of stressed soil and stressed grass. This was evident when we visited the site in May 2025, where chlorosis was seen along a column of cool-season grass above LA6. This would suggest that the ground above LA6 is vulnerable to overheating in warm weather, an effect often exacerbated by shallow, solid objects in the near-surface (Douaoui et al., 2006; Onwuka, 2016).

In our heat retention study (Section 5.3.3), LA6 is most apparent in the dusk image (Figure 5.6g), where the ground above the anomaly is warmer than its surroundings. In concert with its vague representation in the daytime thermal image, the ground above LA6 warms slowly and cools slowly. This indicates that LA6, and certainly the ground above, has a higher specific heat capacity than the thermal striations in LA4.

To further interpret LA6, we inspect the relevant section of a 2D ERT profile which we position across the centre of the anomaly. Subsequently, a 71 m long resistivity profile, Y-Y', was positioned across LA6 as per the layout in Figure M1b. A Wenner-Schlumberger resistivity array with 1-m-electrode spacings was again used to produce an apparent resistivity profile which we then invert to produce the model ERT profile in Figure M2b. Four iterations were used in the inversion process, resulting in a reliable model ERT profile with an RMSE of 0.78.

Figure 5.8 aligns the relevant section of 2D ERT profile Y–Y' from Figures M1b and M2b with the normalised and centred average elevation-change profile along A6 – A6' (from Figure 5.4f). Imitating our steps in Section 5.4.1, we also include the normalised and centred average Iron Oxide index, SI7 and SIPI profiles and a normalised and centred average relative heat loss profile.

The elevation uplift 10 - 12 m along A6 – A6' coincides with a very clear rise in Iron Oxide index, SI7 and SIPI (Figure 5.8). Therefore, when stressed from warm and dry weather, the ground above LA6 produces greater concentrations of iron oxide and ground salt. Also, in Figure 5.8, the relative heat loss profile (in red) reveals a small peak above LA6, suggesting slightly lower rates of heat loss either side of the anomaly (Figure 5.8).

The remotely sensed ground anomalies halfway along A6 – A6' coincide with a distinct change in electrical resistivity at LA6, which we observe in the first metre of the subsurface. This is seen as a 75 Ω.m resistivity anomaly that is semi-circular in shape and approximately 1 m wide (crimson red ERT anomaly in Figures 5.8 and M2b). In contrast to its surroundings, this resistivity anomaly is also c.35 Ω.m higher than the soil columns either side of it.

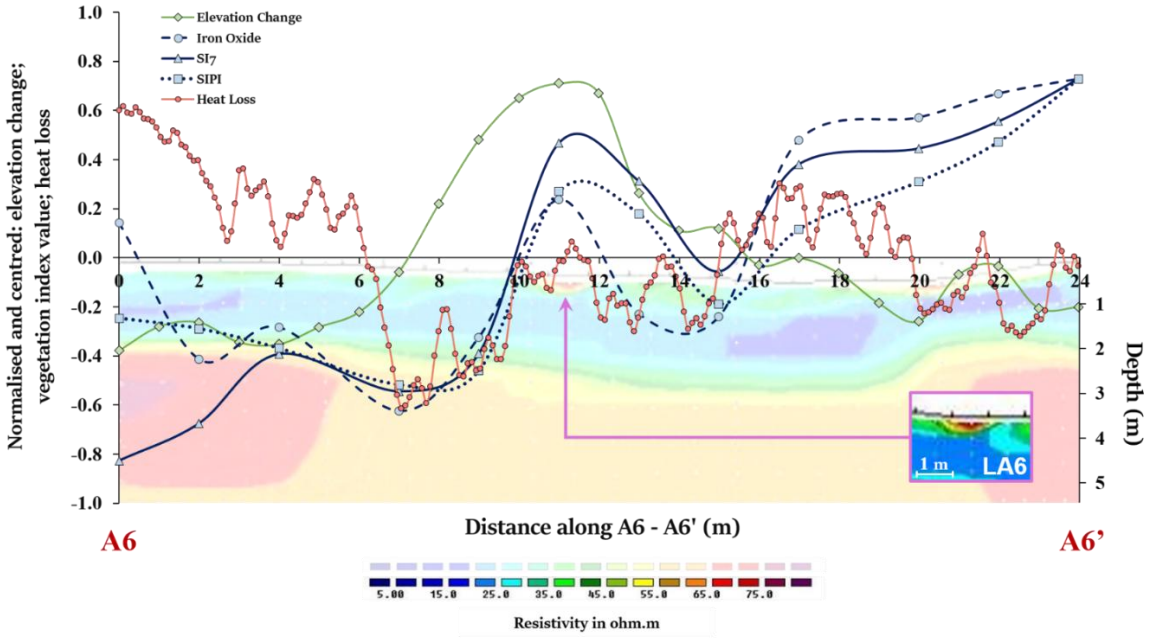



**Figure 5.8**. Averaged and normalised elevation-change profile across linear anomaly 6 (LA6) using collective profile markers A6 - A6' from Figure 5.3g. Averaged and normalised Iron Oxide index, Soil Salinity Index 7 (SI7) and Structure Insensitive Pigment Index (SIPI) reflection values from Maxar multispectral imaged dated 21 June 2017 are also shown, along with an averaged and normalised relative heat loss profile from the airborne thermal survey. All remotely sensed profiles are aligned with the relevant section of a 2D electrical resistivity tomography (ERT) profile across LA6. The full ERT profile Y-Y' (a single resistivity profile) in bold colour, and its location, can be found in Appendix M (Figures M1b and M2b). Image inset shows resistivity anomaly beneath LA6 between 10 and 12 m along A6 - A6'; resistivity values relate to colour bar under profile in ohm.metres (Ω.m).

Given the very clear observations across LA6 in Figure 5.8, we believe LA6 is a utility pipe that extends east to west beneath Field 9. We cannot be entirely sure of the material or its purpose, but the resistivity values in the 2D ERT profile (Figures 5.8 and M2b) would suggest it is a clay or concrete water *or* drainage pipe (Supandi, 2021; Vickery and Hobbs, 2002). Clay and concrete are poor heat conductors; absorbing heat slowly and releasing it gradually (Xu et al., 2019). Therefore, because the pipe is shallow, these thermal characteristics are likely to influence the warming and cooling properties of the soil in the near-surface. Moreover, in considerably warm and dry weather, the utility pipe is expected to overheat the ground above, affecting iron and salt concentrations and ultimately, the condition of overlying vegetation (Douaoui et al., 2006). Gradual uplift along the length of shallow pipes is also not uncommon, especially when they are buried in clay rich soils from the Martock and Pennard series (Avery, 1955). In these settings, clay soils can swell, often creating a *flotation force* beneath the pipe that exceeds the weight of overlying soil (Sinclair and Andrews, 1984).

## 5.5 Discussion

Our LiDAR elevation differencing was a quick and effective way to identify high-resolution linear elevation anomalies across reasonably flat, grass covered fields (Figure 5.3). To increase the likelihood of detecting shallow, subsurface features with this technique, we recommend the DTMs are: 1) high or very high resolution (VHR); 2) at least five years apart in acquisition date; 3) snapped

together prior to DTM subtraction. When doing so, uncertainty levels should also be monitored, especially when using low resolution DTMs. In this study, the UK Environment Agency DTMs are 1 m resolution and elevations heights are +/- 0.1 m on soft detail like the fields north of Glastonbury Tor (UK Environment Agency, 2025b). Therefore, elevation-change values in the differenced DTM become +/- 0.2 m (Lonseth, 1947), which is relatively significant when dealing with uplift and subsidence rates less than 0.5 cm/year. However, detecting a *linear* elevation-change anomaly in 2D will reduce this pixel-level uncertainty.

To determine which LAs are statistically significant (i.e., LAs with abnormal elevation change), we recommend calculating, stacking and averaging across several elevation-change profiles along the length of a LA. The averaged profile is then inspected for statistical outliers with a technique that is simple and clear to represent graphically, like Tukey's IQR method (Tukey, 1970). However, future work could explore alternatives like Z-scores (e.g., Senthamarai Kannan et al., 2015). Moving forward, this 'anomaly validation' technique could become an automated tool in GIS software and web service applications for professional disciplines like archaeological prospecting, environmental risk mitigation and defence and security intelligence assessments.

When using the multispectral image processing workflow (Appendix K), the SIPI was the most effective at revealing reflection anomalies along LA4 and LA6 (Figure 5.5). This is to be expected, because we used a multispectral satellite image from a considerably warm and dry day in Glastonbury, where a maximum temperature of 32°C was recorded (Weather Online, 2025). During extremely warm and dry weather, the SIPI becomes much more responsive to subsurface heterogeneity, where it exploits reflection sensitivities in the NIR and the Red/Blue reflectance ratio to delineate regions of vegetation stress over subsurface features (Morley et al., 2025b; Chapter 3). However, when compared to our airborne techniques, its spatial resolution is nondescript. Therefore, where possible, the multispectral detection of buried anthropogenic features like tunnels, pipes and drains should be done at VHR; an ambition which is becoming far easier to accomplish with more affordable rotary drones and VHR payloads (e.g., Abate et al., 2021; Ronchi et al., 2020).

At VHR, the airborne thermal survey using a DJI M300 rotary drone successfully detected linear, thermal anomalies from subsurface features. The *daytime* and *heat loss* images of Field 2 distinctly reveal a series of anomalous, thermal striations along the length of LA4 (Figures 5.6b and 5.6d), which we suspect to be the surface expressions of a shallow, underground spring extending radially from the Tor. Similarly, the dusk image of Field 9 revealed the orientation of a buried utility pipe trending east-west (Figure 5.6g). However, we acknowledge the timing of an airborne thermal survey is critical. If there is a need for 'warming' *and* 'cooling' imagery in subsurface detection, the acquisition window for *both* must contain considerable variation in ground temperature. If the warming window is "too hot" or the cooling window is "too cold", the likelihood of using ground surface temperatures to reveal *heat retention* and *heat loss* anomalies from subsurface features is considerably reduced.

The anomalous ground signatures from the underground spring (LA4) in Field 2 (Figure 5.7) align with the dowsing results in Stray (2018) which, although a controversial technique (e.g., More, 2014), signify an underground spring beneath this field (Figure 5.1d). This spring extends directly to the site of the 2016 Lypyatt Lane excavation which, according to Stray (2018), is likely to be the site of a medieval "well house" – *aligning with our detection of an underground spring*. Yet disagreeing with previously acquired data, the utility pipe (LA6) in Field 9 (Figure 5.8) is separate to the Bristol Water pipeline in Figure 5.3, suggesting it is owned and managed by a different service provider or, it is a pipe that has never been *or* no longer registered with Bristol Water.

Nonetheless, we do not interpret either of these LAs to be a tunnel, even though the presence of tunnels extending beneath these fields and towards the Tor have been postulated (e.g., Bond, 1924, 1918; Mantle, 1911; Stray, 2018; Wakefield, 1814). Our ERT results along resistivity profiles X-X' and Y-Y' in Appendix M also support this conclusion; there are no electrical resistivity anomalies characteristic in size, shape or resistivity of an air-filled or partially collapsed tunnel along either profile. Moreover, our remote sensing observations reveal *no* northeast-southwest trending elevation, vegetation or thermal anomalies across Field 2, thereby challenging the dowsed tunnel results in Figure 5.1d (Stray, 2018).

To clarify this, a third 2D ERT profile was conducted along the centre line of Field 2. This resistivity profile, Z-Z', was parallel to LA4 and therefore perpendicular to a prospective tunnel or drain extending across the field from the dowsed results in Stray (2018). As before, a 71 m long resistivity profile, Z-Z', was positioned along the centre line of Field 2 as per the RGB image inset in Figure 5.9a. A Wenner-Schlumberger resistivity array with 1 m electrode spacings was again used to produce the model ERT profile in Figure 5.9a. Consequently, between 42 – 43 m along Z-Z' (and no more than 2 m deep), a 2 m high and 1 m wide resistivity 'high' was seen protruding from a significantly high resistivity wedge. As seen in Figure 5.9a, this resistivity anomaly is the *typical* shape and size of a tunnel or drain, and it has the typical resistivity (c.70 – 75 Ω.m) of a partially filled or partially collapsed man-made structure (Ducut et al., 2022; Park et al., 2014).

Figure 5.9b shows the dowsing results for Field 2 and the location of the suspected "well house" from the 2016 Lypyatt Lane excavation (Stray, 2018). Figure 5.9c then shows the location of the tunnel shaped resistivity anomaly (purple circles) along the 2D ERT profile Z-Z'. Of note, the resistivity anomaly along Z-Z' is approximately 20 m from the dowsed tunnel anomaly in Stray (2018), although according to Stray (2025), this sits within the positional error of the dowsing traces.

The blue-lined rectangle in Figure 5.9c delineates a 12 m x 8 m ground penetrating radar (GPR) grid which encompasses resistivity profile Z-Z' and the tunnel/drain shaped resistivity anomaly in Figure 5.9a. Using an IDS GeoRadar Chaser XR GPR, a rectangular shaped structural anomaly was then found 5.1 m beneath Field 2, coinciding laterally with the tunnel-like resistivity anomaly along Z-Z' (Figure 5.9d). Along with the high heat loss striations and the semi-circular feature c.20

m northwest of this resistivity anomaly, we expect the near-surface of this field to be more complex than other fields. Geological processes *could* account for these observations, but given the: 1) peculiar shape, size and location of the resistivity anomaly along Z-Z'; 2) the location of the dowsed tunnel in Stray (2018); 3) the location of the buried "well house" discovered in 2016 (Stray, 2018), further high-resolution, geophysical survey of Field 2 is required to explain Field 2's below ground complexity.

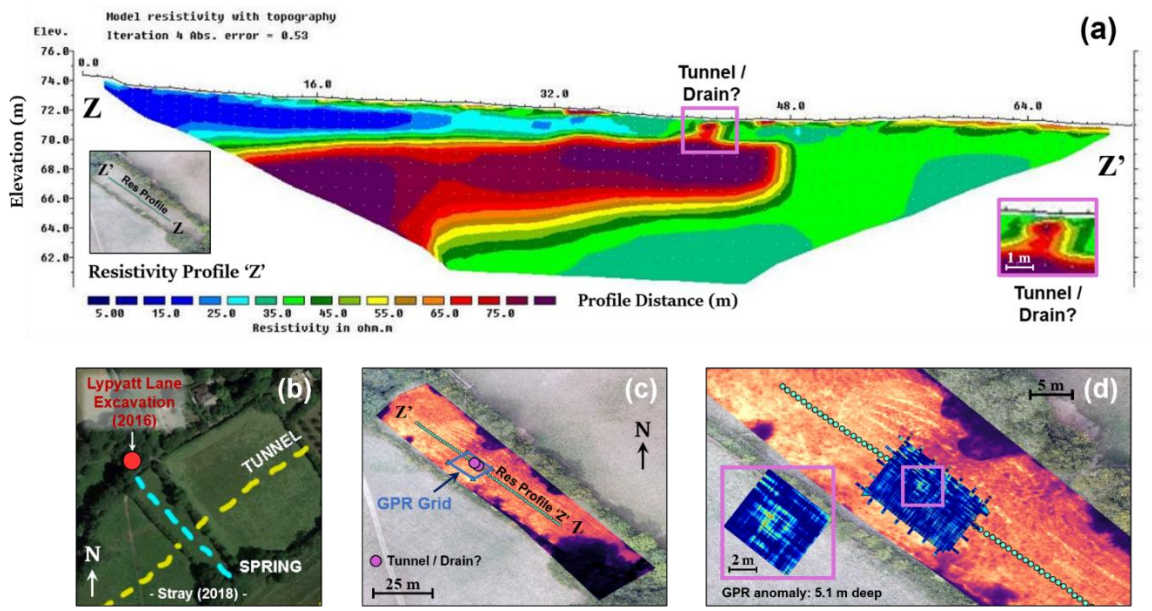



**Figure 5.9**. A near-surface inspection along Field 2 using electrical resistivity tomography (ERT) and ground penetrating radar (GPR). a). A 2D ERT profile, Z-Z', along Field 2; parallel to LA4 and radial from the Tor. Profile distance and profile elevation above mean sea level (MSL) are as shown and resistivity values relate to colour bar under profile in ohm.metres (Ω.m). From left to right, inset images show: orientation of ERT profile Z-Z' in Field 2; a tunnel or drain-like resistivity anomaly at 42 – 43 m along Z–Z'. b). Location of: the Lypyatt Lane "well house" excavation; a dowsed tunnel (yellow dashed line); a dowsed underground spring in Field 2 (blue dashed line). Figure 5.9b adapted from Stray (2018). c). Location of the tunnel-like anomaly (purple circles) along ERT profile Z-Z' and position of 12 m x 8 m GPR grid (blue rectangle). d). Results from GPR survey over the tunnel-like resistivity anomaly in Figure 5.9a. Image inset shows rectangular shaped GPR anomaly 5.1 m deep; coinciding laterally with the location of the tunnel-like resistivity anomaly along Z-Z'.

Without conducting further high-resolution near-surface geophysics in Field 2, a confident understanding of the subsurface remains uncertain. A follow-up investigation with additional ERT, GPR and electromagnetism (EM) is recommended to verify the detection, description and purpose of our remotely sensed observations and the tunnel-like resistivity anomaly along Z-Z'. Also, filtering and thresholding remotely sensed datasets *by pixel value* could be explored. Here, the prospect of accentuating subtle elevation, reflection and thermal anomalies (which are otherwise masked by regions of low and high pixel values) could reveal new LAs in different locations and at different orientations.

We also see great potential in imaging beneath the grounds of Glastonbury Abbey *and* within the interior of Glastonbury Tor and Chalice Hill. To augment the observations and deductions from Gilchrist and Green (2015), the remote sensing techniques and ground verification procedures used in this study should be considered for the grass covered sections of Glastonbury Abbey. However,

for the latter, Synthetic Aperture Radar (SAR) Tomography used by Biondi (2022) and Biondi and Malanga (2022) could be used to assess the technique's imaging capabilities on semi-rigid structures like grass covered hills and tors - where SAR returns are typically less coherent (e.g., Morley et al., 2025a; Chapter 2). These results could then be compared with an ambient noise tomography study of each structure (e.g., Paustian, 2021; Torrese, 2025; Wang et al., 2023) which, given the location, is expected to work well during the Glastonbury Festival and peak tourism - when ambient noise is high.

## 5.6 Concluding remarks

This study uses high-resolution LiDAR elevation differencing, multispectral analyses and very-high-resolution (VHR) thermal imagery to detect linear, subsurface features beneath the border fields north of Glastonbury Tor. To date, no records of archaeological investigation exist for these fields, contrasting considerably with the research and archaeological excavations on Glastonbury Tor (e.g., Rahtz, 1970).

These border fields are situated between the Tor, Chalice Hill and Glastonbury Abbey, becoming favourable sites for legacy tunnels, drains and pipes between the Tor, the town and the abbey. Water supply from the Tor is the most obvious need for such structures, although alternative hypotheses imply that tunnels were needed by the monks in Glastonbury Abbey for safeguarding wealth and evading persecution (Bond, 1918; Mantle, 1911; Stray, 2018; Wakefield, 1814).

Our LiDAR elevation differencing reveals six linear anomalies (Figure 5.3), with two showing statistically anomalous elevation change over a six-year period (Figures 5.4d and 5.4f). We inspect the soil and cool-season grass above these two linear anomalies (LAs) with a high-resolution multispectral satellite image and vegetation indices Iron Oxide, Soil Salinity Index 7 (SI7) and the Structure Insensitive Pigment Index (SIPI). In doing so, the same two LAs show high levels of iron oxide, soil salinity and vegetation stress in warm and dry weather (Figure 5.5). Using VHR thermal imaging, one of these LAs is a series of parallel, thermal striations with poor heat retention and the other is a single, linear feature with reasonably high heat retention (Figure 5.6).

To interpret these two anomalous LAs, we relate our remotely sensed observations to a 2D electrical resistivity tomography (ERT) profile across each anomaly. When augmented with average elevation change, vegetation index and heat loss profiles (Figures 5.7 and 5.8), the resistivity anomalies infer one LA is a shallow, underground spring and the other is a buried utility pipe. However, a third 2D ERT profile extending radially from the Tor in the field closest to the 2016 Lypyatt Lane "well house" excavation (Stray, 2018) reveals an anomaly with the typical size, shape, depth and resistivity of a tunnel or drain (Figure 5.9). This anomaly aligns with a deeper ground penetrating radar (GPR) anomaly (Figure 5.9d) and a dowsed tunnel observation in Stray (2018), signifying the *possibility* of a tunnel-like feature beneath the border fields north of Glastonbury Tor.

If this is so, our remotely sensed observations were unsuccessful at accentuating anomalous ground behaviour above the tunnel-shaped anomaly. This signposts a need for systematically filtering and thresholding remotely sensed datasets by pixel value, whereby subtle linear anomalies in elevation change, multispectral reflection and heat retention may eventually reveal themselves. A follow-up investigation of this anomaly is recommended, where further high-resolution and VHR remote sensing should be integrated with additional ERT, GPR and electromagnetism (EM).

More broadly, the opportunity to remotely image *beneath* Glastonbury Abbey and *inside* Glastonbury Tor *and* Chalice Hill should be embraced. Imaging beneath Glastonbury Abbey warrants a similar approach to this study, but imaging inside Glastonbury Tor and Chalice Hill require a deeper imaging technique. Here, Synthetic Aperture Radar (SAR) Tomography (e.g., Biondi, 2022; Zhao et al., 2025) supplemented with Ambient Noise Tomography (e.g., Torrese, 2025; Wang et al., 2023) show potential. For clear results and a renewed understanding of each structure, we advise applying these techniques during high levels of ambient noise; Glastonbury Festival and peak tourist season are obvious choices.

# 6

# Conclusions

In this thesis, I explore the merits and limitations of using high-resolution and very-high-resolution (VHR) remote sensing datasets to detect subsurface anomalies from air and space. Using high-resolution multispectral imaging sensors, high-resolution and VHR light detection and ranging (LiDAR) sensors and a VHR thermal imaging sensor, I devise a series of algorithms, workflows and recommendations to detect unique ground signatures from several near-surface structures. These include an Iron Age fogou, a medieval tunnel, a legacy drainage system, different utility pipes, a suspected underground spring and several buried garden features. Underpinning these algorithms, workflows and recommendations, are various multispectral image processing techniques, LiDAR hillshade analyses, LiDAR elevation differencing, heat retention assessments, graphical analyses and statistical observations.

Initially, I review the detection of shallow subsurface anomalies with airborne and spaceborne remote sensing. I then, as a proof of concept, recalibrate and redefine the subsurface detection efficiency of 37 broadband vegetation indices (VIs) in temperate, vegetated terrain using geophysical observations. The three most responsive VIs become the building blocks of a multispectral image processing workflow which, when layer stacked with their gradient magnitude equivalents, become optimised and primed for the detection of anomalous reflectance behaviour from cool-season vegetation over shallow, subsurface features in temperate environments. When the workflow is applied to other temperate, vegetated sites, anomalous ground behaviour is accentuated to reveal the location of various drainage systems, a medieval tunnel and several structural features from a seventeenth-century monastic garden. When the reflection behaviour of the VIs are inspected as distance profiles and when the multispectral workflow is combined with LiDAR hillshade analyses, the remote detection of near-surface structures becomes even more pronounced. A multi-sensor approach is then explored, where the location of several linear subsurface anomalies are exposed with LiDAR elevation differencing. Those with statistically abnormal ground behaviour are inspected more closely with the same high-resolution, multispectral

image processing workflow and a VHR airborne heat retention survey, revealing the inferred location of an underground spring and a utility pipe.

In support of the review, the application of c.70 airborne and spaceborne subsurface detection techniques were evaluated, and multiple research trends were identified. These research trends were observed as functions of sensor type, research motive and the subsurface anomaly characteristic being pursued (Morley et al., 2025a; Chapter 2). This analysis was used to frame several research objectives for this thesis (and future study), based on a premise of recognising and critically evaluating the work that has already been done, the work that has not been done and more importantly, the work that could be done. The review also emphasised the importance of verifying remotely sensed observations of the subsurface with ground reconnaissance, field spectroscopy, geophysical survey and multi-sensor workflows (Morley et al., 2025a; Chapter 2).

In support of remote subsurface detection, the most suitable broadband, multispectral vegetation indices (VIs) were reprioritised using geophysical field observations. Using 1D and 2D correlations, the VIs were statistically selected and numerically validated with gravity and GPR data across an Iron Age fogou; a stone-walled underground passage in the ancient settlement of Carn Euny in Cornwall, UK (Morley et al., 2025b; Chapter 3). High-resolution spectral analyses were performed as a function of distance and area above the Iron Age fogou, along with a study of the rate of change (gradient magnitude) in VI. The most responsive VIs were the Iron Oxide index (IO), Soil Salinity Index 7 (SI7) and the Structure Insensitive Pigment Index (SIPI); all numerically described as algebraic manifestations of the Red/Blue reflectance ratio. These three VIs and their gradient magnitude (Gmag) equivalents were subsequently recommended for use in future, temperate and vegetated, subsurface detection studies (Morley et al., 2025b; Chapter 3). By definition, these VIs accentuate abnormal levels of iron oxide, ground salt and chlorophyll in and on the overlying ground, thereby defining the location and orientation of possible near-surface features from irregular drainage rates, ground temperature changes and chemical weathering.

Remote sensing datasets with high spatial resolution can also liberate the utility of graphical analysis in support of remote subsurface detection. This is particularly useful for inspecting ground behaviour along linear sections of an image, including: field boundaries, box isolations of existing buildings and grid sections across a study site. In turn, the results from these graphical techniques can be used to prioritise pedestrian survey programmes, geophysical fieldwork and field spectroscopy schedules.

When Tukey's IQR thresholds (Tukey, 1970) were applied to average Iron Oxide, SI7 and SIPI reflection profiles along a medieval boundary wall in Normandy's Aunay Abbey, anomalous ground behaviour was seen to reoccur at specific distances throughout the calendar year. Ground reconnaissance at these specific distances revealed the location of an entrance to a stone-walled tunnel. This tunnel extends beneath the shared boundary wall, accounting for the abnormally high

reflection levels of iron oxide, ground salt and vegetation stress in the Iron Oxide index, SI7 and SIPI reflection profiles.

High spatial resolution imaging can also increase the likelihood of detecting many other types of underground, anthropogenic structure, like the buried garden features of a seventeenth-century garden in Chapter 4. In this study, the advantage of using several multispectral images from different sensor types *and* different times of year were demonstrated. This broadens the detection range, allowing different sensor capabilities, drainage regimes, soil condition and vegetation behaviour to reveal individual and repeated sections of abnormal ground behaviour from subsurface features in different scenes. The weather conditions prior to remote image acquisition are also important. In this research, the most effective weather settings are those which *differentiate* ground condition, thereby emphasising local variations in drainage, ground temperature and underground weathering across a study area (e.g., after excessive rainfall, hot and dry weather settings and drought).

A high resolution or VHR multi-sensor detection regime can increase the likelihood of remotely detecting a near-surface feature. Different sensor types typically observe different ground characteristics. For example, regular shaped micro-relief anomalies are often difficult to recognise in situ, but an aerial assessment of a LiDAR derived digital elevation model (DEM) will often provide the broad and balanced perspective needed to identify topographic anomalies and geometric arrangements that are unnatural. In this research, combining LiDAR derived micro-relief anomalies with VI reflection anomalies both augmented and substantiated the shape and form of several structural features from a now dilapidated and ensconced seventeenth-century garden. Similarly, LiDAR elevation differencing in the border fields north of Glastonbury Tor revealed several linear elevation-change anomalies that were substantiated with: linear reflection anomalies in a high-resolution multispectral image and linear heat-retention anomalies in a VHR thermal image. Average elevation change profiles with statistical thresholds were also generated across each linear anomaly (LA) around the Tor to determine statistically and graphically, which linear elevation-change anomalies had experienced abnormal height change in six years. This 1D graphical solution to a 2D pixel-contrast dilemma could, in future work, be used to identify statistically abnormal linear anomalies in remote sensing data, demonstrating the potential to become an automated tool for GIS and various specialist web services.

However, regardless of the remote detection regime employed, the timing of the observations is critical. For subsurface detection using multispectral imaging, optimal acquisition times are observed after weather events that significantly impact ground condition. For subsurface detection using LiDAR elevation differencing, optimal DEM acquisition times should be at least five years apart or if elevation change is seasonal, at different times of year. For subsurface detection using heat retention analyses, optimal acquisition times are during extreme periods of ground warming and ground cooling. Albert Einstein once said “Look deep into nature, and then you will understand

everything better" (Isaacson, 2008). He is of course correct, but to detect subsurface anomalies from air and space, you have to look at the right time.

Taken together, these recommendations, techniques and procedures are integrated, sequenced and generalised to form a high-level data processing workflow for the high resolution and VHR detection of subsurface anomalies from air and space (Figure 6.1).

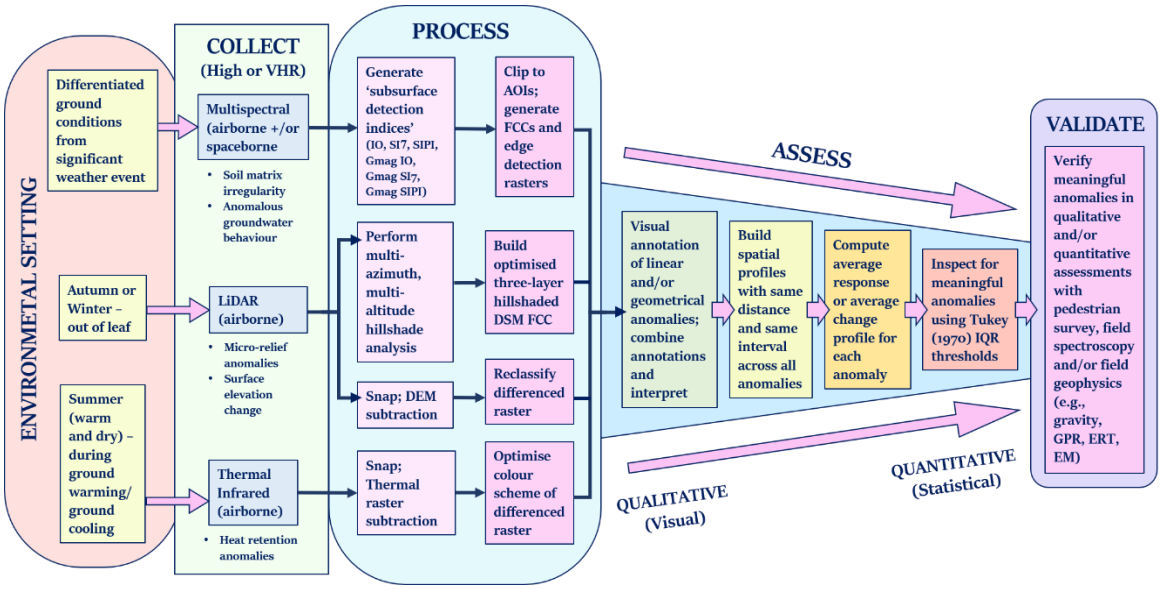



**Figure 6.1**. A generalised workflow of the stages, techniques and sequencing used in this research for the high resolution and very high resolution (VHR) detection of subsurface anomalies from air and space. Successful subsurface detection begins with collecting remotely sensed datasets in specific environmental settings; optimal conditions are sensor dependent. The high or VHR resolution dataset is then processed and qualitatively and quantitatively assessed. Subsurface anomalies are then validated with pedestrian survey, field spectroscopy and/or geophysical survey.

## 6.1 Summary of chapter conclusions

### 6.1.1 Chapter 2 - Detecting shallow subsurface anomalies with airborne and spaceborne remote sensing: A review

This review evaluated the subsurface detection capabilities of photogrammetry, thermal infrared, multispectral and hyperspectral imaging, synthetic aperture radar (SAR), airborne LiDAR, airborne gravity and aeromagnetics. The review also identified five principal motivations for remote sensing the subsurface from air and space. These are: archaeological prospecting, environmental risk mitigation, natural resource exploration, defence and security and speleological research. The study then categorised the distinct ground indicators and potential field characteristics of a subsurface anomaly. These are: visual identification, soil matrix irregularity, anomalous groundwater behaviour, surface elevation change, anomalous heat retention, subsurface density

change and magnetic field variation. These categorisations allowed the review to document previous studies by sensor type, research motivation and subsurface anomaly characteristic.

Following an appraisal of 113 research papers, 78% of photogrammetry papers detected visible signatures above archaeological sites; 43% of multispectral papers detected soil matrix irregularities over buried archaeological features; anomalous groundwater behaviour was observed by all major sensor types less airborne gravity and aeromagnetics; anomalous heat retention was a useful ground proxy for shallow subsurface detection across all five research motivations; changes in subsurface density were detected or assisted with airborne gravity, airborne LiDAR and SAR; and 57% of LiDAR papers and 50% of SAR papers detected changes in surface elevation.

Across the 8 sensor types, over 70 air and space remote sensing techniques were registered, each designed to accentuate subsurface anomalies in the visible, spectral, thermal, spatial, gravitational or magnetic domains, through exploiting a subsurface anomaly's unique ground indication, surface expression and potential field. The review grouped these techniques into 7 technique tables which, by design, recommend the most suitable subsurface detection technique by: the subsurface anomaly characteristic being pursued, the investigable feature being detected and the remote sensor type used. In combination, these tables provide a structured catalogue of recommendations for effective remote subsurface detection.

### 6.1.2 Chapter 3 - Using gravity, ground penetrating radar and vegetation indices to derive a multispectral recipe for subsurface detection

In this study, I reset the use and manipulation of vegetation indices (VIs) in their multispectral detection of shallow subsurface features in temperate, vegetated terrain. By using geophysical field observations as a proof of concept, high performing broadband VIs from high-resolution multispectral satellite imagery were statistically reprioritised, numerically validated and then assigned gradient magnitude (Gmag) equivalents (rate of change in VI). In 1D, I correlated and compared VI spectral profiles to changes in gravity along a specified *distance* across an Iron Age tunnel, locally known as a 'fogou'. In 2D, I correlated and compared their spectral response to GPR data across a specified *area*. In one and two dimensions, the Iron Oxide index, Soil Salinity Index 7 (SI7) and the Structure Insensitive Pigment Index (SIPI) were the most successful at detecting stressed soil and deprived meadow grass over the Iron Age fogou.

More broadly, the Iron Oxide index, SI7 and SIPI revealed a clay drainage pipe and a buried ditch system beneath similar, temperate vegetated terrain. From analysing the behaviour of these VIs as spectral profiles, false colour composites (FCCs) and edge detection image subsets, greater concentrations of iron (III) oxide, higher levels of soil salinity and a reduction in chlorophyll production were identified above the subsurface anomalies. According to VI definitions, these observations qualitatively demonstrate changes in drainage rate, temperature profile and chemical

weathering above a buried structure. Algebraically, the Iron Oxide index, SI7 and SIPI are also mathematical manifestations of the Red/Blue reflectance ratio, emphasising its notable detection efficiency in support of shallow, underground detection. Subsequently, these three VIs (which I term subsurface detection indices), and their Gmag equivalents, become the building blocks of a high-resolution multispectral image processing workflow which, using field geophysics, is correctly calibrated to detect shallow subsurface features in temperate, vegetated terrain.

### 6.1.3 Chapter 4 - Remote sensing the subsurface between a Cistercian abbey and a medieval grange

Using high-resolution multispectral satellite imagery and a very-high-resolution (VHR) LiDAR derived digital surface model (DSM), a tunnel was found between the abbey of Aunay and a nearby medieval grange in Normandy, France. This study also detects various buried garden features, once delineating the shape, size and form of a formal, Cistercian, baroque garden.

To find the tunnel, average Iron Oxide, SI7 and SIPI reflection profiles were generated along the two walls of the abbey-grange boundary. By thresholding these index reflection profiles with statistical limits, I exposed several anomalous reflection values from the cool-season grass along the north and east boundary wall of the abbey field. High Iron Oxide, SI7 and SIPI reflection values were observed from imagery taken soon after adverse weather events like intense rainfall or prolonged drought. These high concentrations of iron oxide and ground salt are expected to be the secondary effects of: 1) a different drainage regime above the subsurface structure; 2) the chemical weathering and leaching of a subsurface structure. Within the medieval grange, a quantitative inspection of anomalous Iron Oxide, SI7 and SIPI reflection values along the east perimeter wall of the abbey field revealed the entrance of a stone-lined tunnel.

In parallel, the same subsurface detection indices, and their Gmag equivalents, were generated for the abbey field and then analysed using FCCs and Sobel edge detection filters. A 50 cm resolution DSM of the abbey field was also analysed using a multi-azimuth and multi-altitude hillshade sequence. All results were graded using a qualitative three-tier subsurface detection rating, prescribed by the levels of accentuation of the reflection and micro-relief anomalies inside the field. I then combined all reflection and elevation anomalies to reveal several linear and geometric shaped distinctions in soil type, drainage, vegetation stress and micro-relief. These subsurface anomalies were compared to an eighteenth-century garden plan of the abbey field, sourced from the Bibliothèque nationale de France (BnF). In doing so, the lay down and configuration of these subsurface anomalies disclosed the inferred location of several stone foundations, edge arrangements and ground composition variations, each signifying a component part of a formal French, baroque garden, reinstated by Cistercian monks during their seventeenth-century restoration of Aunay Abbey.

### 6.1.4 Chapter 5 - Remote detection of linear subsurface features around Glastonbury Tor: A multi-sensor approach

To detect linear, subsurface features beneath the border fields north of Glastonbury Tor in Somerset, UK, high-resolution LiDAR elevation differencing, multispectral analyses (from Chapters 3 and 4) and VHR thermal imaging techniques were used. The border fields have, in recent times, become favourable sites for legacy tunnels, drains and pipes between the Tor, Glastonbury town and Glastonbury Abbey. Water supply from the Tor is the most logical need for these alleged structures, although alternative hypotheses suggest the tunnels were needed by Benedictine monks in Glastonbury Abbey for safeguarding wealth and evading persecution.

The LiDAR elevation differencing revealed 6 linear anomalies beneath these fields, with 2 showing statistically anomalous elevation change over a 6-year period. Consequently, this study inspected the soil and cool-season grass above these two statistically anomalous linear anomalies (LAs) using a high-resolution multispectral satellite image and subsurface detection indices Iron Oxide, SI7 and SIPI. In doing so, the same two LAs showed high levels of iron oxide, soil salinity and vegetation stress in warm and dry weather. Using VHR thermal imaging, one of these LAs featured a series of parallel, thermal striations with poor heat retention and the other exhibited a single, linear feature with good heat retention. To interpret these two anomalous LAs, I related the remotely sensed observations to a 2D electrical resistivity tomography (ERT) profile across each anomaly. When augmented with average elevation change, vegetation index and heat loss profiles, the resistivity anomalies implied that one LA was a shallow, underground spring and the other was a buried utility pipe.

A third 2D ERT profile extending radially from the Tor in the field closest to a recent excavation of a medieval “well house”, revealed an anomaly with the typical size, shape, depth and resistivity of a tunnel or drain. This anomaly aligned with a deeper ground penetrating radar (GPR) anomaly and a dowsed tunnel observation in Stray (2018), signifying the *possibility* of a tunnel-like feature beneath the border fields north of Glastonbury Tor.

## 6.2 Summary of algorithms and workflows

To draw the conclusions in Section 6.1, I developed several new image processing and image analysis techniques. To do this, I wrote three bespoke scripts in MATLAB and I designed a bespoke workflow for: 1) multispectral image processing; 2) LiDAR hillshade analysis; 3) the graphical inspection of abnormal ground behaviour.

### 6.2.1 Algorithms

- A bespoke MATLAB script was developed to calculate the ‘rate of change’ of VI for any given image subset. The algorithm reads a VI image subset (TIFF file) as a geo raster file.

The algorithm then applies the GRADIENTWEIGHT function, transforming the VI image subset into a VI 'rate of change' image subset, otherwise termed the gradient magnitude (Gmag) of a VI. This is a useful operation for identifying "edge effects" around shallow, subsurface features in vegetated terrain, where the rate of change in VI is expected to be high. After computing a VI's Gmag, the algorithm generates a new image subset (GeoTIFF file), showing the 'rate of change' of VI in a user-defined, projected coordinate system. This algorithm was used to generate Gmag image subsets of the Iron Oxide index, SI7 and SIPI in support of subsurface detection analyses in Chapters 3, 4 and 5.

- A second MATLAB script was developed to perform image comparisons between VI image subsets and GPR C-scans of underground objects (2D depth slices). Prior to use, both image subsets must be 8-bit unsigned TIFF files with identical image and cell size. When in operation, the two TIFF files are individually read by the algorithm and then a 2D cross-correlation and structural similarity index measurement are performed and displayed to the user. The 2D cross-correlation uses MATLAB function CORR2 and the structural similarity index measurement uses MATLAB function SSIM. This algorithm was used to identify the best performing VIs, FCC band combinations and edge detection raster images in Section 3.4 of Chapter 3.

- A final MATLAB script was written and used to generate a CSV file with pixel values (e.g., spectral reflection values, elevation change, heat loss) along a user-defined number of distance profiles across a linear subsurface anomaly. All distance profiles must be the same length and the same distance from the linear anomaly. The output CSV file is then used to produce average pixel value profiles across a specific linear anomaly in a raster image. Prior to operation, this algorithm requires a raw CSV file of pixel values from ArcGIS Pro, generated using Esri's MERGE and STACK PROFILE geoprocessing tools. This algorithm was used to generate average spectral band reflectance profiles along the abbey-grange boundary wall in Chapter 4, and average elevation change, VI and heat loss profiles across linear subsurface anomalies in Chapter 5.

### 6.2.2 Workflows

- In support of the research in Chapters 3, 4 and 5, a multispectral image processing workflow was devised to detect anomalous reflectance behaviour from cool-season vegetation over shallow, subsurface features in temperate environments. The workflow used the highest performing VIs from a correlation study with gravity and GPR data over a known Iron Age tunnel in Cornwall, UK (Chapter 3). The VIs, which in this thesis are termed 'subsurface detection indices', were the Iron Oxide index, SI7 and the SIPI. For any given site that is temperate and vegetated, the three 'subsurface detection indices' must first be produced, along with their Gmag equivalents (using the relevant algorithm in Section 6.2.1).

All six indexed images are then clipped to the specific site of interest before stacking to form a six-layer image stack. This then sets the conditions for a systematic inspection of anomalous reflectance behaviour from subsurface features in high-resolution multispectral satellite imagery, where twenty FCC band combinations and six edge detection raster images can be used to locate reflection anomalies from prospective near-surface features.

- To detect regular shaped micro-relief anomalies from near-surface structural features in a seventeenth-century baroque-style garden (Chapter 4), a multi-directional and multi-altitude LiDAR hillshade sequence was devised. Using the traditional HILLSHADE raster function in ArcGIS Pro, this sequence generated a VHR six-layer hillshaded DSM stack of a clipped study area using six different sun azimuths at a fixed sun altitude. Regular shaped micro-relief anomalies were then found and annotated, whilst systematically inspecting each three-band DSM FCC in red-green-blue (RGB). This process was repeated for nine different sun azimuths before the three highest performing DSM FCCs and their optimal sun altitudes were identified. These three DSM FCCs were then converted to greyscale images and restacked to produce an optimised three-layer hillshaded DSM FCC, tailored for enhanced, site-specific subsurface detection.

- To identify abnormal ground behaviour across linear anomalies (LAs) and field boundaries in raster imagery, a workflow was used to produce average pixel value profiles across each LA. John Tukey's Interquartile Range (IQR) thresholds for outside and detached observations (Tukey, 1970) were applied to these profiles to identify statistical outliers as a function of distance along an averaged profile. Initially, the workflow required the build of several spatial profiles (GIS polylines) across a LA, ensuring each profile is parallel to one another, the same length and the same distance from the LA. These individual profiles were then grouped into one vector dataset using the MERGE geoprocessing tool in ArcGIS Pro. The STACK PROFILE geoprocessing tool was then used to extract the individual pixel values along each profile in the merged vector dataset. These pixel values were exported as a CSV file and read by a bespoke MATLAB algorithm (Section 6.2.1), which then generates a new CSV file with pixel values along a user-defined number of distance profiles across the LA. An average pixel value profile was then produced across each LA and Tukey's IQR thresholds were applied. This workflow was used to identify reflection outliers from average Iron Oxide, SI7 and SIPI reflection profiles along the two abbey-grange boundary walls in Chapter 4. It was also used to identify abnormal elevation change, anomalous VI reflections and atypical heat loss across linear subsurface anomalies in Chapter 5.

## 6.3 Future work

### 6.3.1 With different high-resolution remote detection regimes

Recent advances in computer vision and deep learning showcase the potential to improve the recognition of abnormal ground behaviour above subsurface features. The prospect of employing convolutional neural networks (CNNs) to recognise, assess and reveal the location of anomalous ground characteristics from prospective subsurface anomalies will, almost certainly, broaden search areas and accelerate detection speeds (Aslan and Özüpak, 2025; Yuan et al., 2025). This will allow the user community (e.g., archaeologists, environmental agencies, defence intelligence analysts) to efficiently and economically prioritise land resources and any additional high resolution or VHR remote sensing assets. Training and exercising CNNs on the numerous pixel values in airborne hyperspectral data and narrowband VIs is in particular, in its infancy, and certainly worth due consideration in any future remote, subsurface detection study.

The utility of graph neural networks (GNNs) should also be explored, especially across large areas of interest or multiple target sites (Dilena, 2024). Here, relationships between the location and depth of suspected subsurface objects (positional anomalies), known underground features (relational objects) and the surrounding landscape could be modelled using the various sensor types discussed in this research. Similarly, the opportunity to merge different types of high resolution and/or VHR imagery is expected to enhance different sections of a subsurface anomaly. To do this, raster images from each sensor type should be resampled, normalised and then combined to form a composite subsurface detection raster which, by design, is capable of accentuating more abnormal ground characteristics from a subsurface feature.

In equal measure, multi-sensor subsurface detection algorithms should be developed to systematically search for anomalies in the visual, spectral, thermal, spatial, gravitational and magnetic domains of a study area. Various machine learning techniques are well placed to support (Shirmard et al., 2022). Xu et al. (2018) train a two-branch convolutional neural network (CNN) to “feature fuse” hyperspectral imagery with LiDAR data, increasing the classification accuracy of stressed grassland above a subsurface feature. If specific environmental parameters are defined by the user (e.g., subsurface target type, terrain, land cover, climate), a multi-branch CNN could, in theory, be trained to statistically detect composite subsurface anomalies in different imagery types using the seven subsurface anomaly characteristics presented in this research.

This research also identifies the need for new and innovative approaches to remotely detect subsurface density changes and magnetic field variations from near-surface structures. Currently, little airborne or spaceborne remote sensing methodology exists outside of traditional airborne gravity and aeromagnetic survey protocols. However, Biondi (2022) and Biondi and Malanga (2022) have made good progress, showcasing SARs tomographic ability to image density variations

inside rigid structures like volcanoes and ancient pyramids. This presents an opportunity to trial similar techniques on semi-rigid structures like grass covered tors and caves, where SAR returns are usually less coherent. According to Biondi (2022), SAR tomography uses photons as a carrier medium for phononic information, inviting future work to consider other ways in which photons could reveal the presence of subsurface anomalies in variable gravitational and magnetic fields. For example, the effect of near-surface density variations on full waveform LiDAR is an interesting concept. By exploiting the change in light photon energy through a gravitational potential, future work could analyse statistical correlations between returned LiDAR frequencies and the Earth's gravitational field over large near-surface anomalies like disused railway tunnels and major cave systems.

### 6.3.2 At other sites

In Chapters 4 and 5, airborne and spaceborne remote sensing techniques were used to detect medieval, monastic structures in the immediate vicinity of a Cistercian abbey in Normandy, France (Chapter 4), and Glastonbury Tor in Somerset, UK (Chapter 5). However, there are several other monastic sites worth exploring. In this research, the discovery of a tunnel connecting a medieval grange to the nearby grounds of Aunay Abbey in Normandy, France, present a reason and an opportunity to inspect the subsurface in and around other daughter abbeys belonging to the monastic Congregation of Savigny and the Clairvaux lineage of the Cistercians[25]. Also, previous accounts of Benedictine tunnels from Glastonbury Abbey (Bond, 1918; Mantle, 1911; Stray, 2018; Wakefield, 1814) indicate the need for a high or VHR remote sensing study within and around the grounds of Glastonbury Abbey.

At these sites, a LiDAR elevation differencing study becomes a sensible start point (digital terrain model (DTM) permitting). As witnessed in Chapter 5, this is a quick and easy way to detect linear elevation-change anomalies at scale. Average elevation-change profiles could follow, along with average Iron Oxide index, SI7 and SIPI reflection profiles, *assuming high-resolution multispectral data is available*. If so, the opportunity to correlate these VI reflection profiles with in situ iron oxide, soil salinity, soil moisture, soil temperature and soil pH profiles is encouraged. These soil profiles should be taken several times a year or, as a minimum, during the same month as the multispectral image acquisition date. The resulting soil profiles could then be used to verify (and calibrate) the accuracy of the average VI reflection profiles from the high-resolution satellite or VHR airborne multispectral imagery. As seen in Chapters 4 and 5, statistical thresholds like Tukey's IQR method (Tukey, 1970) could then be applied to the average change profiles to determine which LAs exhibit anomalous ground behaviour from alleged underground structures.

[25] Originally belonging to the monastic Congregation of Savigny, the abbey of Aunay was the ninth daughter house of Savigny Abbey in Manche, Normandy, before merging with the Order of Cistercians and their Clairvaux lineage in 1147 (Allen, 2021).

The opportunity to exercise these detection regimes in different environments should also be considered. Arid landscapes and forested terrain are of particular interest, with multispectral, hyperspectral and thermal detection regimes favouring the former, and multispectral, hyperspectral and LiDAR detection regimes favouring the latter. In particular, the woodland immediately west of Carn Euny (Chapter 3) is an ideal site for exploring the time-sensitive reflection behaviour of VIs in deciduous woodland, especially when there is speculation of a site extension to Carn Euny residing beneath the surface (Young, 2024).

To close, due consideration is given to the detection of shallow cave systems. To locate their entrance points, the opportunity to explore the nature of point cloud outliers in full waveform LiDAR data of known cave entrances is worth contemplation. These full waveform LiDAR returns could be compared with the LiDAR returns of point cloud outliers from elsewhere in a landscape. From conducting this comparison, the prospect of identifying specific waveform signatures and LiDAR characteristics from known cave entrances is posed (e.g., amplitude, intensity, frequency etc).

To detect cave systems *without* entrance points, the SAR tomography techniques employed by Biondi (2022) and Biondi and Malanga (2022) could be used to assess the imaging capabilities, accuracy and reliability of using SAR tomography on semi-rigid structures like grass covered hills and tors - where SAR returns are less coherent (e.g., Morley et al., 2025a; Chapter 2). To examine the reliability and accuracy of SAR tomography, the results could be compared with an ambient noise tomography study (e.g., Paustian, 2021; Torrese, 2025; Wang et al., 2023). In support of Chapter 5, sites of interest include Glastonbury Tor and Chalice Hill in Somerset, UK. Obvious sources of ambient noise then become the tourists in peak tourism and music from the annual Glastonbury Festival.

## 6.4 Final word

You are only as good as the pixel you're working with. High *"pixel power"* is a composite function of high spatial resolution, high value attribution, high radiometric resolution and high temporal resolution; a much-needed *recipe* for the successful detection of subsurface anomalies from air and space (Figure 6.2). Only then can you: 1) analyse the ground at the right time; 2) accurately examine the pixel response from a scene as a function of *distance* or *area* above a prospective subsurface feature; 3) correlate pixel values and forge relationships with near-surface geophysics; 4) statistically detect pixel value outliers with graphical analyses; 5) identify statistically significant linear anomalies with average change profiles; 6) locate anomalous ground signatures from small to medium-scale near-surface anthropogenic structures like tunnels, pipelines and drains. In doing this, the opportunity to see below *really does* come from above.

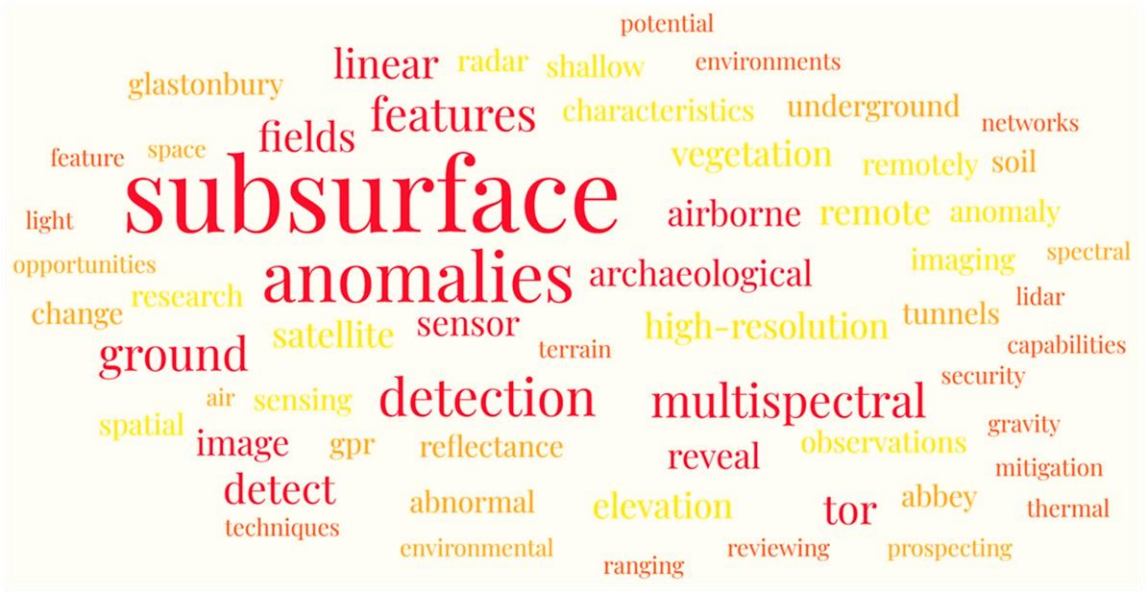



**Figure 6.2**. Word cloud showing most used words in the abstracts from Chapters 2, 3, 4 and 5. In this research, these words are the key *ingredients* for successful subsurface detection from air and space.

# Appendices

# A

*Appendix to Chapter 2*

# Major spaceborne imaging sensors for passive Earth observation

**Table A1**
Table listing some of the major spaceborne imaging sensors for passive Earth observation, ordered by launch year. The list of panchromatic (PAN), multispectral (MSI) and thermal infrared (TIR) imaging sensors is not exhaustive; all entries are sourced from the European Space Agency's 'Satellite Mission Catalogue' on the eoPortal (ESA, 2023).

| Satellite / Sensor | Sensor Type | No of Spectral Bands | Spectrum (nm) | Launch Year | Spatial Resolution (m) | | Remarks |
|---|---|---|---|---|---|---|---|
| | | | | | PAN | VIS – NIR/SWIR/TIR | |
| LANDSAT-1 / MSS | MSI | 7 | 500-1100 | 1972 | N/A | 79 | Landsat was a pioneering land remote sensing programme, conceived by USGS and NASA. Landsat satellites 1-4 used a Multispectral Scanner (MSS). |
| LANDSAT-2 / MSS | MSI | 7 | 500-1100 | 1975 | N/A | 79 | |
| LANDSAT-3 / MSS | MSI | 7 | 500-1100 | 1978 | N/A | 79 | |
| LANDSAT-4 / TM | MSI + TIR | 7 | 450-12500 | 1982 | N/A | 30 + 120 (TIR) | Thematic Mapper (TM) is a multispectral mechanically scanning optical imager which images in the visible, infrared and thermal spectrum. |
| LANDSAT-5 / TM | MSI + TIR | 7 | 450-12500 | 1984 | N/A | 30 + 120 (TIR) | |
| SPOT-1 / HRV | PAN + MSI | 3 | 500-890 | 1986 | 10 | 20 | Satellite Pour l'Observation de la Terre was a commercial earth-imaging satellite from CNES, the French Space Agency. |
| IRS-1A | MSI | 4 | 450-860 | 1988 | N/A | 36 | |
| SPOT-2 / HRV | PAN + MSI | 3 | 500-890 | 1990 | 10 | 20 | |
| JERS-1 / OPS | MSI | 8 | 520-2400 | 1992 | N/A | 18.3 | JERS-1 (Japan Earth Resources Satellite) generated data on geological phenomena, agriculture and forestry land usage, coastal regions and environment/disaster management. It features both optical and SAR instruments. |
| SPOT-3 / HRV | PAN + MSI | 3 | 500-890 | 1993 | 10 | 20 | |

| | | | | | | | |
|---|---|---|---|---|---|---|---|
| IRS-P2 | MSI | 4 | 450-860 | 1994 | N/A | 23.5 | |
| IRS-1C | PAN + MSI | 4 | 500-1750 | 1995 | 5.8 | 23.5 | IRS-1C and -1D are EO satellites from the Indian Space Research Organisation (ISRO). |
| IRS-1D | PAN + MSI | 4 | 500-1750 | 1997 | 5.8 | 23.5 | IRS-1C and -1D carried three pushbroom sensors. Two were optical imagers with different swaths and spatial resolutions: Linear Imaging Self Scanner-III (LISS-III) and Panchromatic Sensor (PAN). The other sensor was an imaging radiometer called WiFS (Wide Field Sensor). |
| SPOT-4 / HRVIR | PAN + MSI | 4 | 500-890 | 1998 | 10 | 20 | |
| CBERS-1 / CCD | PAN + MSI | 4 | 420-890 | 1999 | 3 | 20 | Operated as part of the China-Brazil Earth Resources satellite programme. |
| IKONOS - 2 | PAN + MSI | 4 | 450-900 | 1999 | 1 | 4 | Launched by Space Imaging in 1999, Ikonos-2 was the world's first commercial high-resolution imaging satellite. |
| LANDSAT-7 / ETM+ | PAN, MSI + TIR | 7 | 450-12500 | 1999 | 15 | 31 + 60 (TIR) | Landsat-7 features the Enhanced Thermal Mapper Plus (ETM+) developed by Raytheon SBRS (Santa Barbara Remote Sensing), building upon the Thematic Mapper (TM) onboard Landsat-4 & -5. |
| TERRA / ASTER | MSI + TIR | 14 | 520-860 | 1999 | N/A | 15 + 30 (SWIR) + 90 (TIR) | Terra (formerly known as EOS/AM-1) is a joint mission within NASA's ESE (Earth Science Enterprise) programme between the US, Japan and Canada. The Advanced Spaceborne Thermal Emission and Reflection Radiometer (ASTER) is a Japanese sensor with visible, NIR, SWIR and TIR sensor range. TERRA also carries four additional remote sensors: CERES (Clouds and the Earth's Radiant Energy System); MISR (Multi-angle Imaging SpectroRadiometer); MODIS (Moderate-resolution Imaging Spectroradiometer); MOPITT (Measurements of Pollution in the Troposphere). |
| EO-1/ALI | PAN + MSI | 8 | 433-890 | 2000 | 10 | 30 | Managed and operated by NASA's Goddard Space Flight Centre, featuring the Advanced Land Imager (ALI) sensor. |
| QUICKBIRD -2 | PAN + MSI | 4 | 450-900 | 2001 | 0.61 | 2.4 | DigitalGlobe (now Maxar Technologies), launched QuickBird-2 from California, USA in October 2001. |
| PROBA-1 | PAN + MSI | 62 | 450-1050 | 2001 | 5 | 18 | The Project for On-Board Autonomy - 1 (PROBA-1) is a minisatellite technology demonstration mission in ESA's General Study Program, aiming to tackle issues related to the on-board operational autonomy of a generic platform. It features the Compact High-Resolution Imaging Spectrometer (CHRIS). |
| SPOT-5 / HRG | PAN + MSI | 4 | 480-1750 | 2002 | 5 | 10 | |
| IRS-P6 (RESOURCESAT-1) / LISS-IV | MSI | 3 | 520-860 | 2003 | N/A | 5.8 | Indian Remote-Sensing Satellite-P6 (IRS-P6), renamed ResourceSat-1, was an optical imaging satellite operated by the Indian Space Research Organisation (ISRO). |

| | | | | | | | |
|---|---|---|---|---|---|---|---|
| ORBVIEW-3 | PAN + MSI | 4 | 450-900 | 2003 | 1 | 4 | A US commercial high-resolution imaging minisatellite developed by Orbital Imaging Corporation. In 2006, ORBIMAGE merged with Space Imaging of Thornton, Colorado USA, to establish the commercial imaging company GeoEye. |
| NIGERIASAT-1 | MSI | 3 | 450-900 | 2003 | N/A | 32 | |
| DMC-1G / SLIM6 | MSI | 3 | 520-900 | 2003 | N/A | 32 | The Disaster Monitoring Constellation (DMC) is an international program initially proposed in 1996 and led by SSTL (Surrey Satellite Technology Ltd), Surrey, UK, to construct a network of five affordable LEO microsatellites. The objective is to provide a daily global imaging capability at medium resolution (30-40 m) in 3-4 spectral bands for rapid-response disaster monitoring and mitigation. |
| CBERS-2 | PAN, MSI + TIR | 4 | 420-890 | 2003 | 2.7 | 20 + 160 (TIR) | |
| IRS-P5 / CartoSat-1 | PAN | 0 | 500-750 | 2005 | 2.5 | N/A | IRS-P5 is a spacecraft of ISRO. The mission objectives included geo-engineering (mapping) applications, requiring high-resolution panchromatic imagery with high pointing accuracies. The spacecraft features two high-resolution panchromatic cameras that may be used for in-flight stereo imaging. |
| ALOS / PRISM + AVNIR-2 | PAN + MSI | 4 | 420-890 | 2006 | 2.5 | 10 | Advanced Land Observing Satellite (ALOS) was a Japanese EO mission. |
| KOMPSAT-2 / MSC | PAN + MSI | 4 | 450-900 | 2006 | 1 | 4 | Launched in July 2006, KOMPSAT-2 (Korea Multi-Purpose Satellite) was developed and operated by KARI (Korea Aerospace Research Institute). |
| IRS-P5 / CartoSat-2 | PAN | 0 | 500-850 | 2007 | 1 | N/A | |
| WORLDVIEW-1 | PAN | 0 | 450-900 | 2007 | 0.5 | N/A | WorldView-1 (WV-1) is a commercial mission owned and operated by Maxar Technologies Inc. WV-1 is the successor to QuickBird-2 and aims to provide high spatial resolution imagery of the Earth's surface to defence, intelligence and commercial industries. |
| GEOEYE-1 | PAN + MSI | 4 | 450-920 | 2008 | 0.41 | 1.65 | Included in the WorldView constellation and operated by Maxar. |
| PLANET - RAPIDEYE | MSI | 5 | 440-850 | 2008 | N/A | 6.5 | The RapidEye Earth observation system was a commercial constellation of five minisatellites, originally owned and operated by BlackBridge and acquired by Planet Labs in 2015. |
| WORLDVIEW-2 | PAN + MSI | 8 | 400-1040 | 2009 | 0.46 | 1.84 | Launched October 2009, WorldView-2 (WV-2) is a commercial imaging satellite, owned and operated by Maxar Technologies Inc. |
| PLÉIADES-HR | PAN + MSI | 4 | 430-915 | 2011 | 0.7 | 2.8 | Pléiades 1A and 1B are a two-satellite environment focussed high resolution (HR) constellation from the French Space Agency, Centre National D'Etudes Spatiales (CNES). |

| | | | | | | | |
|---|---|---|---|---|---|---|---|
| NIGERIASAT-2 | PAN + MSI | 4 | 450-900 | 2011 | 2.5 | 5 | NigeriaSat-2 is a Nigerian government imaging satellite and successor to NigeriaSat-1, produced by SSTL (Surrey Satellite Technology Ltd.) under a contract with the National Space Research and Development Agency (NASRDA) of Nigeria. |
| KOMPSAT-3 / AEISS | PAN + MSI | 4 | 450-900 | 2012 | 0.7 | 2.8 | KOMPSAT-3 is a Korean Earth observation mission of KARI, funded by the Ministry of Education, Science and Technology and features an Advanced Electronic Image Scanning System (AEISS). |
| SPOT-6 / HRG | PAN + MSI | 4 | 455-890 | 2012 | 1.5 | 6 | Owned and operated by Airbus Defence and Space. |
| GAOFEN-1 / PMC | PAN + MSI | 4 | 450-890 | 2013 | 2 | 8 | Developed in Beijing by the China National Space Administration (CNSA). |
| LANDSAT-8 / OLI | PAN + MSI | 8 | 433-2300 | 2013 | 15 | 30 | Features the Operational Land Imager (OLI) sensor. |
| LANDSAT-8 / TIRS | TIR | 2 | 10800-12000 | 2013 | N/A | 100 | Features the Thermal Infrared Sensor (TIRS). |
| PLANET - SKYSAT | PAN + MSI | 4 | 450-900 | 2013 | 0.86 | 1 | The Planet SkySat constellation is comprised of 21 satellites which are tasked to image any point on Earth in very high resolution and at sub-daily frequency. They can also capture stereo imagery and video footage. |
| GAOFEN-2 / PMC | PAN + MSI | 4 | 450-890 | 2014 | 0.81 | 3.24 | Developed in Beijing by the China National Space Administration (CNSA). |
| SPOT-7 / HRG | PAN + MSI | 4 | 455-890 | 2014 | 1.5 | 6 | Owned and operated by Airbus Defence and Space. |
| WORLDVIEW-3 | PAN + MSI | 16 | 400-2365 | 2014 | 0.31 | 1.24 | WV-3 also features 12 CAVIS (Clouds, Aerosols, Vapours, Ice, and Snow) bands which monitor the atmosphere and provide correction data to improve WV-3's high-resolution imagery through haze, soot and dust. |
| SENTINEL-2 / MSI | MSI | 13 | 450-2200 | 2015 | N/A | 10 | Sentinel-2 is a constellation of two optical imaging satellites, which are a part of Copernicus - the European Union's Earth Observation (EO) programme. |
| PLANET - DOVES | MSI | 4 | 450-900 | 2015 | N/A | 5 | Planet Doves (CubeSats) are 10x10x30 centimetres in size. |
| DMC-3 / SSTL 300 S1 | PAN + MSI | 3 | 450-900 | 2015 | 1 | 4 | DMC-3 (Disaster Monitoring Constellation-3) is a constellation of three optical imagers owned and operated by DMCii (DMC International Imaging Ltd.). DMCii is a subsidiary of Surrey Satellite Technology Ltd. (SSTL), the world leader in small satellite technology. |
| WORLDVIEW-4 | PAN + MSI | 4 | 450-920 | 2016 | 0.31 | 1.24 | WV-4 suffered a failure in one of its control moment gyroscopes in Jan 19 and operations ceased. |
| VISION-1 | PAN + MSI | 4 | 440-910 | 2018 | 0.87 | 3.48 | |
| CBERS-4A / WPM | PAN + MSI | 4 | 510-890 | 2019 | 2 | 8 | The China-Brazil Earth Resources Satellite-4A (CBERS-4A) is an optical imaging satellite collaboratively operated by the China Centre for Resources Satellite and Data Application (CRESDA) and the Instituto Nacional del Pesquisas Espacias (INPE) - Brazil's National Institute of Space Research. |

| | | | | | | | |
|---|---|---|---|---|---|---|---|
| PLANET - SUPER DOVES | MSI | 8 | 430-885 | 2021 | N/A | 3.7 | 48 x Super Dove Planet satellites designed and configured to join the existing PlanetScope satellite constellation of c200 satellites. |
| PLÉIADES NEO | PAN + MSI | 6 | 400-880 | 2021 | 0.3 | 1.2 | Pléiades Neo is a constellation of very-high-resolution (VHR) optical satellites. The first two satellites were launched in 2021, and the final 2 satellites launched in 2022. |

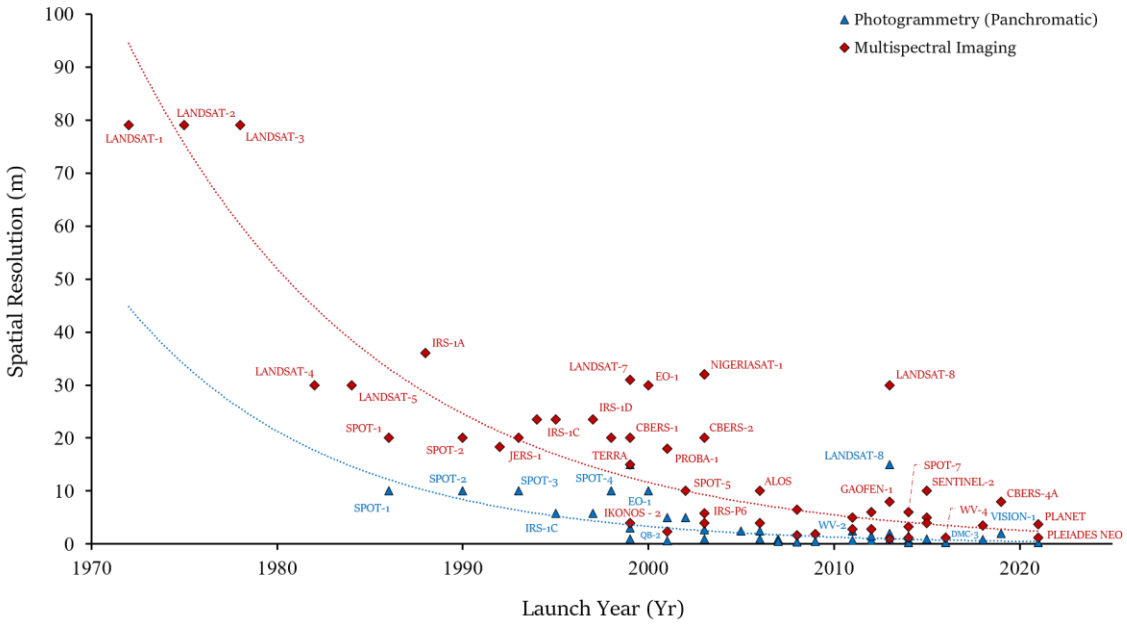



**Figure A1**. Spatial resolution of passive spaceborne imaging sensors since 1972. The list of passive imaging sensors used in this scatter plot is not exhaustive; all data points are sourced from the European Space Agency's 'Satellite Mission Catalogue' on the eoPortal (ESA, 2023) and are tabulated in Table A1.

# B

*Appendix to Chapter 2*

# Major spaceborne imaging sensors for active Earth observation

**Table B1**
Table listing some of the major spaceborne imaging sensors for active Earth observation, ordered by launch year. The list of active imaging sensors (SAR sensors) is not exhaustive; all entries are sourced from the European Space Agency's 'Satellite Mission Catalogue' on the eoPortal (ESA, 2023).

| Satellite / Sensor | Acquisition Mode | No of Bands | Polarization | Launch Year | Spatial Resolution (m) | Remarks |
|---|---|---|---|---|---|---|
| SEASAT | Active | 1 (L) | HH | 1978 | 25 | SeaSat was a pioneering Earth observation experimental mission of NASA's Jet Propulsion Laboratory (JPL), demonstrating the viability of imaging radar for EO and becoming a precursor to many missions that investigated the Earth's oceans, land and ice. |
| SIR-A | Active | 1 (L) | HH | 1981 | 30 | |
| SIR-B | Active | 1 (L) | HH | 1984 | 30 | |
| ALMAZ-1 | Active | 1 (S) | HH | 1991 | 25 | The Almaz programme (Russian for "diamond") was a military space programme of the former Soviet Union. |
| ERS-1 | Active | 1 (C) | VV | 1991 | 30 | The ERS-1 was the first environmental monitoring satellite developed by ESA. The mission detected land and ocean surface change and provided observation data on oceans, polar ice, vegetation, geology, meteorology and ecology. |
| JERS-1 / SAR | Active | 1 (L) | HH | 1992 | 18 | JERS-1 is a Japanese Earth Resources Satellite, designed to support a SAR and Optical mission - developed by The National Space Development Agency of Japan. |
| SIR-C / X-SAR | Active | 3 (C, L, X) | All (L, C); VV (X) | 1994 | 13 (L), 26 (C), 10 (X) | SIR-C/X-SAR (Spaceborne Imaging Radar C/X-band Synthetic Aperture Radar) was an imaging radar system developed by NASA, the German Space Agency (DLR) and the Italian Space Agency (ASI). It was used to obtain SAR imagery for scientific research, calibration, and technological experiments. SIR-C/X-SAR was a payload on the SRL-1 (Space Radar Laboratory-1) shuttle and the SRL-2 (Space Radar Laboratory-2). |
| ERS-2 | Active | 1 (C) | VV | 1995 | 30 | ERS-2 saw enhancements to the previous ERS-1 mission. ERS-2 provided microwave spectrum environmental monitoring across a range of disciplines including oceans, polar ice and forestry. |
| RADARSAT-1 | Active (Scan SAR) | 1 (C) | HH | 1995 | 10 | RADARSAT-1 was the first commercial Earth observation mission of the Canadian Space Agency (CSA). It used a microwave radar sensor to monitor environmental changes and Earth's natural resources. |

| | | | | | | |
|---|---|---|---|---|---|---|
| SRTM | Active | 2 (C, X) | HH+HV or VV+VH (C), VV (X) | 2000 | 30 | SRTM is a international shuttle mission between NASA, DoD/NGA (National Geospatial-Intelligence Agency), DLR (German Aerospace Center - Deutsches Zentrum für Luft- und Raumfahrt), and ASI (Agenzia Spaziale Italiana). The mission objective was to obtain single-pass interferometric SAR imagery to be used for Digital Elevation Model (DEM) generation. Coverage of the Earth's land surfaces is provided between the latitudes of -54º and +60º, representing nearly 80% of the land masses. |
| ENVISAT / ASAR | Active (Image Mode) | 1 (C) | HH or VV | 2002 | 28 | EnviSat was ESA's successor to ERS 1 & 2, designed to monitor the Earth's environment including: meteorology, climatology, environment, atmospheric chemistry, vegetation, hydrology, land use, and ocean and ice processes. |
| SAR - LUPE | Active (Spot Light) | 1 (X) | VV | 2006 | 0.5 | SAR-Lupe is Germany's first satellite-based reconnaissance system, developed for the German Ministry of Defence. This SAR project consists of five identical satellites with the objective of providing high-resolution radar imagery to German defence forces. |
| ALOS / PALSAR | Active (Fine Beam) | 1 (L) | HH or VV (single pol) HH+HV or VV+VH (dual pol) | 2006 | 7 | ALOS (Advanced Land Observing Satellite) was a Japanese Earth observation mission developed by JAXA (Japan Aerospace Exploration Agency). The mission's objectives required high resolution imagery for applications in cartographic mapping, regional observation, disaster monitoring and resource surveying. A PAN sensor (PRISM) and MSI sensor (AVNIR-2) were also part of the ALOS multi-sensor payload. |
| RADARSAT-2 | Active | 1 (C) | Fully polarimetric | 2007 | 3 | RADARSAT-2 is a jointly-funded satellite mission of CSA (Canadian Space Agency) and MDA (MacDonald Dettwiler Associates Ltd. of Richmond, BC), representing a Canadian government/industry partnership [or PPP (Public Private Partnership)] in a commercial venture. In Feb. 1998, CSA awarded a contract to MDA to build RADARSAT-2. |
| COSMO-SKY MED (CSK) | Active (Spot Light) | 1 (X) | HH, VV, HV/VH | 2007 | 1 | COSMO-SkyMed (Constellation of Small Satellites for Mediterranean basin Observation - CSK) is a four-spacecraft constellation. The mission is jointly funded by the Italian Ministry of Research and the Italian Ministry of Defence and developed by Agenzia Spaziale Italiana (ASI) for both military and civil application. ScanSAR and StripMap acquisition modes also operational. |
| TERRASAR-X / TANDEM-X | Active (Spot Light) | 1 (X) | (HH, VV), (HH/VV) | 2007 | 1 | TanDEM-X and TerraSAR-X are twin interferometric SAR satellites, funded in a public/private collaboration between the German Aerospace Centre (DLR) and Airbus Defence and Space. The satellites construct three-dimensional images of the Earth's surface in order to generate a World DEM; ScanSAR and StripMap acquisition modes are also operational. |
| SENTINEL-1 | Active (Strip Map) | 1 (C) | HH or VV (single pol) HH+HV or VV+VH (dual pol) | 2014 | 5 | Sentinel-1 is a constellation of two imaging radar satellites operated by ESA under the Copernicus programme. Sentinel-1B experienced an anomaly which rendered it unable to deliver radar data in December 2021, and the launch of Sentinel-1C is planned for 2023. Interferometric Wide, Extra Wide and Wave acquisition modes are also operational on Sentinel-1A. |
| ALOS-2 / PALSAR-2 | Active (Spot Light) | 1 (L) | VV/HH VV+HH | 2014 | 1 | ALOS-2 features PALSAR-2 (Phased Array type L-band Synthetic Aperture Radar-2) and a multi-purpose imaging vis/IR (visual/infrared) radiometer named CIRC (Compact InfraRed Camera). PALSAR-2 monitors Japanese natural disasters, land and agriculture and also explores natural resources in the ground and seabeds of Japan. The CIRC instrument measures land surface temperature and can detect and monitor active forest fires. ScanSAR and StripMap acquisition modes are also operational. |
| GAOFEN-3 | Active (Spot Light) | 1(C) | HH or VV | 2016 | 1 | Gaofen-3 is the third satellite in the China High-Resolution Earth Observation System (CHEOS) series. |

| | | | | | | |
|---|---|---|---|---|---|---|
| ICEYE | Active (Spot Imaging) | 1 (X) | VV | 2018 | 1 | The commercial ICEYE constellation is a constellation of X-band SAR Satellites. The ICEYE satellites provide high-resolution images the Earth's surface to enable better decision making based on the Earth observation data. Three other acquisition modes are employed; Spot extended area imaging, Strip imaging and Scan imaging. |
| PAZ | Active (High Res Spot Light) | 1 (X) | HH or VV or VH or HV (single pol) HH+HV or VV+VH (dual pol) | 2018 | 1 | PAZ is an X band Synthetic Aperture Radar mission of Spain. It is a dual-use mission, aimed at serving the security and defence needs of the Ministry of Defence. PAZ is managed by Hisdesat, a Spanish commercial company that provides its service to the Ministry of Defence (who funded and own the satellite). Five other imaging modes are available. |
| SAOCOM | Active (Strip Map) | 1(L) | HH or VV (single pol) HH+HV or VV+VH (dual pol) HH+HV+VV+VH (quad pol) | 2018 | 10 | Satélite Argentino de Observación COn Microondas (SAOCOM), which translates to Argentine MicroWave Observation Satellite, is a constellation of two satellites, SAOCOM-1A and SAOCOM-1B, owned and operated by the Argentinian Space Agency. The mission aims to provide effective Earth observation and disaster monitoring. |
| COSMO-SKY MED SECOND GENERATION (CSG) | Active (Spot Light) | 1(X) | HH or VV or VH or HV (single pol) HH+HV or VV+VH (dual pol) | 2019 | 0.35 | The COSMO-SkyMed Second Generation (CSG) is a constellation of four satellites, aimed at enhancing the quality and capability of imaging of the original COSMO-SkyMed constellation (CSK). Ten different imaging modes are available. |
| CAPELLA X-SAR | Active (Staring Spot Light) | 1(X) | HH | 2021 | 0.3 | Based in California, USA, the commercial start-up company Capella Space is developing the Capella X-SAR (Synthetic Aperture Radar) constellation consisting of 36 microsatellites to provide global high-resolution commercial SAR imagery. Imaging modes include Stripmap, multi-swath stripmap, staring spotlight and sliding spotlight. |
| Lu Tan-1 (LT-1) | Active (Strip Map) | 1 (L) | HH or VV (single pol) HH+HV or VV+VH (dual pol) | 2022 | 3 | A Chinese satellite constellation consisting of two satellites: LT-1 A and LT-1 B. LT-1 is used for digital elevation model (DEM) generation and deformation monitoring. The constellation can also operate in ScanSAR imaging mode. |

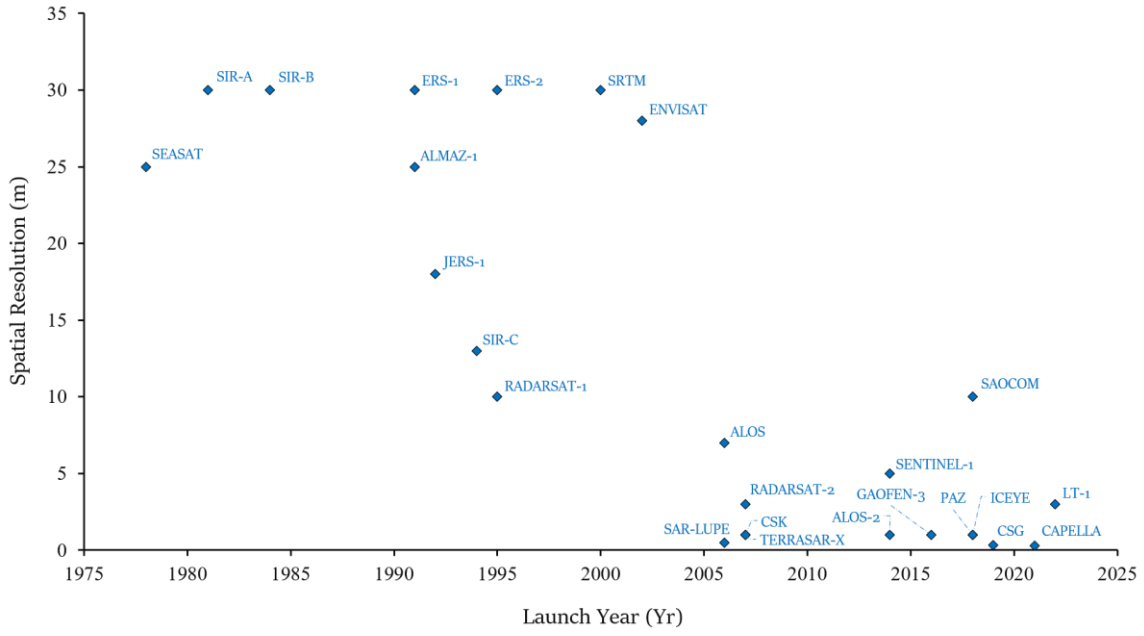



**Figure B1**. Spatial resolution of active spaceborne imaging (i.e. SAR) sensors since 1978. The implementation of new SAR imaging modes from 2000 onwards has significantly increased the spatial resolution of spaceborne SAR. The list of SAR sensors used in this scatter plot is not exhaustive; all data points are sourced from the European Space Agency's 'Satellite Mission Catalogue' on the eoPortal (ESA, 2023) and are tabulated in Table B1.

# C

*Appendix to Chapter 2*

# Search strategy and paper statistics

The Google Scholar and Oxford University 'Search Oxford Libraries Online' (SOLO) databases were used to find and retrieve all papers examined in this review. The following search strings were used systematically to explore each database:

- **Search String #1**: [Reviewing/using] [remote sensing/insert sensor type] to find [tunnels/caves/mines/underground facilities/subsurface structures/underground cavities/underground voids]

- **Search String #2**: Remote sensing [tunnels/caves/mines/underground facilities/subsurface structures/underground cavities/underground voids] using (insert sensor type)

Each variable term in each search string was entered systematically to ensure all combinations of the search query were used in the Google Scholar and SOLO search engines. Results were filtered by "most relevant" in 'pass one' and "most recent" in 'pass two' for each string combination.

All papers reviewed were documented in a three-dimensional reference matrix (Figure C1) which registered the papers by the major sensor type used, the subsurface anomaly characteristic being investigated, and the authors' motivation for exploring the subsurface from air or space.

In total, 113 papers were reviewed in detail and 91 use cases (case studies) were appraised. Various percentages can be calculated from Figure C1, acknowledging our assumption that the sample of papers reviewed is a fair and accurate representation of the entire population of subsurface remote sensing publications in circulation. Of note, 20% of all papers reviewed used LiDAR to detect subsurface features, followed by SAR (19%), hyperspectral imaging (15%),

multispectral imaging (12%), thermal infrared (11%), airborne magnetics (10%), photogrammetry (8%) and airborne gravity (5%).

Also, of the 113 papers reviewed, 23% examined the visual indicators of near subsurface anomalies, 22% pursued surface elevation change, 17% identified soil matrix irregularities, 12% detected heat retention anomalies, 10% recorded magnetic field variations, 9% studied anomalous groundwater behaviour and 7% measured changes in subsurface density.

Finally, from an authors' motivational perspective, 38% used airborne and spaceborne remote sensing techniques to detect buried archaeological features, 31% were attempting to mitigate risk from environmental hazards, 13% were finding natural resources, 11% were in support of defence and security activity and 7% were undertaking speleological research.

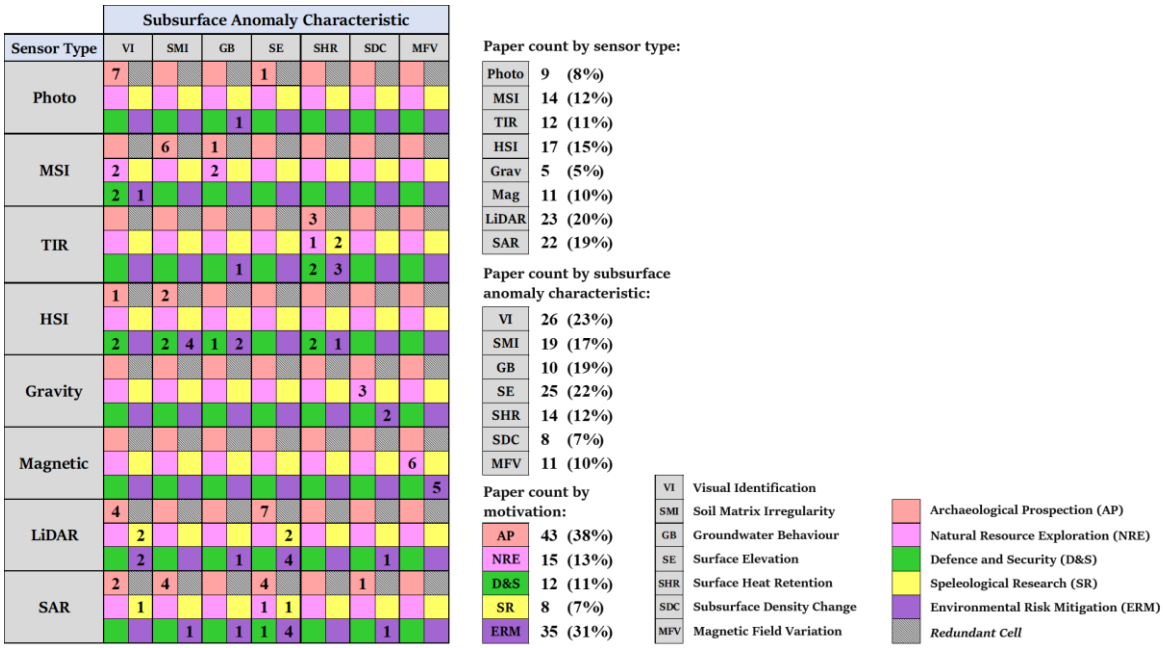



**Figure C1**. Three-dimensional reference matrix for documenting peer-reviewed publications and paper statistics. All papers reviewed were registered by the sensor type used, the subsurface anomaly characteristic being investigated and the author's motivation for exploring the subsurface from air or space. In total, and as documented above, 113 papers have been reviewed.

# D

*Appendix to Chapter 2*

# Principles of air and space remote sensing

Figures D1 to D8 are information flow graphics, each describing the fundamental principles that underpin the operation and application of each sensor type considered in this review. The arrows denote the logical flow of information, beginning with a baseline concept inside a coloured text box.

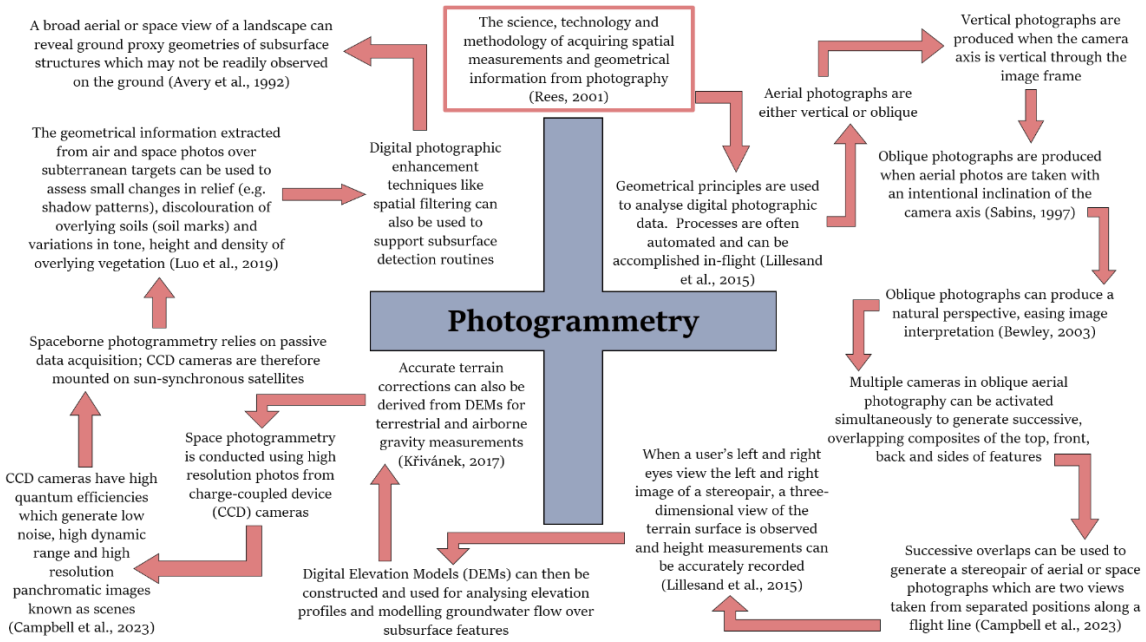



**Figure D1**. Principles of air and space photogrammetry. Red box denotes beginning of flow graphic and red arrows depict flow of information.

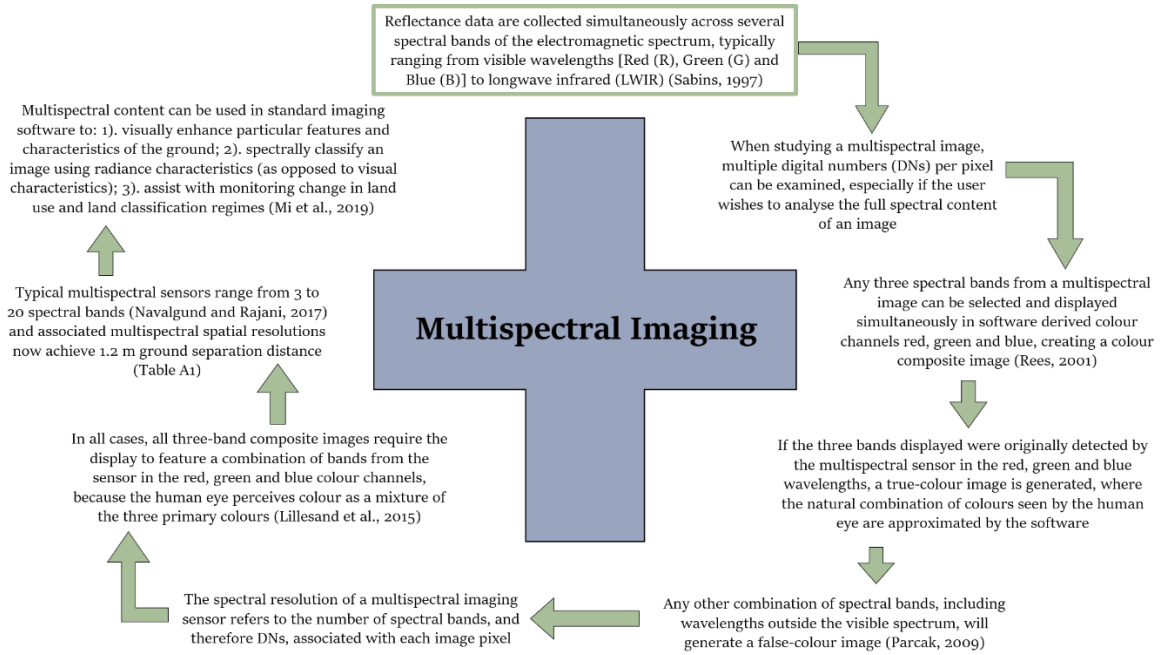



**Figure D2**. Principles of multispectral imaging. Dark green box denotes beginning of flow graphic and dark green arrows depict flow of information.

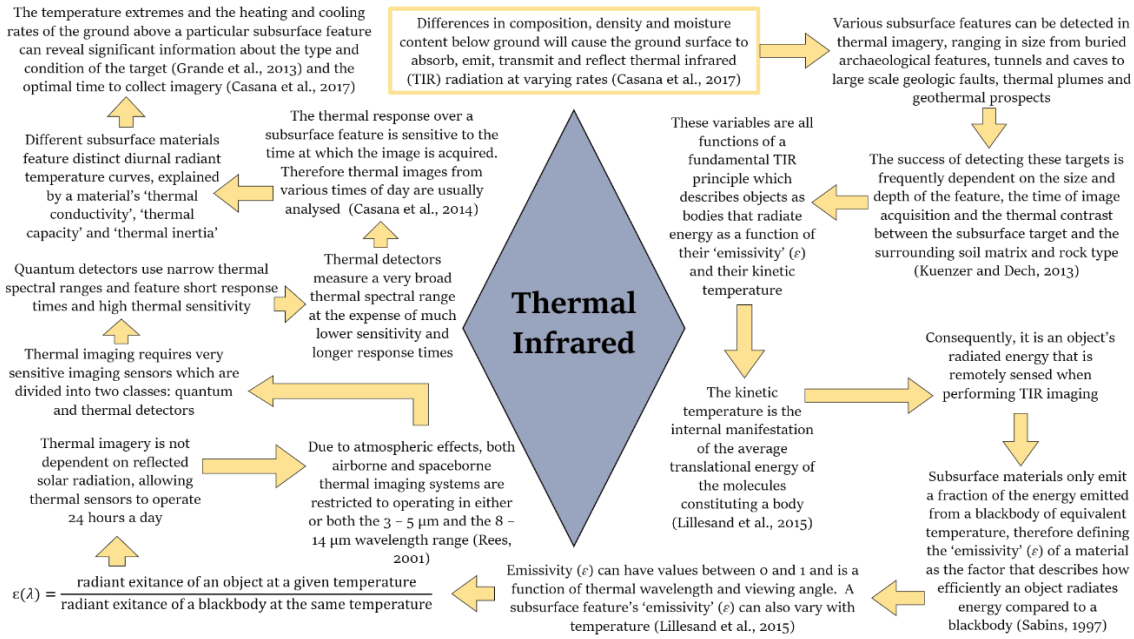



**Figure D3**. Principles of thermal infrared imaging. Yellow box denotes beginning of flow graphic and yellow arrows depict flow of information.

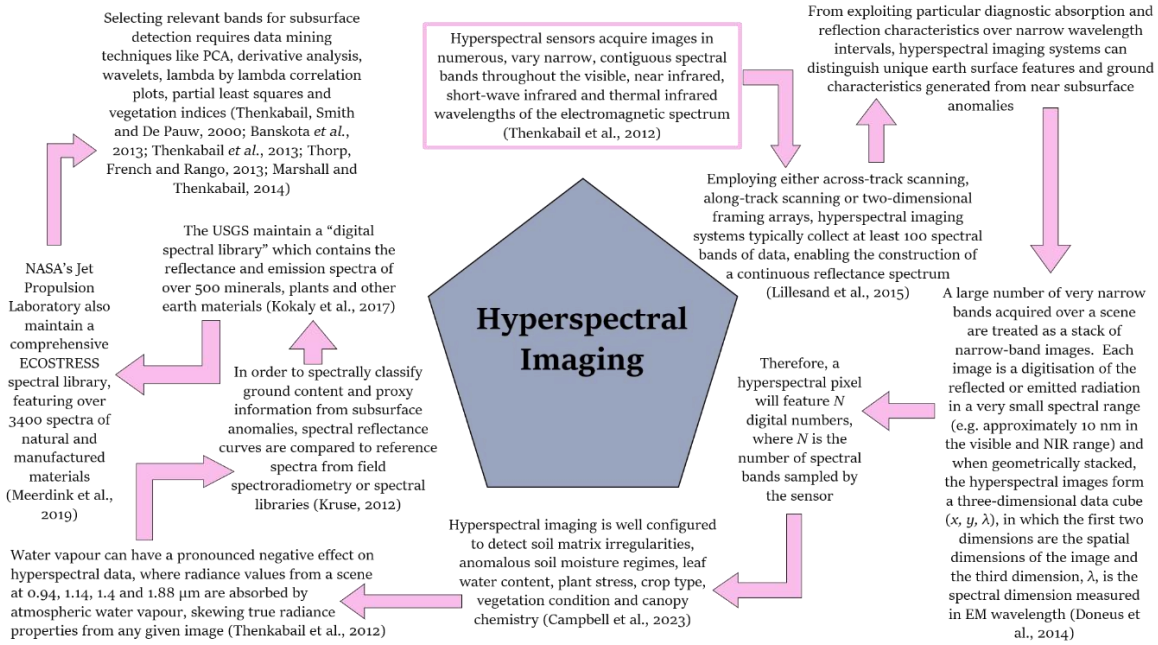



**Figure D4**. Principles of hyperspectral imaging. Pink box denotes beginning of flow graphic and pink arrows depict flow of information.

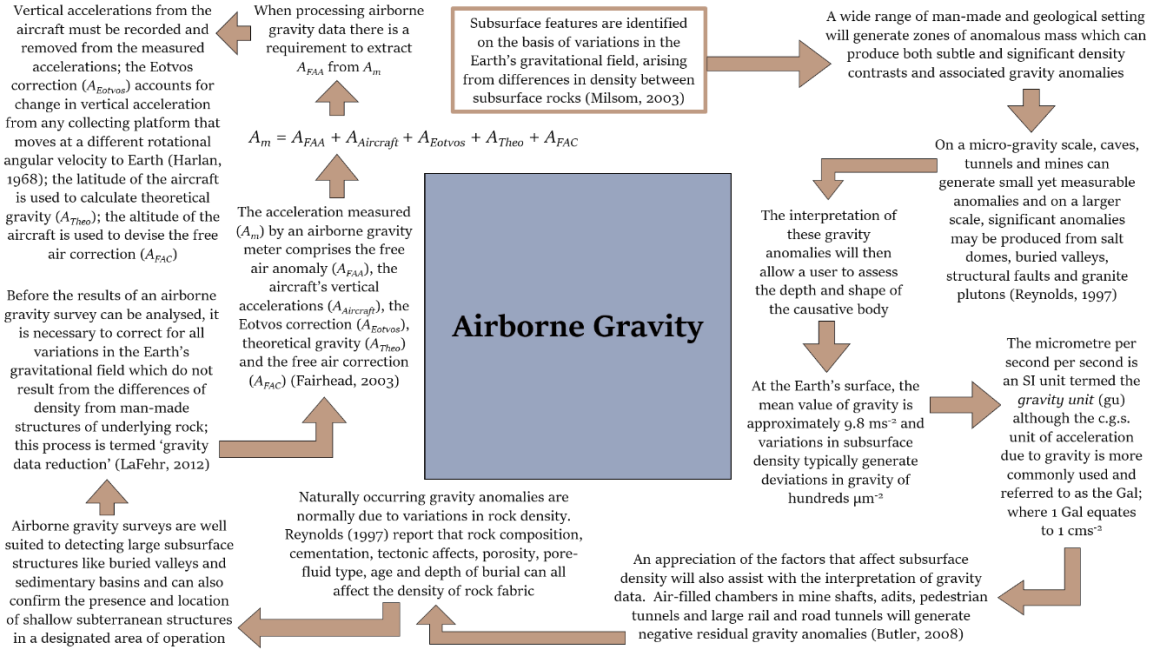



**Figure D5**. Principles of airborne gravity. Brown box denotes beginning of flow graphic and brown arrows depict flow of information.

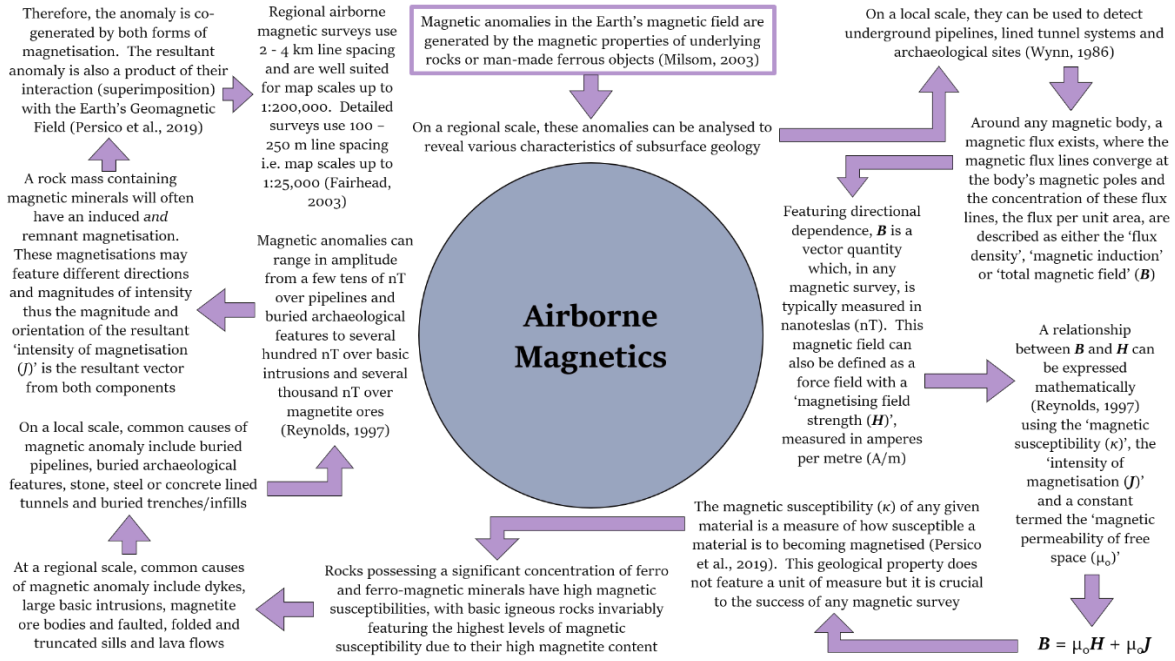



**Figure D6**. Principles of airborne magnetics. Purple box denotes beginning of flow graphic and purple arrows depict flow of information.

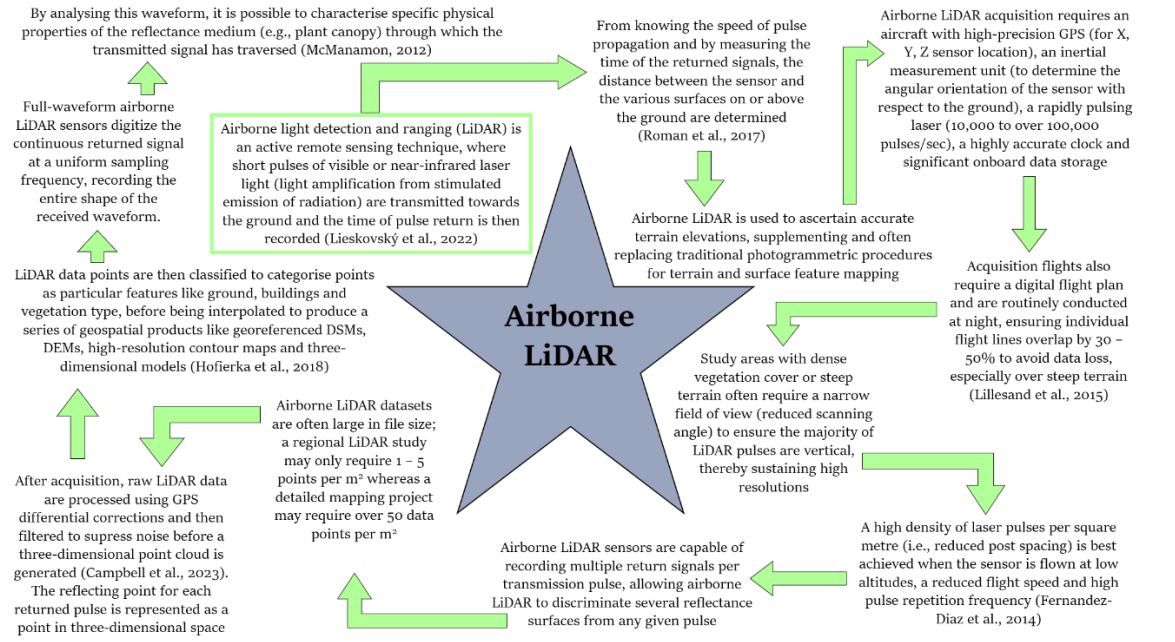



**Figure D7**. Principles of airborne LiDAR. Light green box denotes beginning of flow graphic and light green arrows depict flow of information.

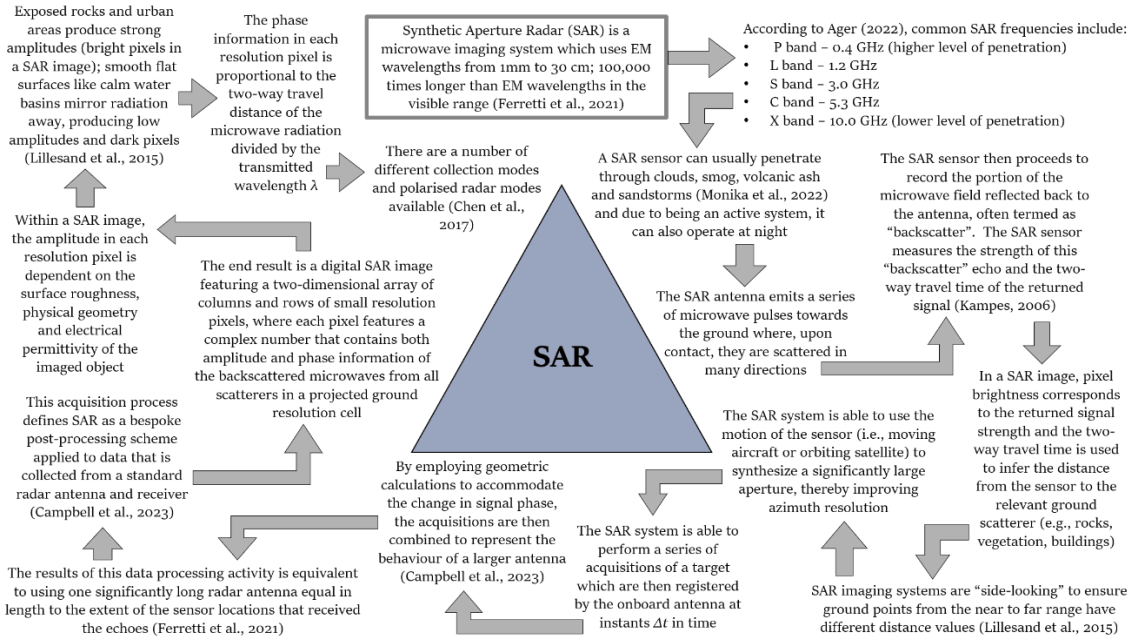



**Figure D8**. Principles of synthetic aperture radar (SAR). Grey box denotes beginning of flow graphic and grey arrows depict flow of information.

# E

*Appendix to Chapter 3*

# Maxar image metadata for Carn Euny

Maxar image bundles containing a high-resolution multispectral TIFF file, a panchromatic image and a pansharpened RGB image are selected from a catalogue of image tiles over Carn Euny using the Maxar ARD Dashboard. Each image tile contains a user defined area of interest (AOI) and satisfies a user-controlled selection criterion. The Maxar high-resolution image bundles listed in Table E1 contain the images used in this study. Each image file is clipped to the predefined AOI, bundle block adjusted (i.e. aligning pixels within a stack of images), greater than three years old (Maxar training data), contain less than 40% cloud cover, off-nadir angles no greater than 30 degrees and a minimum sun elevation of 5 degrees. The projected coordinate system of each image is: WGS 1984 UTM Zone 30N.

**Table E1**
The eight Maxar high-resolution image bundles of Carn Euny used in this study are listed below in order of calendar month. Each image bundle of Carn Euny contains a clipped multispectral TIFF file, a panchromatic image and a pansharpened RGB image. Image bundle file names are shown in the first column with supporting metadata in successive columns. All images files are sourced from the Maxar ARD Dashboard.

| Maxar Image Bundle (filename) | Image Acquisition Date | Maxar Earth Observation Satellite Sensor | No of Spectral Bands | Spatial Resolution (m) | |
|---|---|---|---|---|---|
| | | | | PAN | Multispectral |
| AE025918-BBAD-489C-B7DC-813221CCF056-INV | 6 Jan 18 | WorldView-4 | 4 | 0.33 | 1.31 |
| 103001001174D000 | 3 Mar 12 | WorldView-2 | 8 | 0.55 | 2.21 |
| 1030050087F96A00 | 21 Apr 19 | WorldView-2 | 8 | 0.58 | 2.31 |
| 1030010068BBF200 | 23 Apr 17 | WorldView-2 | 8 | 0.49 | 1.98 |
| 48156F7F-9FFA-4FB3-BDB0-8E2E641D996E-INV | 26 Jul 18 | WorldView-4 | 4 | 0.35 | 1.41 |
| 1050410002390E00 | 16 Aug 13 | GeoEye-01 | 4 | 0.45 | 1.80 |
| 1050410003EEA000 | 10 Oct 13 | GeoEye-01 | 4 | 0.45 | 1.80 |
| 1030050035F9B800 | 24 Nov 14 | WorldView-2 | 8 | 0.47 | 1.89 |

# F

*Appendix to Chapter 3*

# Broadband vegetation indices

Numerous broadband and narrowband vegetation indices are available in published literature, each using a different algebraic computation of the various spectral bands from airborne and spaceborne multispectral imaging to determine specific physiological and phenological information from vegetated scenes (Basso et al., 2004).

From examining several recent publications (Agapiou et al., 2012a; Allbed and Kumar, 2013; Bennett et al., 2012; Cerra et al., 2018; James et al., 2020; Moriarty et al., 2018), 37 VIs were selected in this study (Table F1), each applied as a unique broadband computation of the spectral information from eight Maxar high-resolution multispectral images of Carn Euny. The VI names, abbreviations, equations and supporting references are shown in Table F1, along with the acquisition dates for each of the eight multispectral images (columns 5 to 12). For each image, correlation coefficients, *R*, between each VI and residual gravity over the fogou are shown. Cooler months see weak correlations and warmer months see stronger correlations. The six VIs with correlation coefficients greater than |0.7| are from the multispectral image dated 16 Aug 13 and highlighted green. Of note, the VI correlations with gravity from the multispectral image dated 23 Apr 17 are poor performing and inconsistent with the general trend in observed correlations across the four seasons of a temperate calendar year. Significant amounts of rainfall and/or cooler temperatures in the days and weeks leading up to this image acquisition date is a likely explanation for these observations.

**Table F1**

All 37 VIs used in this study are in the first column. Each VI is applied as a broadband computation of the spectral information from each high-resolution multispectral TIFF file. Each multispectral TIFF file is contained within an image bundle found at Appendix E. Abbreviations, spectral equations and example references are shown for each VI, where R = Red, G = Green, B = Blue and NIR = Near Infrared. For the Global Environmental Monitoring Index (GEMI), the mathematical expression for *n* can be found in table footnote 1. For each VI and image date combination, correlation coefficients, *R*, with residual gravity across the fogou are shown. Poor correlations (R < |0.3|) are highlighted red and strong correlations (R > |0.7|) are highlighted green. Of note, VIs with strong correlations (R > |0.7|) are all algebraic manifestations of Red/Blue (R/B).

| Vegetation Index (VI) | VI Abb. | VI Equation | Example References | Correlation coefficient, *R*, between VI profile and residual bouguer anomaly | | | | | | | |
|---|---|---|---|---|---|---|---|---|---|---|---|
| | | | | 6 Jan 18 | 3 Mar 12 | 21 Apr 19 | 23 Apr 17 | 26 Jul 18 | 16 Aug 13 | 10 Oct 13 | 24 Nov 14 |
| Enhanced Vegetation Index | EVI | 2.5[(NIR - R) / (NIR + 6R - 7.5B + 1)] | Agapiou et al., 2012a; Evrendilek and Gulbeyaz, 2008; Huete et al., 2014, 2002, 1997; Jiang et al., 2008; Matsushita et al., 2007 | 0.09 | 0.58 | 0.45 | 0.01 | 0.51 | 0.73 | 0.22 | 0.01 |
| Green Normalised Difference Vegetation Index | Green NDVI | (NIR – G) / (NIR + G) | Agapiou et al., 2012a; Cerra et al., 2018; Gitelson et al., 1996; James et al., 2020; Moriarty et al., 2018 | 0.02 | 0.59 | 0.41 | -0.11 | 0.52 | 0.44 | -0.16 | 0.05 |
| Normalised Difference Vegetation Index | NDVI | (NIR – R) / (NIR + R) | Agapiou et al., 2012a; Basso et al., 2004; Huete et al., 2002; Rondeaux et al., 1996; Rouse et al., 1973; Zeng et al., 2023 | 0.03 | 0.52 | 0.43 | -0.09 | 0.54 | 0.59 | -0.03 | -0.01 |
| Simple Ratio | SR | NIR/R | Agapiou et al., 2012a; Bennett et al., 2012; Birth and McVey, 1968; James et al., 2020; Jordan, 1969; Moriarty et al., 2018 | 0.22 | 0.48 | 0.42 | 0.05 | 0.51 | 0.57 | 0.27 | 0.24 |
| Modified Simple Ratio | MSR | [(NIR/R)-1] / [(NIR/R)$^{0.5}$ + 1] | Agapiou et al., 2012a; Chen, 1996; James et al., 2020; Moriarty et al., 2018 | 0.24 | 0.49 | 0.42 | 0.01 | 0.52 | 0.58 | 0.21 | 0.22 |
| Simple Ratio x Normalised Difference Vegetation Index | SR x NDVI | (NIR/R) x [(NIR – R) / (NIR + R)] | Agapiou et al., 2012a; Gong et al., 2003; Huete et al., 2014 | 0.23 | 0.48 | 0.42 | 0.06 | 0.47 | 0.56 | 0.31 | 0.24 |
| Modified Triangular Vegetation Index | MTVI | 1.2[(1.2(NIR-G)) - (2.5(R-G))] | Haboudane et al., 2004; Huete et al., 2014; Liu et al., 2010; Moriarty et al., 2018 | -0.15 | 0.19 | 0.40 | -0.06 | 0.56 | 0.59 | 0.06 | 0.20 |
| Modified Triangular Vegetation Index 2 | MTVI2 | 1.2[(1.2(NIR-G)) - (2.5(R-G))] / [(2NIR + 1)$^2$ – (6NIR – 5R$^{0.5}$)] | Haboudane et al., 2004; Nguy-Robertson, 2013; Smith et al., 2008 | 0.03 | 0.51 | 0.43 | -0.08 | 0.53 | 0.62 | 0.00 | 0.16 |
| Renormalized Difference Vegetation Index | RDVI | (NIR – R) / (NIR + R)$^{0.5}$ | Agapiou et al., 2012a; Cerra et al., 2018; Roujean and Breon, 1995 | -0.11 | 0.26 | 0.41 | -0.08 | 0.57 | 0.58 | 0.00 | 0.18 |
| Ratio Vegetation Index | RVI | R/NIR | Agapiou et al., 2012a; Bannari et al., 1995; Basso et al., 2004 | -0.03 | -0.53 | -0.43 | 0.11 | -0.54 | -0.59 | 0.07 | 0.03 |
| Difference Vegetation Index | DVI | NIR - R | Agapiou et al., 2012a; Basso et al., 2004; Cerra et al., 2018; Huete et al., 2014; Tucker, 1979 | -0.16 | 0.18 | 0.40 | -0.08 | 0.58 | 0.57 | 0.02 | 0.23 |
| Modified Soil Adjusted Vegetation Index | MSAVI | [2NIR + 1 - ((2NIR + 1)$^{0.5}$ - 8(NIR - R))$^{0.5}$] / 2 | Agapiou et al., 2012a; Basso et al., 2004; Qi et al., 1994; Rondeaux et al., 1996 | 0.03 | 0.55 | 0.42 | -0.09 | 0.54 | 0.59 | -0.07 | -0.07 |

| | | | | | | | | | | | |
|---|---|---|---|---|---|---|---|---|---|---|---|
| Global Environmental Monitoring Index[1] | GEMI[1] | n(1 - 0.25n) x (R - 0.125) / (1 - R) | Agapiou et al., 2012a; Cerra et al., 2018; Pinty and Verstraete, 1992; Rondeaux et al., 1996 | -0.16 | 0.32 | 0.38 | -0.01 | 0.58 | 0.57 | 0.02 | 0.12 |
| Green Difference Vegetation Index | GDVI | NIR-G | Cerra et al., 2018; Huete et al., 2014; Sripada et al., 2006 | -0.17 | 0.17 | 0.39 | -0.09 | 0.60 | 0.55 | -0.02 | 0.26 |
| Green Ratio Vegetation Index | GRVI | NIR/G | Cerra et al., 2018; James et al., 2020; Moriarty et al., 2018; Sripada et al., 2006 | 0.10 | 0.51 | 0.42 | -0.05 | 0.52 | 0.39 | -0.06 | 0.32 |
| Infrared Percentage Vegetation Index | IPVI | NIR / (NIR + R) | Cerra et al., 2018; Crippen, 1990; Huete et al., 2014 | 0.03 | 0.55 | 0.42 | -0.07 | 0.54 | 0.59 | -0.06 | -0.05 |
| Iron Oxide | Iron Oxide | R/B | Al-Quraishi et al., 2022; Dogan, 2008; Ducart et al., 2016; Huete et al., 2014; Mendes et al., 2022; Segal, 1982; Zaigham Abbas Naqvi et al., 2021 | 0.21 | 0.04 | -0.43 | -0.02 | -0.29 | -0.82 | -0.64 | 0.17 |
| Nonlinear Vegetation Index | NLI | $(NIR^2 – R) / (NIR^2 + R)$ | Cerra et al., 2018; Goel and Qin, 1994; James et al., 2020; Moriarty et al., 2018 | -0.06 | 0.32 | 0.42 | -0.14 | 0.60 | 0.62 | -0.14 | -0.06 |
| Soil Adjusted Vegetation Index | SAVI | 1.5(NIR – R) / (NIR + R + 0.5) | Basso et al., 2004; Cerra et al., 2018; Major et al., 1990; Rondeaux et al., 1996 | 0.03 | 0.52 | 0.43 | -0.09 | 0.54 | 0.59 | -0.03 | -0.01 |
| Transformed Vegetation Index | TrVI | $[0.5 + ((NIR - R) / (NIR + R))]^{0.5}$ | Cerra et al., 2018; Huete et al., 2014; Tucker, 1979 | 0.03 | 0.53 | 0.43 | -0.10 | 0.54 | 0.59 | -0.04 | -0.02 |
| Visible Atmospherically Resistant Index | VARI | (G - R) / (G + R - B) | Cerra et al., 2018; Gitelson et al., 2002; Huete et al., 2014 | 0.11 | 0.42 | 0.41 | 0.05 | 0.45 | 0.64 | 0.25 | -0.02 |
| Brightness Index | BI | $(R^2 + NIR^2)^{0.5}$ | Allbed and Kumar, 2013; Khan et al., 2005 | -0.20 | 0.09 | 0.36 | -0.07 | 0.41 | 0.56 | 0.04 | 0.25 |
| Red Green Ratio Index | RGRI | R/G | Hak et al., 2023; James et al., 2020; Mallmann et al., 2020; Moriarty et al., 2018 | -0.08 | -0.43 | -0.42 | -0.08 | -0.42 | -0.63 | -0.18 | -0.01 |
| Plant Senescence Reflectance Index | PSRI | (R - G) / NIR | Bennett et al., 2012; Cerra et al., 2018; James et al., 2020; Merzlyak et al., 1999; Moriarty et al., 2018 | -0.04 | -0.31 | -0.41 | -0.01 | -0.50 | -0.64 | -0.22 | 0.48 |
| Optimised Soil Adjusted Vegetation Index | OSAVI | [1.5(NIR – R)] / (NIR + R +0.16) | Agapiou et al., 2012a; James et al., 2020; Moriarty et al., 2018; Rondeaux et al., 1996 | 0.03 | 0.52 | 0.43 | -0.09 | 0.54 | 0.59 | -0.03 | -0.01 |
| Structure Insensitive Pigment Index | SIPI | (NIR - B) / (NIR - R) | Cerra et al., 2018; Kureel et al., 2022; Lakkaraju et al., 2010; Lees et al., 2020; Penuelas et al., 1995; Susantoro et al., 2018 | -0.09 | -0.55 | -0.48 | 0.09 | -0.53 | -0.73 | -0.07 | 0.06 |
| Atmospherically Resistant Vegetation Index | ARVI | (NIR - (2R - B)) / (NIR + (2R - B)) | Bennett et al., 2012; Kaufman and Tanre, 1992; Miura et al., 2000; Xue and Su, 2017 | 0.06 | 0.55 | 0.45 | -0.05 | 0.52 | 0.64 | 0.05 | -0.10 |
| Soil Salinity Index 1 | SI1 | $(B \times R)^{0.5}$ | Allbed and Kumar, 2013; Douaoui et al., 2006 | -0.20 | -0.49 | -0.40 | 0.08 | -0.36 | -0.39 | 0.06 | -0.07 |
| Soil Salinity Index 2 | SI2 | $(G \times R)^{0.5}$ | Allbed and Kumar, 2013; Douaoui et al., 2006 | -0.25 | -0.52 | -0.46 | 0.08 | -0.35 | -0.45 | -0.01 | -0.05 |
| Soil Salinity Index 3 | SI3 | $(G^2 + R^2 + NIR^2)^{0.5}$ | Allbed and Kumar, 2013; Douaoui et al., 2006 | -0.02 | 0.09 | 0.36 | -0.06 | 0.36 | 0.56 | 0.05 | 0.25 |

| | | | | | | | | | | | |
|---|---|---|---|---|---|---|---|---|---|---|---|
| Soil Salinity Index 4 | SI4 | $(R^2 + G^2)^{0.5}$ | Allbed and Kumar, 2013; Douaoui et al., 2006 | -0.25 | -0.50 | -0.47 | 0.09 | -0.36 | -0.37 | 0.12 | -0.03 |
| Soil Salinity Index 5 | SI5 | B/R | Abbas and Khan, 2007; Allbed and Kumar, 2013; Metternicht and Zinck, 1997 | 0.31 | 0.02 | 0.41 | -0.04 | 0.35 | 0.80 | 0.56 | -0.07 |
| Soil Salinity Index 6 | SI6 | (B - R) / (B + R) | Abbas and Khan, 2007; Allbed and Kumar, 2013; Metternicht and Zinck, 1997 | 0.23 | 0.00 | 0.42 | -0.02 | 0.33 | 0.81 | 0.60 | -0.12 |
| Soil Salinity Index 7 | SI7 | (R x G) / B | Abbas and Khan, 2007; Allbed and Kumar, 2013; Metternicht and Zinck, 1997 | -0.26 | -0.34 | -0.56 | 0.05 | -0.36 | -0.73 | -0.35 | 0.08 |
| Soil Salinity Index 8 | SI8 | $(B \times R)^{0.5}$ | Abbas and Khan, 2007; Allbed and Kumar, 2013; Metternicht and Zinck, 1997 | -0.20 | -0.49 | -0.40 | 0.08 | -0.36 | -0.39 | 0.06 | -0.07 |
| Soil Salinity Index 9 | SI9 | (B x R) / G | Abbas and Khan, 2007; Allbed and Kumar, 2013; Metternicht and Zinck, 1997 | -0.07 | -0.48 | -0.38 | 0.10 | -0.41 | -0.40 | 0.11 | 0.02 |
| Soil Salinity Index 10 | SI10 | (R x NIR) / G | Abbas and Khan, 2007; Allbed and Kumar, 2013; Metternicht and Zinck, 1997 | -0.29 | -0.27 | -0.48 | -0.42 | -0.09 | -0.60 | -0.31 | -0.01 |

[1] For Global Environmental Monitoring Index (GEMI) broadband spectral equation, *n* = [2(NIR**2 - R**2) + 1.5NIR + 0.5R] / (NIR + R + 0.5).

# G

*Appendix to Chapter 3*

# Modelling gravity across Carn Euny's fogou

Along profile A-A', observed gravity readings are recorded every 2 m to an accuracy of +/- 2 µGals and then reduced to bouguer anomaly values using instrumental and tidal drift corrections, free air adjustments and bouguer corrections. At 12 m, the observed 0.06 mGal reduction in gravitational field strength is caused by the lower density air column extending along the length of the fogou, closely matched by the theoretical gravity anomaly generated using gravity modelling freeware 'Grav2dc' (Cooper, 1998). Away from the fogou at 4 m and 22 m, localised gravity 'highs' of approximately 0.03 mGal are observed. Albeit not modelled, these are expected to represent shallow rock formations from the original Iron Age settlement, noting Carn Euny is only partially excavated (Greaney, 2017). There is also an unaccountable -0.03 mGal gravity 'low' observed at 18 m which, without further geophysical investigation, is beyond the scope of our interpretation.

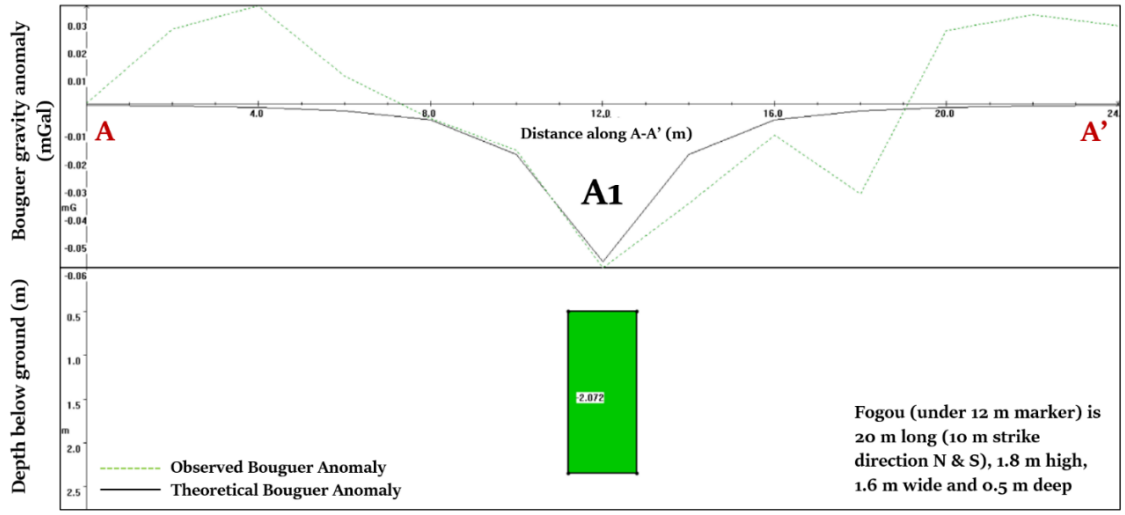



**Figure G1**. Modelling residual gravity over the fogou in Carn Euny Ancient Village. Green dashed line denotes observed residual bouguer anomaly along profile A-A'. Black continuous line denotes theoretical bouguer anomaly along profile A-A', calculated by approximating the fogou to a 20 m long rectangular conduit of air in gravity modelling program 'Grav2dc'. In this model, the density contrast between the air in the fogou and the surrounding soil and rock matrix is -2.072 g/cm$^3$. The survey profile A-A' is 24 m long and the Iron Age fogou (stone lined underground passage) is 1.6 m wide, 1.8 m high and 0.5 m deep, with a 20 m tunnel azimuth perpendicular to the profile at 12 m.

# H

*Appendix to Chapter 4*

# Maxar image metadata for Aunay Abbey

Maxar image bundles containing a high-resolution multispectral TIFF file, a panchromatic image and a pansharpened RGB image are selected from a catalogue of image tiles over Aunay Abbey and La Garenne using the Maxar ARD Dashboard. Each image tile contains a user defined area of interest (AOI) and satisfies a user-controlled selection criterion. The Maxar high-resolution image bundles listed in Table H1 contain the images used in this study. Each image file is clipped to the predefined AOI of Aunay Abbey and La Garenne, bundle block adjusted (i.e. aligning pixels within a stack of images), greater than three years old (Maxar training data), contain less than 40% cloud cover, off-nadir angles no greater than 30 degrees and a minimum sun elevation of 5 degrees. The projected coordinate system of each image is WGS 1984 UTM Zone 30N and each image has a 16-bit pixel depth.

**Table H1**
The six Maxar high-resolution image bundles of Aunay Abbey and La Garenne are listed below in order of calendar month. Each image bundle of the study area contains a clipped multispectral TIFF file, a panchromatic image and a pansharpened RGB image. Image bundle file names are shown in the first column with supporting metadata in successive columns. All images files are sourced from the Maxar ARD Dashboard.

| Maxar Image Bundle (filename) | Image Acquisition Date | Maxar Earth Observation Satellite Sensor | No of Spectral Bands | Spatial Resolution [Multispectral] (m) | Meteorological Data[1] | |
|---|---|---|---|---|---|---|
| | | | | | Max Daily Temp (°C) | Three-day accumulated precipitation (mm) |
| 10300100A0CD5900 | 17 Feb 20 | WorldView-2 | 8 | 2.00 | 11 | 13 |
| 103005000AF98700 | 23 Mar 11 | WorldView-2 | 8 | 1.96 | 16 | 0 |
| 103005004DF8C800 | 6 May 16 | WorldView-2 | 8 | 2.04 | 23 | 0 |
| 103005003CF9B800 | 22 May 15 | WorldView-2 | 8 | 1.91 | 18 | 1 |
| 105005000BDD9200 | 23 May 17 | GeoEye-01 | 4 | 1.99 | 21 | 1 |
| 1030050094F8C100 | 21 Sep 19 | WorldView-2 | 8 | 1.95 | 29 | 0 |

[1] Archived meteorological data shown for Caen (20 miles from Aunay Abbey) - sourced from: www.weatheronline.co.uk/France/Caen.

# J

*Appendix to Chapter 4*

# Example catalogue of black, grey and white (BGW) graded imagery using multispectral FCCs, edge detection and LiDAR hillshade analysis

In total, we apply a black, grey or white (BGW) subsurface detection rating to 120 multispectral FCCs, 36 multispectral edge detection raster images and 180 LiDAR DSM FCCs. A black subsurface detection rating is awarded to images where distinct surface expressions from subsurface anomalies are evident. A grey subsurface detection rating is awarded to images that contain *vague* surface expressions from suspected underground features, and a white subsurface detection rating is assigned to those images where no obvious subsurface anomaly is seen. For each image processing technique, BGW subsurface detection percentages can be found in Tables 4.3, 4.4 and 4.5 respectively.

In our multispectral FCCs and Sobel edge detection raster images, linear and regular shaped surface expressions from subsurface irregularities are observed as anomalous reflectance values from overlying vegetation, which within the abbey field, is cool-season grass comprising meadow grass, couch grass and Festuca. In our LiDAR hillshade analysis, surface expressions from subsurface features are observed as linear and regular shaped micro-relief anomalies.

Figures J1a, J1b and J1c are examples of black, grey and white-rated FCCs, using the six-layer image stack from Figure 4.4 and multispectral imaged dated 23 May 2017. Detection performance as a function of season and FCC band combination are discussed in detail in Section 4.4.2.1. Similarly, Figures J1d, J1e and J1f are examples of black, grey and white Sobel edge detection

rasters, produced from the various subsurface detection indices of the same multispectral image. Edge detection performance is also discussed in detail in Section 4.4.2.2. Figures J1g, J1h and J1i are examples of black, grey and white DSM FCCs. The dependencies on DSM FCC band combination (sun azimuth) and sun elevation angle are discussed in Section 4.4.2.3. Of note, and in addition to the distinct horizontal anomalies in Figures J1a, J1d and J1g, a closer inspection of Figures J1a and J1d reveal diagonal lines radiating from the centre of the abbey field. These unique linear reflection anomalies, along with all others, are interpreted in Section 4.5.

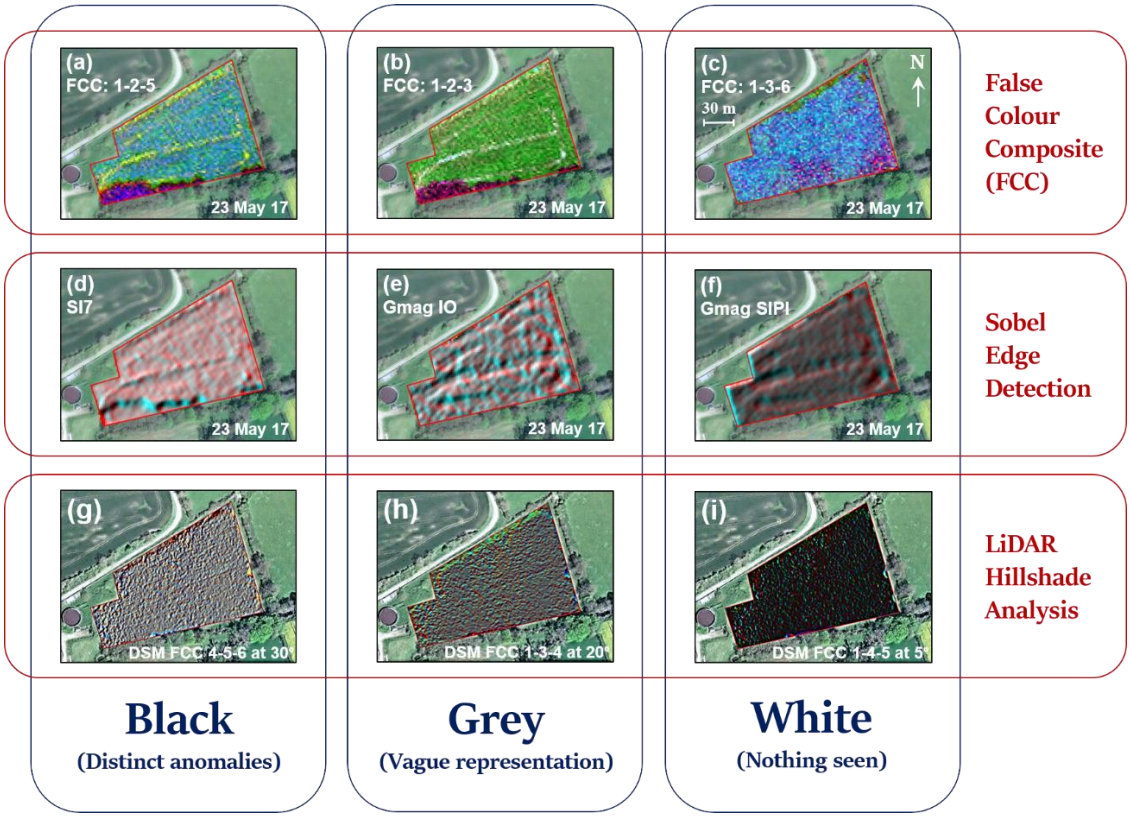



**Figure J1**. A catalogue of imagery examples featuring black, grey and white (BGW) subsurface detection ratings with multispectral false colour composites (FCCs), Sobel edge detection raster images and hillshaded digital surface model (DSM) FCCs. Figures J1a – J1f use multispectral image dated 23 May 2017 and Figures J1g – J1i use a very-high-resolution (VHR) DSM produced in 2023. a). Example of a black grade FCC with band combination 1-2-5. b). Example of a grey grade FCC with band combination 1-2-3. c). Example of a white grade FCC with band combination 1-3-6. d). Example of a black grade edge detection raster image using soil salinity index 7 (SI7), filtered with Sobel horizontal (layer 1) and Sobel vertical (layer 2) edge detection filters; stacked and observed in Red-Green-Blue (RGB) as layers 1-2-2. e). Example of a grey grade edge detection raster image using the gradient magnitude (Gmag) of the Iron Oxide (IO) index, filtered and stacked as per Figure J1d. f). Example of a white grade edge detection raster image using Gmag of the Structure Insensitive Pigment Index (SIPI), filtered and stacked as per Figure J1d. g). Example of a black grade hillshaded DSM FCC with DSM bands 4-5-6 in RGB and a sun elevation angle of 30 degrees. h). Example of a grey grade hillshaded DSM FCC with DSM bands 1-3-4 and a sun elevation angle of 20 degrees. i). Example of a white grade hillshaded DSM FCC with DSM bands 1-4-5 and a sun elevation angle of 5 degrees.

# K

*Appendix to Chapter 5*

# Multispectral image processing workflow

The multispectral image processing workflow used in this study was adapted from Morley et al. (2025b; Chapter 3). The vegetation indices (VIs) used in the workflow, termed subsurface detection indices, correlated considerably well with gravity and ground penetrating radar (GPR) data over a near-surface tunnel in Morley et al. (2025b; Chapter 3).

The SI7 and SIPI have also been celebrated in previous studies; SI7 was the best performing index in an appraisal of irrigated soil salinity (Abbas and Khan, 2007) and SIPI was the most effective at detecting the carotenoid to chlorophyll *a* ratio in leaves (Penuelas et al., 1995).

Of note, all three of these vegetation indices in the workflow are algebraic manifestations of the Red/Blue reflectance ratio (Figure K1). As demonstrated in Morley et al. (2025b; Chapter 3), this reflectance ratio is sensitive to near-surface incongruities, especially when using Maxar imaging sensors in the warm summer months of a temperate, vegetated landscape.

Compared to the image processing workflow in Morley et al. (2025b; Chapter 3), this workflow bypasses the requirement to pansharpen the vegetation indices because the border fields around Glastonbury Tor are sufficiently large enough to omit the need for higher spatial resolution. This way, the spectral fidelity of the vegetation indices are preserved, guaranteeing higher levels of accuracy in our false colour composite (FCC) and edge detection analyses.

The workflow in Figure K1 also calculates the VIs gradient magnitude (Gmag), before clipping all six image tiles to the individual extent of each border field north of Glastonbury Tor. For each field, these six clipped vegetation indices are layer stacked, forming an optimised six-layer image stack (Figure K1). Using FCCs and edge detection analyses, these image stacks were used to detect

linear reflectance anomalies in the border fields which already contain abnormal elevation change (Section 5.2.1 and 5.3.1).

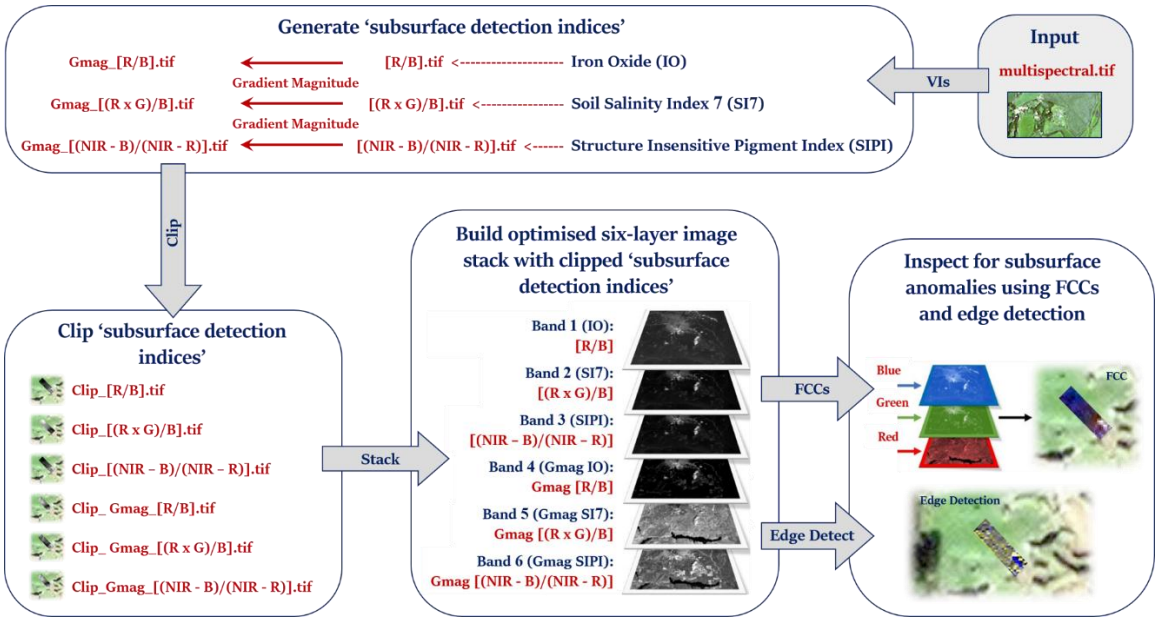



**Figure K1**. The multispectral image processing workflow used to inspect linear anomaly 4 (LA4) in Field 2 and linear anomaly 6 (LA6) in Field 9, north of Glastonbury Tor. Adapted from Morley et al. (2025b; Chapter 3), this workflow is designed to detect anomalous reflectance behaviour from soil and cool-season vegetation over shallow, subsurface anomalies in temperate environments.

# M

*Appendix to Chapter 5*

# Electrical Resistivity Tomography (ERT) profiles

Electrical resistivity tomography (ERT) profiles were performed across two statistically anomalous elevation-change profiles in our LiDAR elevation differencing (Figures 5.3 and 5.4). These anomalous elevation profiles were average elevation-change profiles from linear anomaly 4 (LA4) in Field 2 (Figures 5.3e and 5.4d) and linear anomaly 6 (LA6) in Field 9 (Figures 5.3g and 5.4f).

A single 71 m long resistivity profile was positioned perpendicular-to and across the centre of LA4 and LA6 using 72 stainless-steel electrodes at 1 m intervals. Electrical resistivity values of the near-surface along each profile were then retrieved using a Wenner-Schlumberger acquisition configuration (e.g., Supandi, 2021). Figure M1a shows the location and orientation of resistivity profile X-X' across LA4 in Field 2, and Figure M1b shows the location and orientation of resistivity profile Y-Y' across LA6 in Field 9.

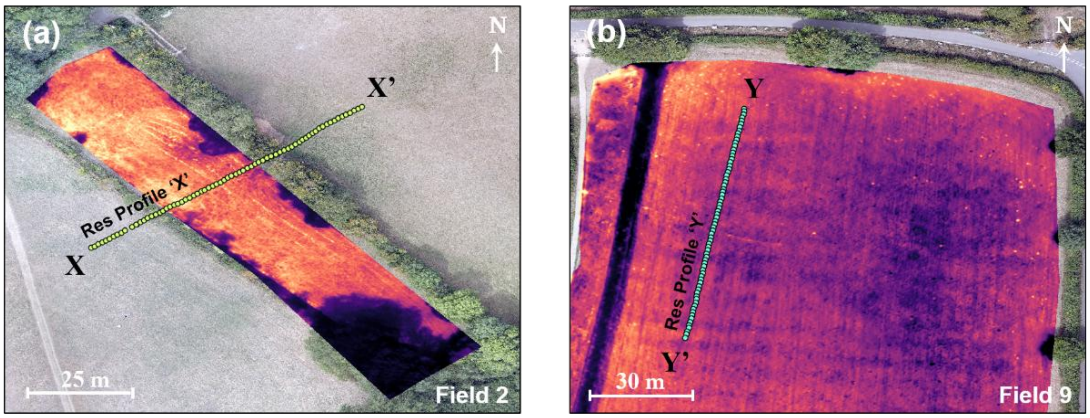



**Figure M1**. Location and orientation of 71 m long electrical resistivity tomography (ERT) profiles across linear anomaly 4 (LA4) in Field 2 and linear anomaly 6 (LA6) in Field 9. ERT profiles are superimposed with very-high-resolution (VHR) red-green-blue (RGB) imagery and thermal imagery from a DJI M300 rotary drone survey. a). Location and orientation of ERT profile X-X' across LA4 in Field 2. Yellow dots resemble locations of individual electrodes along X-X'. b). Location and orientation of ERT profile Y-Y' across LA6 in Field 9. Cyan dots resemble locations of individual electrodes along Y-Y'.

The 2D ERT profiles along resistivity profiles X-X' and Y-Y' are seen in Figure M2. After recording the ground elevation at each electrode, the apparent (observed) resistivity profiles from each field were inverted iteratively to produce the model ERT profiles in Figure M2. Four iterations of this inversion process were performed for each resistivity profile, producing two model ERT profiles. Figure M2a is the model 2D ERT profile across LA4 (X-X') and Figure M2b is the model 2D ERT profile across LA6 (Y-Y'). Profile distance and profile elevation above mean sea level (MSL) are as shown. Resistivity values relate to the colour bar under the profile and the accuracy of the model 2D ERT profiles are defined by the root mean square error (RMSE) value above each profile.

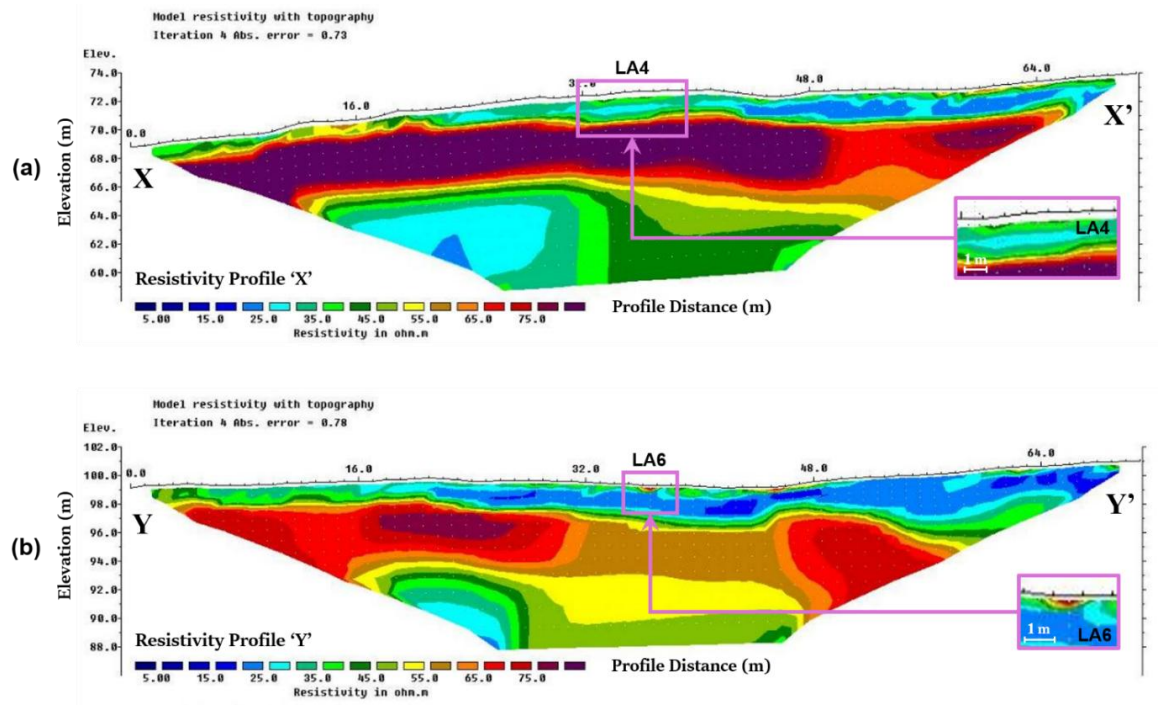



**Figure M2**. 2D electrical resistivity tomography (ERT) profiles across linear anomaly 4 (LA4) in Field 2 and linear anomaly 6 (LA6) in Field 9. a). 2D ERT profile X-X' across LA4 in Field 2. Profile distance and profile elevation above mean sea level (MSL) are as shown and resistivity values relate to colour bar under profile in ohm.metres (Ω.m). Image inset shows close up of resistivity anomaly from suspected underground spring beneath LA4. b). 2D ERT profile Y-Y' across LA6 in Field 9. Profile distance and profile elevation above MSL are as shown and resistivity values relate to colour bar under profile in ohm.metres (Ω.m). Image inset shows close up of resistivity anomaly from suspected utility pipe beneath LA6.

In Figure M2a, LA4 shows a distinct change in electrical resistivity within the first 0.5 m of the subsurface. Here, resistivity is 40 – 45 Ω.m (dark green and light green ERT anomalies), which is approximately 10 Ω.m higher than the shallow ground matrix beside LA4. Below this high resistivity anomaly (c.0.5 – 1 m depth) is a significant wedge of comparably lower resistivity material, which we suspect is closer to 30 Ω.m (light blue ERT wedge). When combined with our LiDAR elevation change, multispectral analyses and thermal observations, we define LA4 as a series of shallow, hydrological anomalies, where groundwater is carried away from the Tor. Collectively, we describe this LA as a shallow, underground spring, which appears to be no deeper than 1 m below the ground surface.

In Figure M2b, LA6 is a small, 1 m wide semi-circular shaped 75 Ω.m resistivity anomaly (crimson red ERT anomaly). In contrast to its surroundings, this resistivity anomaly is also c.35 Ω.m higher than the shallow soil columns either side of it. When combined with our remote sensing analyses, evidence suggests LA6 is a shallow utility pipe, extending east to west beneath Field 9. We are not confident of the pipe's material or its purpose, but the resistivity values in the 2D ERT profile (Figure M2b) suggest it is a clay or concrete pipe (Supandi, 2021; Vickery and Hobbs, 2002) which, given its setting, is likely used for water supply or drainage.

# References


Abate, N., Elfadaly, A., Masini, N., Lasaponara, R., 2020. Multitemporal 2016-2018 Sentinel-2 Data Enhancement for Landscape Archaeology: The Case Study of the Foggia Province, Southern Italy. Remote Sens. 12, 1309. https://doi.org/10.3390/rs12081309

Abate, N., Frisetti, A., Marazzi, F., Masini, N., Lasaponara, R., 2021. Multitemporal–Multispectral UAS Surveys for Archaeological Research: The Case Study of San Vincenzo Al Volturno (Molise, Italy). Remote Sens. 13, 2719. https://doi.org/10.3390/rs13142719

Abate, N., Ronchi, D., Vitale, V., Masini, N., Angelini, A., Giuri, F., Minervino Amodio, A., Gennaro, A.M., Ferdani, D., 2023. Integrated Close Range Remote Sensing Techniques for Detecting, Documenting, and Interpreting Lost Medieval Settlements under Canopy: The Case of Altanum (RC, Italy). Land 12, 310. https://doi.org/10.3390/land12020310

Abbas, A., Khan, S., 2007. Using Remote Sensing Techniques for Appraisal of Irrigated Soil Salinity: International Congress on Modelling and Simulation (MODSIM). Adv. Appl. Manag. Decis. Mak. Land Water Environ. Manag. 2632–2638.

Abdel Zaher, M., Saibi, H., Mansour, K., Khalil, A., Soliman, M., 2018. Geothermal exploration using airborne gravity and magnetic data at Siwa Oasis, Western Desert, Egypt. Renew. Sustain. Energy Rev. 82, 3824–3832. https://doi.org/10.1016/j.rser.2017.10.088

Abdel-Hardy, M., 1970. Subsurface drainage mapping by airborne infrared imagery techniques, in: Proceedings of the Oklahoma Academy of Science. pp. 10–18.

Abuzied, S.M., Kaiser, M.F., Shendi, E.-A.H., Abdel-Fattah, M.I., 2020. Multi-criteria decision support for geothermal resources exploration based on remote sensing, GIS and geophysical techniques along the Gulf of Suez coastal area, Egypt. Geothermics 88, 101893. https://doi.org/10.1016/j.geothermics.2020.101893

Achmon, M., Ben-Avraham, Z., 1997. The deep structure of the Carmel fault zone, northern Israel, from gravity field analysis. Tectonics 16, 563–569. https://doi.org/10.1029/96TC02912

Agapiou, A., Alexakis, D., Sarris, A., Hadjimitsis, D., 2013b. Orthogonal Equations of Multi-Spectral Satellite Imagery for the Identification of Un-Excavated Archaeological Sites. Remote Sens. 5, 6560–6586. https://doi.org/10.3390/rs5126560

Agapiou, A., Alexakis, D.D., Hadjimitsis, D.G., 2014. Spectral sensitivity of ALOS, ASTER, IKONOS, LANDSAT and SPOT satellite imagery intended for the detection of archaeological crop marks. Int. J. Digit. Earth 7, 351–372. https://doi.org/10.1080/17538947.2012.674159

Agapiou, A., Hadjimitsis, D., Alexakis, D., 2012a. Evaluation of Broadband and Narrowband Vegetation Indices for the Identification of Archaeological Crop Marks. Remote Sens. 4, 3892–3919. https://doi.org/10.3390/rs4123892

Agapiou, A., Hadjimitsis, D., Sarris, A., Themistocleous, K., Papadavid, G., 2010. Hyperspectral Ground Truth Data for the Detection of Buried Architectural Remains, in: Ioannides, M., Fellner, D., Georgopoulos, A., Hadjimitsis, D.G. (Eds.), Digital Heritage, Lecture Notes in Computer Science. Springer Berlin Heidelberg, Berlin, Heidelberg, pp. 318–331. https://doi.org/10.1007/978-3-642-16873-4_24

Agapiou, A., Hadjimitsis, D.G., Georgopoulos, A., Sarris, A., Alexakis, D.D., 2012b. Towards an Archaeological Index: Identification of the Spectral Regions of Stress Vegetation due to Buried Archaeological Remains, in: Ioannides, M., Fritsch, D., Leissner, J., Davies, R., Remondino, F., Caffo, R. (Eds.),

Progress in Cultural Heritage Preservation, Lecture Notes in Computer Science. Springer Berlin Heidelberg, Berlin, Heidelberg, pp. 129–138. https://doi.org/10.1007/978-3-642-34234-9_13

Agapiou, A., Hadjimitsis, D.G., Sarris, A., Georgopoulos, A., Alexakis, D.D., 2013a. Optimum temporal and spectral window for monitoring crop marks over archaeological remains in the Mediterranean region. J. Archaeol. Sci. 40, 1479–1492. https://doi.org/10.1016/j.jas.2012.10.036

Agapiou, A., Hegyi, A., Gogâltan, F., Stavilă, A., Sava, V., Sarris, A., Floca, C., Dorogostaisky, L., 2023. Exploring the largest known Bronze Age earthworks in Europe through medium resolution multispectral satellite images. Int. J. Appl. Earth Obs. Geoinformation 118, 103239. https://doi.org/10.1016/j.jag.2023.103239

Ager, T.P., 2022. The essentials of SAR: a conceptual view of synthetic aperture radar and its remarkable capabilities, First edition, revision April 2022. ed. TomAger LLC, Lewes, Delaware.

Airbus, 2022. Using Synthetic Aperture Radar (SAR) to detect objects and dark vessels. Air and Space Remote Sensing of the Subsurface dated 29 November 2022.

Alberti, S., Ferretti, A., Leoni, G., Margottini, C., Spizzichino, D., 2017. Surface deformation data in the archaeological site of Petra from medium-resolution satellite radar images and SqueeSAR™ algorithm. J. Cult. Herit. 25, 10–20. https://doi.org/10.1016/j.culher.2017.01.005

Alexakis, D., Sarris, A., Astaras, T., Albanakis, K., 2009. Detection of Neolithic Settlements in Thessaly (Greece) Through Multispectral and Hyperspectral Satellite Imagery. Sensors 9, 1167–1187. https://doi.org/10.3390/s90201167

Aljammaz, A., Sultan, M., Izadi, M., Abotalib, A.Z., Elhebiry, M.S., Emil, M.K., Abdelmohsen, K., Saleh, M., Becker, R., 2021. Land Subsidence Induced by Rapid Urbanization in Arid Environments: A Remote Sensing-Based Investigation. Remote Sens. 13, 1109. https://doi.org/10.3390/rs13061109

Allbed, A., Kumar, L., 2013. Soil Salinity Mapping and Monitoring in Arid and Semi-Arid Regions Using Remote Sensing Technology: A Review. Adv. Remote Sens. 02, 373–385. https://doi.org/10.4236/ars.2013.24040

Allen, R., 2021. History, Memory and Community in Cistercian Normandy (12th–13th Centuries). Downside Rev. 139, 44–64. https://doi.org/10.1177/0012580621995456

Al-Quraishi, A., Mustafa, B., Gopinathan, P., Divya, Y., 2022. Potential of Multispectral Satellite Data for Superficial Iron Oxide Detection in Sulaimaniyah, Iraqi Kurdistan Region. J. Appl. Sci. Technol. Trends 3, 45–52. https://doi.org/10.38094/jastt301171

Ammirati, L., Mondillo, N., Rodas, R.A., Sellers, C., Di Martire, D., 2020. Monitoring Land Surface Deformation Associated with Gold Artisanal Mining in the Zaruma City (Ecuador). Remote Sens. 12, 2135. https://doi.org/10.3390/rs12132135

Amro, I., Mateos, J., Vega, M., Molina, R., Katsaggelos, A.K., 2011. A survey of classical methods and new trends in pansharpening of multispectral images. EURASIP J. Adv. Signal Process. 2011, 79. https://doi.org/10.1186/1687-6180-2011-79

Anantrasirichai, N., Biggs, J., Kelevitz, K., Sadeghi, Z., Wright, T., Thompson, J., Achim, A.M., Bull, D., 2021. Detecting Ground Deformation in the Built Environment Using Sparse Satellite InSAR Data with a Convolutional Neural Network. IEEE Trans. Geosci. Remote Sens. 59, 2940–2950. https://doi.org/10.1109/TGRS.2020.3018315

Anselin, L., 1995. Local Indicators of Spatial Association—LISA. Geographical Analysis 27, 93–115. https://doi.org/10.1111/j.1538-4632.1995.tb00338.x

Aslan, E., Özüpak, Y., 2025. Detection of road extraction from satellite images with deep learning method. Clust. Comput. 28, 72. https://doi.org/10.1007/s10586-024-04880-y

AtkinsRéalis, 2025. AtkinsRéalis - The brilliant way forward. URL https://www.atkinsrealis.com/en/about (accessed 20 Sep 25).

Avery, B.W., 1955. The Soils of the Glastonbury District of Somerset, 1st ed, Memoirs of the soil survey of Great Britain. Her Majesty's Stationary Office, London.

Avery, T.E., Berlin, G.L., 1943-, Avery, T.E., 1992. Fundamentals of remote sensing and airphoto interpretation. Macmillan.

Bannari, A., Morin, D., Bonn, F., Huete, A.R., 1995. A review of vegetation indices. Remote Sens. Rev. 13, 95–120. https://doi.org/10.1080/02757259509532298

Banskota, A., Wynne, R., Thomas, V., Serbin, S., Kayastha, N., Gastellu-Etchegorry, J., Townsend, P., 2013. Investigating the Utility of Wavelet Transforms for Inverting a 3-D Radiative Transfer Model Using Hyperspectral Data to Retrieve Forest LAI. Remote Sens. 5, 2639–2659. https://doi.org/10.3390/rs5062639

Baridon, M., 1998. The scientific imagination and the Baroque garden. Stud. Hist. Gard. Des. Landsc. 18, 5–19. https://doi.org/10.1080/14601176.1998.10435529

Barla, G., Tamburini, A., Del Conte, S., Giannico, C., 2016. InSAR monitoring of tunnel induced ground movements. Geomech. Tunn. 9, 15–22. https://doi.org/10.1002/geot.201500052

Bassani, C., Cavalli, R.M., Goffredo, R., Palombo, A., Pascucci, S., Pignatti, S., 2009. Specific spectral bands for different land cover contexts to improve the efficiency of remote sensing archaeological prospection: The Arpi case study. J. Cult. Herit., ICT and Remote sensing for Cultural Resource Management and Documentation 10, e41–e48. https://doi.org/10.1016/j.culher.2009.09.002

Basso, B., Cammarano, D., De Vita, P., 2004. Remotely sensed vegetation indices: Theory and applications for crop management. Riv. Ital. Agrometeorol. 1, 36–53.

Belesky, D.P., Fedders, J.M., 1995. Comparative Growth Analysis of Cool- and Warm-Season Grasses in a Cool–Temperate Environment. Agron. J. 87, 974–980. https://doi.org/10.2134/agronj1995.00021962008700050034xdup

Bell Geospace, 2021. Exploration Advances in Airborne Gravity Gradiometry Technology. EP News.

Beltrão, J.F., Silva, J.B.C., Costa, J.C., 1991. Robust polynomial fitting method for regional gravity estimation. Geophysics, 56, 80–89. https://doi.org/10.1190/1.1442960

Bennett, R., Welham, K., Hill, R.A., Ford, A., 2010. Making the most of airborne remote sensing techniques for archaeological survey and interpretation (EAC Occasional Paper No. 5), Remote Sensing for Archaeological Heritage Management. 11th EAC Heritage Management Symposium, Reykjavik, Iceland.

Bennett, R., Welham, K., Hill, R.A., Ford, A., 2012. The Application of Vegetation Indices for the Prospection of Archaeological Features in Grass-dominated Environments: Application of Vegetation Indices in Grass-dominated Environments. Archaeol. Prospect. 19, 209–218. https://doi.org/10.1002/arp.1429

Bennett, R., Welham, K., Hill, R.A., Ford, A., 2013. Airborne spectral imagery for archaeological prospection in grassland environments—an evaluation of performance. Antiquity 87, 220–236. https://doi.org/10.1017/S0003598X00048730

Berezowski, V., Mallett, X., Ellis, J., Moffat, I., 2021. Using Ground Penetrating Radar and Resistivity Methods to Locate Unmarked Graves: A Review. Remote Sens. 13, 2880. https://doi.org/10.3390/rs13152880

Berger, Z., 1994. Satellite Hydrocarbon Exploration: Interpretation and Integration Techniques. Spinger-Verlag, Berlin.

Bernatek-Jakiel, A., Jakiel, M., 2021. Identification of soil piping-related depressions using an airborne LiDAR DEM: Role of land use changes. Geomorphology 378, 107591. https://doi.org/10.1016/j.geomorph.2020.107591

Bewley, R.H., 2003. Aerial survey for archaeology: Aerial survey for archaeology. Photogramm. Rec. 18, 273–292. https://doi.org/10.1046/j.0031-868X.2003.00023.x

Bigman, D.P., 2018. GPR basics: a handbook for ground penetrating radar users, First edition. ed. Bigman Geophysical, LLC, Suwanee, GA.

Biondi, F., 2022. Scanning Inside Volcanoes with Synthetic Aperture Radar Echography Tomographic Doppler Imaging. Remote Sens. 14, 3828. https://doi.org/10.3390/rs14153828

Biondi, F., Malanga, C., 2022. Synthetic Aperture Radar Doppler Tomography Reveals Details of Undiscovered High-Resolution Internal Structure of the Great Pyramid of Giza. Remote Sens. 14, 5231. https://doi.org/10.3390/rs14205231

Birth, G.S., McVey, G.R., 1968. Measuring the Color of Growing Turf with a Reflectance Spectrophotometer. Agron. J. 60, 640–643. https://doi.org/10.2134/agronj1968.00021962006000060016x

Błażejczyk, K., Twardosz, R., Wałach, P., Czarnecka, K., Błażejczyk, A., 2022. Heat strain and mortality effects of prolonged central European heat wave—an example of June 2019 in Poland. Int. J. Biometeorol. 66, 149–161. https://doi.org/10.1007/s00484-021-02202-0

BnF, 2025. Plan of the garden of the abbey of Aunay, including the line of the dormitory, the house, the courtyard, the fields and lands being worked (18th century) [WWW Document]. Gard. Plan. URL http://gallica.bnf.fr/ark:/12148/btv1b84459796 (accessed 27 Jul 25).

Bond, F.B., 1918. The Gate of Remembrance. Kessinger Publishing.

Bond, F.B., 1924. The Company of Avalon: A Study of the Script of Brother Symon, Sub-prior of Winchester Abbey in the Time of King Stephen. Basil Blackwell.

Bonì, R., Meisina, C., Cigna, F., Herrera, G., Notti, D., Bricker, S., McCormack, H., Tomás, R., Béjar-Pizarro, M., Mulas, J., Ezquerro, P., 2017. Exploitation of Satellite A-DInSAR Time Series for Detection, Characterization and Modelling of Land Subsidence. Geosciences 7, 1–23. https://doi.org/10.3390/geosciences7020025

Braitenberg, C., Sampietro, D., Pivetta, T., Zuliani, D., Barbagallo, A., Fabris, P., Rossi, L., Fabbri, J., Mansi, A.H., 2016. Gravity for Detecting Caves: Airborne and Terrestrial Simulations Based on a Comprehensive Karstic Cave Benchmark. Pure Appl. Geophys. 173, 1243–1264. https://doi.org/10.1007/s00024-015-1182-y

Brown, J.C., 1961. Iron Chlorosis in Plants. Adv. Agron. 13, 329–369.

Brunet, D., Vrscay, E.R., Wang, Z., 2012. On the Mathematical Properties of the Structural Similarity Index. IEEE Trans. Image Process. 21, 1488–1499. https://doi.org/10.1109/TIP.2011.2173206

Bruschi, D.E., Ralph, T.C., Fuentes, I., Jennewein, T., Razavi, M., 2014. Spacetime effects on satellite-based quantum communications. Phys. Rev. D 90, 045041_1-045041–13. https://doi.org/10.1103/PhysRevD.90.045041

Bubenzer, O., Bolten, A., 2008. The use of new elevation data (SRTM/ASTER) for the detection and morphometric quantification of Pleistocene megadunes (draa) in the eastern Sahara and the southern Namib. Geomorphology 102, 221–231. https://doi.org/10.1016/j.geomorph.2008.05.003

Bunting, J., 2025. Grass Types north of Glastonbury Tor, (pers. comm, 6 October 2025).

Burns, R., 2023. The Faringdon Tunnels: An Intriguing Possibility [WWW Document]. Faringdon Town Counc. URL https://www.faringdontowncouncil.gov.uk/wp-content/uploads/2023/03/Faringdon-Tunnels-leaflet-A5-v5-final-1.pdf (accessed 15 May 25).

Burton, J.E., Kerr, J., 2011. The Cistercians in the Middle Ages, Monastic orders. Boydell Press, Woodbridge, Suffolk, UK; Rochester, NY.

Butcher, A., Murphy, P.J., Beaney, S., Clark, R., 2006. The search for Palmer's Chamber, Lamb Leer, Somerset, United Kingdom. Cave Karst Sci. 33, 101–104.

Butler, D.K., 2008. Detection and characterization of subsurface cavities, tunnels and abandoned mines. -Surf. Geophys. Hum. Act. 578–584.

Calleja, J.F., Requejo Pagés, O., Díaz-Álvarez, N., Peón, J., Gutiérrez, N., Martín-Hernández, E., Cebada Relea, A., Rubio Melendi, D., Fernández Álvarez, P., 2018. Detection of buried archaeological remains with the combined use of satellite multispectral data and UAV data. Int. J. Appl. Earth Obs. Geoinformation 73, 555–573. https://doi.org/10.1016/j.jag.2018.07.023

Campbell, J.B., Wynne, R.H., Thomas, V.A., 2023. Introduction to remote sensing, 6. edition. ed. Guilford Press, New York.

Campbell, W.H., 2003. Introduction to geomagnetic fields, 2nd. ed. ed. Cambridge University Press, Cambridge; New York.

Carrer, L., Castelletti, D., Pozzobon, R., Sauro, F., Bruzzone, L., 2015. A Novel Method for Hidden Natural Caves Characterization and Accessibility Assessment from Spaceborne VHR SAR Images. IEEE Trans. Geosci. Remote Sens. 14, 1–11. https://doi.org/10.1109/TGRS.2022.3222991

Casana, J., 2021. Rethinking the Landscape: Emerging Approaches to Archaeological Remote Sensing. Annu. Rev. Anthropol. 50, 167–186. https://doi.org/10.1146/annurev-anthro-101819-110344

Casana, J., Ferwerda, C., 2024. Drone-Acquired Short-Wave Infrared (SWIR) Imagery in Landscape Archaeology: An Experimental Approach. Remote Sens. 16, 1671. https://doi.org/10.3390/rs16101671

Casana, J., Kantner, J., Wiewel, A., Cothren, J., 2014. Archaeological aerial thermography: a case study at the Chaco-era Blue J community, New Mexico. J. Archaeol. Sci. 45, 207–219. https://doi.org/10.1016/j.jas.2014.02.015

Casana, J., Wiewel, A., Cool, A., Hill, A.C., Fisher, K.D., Laugier, E.J., 2017. Archaeological Aerial Thermography in Theory and Practice. Adv. Archaeol. Pract. 5, 310–327. https://doi.org/10.1017/aap.2017.23

Cavalli, R.M., Pascucci, S., Pignatti, S., 2009. Optimal Spectral Domain Selection for Maximizing Archaeological Signatures: Italy Case Studies. Sensors 9, 1754–1767. https://doi.org/10.3390/s90301754

Cerra, D., Agapiou, A., Cavalli, R., Sarris, A., 2018. An Objective Assessment of Hyperspectral Indicators for the Detection of Buried Archaeological Relics. Remote Sens. 10, 500. https://doi.org/10.3390/rs10040500

Challis, K., Carey, C., Kincey, M., Howard, A.J., 2011. Airborne lidar intensity and geoarchaeological prospection in river valley floors. Archaeol. Prospect. 18, 1–13. https://doi.org/10.1002/arp.398

Challis, K., Kincey, M., Howard, A.J., 2008. Airborne Remote Sensing of Aggregate Landscapes. Trent Val. Geoarchaeology.

Challis, K., Kincey, M., Howard, A.J., 2009. Airborne remote sensing of valley floor geoarchaeology using Daedalus ATM and CASI. Archaeol. Prospect. 16, 17–33. https://doi.org/10.1002/arp.340

Chaney, R.L., Bell, P.F., 1987. Complexity of iron nutrition: Lessons for plant-soil interaction research. J. Plant Nutr. 10, 963–994. https://doi.org/10.1080/01904168709363626

Chase, A.S.Z., Chase, D.Z., Chase, A.F., 2017. LiDAR for Archaeological Research and the Study of Historical Landscapes, in: Masini, N., Soldovieri, F. (Eds.), Sensing the Past, Geotechnologies and the Environment. Springer International Publishing, Cham, pp. 89–100. https://doi.org/10.1007/978-3-319-50518-3_4

Chen, F., Lasaponara, R., Masini, N., 2017. An overview of satellite synthetic aperture radar remote sensing in archaeology: From site detection to monitoring. J. Cult. Herit. 23, 5–11. https://doi.org/10.1016/j.culher.2015.05.003

Chen, F., Masini, N., Liu, J., You, J., Lasaponara, R., 2016. Multi-frequency satellite radar imaging of cultural heritage: the case studies of the Yumen Frontier Pass and Niya ruins in the Western Regions of the Silk Road Corridor. Int. J. Digit. Earth 9, 1224–1241. https://doi.org/10.1080/17538947.2016.1181213

Chen, F., Masini, N., Yang, R., Milillo, P., Feng, D., Lasaponara, R., 2014. A Space View of Radar Archaeological Marks: First Applications of COSMO-SkyMed X-Band Data. Remote Sens. 7, 24–50. https://doi.org/10.3390/rs70100024

Chen, J.M., 1996. Evaluation of Vegetation Indices and a Modified Simple Ratio for Boreal Applications. Can. J. Remote Sens. 22, 229–242. https://doi.org/10.1080/07038992.1996.10855178

Chen, Y., Tang, Y., Xiao, Y., Yuan, Q., Zhang, Y., Liu, F., He, J., Zhang, L., 2024. Satellite video single object tracking: A systematic review and an oriented object tracking benchmark. ISPRS J. Photogramm. Remote Sens. 210, 212–240. https://doi.org/10.1016/j.isprsjprs.2024.03.013

Choi, S., Götze, H.-J., Meyer, U., Group, D., 2011. 3-D density modelling of underground structures and spatial distribution of salt diapirism in the Dead Sea Basin: Gravity modelling and salt diapirism in the DSB. Geophys. J. Int. 184, 1131–1146. https://doi.org/10.1111/j.1365-246X.2011.04939.x

Clarke, J.P., 1963. Souterrain at Crossabeagh, Co. Louth. J. Cty. Louth Archaeol. Soc. 15, 255–261. https://doi.org/10.2307/27729056

Clayton, A., 2015. Secret Tunnels of England: Folklore and Fact. Accumulator Press, London.

Comer, D., Chapman, B., Comer, J., 2017. Detecting Landscape Disturbance at the Nasca Lines Using SAR Data Collected from Airborne and Satellite Platforms. Geosciences 7, 106. https://doi.org/10.3390/geosciences7040106

Cooper, G.R.J., 1998. GRAV2DC for Windows user's manual (version 2.05). Geophys. Dep. Univ. Witwatersrand Johannesbg.

Coppack, G., 2000. The white monks: the Cistercians in Britain, 1128 - 1540, 1. Paperback ed. ed. Tempus, Stroud.

Cornwall Heritage Trust, 2020. About Cornwall Heritage Trust [www document]. Corn. Herit. Trust. URL https://www.cornwallheritagetrust.org/ (accessed 7 Aug 24).

Costen, M., 2005. Costen, Michael D. "Peter Clery, The Wealth and Estates of Glastonbury Abbey at the Dissolution in 1539, Curlew, 2003." Somerset Archaeology and Natural History 148 (2005): 149-50. Somerset Archaeol. Nat. Hist. 149–150.

Cover, T.M., Thomas, J.A., 1991. Elements of information theory, Wiley series in telecommunications. Wiley, New York.

Crippen, R.E., 1990. Calculating the vegetation index faster. Remote Sens. Environ. 34, 71–73. https://doi.org/10.1016/0034-4257(90)90085-Z

Da Lio, C., Tosi, L., 2018. Land subsidence in the Friuli Venezia Giulia coastal plain, Italy: 1992–2010 results from SAR-based interferometry. Sci. Total Environ. 633, 752–764. https://doi.org/10.1016/j.scitotenv.2018.03.244

Dace, R., 1999. Bertran de Verdun: Royal Service, Land, and Family in the Late Twelfth Century. Mediev. Prosopgraphy 20, 75–93.

Daehne, A., Corsini, A., 2013. Kinematics of active earthflows revealed by digital image correlation and DEM subtraction techniques applied to multi-temporal LiDAR data. Earth Surf. Process. Landf. 38, 640–654. https://doi.org/10.1002/esp.3351

Dana Negula, I., Moise, C., Lazăr, A.M., Rișcuța, N.C., Cristescu, C., Dedulescu, A.L., Mihalache, C.E., Badea, A., 2020. Satellite Remote Sensing for the Analysis of the Micia and Germisara Archaeological Sites. Remote Sens. 12, 2003. https://doi.org/10.3390/rs12122003

Dao, M., Kwan, C., Koperski, K., Marchisio, G., 2017. A joint sparsity approach to tunnel activity monitoring using high resolution satellite images, in: 2017 IEEE 8th Annual Ubiquitous Computing, Electronics and Mobile Communication Conference (UEMCON). IEEE, New York City, NY, pp. 322–328. https://doi.org/10.1109/UEMCON.2017.8249061

Davis, D.S., 2019. Object-based image analysis: a review of developments and future directions of automated feature detection in landscape archaeology. Archaeol. Prospect. 26, 155–163. https://doi.org/10.1002/arp.1730

Del Grande, N.K., 2009. Thermal inertia contrast detection of subsurface structures. Thermosense XXXI. SPIE. 7299, 115-121 https://doi.org/10.1117/12.829407

Deng, B., Guo, H.D., Wang, C.L., Nie, Y.P., 2010. Applications of remote sensing technique in archaeology: a review. J. Remote Sens. 14, 187–196.

Deng, W., Wang, K., Liu, X., Zhang, T., Liu, H., Liu, J., 2022. Research on remote sensing detection method for distributed subsurface targets inside mountain bodies, in: 2022 International Conference on Artificial Intelligence and Computer Information Technology (AICIT). Presented at the 2022 International Conference on Artificial Intelligence and Computer Information Technology (AICIT), IEEE, Yichang, China, pp. 1–6. https://doi.org/10.1109/AICIT55386.2022.9930298

Devereux, B.J., Amable, G.S., Crow, P., 2008. Visualisation of LiDAR terrain models for archaeological feature detection. Antiquity 82, 470–479. https://doi.org/10.1017/S0003598X00096952

Dilena, M.Á., 2024. Working in Tandem to Uncover 3D Artefact Distribution in Archaeological Excavations: Mathematical Interpretation through Positional and Relational Methods. Heritage 7, 4472–4499. https://doi.org/10.3390/heritage7080211

DJI, 2025. DJI. URL https://www.dji.com/uk (accessed 16 Jul 25).

Dogan, H.M., 2008. Applications of remote sensing and Geographic Information Systems to assess ferrous minerals and iron oxide of Tokat province in Turkey. Int. J. Remote Sens. 29, 221–233. https://doi.org/10.1080/01431160701269010

Doneus, M., Verhoeven, G., Atzberger, C., Wess, M., Ruš, M., 2014. New ways to extract archaeological information from hyperspectral pixels. J. Archaeol. Sci. 52, 84–96. https://doi.org/10.1016/j.jas.2014.08.023

Dosselmann, R., Yang, X.D., 2011. A comprehensive assessment of the structural similarity index. Signal Image Video Process. 5, 81–91. https://doi.org/10.1007/s11760-009-0144-1

Douaoui, A.E.K., Nicolas, H., Walter, C., 2006. Detecting salinity hazards within a semiarid context by means of combining soil and remote-sensing data. Geoderma 134, 217–230. https://doi.org/10.1016/j.geoderma.2005.10.009

Droppa, A., 1972. Contribution to the evolution of the Domica cave. Ceskoslovensky kras. 22, 65-72 (in Slovak).

Du, X., Sun, D., Li, F., Tong, J., 2022. A Study on the Propagation Trend of Underground Coal Fires Based on Night-Time Thermal Infrared Remote Sensing Technology. Sustainability 14, 14741. https://doi.org/10.3390/su142214741

Ducart, D.F., Silva, A.M., Toledo, C.L.B., Assis, L.M. de, 2016. Mapping iron oxides with Landsat-8/OLI and EO-1/Hyperion imagery from the Serra Norte iron deposits in the Carajás Mineral Province, Brazil. Braz. J. Geol. 46, 331–349.

Ducut, J.D., Alipio, M., Go, P.J., Concepcion Ii, R., Vicerra, R.R., Bandala, A., Dadios, E., 2022. A Review of Electrical Resistivity Tomography Applications in Underground Imaging and Object Detection. Displays 73, 102208. https://doi.org/10.1016/j.displa.2022.102208

Dugdale, W., 1846. Abbey of Aunay, in Normandy, in: Monasticon Anglianum: A history of the abbies and other monasteries, hospitals, frieries, and catherdral and collegiate churches, with their dependencies, in England and Wales, 2. James Bohn, London.

Ekaran, S., 2022. The 5 Best 3D Scanning Apps for iPhone [WWW Document]. MUO. URL https://www.makeuseof.com/best-3d-scanning-apps-iphone/ (accessed 1 Aug 23).

ElBedwehy, M.N., Behery, G.M., Elbarougy, R., 2020. Face Recognition Based on Relative Gradient Magnitude Strength. Arab. J. Sci. Eng. 45, 9925–9937. https://doi.org/10.1007/s13369-020-04538-y

El-Behaedi, R., 2021. Detection and 3D Modeling of Potential Buried Archaeological Structures Using WorldView-3 Satellite Imagery. Remote Sens. 14, 92. https://doi.org/10.3390/rs14010092

El-Kelani, R., 2020. A Review of Gravity and Magnetic Studies in the Jordan Dead Sea Transform Zone. Jordan Journal of Earth and Environmental Sciences, 11, 1.

El-Raouf, A.A., Doğru, F., Abdelrahman, K., Fnais, M.S., El Manharawy, A., Amer, O., 2023. Using Airborne Geophysical and Geochemical Methods to Map Structures and Their Related Gold Mineralization. Minerals 13, 237. https://doi.org/10.3390/min13020237

English Heritage, 2015. Croxden Abbey Site Plan.

English Heritage, 2024a. History of Carn Euny [WWW Document]. Engl. Herit. URL https://www.english-heritage.org.uk/visit/places/carn-euny-ancient-village/history/ (accessed 8 Jul 24).

English Heritage, 2024b. Description of Carn Euny [WWW Document]. Engl. Herit. URL https://www.english-heritage.org.uk/visit/places/carn-euny-ancient-village/history/description/ (accessed 8 Jul 24).

Errand, J., 1974. Secret Passages and Hiding-Places. David & Charles, London.

ESA, 2023. Satellite Missions catalogue - eoPortal [WWW Document]. Satell. Missions Cat. URL https://www.eoportal.org/satellite-missions (accessed 1 Aug 23).

Everett, M.E., 2013. Near-surface applied geophysics. Cambridge University Press, Cambridge; New York.

Evrendilek, F., Gulbeyaz, O., 2008. Deriving Vegetation Dynamics of Natural Terrestrial Ecosystems from MODIS NDVI/EVI Data over Turkey. Sensors 8, 5270–5302. https://doi.org/10.3390/s8095270

Ezersky, M.G., Eppelbaum, L.V., Al-Zoubi, A., Keydar, S., Abueladas, A., Akkawi, E., Medvedev, B., 2013. Geophysical prediction and following development sinkholes in two Dead Sea areas, Israel and Jordan. Environ. Earth Sci. 70, 1463–1478. https://doi.org/10.1007/s12665-013-2233-2

Fahnestock, J.D., Schowengerdt, R.A., 1983. Spatially Variant Contrast Enhancement Using Local Range Modification. Opt. Eng. 22, 378–381. https://doi.org/10.1117/12.7973124

Fairhead, J.D., 2003. Gravity and magnetics in today's oil and mineral industry. GETECH, School of Earth Sciences, University of Leeds, UK

Fairhead, J.D., Cooper, G.R.J., Sander, S., 2017. Advances in airborne gravity and magnetics. Proc. Explor. 17, 113–127.

Featherstone, R., Horne, P., Macleod, D., Bewley, R., (with reports by J. Collens and R. Philpott, D. A. Edwards, F. Griffith and W. Horner, S. Hartgroves, P. Markham, D. Motkin, C. R. Musson, F. Radcliffe, D. Strachan, B. Vyner and R. Yarwood), 1999. Aerial reconnaissance over England in summer 1996. Archaeol. Prospect. 6, 47–62.

Fernandez-Diaz, J., Carter, W., Shrestha, R., Glennie, C., 2014. Now You See It… Now You Don't: Understanding Airborne Mapping LiDAR Collection and Data Product Generation for Archaeological Research in Mesoamerica. Remote Sens. 6, 9951–10001. https://doi.org/10.3390/rs6109951

Ferretti, A., Passera, E., Capes, R., 2021. End-to-end implementation and operation of the European Ground Motion Service (EGMS): Algorithm Theoretical Basis Document. Technical Report EGMS-D3-ALG-SC1-2.0-006.

Findlay, D.C., Colborne, G.J.N., Cope, D.W., Harrod, T.R., Hogan, D.V., Staines, S.J., 1984. Soils and their use in South West England, Bulletin. Soil Survey of England and Wales. Soil Survey, Harpenden.

Finn, M.P., Lewis, M. (David), Bosch, D.D., Giraldo, M., Yamamoto, K., Sullivan, D.G., Kincaid, R., Luna, R., Allam, G.K., Kvien, C., Williams, M.S., 2011. Remote Sensing of Soil Moisture Using Airborne Hyperspectral Data. GIScience Remote Sens. 48, 522–540. https://doi.org/10.2747/1548-1603.48.4.522

Freeland, T., Heung, B., Burley, D.V., Clark, G., Knudby, A., 2016. Automated feature extraction for prospection and analysis of monumental earthworks from aerial LiDAR in the Kingdom of Tonga. J. Archaeol. Sci. 69, 64–74. https://doi.org/10.1016/j.jas.2016.04.011

Frey, O., Natale, A., Neto, J.R.M., Perna, S., 2022. Special Issue "Airborne Synthetic Aperture Radar: Systems, Processing, New Challenges and Opportunities." Remote Sens.

Gaber, A., Mohamed, A.K., ElGalladi, A., Abdelkareem, M., Beshr, A.M., Koch, M., 2020. Mapping the Groundwater Potentiality of West Qena Area, Egypt, Using Integrated Remote Sensing and Hydro-Geophysical Techniques. Remote Sens. 12, 1559. https://doi.org/10.3390/rs12101559

Gao, S., Yan, K., Liu, J., Pu, J., Zou, D., Qi, J., Mu, X., Yan, G., 2024. Assessment of remote-sensed vegetation indices for estimating forest chlorophyll concentration. Ecol. Indic. 162, 112001. https://doi.org/10.1016/j.ecolind.2024.112001

Gao, W., Zhang, X., Yang, L., Liu, H., 2010. An improved Sobel edge detection, in: 2010 3rd International Conference on Computer Science and Information Technology. Presented at the 2010 3rd International Conference on Computer Science and Information Technology, pp. 67–71. https://doi.org/10.1109/ICCSIT.2010.5563693

Ghezzi, A., Schettino, A., Pierantoni, P.P., Conyers, L., Tassi, L., Vigliotti, L., Schettino, E., Melfi, M., Gorrini, M.E., Boila, P., 2019. Reconstruction of a Segment of the UNESCO World Heritage Hadrian's Villa Tunnel Network by Integrated GPR, Magnetic–Paleomagnetic, and Electric Resistivity Prospections. Remote Sens. 11, 1739. https://doi.org/10.3390/rs11151739

Ghorbani, Z., Khosravi, A., Maghsoudi, Y., Mojtahedi, F.F., Javadnia, E., Nazari, A., 2022. Use of InSAR data for measuring land subsidence induced by groundwater withdrawal and climate change in Ardabil Plain, Iran. Sci. Rep. 12, 13998. https://doi.org/10.1038/s41598-022-17438-y

Gilchrist, R., Green, C., 2015. Glastonbury Abbey: Archaeological Investigations 1904-79. The Society of Antiquaries of London, London.

Giovos, R., Tassopoulos, D., Kalivas, D., Lougkos, N., Priovolou, A., 2021. Remote Sensing Vegetation Indices in Viticulture: A Critical Review. Agriculture 11, 457. https://doi.org/10.3390/agriculture11050457

Gitelson, A.A., Kaufman, Y.J., Merzlyak, M.N., 1996. Use of a green channel in remote sensing of global vegetation from EOS-MODIS. Remote Sens. Environ. 58, 289–298. https://doi.org/10.1016/S0034-4257(96)00072-7

Gitelson, A.A., Merzlyak, M.N., Lichtenthaler, H.K., 1996. Detection of Red Edge Position and Chlorophyll Content by Reflectance Measurements Near 700 nm. J. Plant Physiol. 148, 501–508. https://doi.org/10.1016/S0176-1617(96)80285-9

Gitelson, A.A., Stark, R., Grits, U., Rundquist, D., Kaufman, Y., Derry, D., 2002. Vegetation and soil lines in visible spectral space: A concept and technique for remote estimation of vegetation fraction. Int. J. Remote Sens. 23, 2537–2562. https://doi.org/10.1080/01431160110107806

Goel, N.S., Qin, W., 1994. Influences of canopy architecture on relationships between various vegetation indices and LAI and Fpar: A computer simulation. Remote Sens. Rev. 10, 309–347. https://doi.org/10.1080/02757259409532252

Gonenc, A., Ozerdem, M.S., Acar, E., 2019. Comparison of NDVI and RVI Vegetation Indices Using Satellite Images, in: 2019 8th International Conference on Agro-Geoinformatics (Agro-Geoinformatics). Presented at the 2019 8th International Conference on Agro-Geoinformatics (Agro-Geoinformatics), IEEE, Istanbul, Turkey, pp. 1–4. https://doi.org/10.1109/Agro-Geoinformatics.2019.8820225

Gong, P., Pu, R., Biging, G.S., Larrieu, M.R., 2003. Estimation of forest leaf area index using vegetation indices derived from Hyperion hyperspectral data. IEEE Trans. Geosci. Remote Sens. 41, 1355–1362. https://doi.org/10.1109/TGRS.2003.812910

Gonzalez, R.C., Wintz, P., 1987. Image transforms-digital image processing. Addison-Wesley N. Y.

Götze, H.-J., El-Kelani, R., Schmidt, S., Rybakov, M., Hassouneh, M., Förster, H.-J., Ebbing, J., 2007. Integrated 3D density modelling and segmentation of the Dead Sea Transform. Int. J. Earth Sci. 96, 289–302. https://doi.org/10.1007/s00531-006-0095-5

Götze, H.-J., Meyer, U., Choi, S., 2010. Helicopter Gravity Survey in the Dead Sea Area. Eos Trans. Am. Geophys. Union 91, 109–110. https://doi.org/10.1029/2010EO120002

Grande, N.K.D., Ascough, B.M., Rumpf, R.L., 2013. Thermal inertia mapping of below ground objects and voids. Detection and Sensing of Mines, Explosive Objects, and Obscured Targets XVIII. SPIE. 313-322. https://doi.org/10.1117/12.2016144.

Grandjean, G., Paillou, P., Dubois-Fernandez, P., August-Bernex, T., Baghdadi, N.N., Achache, J., 2001. Subsurface structures detection by combining L-band polarimetric SAR and GPR data: example of the Pyla Dune (France). IEEE Trans. Geosci. Remote Sens. 39, 1245–1258. https://doi.org/10.1109/36.927447

Grauch, V.J.S., 2002. High-Resolution Aeromagnetic Survey to Image Shallow Faults (Open-File Report No. 02–384), Open-File Report. USGS, Prepared for the U.S. Department of Energy.

Greaney, S., 2017. Guide Book: Chysauster and Carn Euny Ancient Aillages, 1st ed. English Heritage.

Gris, E., 1844. Nouvelles experiences sur l'action des composes ferrugineux solubles, appliques a la vegetation, et specialement au traitement de la chlorose et de la debilite des plantes. Comptes Rendus Acad. Sci. Paris 19, 1118–1119.

Gruen, A., 2021. Everything moves: The rapid changes in photogrammetry and remote sensing. Geo-Spat. Inf. Sci. 24, 33–49. https://doi.org/10.1080/10095020.2020.1868275

Haboudane, D., Miller, J.R., Pattey, E., Zarco-Tejada, P.J., Strachan, I.B., 2004. Hyperspectral vegetation indices and novel algorithms for predicting green LAI of crop canopies: Modeling and validation in the context of precision agriculture. Remote Sens. Environ. 90, 337–352. https://doi.org/10.1016/j.rse.2003.12.013

Hak, Y.S., Sung, J.J., Choon, C.K., 2023. Comparative Analysis of Italian Ryegrass Vegetation Indices across Different Sowing Seasons Using Unmanned Aerial Vehicles. J. Korean Soc. Grassl. Forage Sci. 43, 103–108. https://doi.org/10.5333/KGFS.2023.43.2.103

Hall, J., 2007. Croxden Abbey Church: Architecture, Burial and Patronage. J. Br. Archaeol. Assoc. 160, 39–128. https://doi.org/10.1179/jba.2007.160.1.39

Hancock, G., 2020. America Before: The Key to Earth's Lost Civilization, 1st ed. Coronet Books, Hodder & Stoughton Ltd, London.

Hartshorn, C.A., Isaacson, S.D., Barrowes, B.E., Perren, L.J., Lozano, D., Shubitidze, F., 2022. Analysis of the Feasibility of UAS-Based EMI Sensing for Underground Utilities Detection and Mapping. Remote Sens. 14, 3973. https://doi.org/10.3390/rs14163973

He, D.C., Wang, Li., Amani, M., 2004. A new technique for multi-resolution image fusion, in: IGARSS '04. Presented at the IEEE International Geoscience and Remote Sensing Symposium, 2004., IEEE, Anchorage, AK, USA, pp. 4901–4904. https://doi.org/10.1109/IGARSS.2004.1370262

Hill, A.C., Laugier, E.J., Casana, J., 2020. Archaeological Remote Sensing Using Multi-Temporal, Drone-Acquired Thermal and Near Infrared (NIR) Imagery: A Case Study at the Enfield Shaker Village, New Hampshire. Remote Sens. 12, 690. https://doi.org/10.3390/rs12040690

Historic Cornwall, 2020. Carn Euny | Historic Cornwall [WWW Document]. Carn Euny. URL https://www.historic_cornwall.org.uk/a2m/rom_british/courtyard_house/carn_euny/carn_euny.htm (accessed 7 Aug 24).

Hofierka, J., Gallay, M., Bandura, P., Šašak, J., 2018. Identification of karst sinkholes in a forested karst landscape using airborne laser scanning data and water flow analysis. Geomorphology 308, 265–277. https://doi.org/10.1016/j.geomorph.2018.02.004

Hool, G.A., Johnson, N.C., 2010. Handbook of Building Construction: Data for Architects, Designing and Constructing Engineers, and Contractors... Nabu Press, New York, USA.

Horler, D.N.H., Dockray, M., Barber, J., 1983. The red edge of plant leaf reflectance. Int. J. Remote Sens. 4, 273–288. https://doi.org/10.1080/01431168308948546
https://doi.org/10.1016/j.jas.2012.10.036

Huete, A., Didan, K., Miura, T., Rodriguez, E.P., Gao, X., Ferreira, L.G., 2002. Overview of the radiometric and biophysical performance of the MODIS vegetation indices. Remote Sens. Environ., The Moderate Resolution Imaging Spectroradiometer (MODIS): a new generation of Land Surface Monitoring 83, 195–213. https://doi.org/10.1016/S0034-4257(02)00096-2

Huete, A., Miura, T., Yoshioka, H., Ratana, P., Broich, M., 2014. Indices of Vegetation Activity, in: Hanes, J.M. (Ed.), Biophysical Applications of Satellite Remote Sensing. Springer, Berlin, Heidelberg, pp. 1–41. https://doi.org/10.1007/978-3-642-25047-7_1

Huete, A.R., Liu, H.Q., Batchily, K., van Leeuwen, W., 1997. A comparison of vegetation indices over a global set of TM images for EOS-MODIS. Remote Sens. Environ. 59, 440–451. https://doi.org/10.1016/S0034-4257(96)00112-5

Huisman, D.J. (Ed.), 2009. Degradation of archaeological remains. Sdu Uitgevers, Den Haag.

IDS GeoRadar, 2021. IDS Opera Duo Datasheet.

IDS GeoRadar, 2023a. IDS Opera Duo Brochure.

IDS GeoRadar, 2023b. IQMaps User Manual.

IRIS Instruments, 2022. Prosys II Software.

Isaacson, W., 2008. Einstein: His Life and Universe. Simon & Schuster, Limited, London.

Jackson, R.D., Slater, P.N., Pinter, P.J., 1983. Discrimination of growth and water stress in wheat by various vegetation indices through clear and turbid atmospheres. Remote Sens. Environ. 13, 187–208. https://doi.org/10.1016/0034-4257(83)90039-1

Jamaludin, S.N.F., Pubellier, M., Sautter, B., 2021. Shallow vs. Deep Subsurface Structures of Central Luconia Province, Offshore Malaysia Reveal by Aeromagnetic, Airborne Gravity and Seismic Data. Appl. Sci. 11, 5095. https://doi.org/10.3390/app11115095

James, K., Nichol, C.J., Wade, T., Cowley, D., Gibson Poole, S., Gray, A., Gillespie, J., 2020. Thermal and Multispectral Remote Sensing for the Detection and Analysis of Archaeologically Induced Crop Stress at a UK Site. Drones 4, 61. https://doi.org/10.3390/drones4040061

James, L.A., Hodgson, M.E., Ghoshal, S., Latiolais, M.M., 2012. Geomorphic change detection using historic maps and DEM differencing: The temporal dimension of geospatial analysis. Geomorphology 137, 181–198. https://doi.org/10.1016/j.geomorph.2010.10.039

Jamroziak, E., 2013. The Cistercian Order in Medieval Europe: 1090-1500, The medieval world. Pearson, New York.

Jaud, M., Rouveure, R., Faure, P., Monod, M.-O., Moiroux-Arvis, L., 2014. Correcting topography effects on terrestrial radar maps, in: 2014 International Radar Conference. Presented at the 2014 International Radar Conference (Radar), IEEE, Lille, France, pp. 1–5. https://doi.org/10.1109/radar.2014.7060379

Jia, J., Wang, Y., Chen, J., Guo, R., Shu, R., Wang, J., 2020. Status and application of advanced airborne hyperspectral imaging technology: A review. Infrared Phys. Technol. 104, 103115. https://doi.org/10.1016/j.infrared.2019.103115

Jiang, Z., Huete, A.R., Didan, K., Miura, T., 2008. Development of a two-band enhanced vegetation index without a blue band. Remote Sens. Environ. 112, 3833–3845. https://doi.org/10.1016/j.rse.2008.06.006

Jordan, C.F., 1969. Derivation of Leaf-Area Index from Quality of Light on the Forest Floor. Ecology 50, 663–666. https://doi.org/10.2307/1936256

Kalayci, T., Simon, F.-X., Sarris, A., 2017. A Manifold Approach for the Investigation of Early and Middle Neolithic Settlements in Thessaly, Greece. Geosciences 7, 79. https://doi.org/10.3390/geosciences7030079

Kalderis, D., Juhasz, A.L., Boopathy, R., Comfort, S., 2011. Soils contaminated with explosives: Environmental fate and evaluation of state-of-the-art remediation processes (IUPAC Technical Report). Pure Appl. Chem. 83, 1407–1484. https://doi.org/10.1351/PAC-REP-10-01-05

Kampes, B.M., 2006. Radar interferometry: persistent scatterer technique, Remote sensing and digital image processing. Springer, Dordrecht, the Netherlands.

Kaufman, Y.J., Tanre, D., 1992. Atmospherically resistant vegetation index (ARVI) for EOS-MODIS. IEEE Trans. Geosci. Remote Sens. 30, 261–270. https://doi.org/10.1109/36.134076

Kearey, P., Brooks, M., Hill, I., 2002. An introduction to geophysical exploration, 3rd ed. ed. Blackwell Science, Malden, MA.

Keller, S., Riese, F.M., Allroggen, N., Jackisch, C., Hinz, S., 2018. Modeling Subsurface Soil Moisture Based on Hyperspectral Data - First Results of a Multilateral Field Campaign 15.

Kennedy, D., 1998. Declassified satellite photographs and archaeology in the Middle East: case studies from Turkey. Antiquity 72, 553–561. https://doi.org/10.1017/S0003598X0008697X

Khan, N.M., Rastoskuev, V.V., Sato, Y., Shiozawa, S., 2005. Assessment of hydrosaline land degradation by using a simple approach of remote sensing indicators. Agric. Water Manag., Special Issue on Land and Water Use: Environmental Management Tools and Practices 77, 96–109. https://doi.org/10.1016/j.agwat.2004.09.038

Kharbish, S., Eldosouky, A.M., Amer, O., 2022. Integrating mineralogy, geochemistry and aeromagnetic data for detecting Fe–Ti ore deposits bearing layered mafic intrusion, Akab El-Negum, Eastern Desert, Egypt. Sci. Rep. 12, 15474. https://doi.org/10.1038/s41598-022-19760-x

Kinder, T.N. (Ed.), 2002. Cistercian Europe: architecture of contemplation, Cistercian studies series. Eerdmans Publishing Co., Grand Rapids, Michigan.

Kokalj, Ž., Hesse, R., 2017. Airborne laser scanning raster data visualization, Prostor, kraj, čas. ZRC SAZU, Založba ZRC. https://doi.org/10.3986/9789612549848

Kokaly, R., Clark, R.N., Swayze, G.A., Livo, K.E., Hoefen, T.M., Pearson, N.C., Wise, R.A., Benzel, W.M., Lowers, H.A., Driscoll, R.L., Klein, A.J., 2017. USGS Spectral Library Version 7 Data. https://doi.org/10.5066/F7RR1WDJ

Konsolaki, A., Vassilakis, E., Kotsi, E., Kontostavlos, G., Lekkas, E., Stavropoulou, M., Giannopoulos, I., 2022. Introducing Interdisciplinary Innovative Techniques for Mapping Karstic Caves. Presented at the 16 th International Congress of the Geological Society of Greece, Bulletin of the Geological Society of Greece, Patras, Greece, p. 2.

Křivánek, R., 2017. Comparison Study to the Use of Geophysical Methods at Archaeological Sites Observed by Various Remote Sensing Techniques in the Czech Republic. Geosciences 7, 81. https://doi.org/10.3390/geosciences7030081

Kruse, F.A., 2012. Mapping surface mineralogy using imaging spectrometry. Geomorphology 137, 41–56. https://doi.org/10.1016/j.geomorph.2010.09.032

Kucukkaya, A.G., 2004. Photogrammetry and remote sensing in archeology. J. Quant. Spectrosc. Radiat. Transf. 88, 83–88. https://doi.org/10.1016/j.jqsrt.2003.12.030

Kuenzer, C., Dech, S., 2013. Remote Sensing and Digital Image Processing. pp. 1–26. https://doi.org/10.1007/978-94-007-6639-6_1

Kureel, N., Sarup, J., Matin, S., Goswami, S., Kureel, K., 2022. Modelling vegetation health and stress using hypersepctral remote sensing data. Model. Earth Syst. Environ. 8, 733–748. https://doi.org/10.1007/s40808-021-01113-8

Kuzia, K., 2018. Utilisation of airborne laser scanning for monitoring of secondary impacts of underground mining exploitation. Q. Environ. Eng. Des. 172, 4–10.

Kwan, C., 2018. Remote Sensing Performance Enhancement in Hyperspectral Images. Sensors 18, 3598. https://doi.org/10.3390/s18113598

Kwan, C., 2019. Methods and Challenges Using Multispectral and Hyperspectral Images for Practical Change Detection Applications. Information 10, 353. https://doi.org/10.3390/info10110353

LaFehr, T.R., Nabighian, M.N., 2012. Fundamentals of gravity exploration. Soc. Explor. Geophys. https://doi.org/10.1190/1.1443137

Lakkaraju, V.R., Zhou, X., Apple, M.E., Cunningham, A., Dobeck, L.M., Gullickson, K., Spangler, L.H., 2010. Studying the vegetation response to simulated leakage of sequestered CO2 using spectral vegetation indices. Ecol. Inform., Special Issue on Advances of Ecological Remote Sensing Under Global Change 5, 379–389. https://doi.org/10.1016/j.ecoinf.2010.05.002

Lasaponara, R., Leucci, G., Masini, N., Persico, R., Scardozzi, G., 2016. Towards an operative use of remote sensing for exploring the past using satellite data: The case study of Hierapolis (Turkey). Remote Sens. Environ. 174, 148–164. https://doi.org/10.1016/j.rse.2015.12.016

Lasaponara, R., Masini, N., 2007. Detection of archaeological crop marks by using satellite QuickBird multispectral imagery. J. Archaeol. Sci. 34, 214–221. https://doi.org/10.1016/j.jas.2006.04.014

Lasaponara, R., Masini, N., 2009. Full-waveform Airborne Laser Scanning for the detection of medieval archaeological microtopographic relief. J. Cult. Herit. 10, e78-e82. https://doi.org/10.1016/j.culher.2009.10.004

Lasaponara, R., Masini, N., 2014. Beyond modern landscape features: New insights in the archaeological area of Tiwanaku in Bolivia from satellite data. Int. J. Appl. Earth Obs. Geoinformation 26, 464–471. https://doi.org/10.1016/j.jag.2013.09.006

Lasaponara, R., Masini, N., 2018. Space-Based Identification of Archaeological Illegal Excavations and a New Automatic Method for Looting Feature Extraction in Desert Areas. Surv. Geophys. 39, 1323–1346. https://doi.org/10.1007/s10712-018-9480-4

Le Hardy, G., 1897. Étude sur la baronnie et l'abbaye d'Aunay-sur-Odon.

Le Hête, T., 2009. An unstudied descent from Robert of Caen, Earl of Gloucester. Foundations 3, 113–126.

Lees, K.J., Artz, R.R.E., Khomik, M., Clark, J.M., Ritson, J., Hancock, M.H., Cowie, N.R., Quaife, T., 2020. Using Spectral Indices to Estimate Water Content and GPP in Sphagnum Moss and Other Peatland Vegetation. IEEE Trans. Geosci. Remote Sens. 58, 4547–4557. https://doi.org/10.1109/TGRS.2019.2961479

LeFehr, T.R., Nabighian, M.N., 2012. Fundamentals of gravity exploration. Society of Exploration Geophysicists.

Leonardi, M., Guerreschi, P., 2021. The use of the high-resolution LiDAR DTM by the Italian Ministry of the Environment and for Protection of the Land and Sea in archeology. Abstr. Int. Cartogr. Assoc. ICA 3, 1–2. https://doi.org/10.5194/ica-abs-3-178-2021

Li, P., Li, D., Hu, J., Fassnacht, F.E., Latifi, H., Yao, W., Gao, J., Chan, F.K.S., Dang, T., Tang, F., 2024. Improving the application of UAV-LiDAR for erosion monitoring through accounting for uncertainty in DEM of difference. CATENA 234, 107534. https://doi.org/10.1016/j.catena.2023.107534

Li, S., Sun, X., Gu, Y., Lv, Y., Zhao, M., Zhou, Z., Guo, W., Sun, Y., Wang, H., Yang, J., 2023. Recent Advances in Intelligent Processing of Satellite Video: Challenges, Methods, and Applications. IEEE J. Sel. Top. Appl. Earth Obs. Remote Sens. 16, 6776–6798. https://doi.org/10.1109/JSTARS.2023.3296451

Li, X., Yuan, Z., Wang, Q., 2019. Unsupervised Deep Noise Modeling for Hyperspectral Image Change Detection. Remote Sens. 11, 258. https://doi.org/10.3390/rs11030258

Lieskovský, J., Lieskovský, T., Hladíková, K., Štefunková, D., Hurajtová, N., 2022. Potential of airborne LiDAR data in detecting cultural landscape features in Slovakia. Landsc. Res. 47, 539–558. https://doi.org/10.1080/01426397.2022.2045923

Lillesand, T.M., Kiefer, R.W., Chipman, J.W., 2015. Remote sensing and image interpretation, Seventh edition. ed. John Wiley & Sons, Inc, Hoboken, N.J.

Lin, A.Y.-M., Novo, A., Har-Noy, S., Ricklin, N.D., Stamatiou, K., 2011. Combining GeoEye-1 Satellite Remote Sensing, UAV Aerial Imaging, and Geophysical Surveys in Anomaly Detection Applied to Archaeology. IEEE J. Sel. Top. Appl. Earth Obs. Remote Sens. 4, 870–876. https://doi.org/10.1109/JSTARS.2011.2143696

Liu, M., Liu, X., Li, M., Fang, M., Chi, W., 2010. Neural-network model for estimating leaf chlorophyll concentration in rice under stress from heavy metals using four spectral indices. Biosyst. Eng. 106, 223–233. https://doi.org/10.1016/j.biosystemseng.2009.12.008

Lohani, B., Ghosh, S., 2017. Airborne LiDAR Technology: A Review of Data Collection and Processing Systems. Proc. Natl. Acad. Sci. India Sect. Phys. Sci. 87, 567–579. https://doi.org/10.1007/s40010-017-0435-9

Loke, M.H., 1999. Electrical imaging surveys for environmental and engineering studies: A practical guide to 2-D and 3-D surveys.

Lonseth, A.T., 1947. The propagation of error in linear problems. Trans Amer Math Soc 62, 193–212. https://doi.org/S0002-9947-1947-0022315-4

Loots, M., Grobbelaar, S., van der Lingen, E., 2022. A review of remote-sensing unmanned aerial vehicles in the mining industry. J. South. Afr. Inst. Min. Metall. 122, 387–396. https://doi.org/10.17159/2411-9717/1602/2022

Luo, L., Wang, X., Guo, H., Lasaponara, R., Zong, X., Masini, N., Wang, G., Shi, P., Khatteli, H., Chen, F., Tariq, S., Shao, J., Bachagha, N., Yang, R., Yao, Y., 2019. Airborne and spaceborne remote sensing for archaeological and cultural heritage applications: A review of the century (1907–2017). Remote Sens. Environ. 232, 111280. https://doi.org/10.1016/j.rse.2019.111280

Luo, L., Wang, X., Liu, J., Guo, H., Zong, X., Ji, W., Cao, H., 2017. VHR GeoEye-1 imagery reveals an ancient water landscape at the Longcheng site, northern Chaohu Lake Basin (China). Int. J. Digit. Earth 10, 139–154. https://doi.org/10.1080/17538947.2016.1214983

Lv, Y., Jiang, Y., Hu, W., Cao, M., Mao, Y., 2020. A review of the effects of tunnel excavation on the hydrology, ecology, and environment in karst areas: Current status, challenges, and perspectives. J. Hydrol. 586, 124891. https://doi.org/10.1016/j.jhydrol.2020.124891

Lyons, J.D., 2019. The Oxford Handbook of the Baroque. Oxford University Press.

Macchiarulo, V., Milillo, P., DeJong, M.J., González Martí, J., Sánchez, J., Giardina, G., 2021. Integrated InSAR monitoring and structural assessment of tunnelling-induced building deformations. Struct. Control Health Monit. 28, 1–26. https://doi.org/10.1002/stc.2781

Mahajan, P.K., Venkatramaiah, S., Shaktawal, K.S., Ganju, J.L., 1984. Geomorphological evolution of Indian coast with spectial reference to hydrocarbon prospects. Unpubl. Rep. 85.

Major, D.J., Baret, F., Guyot, G., 1990. A ratio vegetation index adjusted for soil brightness. Int. J. Remote Sens. 11, 727–740. https://doi.org/10.1080/01431169008955053

Mallmann, C.L., Zaninni, A.F., Filho, W.P., 2020. Vegetation Index Based in Unmanned Aerial Vehicle (Uav) To Improve the Management of Invasive Plants in Protected Areas, Southern Brazil, in: 2020 IEEE Latin American GRSS & ISPRS Remote Sensing Conference (LAGIRS), pp. 66–69. https://doi.org/10.1109/LAGIRS48042.2020.9165598

Mandlburger, G., 2019. Recent Developments in Airborne Lidar. GIM Int.

Mann, N., 1986. Glastonbury Tor: A guide to the history and legends. Annenterprise.

Mann, N.R., 2001. The Isle of Avalon: Sacred Mysteries of Arthur and Glastonbury Tor, Repr. ed. Green Magic, London.

Mantle, G., 1911. Recent Discoveries at Glastonbury Abbey. Gazette Printing Co.

Maritime Archaeology Trust, 2025. Newlyn Ordnance and Other Datums. URL https://maritimearchaeologytrust.org/newlyn-ordnance-and-other-datums/ (accessed 9 Jan 25).

Marshall, M., Thenkabail, P., 2014. Biomass Modeling of Four Leading World Crops Using Hyperspectral Narrowbands in Support of HyspIRI Mission. Photogramm. Eng. Remote Sens. 80, 757–772. https://doi.org/10.14358/PERS.80.8.757

Masini, N., Abate, N., Gizzi, F., Vitale, V., Minervino Amodio, A., Sileo, M., Biscione, M., Lasaponara, R., Bentivenga, M., Cavalcante, F., 2022. UAV LiDAR Based Approach for the Detection and Interpretation of Archaeological Micro Topography under Canopy—The Rediscovery of Perticara (Basilicata, Italy). Remote Sens. 14, 6074. https://doi.org/10.3390/rs14236074

Mathew, S., MacBeth, C., Stevanovic, J., Mangriotis, M.-D., 2023. Detection of Dynamic Phenomena Associated with Underground Nuclear Explosion Using Multiple Seismic Surveys and Machine Learning. Pure Appl. Geophys. 180, 1287–1301. https://doi.org/10.1007/s00024-022-03145-2

Matsushita, B., Yang, W., Chen, J., Onda, Y., Qiu, G., 2007. Sensitivity of the Enhanced Vegetation Index (EVI) and Normalized Difference Vegetation Index (NDVI) to Topographic Effects: A Case Study in High-density Cypress Forest. Sensors 7, 2636–2651. https://doi.org/10.3390/s7112636

Matthews, J., 1993. A Glastonbury reader: selections from the myths, legends and stories of ancient Avalon. Aquarian/Thorsons, London.

Maxar, 12 Jan 2022a. Maxar Analysis Ready Data (ARD).

Maxar, 12 Aug 2022b. Get Started with ARD - Maxar ARD [WWW Document]. Get Started Maxar ARD. URL https://ard.maxar.com/docs/getting-started/getting-started/ (accessed 11 Jul 24).

McFee, J.E., Achal, S., Ivanco, T., Anger, C., 2005. A short wave infrared hyperspectral imager for landmine detection, in: Detection and Remediation Technologies for Mines and Minelike Targets X. Presented at the Detection and Remediation Technologies for Mines and Minelike Targets X, SPIE, pp. 56–67. https://doi.org/10.1117/12.602637

McManamon, P.F., 2012. Review of ladar: a historic, yet emerging, sensor technology with rich phenomenology. Opt. Eng. 51, 060901_1-060901_13. https://doi.org/10.1117/1.OE.51.6.060901

Meerdink, S.K., Hook, S.J., Roberts, D.A., Abbott, E.A., 2019. The ECOSTRESS spectral library version 1.0. Remote Sens. Environ. 230, 111196. https://doi.org/10.1016/j.rse.2019.05.015

Melillos, G., Agapiou, A., Themistocleous, K., Michaelides, S., Papadavid, G., Hadjimitsis, D.G., 2019. Field spectroscopy for the detection of underground military structures. Eur. J. Remote Sens. 52, 385–399. https://doi.org/10.1080/22797254.2019.1625075

Mendes, W. de S., Demattê, J.A.M., Minasny, B., Silvero, N.E.Q., Bonfatti, B.R., Safanelli, J.L., Rizzo, R., Costa, A.C.S. da, 2022. Free iron oxide content in tropical soils predicted by integrative digital mapping. Soil Tillage Res. 219, 105346. https://doi.org/10.1016/j.still.2022.105346

Meng, X., Currit, N., Zhao, K., 2010. Ground Filtering Algorithms for Airborne LiDAR Data: A Review of Critical Issues. Remote Sens. 2, 833–860. https://doi.org/10.3390/rs2030833

Merzlyak, M.N., Gitelson, A.A., Chivkunova, O.B., Rakitin, V.YU., 1999. Non-destructive optical detection of pigment changes during leaf senescence and fruit ripening. Physiol. Plant. 106, 135–141. https://doi.org/10.1034/j.1399-3054.1999.106119.x

Metternicht, G., Zinck, J.A., 1997. Spatial discrimination of salt- and sodium-affected soil surfaces. Int. J. Remote Sens. 18, 2571–2586. https://doi.org/10.1080/014311697217486

Mi, J., Yang, Y., Zhang, S., An, S., Hou, H., Hua, Y., Chen, F., 2019. Tracking the Land Use/Land Cover Change in an Area with Underground Mining and Reforestation via Continuous Landsat Classification. Remote Sens. 11, 1719. https://doi.org/10.3390/rs11141719

Migon, P., 2006. Granite Landscapes of the World. OUP Oxford.

Milsom, J., 2003. Field geophysics, 3rd ed. ed, The geological field guide series. J. Wiley, Chichester, West Sussex, England ; Hoboken, NJ.

Milton, E.J., Schaepman, M.E., Anderson, K., Kneubühler, M., Fox, N., 2009. Progress in field spectroscopy. Remote Sens. Environ. 113, S92–S109. https://doi.org/10.1016/j.rse.2007.08.001

Mitra, D.S., Agarwal, R.P., 1991. Geomorphology and Petroleum Prospects of Cauvery Basin, Tamilnadu, Based on Interpretation of Indian Remote Sensing Satellite (IRS) Data. J. Indian Soc. Remote Sens. 19, 263–268. https://doi.org/10.1007/BF03023973

Miura, T., Huete, A.R., Yoshioka, H., 2000. Evaluation of sensor calibration uncertainties on vegetation indices for MODIS. IEEE Trans. Geosci. Remote Sens. 38, 1399–1409. https://doi.org/10.1109/36.843034

Monika, Govil, H., Kumar, S., 2022. Subsurface feature identification using L Band Synthetic Aperture Radar (SAR) data over Jaisalmer, India, in: Radar Remote Sensing. Elsevier, pp. 109–122. https://doi.org/10.1016/B978-0-12-823457-0.00007-0

More, B., 2014. An Experimental Study on Water Dowsing. Int. J. Res. Innov. Earth Sci. 1, 17–19.

Moriarty, C., Cowley, D.C., Wade, T., Nichol, C.J., 2018. Deploying multispectral remote sensing for multi-temporal analysis of archaeological crop stress at Ravenshall, Fife, Scotland. Archaeol. Prospect. 26, 33–46. https://doi.org/10.1002/arp.1721

Moriarty, C., Cowley, D.C., Wade, T., Nichol, C.J., 2019. Deploying multispectral remote sensing for multi-temporal analysis of archaeological crop stress at Ravenshall, Fife, Scotland. Archaeol. Prospect. 26, 33–46. https://doi.org/10.1002/arp.1721

Morley, A., 2011. Exploring the use of high-resolution multispectral satellite imagery to identify subsurface structures (MSc Thesis). Cranfield University, UK, Royal School of Military Survey, Defence Intelligence Security Centre.

Morley, A., Ekpenyong, F., 2012. Exploring the use of High-Resolution Multi-Spectral Satellite Imagery to identify Subsurface Structures. Presented at the GISRUK 2012, Lancaster University, Lancaster.

Morley, A.M., Mather, T.A., Pyle, D.M., Kendall, J.-M., 2025a. Detecting shallow subsurface anomalies with airborne and spaceborne remote sensing: A review. Sci. Remote Sens. 11, 100187. https://doi.org/10.1016/j.srs.2024.100187

Morley, A.M., Mather, T.A., Pyle, D.M., Kendall, J.-M., 2025b. International Journal of Applied Earth Observation and Geoinformation, in review

Moyes, H., Montgomery, S., 2019. Locating Cave Entrances Using Lidar-Derived Local Relief Modeling. Geosciences 9, 98. https://doi.org/10.3390/geosciences9020098

Murphy, C.A., 2004. The Air-FTG airborne gravity gradiometer system. Airborne Gravity 7–14.

Murphy, C.A., Brewster, J., 2007. Target delineation using Full Tensor Gravity Gradiometry data. ASEG Ext. Abstr. 2007, 1–3. https://doi.org/10.1071/ASEG2007ab096

Navalgund, R., Rajani, M.B., 2017. The Science behind Archaeological Signatures from Space. Curr. Sci. 113, 1859. https://doi.org/10.18520/cs/v113/i10/1859-1872

Ng, A., Wang, H., Dai, Y., Pagli, C., Chen, W., Ge, L., Du, Z., Zhang, K., 2018. InSAR Reveals Land Deformation at Guangzhou and Foshan, China between 2011 and 2017 with COSMO-SkyMed Data. Remote Sens. 10, 813. https://doi.org/10.3390/rs10060813

Nguy-Robertson, A.L., 2013. The mathematical identity of two vegetation indices: MCARI2 and MTVI2. Int. J. Remote Sens. 34, 7504–7507. https://doi.org/10.1080/01431161.2013.823525

Nicholson, H.J., 2017. The everyday life of the Templars: The Knights templar at home. Fonthill, Stroud.

Nicholson, P.T., Shaw, I. (Eds.), 2009. Ancient Egyptian materials and technology. Cambridge University Press, Cambridge; UK.

Nsanziyera, A., Rhinane, H., Oujaa, A., Mubea, K., 2018. GIS and Remote-Sensing Application in Archaeological Site Mapping in the Awsard Area (Morocco). Geosciences 8, 207. https://doi.org/10.3390/geosciences8060207

Oliva, P., Viers, J., Dupré, B., 2003. Chemical weathering in granitic environments. Chem. Geol., Controls on Chemical Weathering 202, 225–256. https://doi.org/10.1016/j.chemgeo.2002.08.001

Olson, K.R., Speidel, D.R., 2020. Review and Analysis: Successful Use of Soil Tunnels in Medieval and Modern Warfare and Smuggling. Open J. Soil Sci. 10, 194–215. https://doi.org/10.4236/ojss.2020.105010

Omali, T.U., 2021. Utilization of Remote Sensing and GIS in Geology and Mining. Int. J. Sci. Res. Multidiscip. Stud. 7, 17–24.

Onwuka, B., 2016. Effects of Soil Temperature on Some Soil Properties and Plant Growth. Adv. Plants Agric. Res. 8. https://doi.org/10.15406/apar.2018.08.00288

Ottesen, D., Stewart, M., Brönner, M., Batchelor, C.L., 2020. Tunnel valleys of the central and northern North Sea (56°N to 62°N): Distribution and characteristics. Mar. Geol. 425, 106199. https://doi.org/10.1016/j.margeo.2020.106199

Parcak, S.H., 2009. Satellite remote sensing for archaeology. Routledge, London; New York.

Park, M.K., Park, S., Yi, M.-J., Kim, C., Son, J.-S., Kim, J.-H., Abraham, A.A., 2014. Application of electrical resistivity tomography (ERT) technique to detect underground cavities in a karst area of South Korea. Environ. Earth Sci. 71, 2797–2806. https://doi.org/10.1007/s12665-013-2658-7

Pascucci, S., Cavalli, R.M., Palombo, A., Pignatti, S., 2010. Suitability of CASI and ATM airborne remote sensing data for archaeological subsurface structure detection under different land cover: the Arpi case study (Italy). J. Geophys. Eng. 7, 183–189. https://doi.org/10.1088/1742-2132/7/2/S04

Patruno, J., Dore, N., Crespi, M., Pottier, E., 2013. Polarimetric Multifrequency and Multi-incidence SAR Sensors Analysis for Archaeological Purposes: The UNESCO Sites of Djebel Barkal and Samarra. Archaeol. Prospect. 20, 89–96. https://doi.org/10.1002/arp.1448

Paustian, J.B., 2021. Void Hunting: Ambient Noise Tomography for Spatio-Temporal Subsurface Imaging and Monitoring in Karst Environments (Master of Science in Geophysics). Boise State University, Boise, ID. https://doi.org/10.18122/td.1832.boisestate

Pedley, M.S., 2005. The Commerce of Cartography: Making and Marketing Maps in Eighteenth-Century France and England. University of Chicago Press.

Penuelas, J., Baret, F., Filella, I., 1995. Semi-Empirical Indices to Assess Carotenoids/Chlorophyll-a Ratio from Leaf Spectral Reflectance. Photosynthetica 31, 221–230.

Perez, D., Banerjee, D., Kwan, C., Dao, M., Shen, Y., Koperski, K., Marchisio, G., Li, J., 2017. Deep learning for effective detection of excavated soil related to illegal tunnel activities, in: 2017 IEEE 8th Annual Ubiquitous Computing, Electronics and Mobile Communication Conference (UEMCON). IEEE, New York City, NY, pp. 626–632. https://doi.org/10.1109/UEMCON.2017.8249062

Perrone, A., Lapenna, V., Piscitelli, S., 2014. Electrical resistivity tomography technique for landslide investigation: A review. Earth-Sci. Rev. 135, 65–82. https://doi.org/10.1016/j.earscirev.2014.04.002

Persico, R., Piro, S., Linford, N. (Eds.), 2019. Innovation in near-surface geophysics: instrumentation, application, and data processing methods. Elsevier, Amsterdam, Netherlands; Cambridge, MA.

Peterken, G.F., 2013. Meadows, 1st ed. Bloomsbury Publishing.

Pinty, B., Verstraete, M.M., 1992. GEMI: a non-linear index to monitor global vegetation from satellites. Vegetatio 101, 15–20. https://doi.org/10.1007/BF00031911

Pisani, L., De Waele, J., 2021. Candidate cave entrances in a planetary analogue evaporite karst (Cordillera de la Sal, Chile): A remote sensing approach and ground-truth reconnaissance. Geomorphology 389, 107851. https://doi.org/10.1016/j.geomorph.2021.107851

Pixxel, 2023. Pixxel | Hyperspectral Imagery and Space Data Company [WWW Document]. Seeing Unseen. URL https://www.pixxel.space/ (accessed 9 Jun 23).

Power, D., 2013. Aristocratic Acta in Normandy and England, c. 1150–c. 1250: The Charters and Letters of the Du Hommet Constables of Normandy, in: Anglo-Norman Studies 35. Boydell and Brewer Limited, pp. 259–286. https://doi.org/10.1017/9781782041085.015

Powlesland, D., Lyall, J., Hopkinson, G., Donoghue, D., Beck, M., Harte, A., Stott, D., 2006. Beneath the sand—remote sensing, archaeology, aggregates and sustainability: a case study from Heslerton, the Vale of Pickering, North Yorkshire, UK. Archaeol. Prospect. 13, 291–299. https://doi.org/10.1002/arp.297

Pratt, W.K., 1991. Digital image processing john wiley & sons. Inc N. Y.

Prins, C., Thuro, K., Krautblatter, M., Schulz, R., 2019. Testing the effectiveness of an inverse Wenner-Schlumberger array for geoelectrical karst void reconnaissance, on the Swabian Alb high plain, new line Wendlingen–Ulm, southwestern Germany. Eng. Geol. 249, 71–76. https://doi.org/10.1016/j.enggeo.2018.12.014

Qi, J., Chehbouni, A., Huete, A.R., Kerr, Y.H., Sorooshian, S., 1994. A modified soil adjusted vegetation index. Remote Sens. Environ. 48, 119–126. https://doi.org/10.1016/0034-4257(94)90134-1

Rahtz, P., 1970. Excavations on Glastonbury Tor, Somerset, 1964–6. Archaeol. J. 127, 1–81. https://doi.org/10.1080/00665983.1970.11078389

Rahtz, P., 2002. Glastonbury Tor: A Modified Landscape. Landscapes 3, 4–19. https://doi.org/10.1179/lan.2002.3.1.4

Ramirez, R.A., Lee, G.-J., Choi, S.-K., Kwon, T.-H., Kim, Y.-C., Ryu, H.-H., Kim, S., Bae, B., Hyun, C., 2022. Monitoring of construction-induced urban ground deformations using Sentinel-1 PS-InSAR: The case study of tunneling in Dangjin, Korea. Int. J. Appl. Earth Obs. Geoinformation 108, 102721. https://doi.org/10.1016/j.jag.2022.102721

Ratner, B., 2009. The correlation coefficient: Its values range between +1/−1, or do they? J. Target. Meas. Anal. Mark. 17, 139–142. https://doi.org/10.1057/jt.2009.5

Rees, G., 2001. Physical principles of remote sensing. 2nd ed. Cambridge, U.K; New York, NY: Cambridge University Press.

Ren, T., Ochsner, T., Horton, R., Ju, Z., 2003. Heat-Pulse Method for Soil Water Content Measurement. Soil Sci. Soc. Am. J. 67, 4.

Reynolds, J.M., 1997. An introduction to applied and environmental geophysics. John Wiley, Chichester; New York.

Richemond-Barak, D., 2018. Underground warfare. Oxford University Press, New York, NY.

Robinson, D., 2006. The Cistercians in Wales: Architecture and Archaeology 1130-1540.

Roman, A., Ursu, T.-M., Lăzărescu, V.-A., Opreanu, C.H., Fărcaş, S., 2017. Visualization techniques for an airborne laser scanning-derived digital terrain model in forested steep terrain: Detecting archaeological remains in the subsurface. Geoarchaeology 32, 549–562. https://doi.org/10.1002/gea.21621

Ronchi, D., Limongiello, M., Barba, S., 2020. Correlation among Earthwork and Cropmark Anomalies within Archaeological Landscape Investigation by Using LiDAR and Multispectral Technologies from UAV. Drones 4, 72. https://doi.org/10.3390/drones4040072

Rondeaux, G., Steven, M., Baret, F., 1996. Optimization of soil-adjusted vegetation indices. Remote Sens. Environ. 55, 95–107. https://doi.org/10.1016/0034-4257(95)00186-7

Roslan, S.A., Yakub, F., Rambat, S., Noor, N.M., Saidin, M., 2020. The Integration of Aerial Sensing and Geophysical Techniques to Identify Buried Archaeological Properties in Sungai Batu, Bujang Valley. IOP Conf. Ser. Earth Environ. Sci. 540, 012013. https://doi.org/10.1088/1755-1315/540/1/012013

Ross, S., 1991. History in Hiding: The story of Britain's secret passages and hiding-places. Robert Hale, London.

Roujean, J.-L., Breon, F.-M., 1995. Estimating PAR absorbed by vegetation from bidirectional reflectance measurements. Remote Sens. Environ. 51, 375–384. https://doi.org/10.1016/0034-4257(94)00114-3

Rouse, J., Haas, R.H., Schell, J.A., Deering, D.W., Harlan, J.C., 1973. Monitoring the Vernal Advancements and Retrogradation (Greenwave Effect) of Nature Vegetation.

Rout, G.R., Sahoo, S., 2015. Role of Iron in Plant Growth and Metabolism. Rev. Agric. Sci. 3, 1–24. https://doi.org/10.7831/ras.3.1

Roux-Perino, J., Andoque, N. d', Jachowicz-Davoust, B., 2014. The Cistercians, 2nd ed. ed, In situ. MSM, Vic-en-Bigorre.

Rowlands, A., Sarris, A., 2007. Detection of exposed and subsurface archaeological remains using multi-sensor remote sensing. J. Archaeol. Sci. 34, 795–803. https://doi.org/10.1016/j.jas.2006.06.018

Sabins, F.F., 1997. Remote sensing: principles and interpretation, 3rd ed. ed. W.H. Freeman and Co, New York.

Saha, S.K., 2022. Remote Sensing and Geographic Information System Applications in Hydrocarbon Exploration: A Review. J. Indian Soc. Remote Sens. 50, 1457–1475. https://doi.org/10.1007/s12524-022-01540-9

Sakuma, A., Yamano, H., 2020. Satellite Constellation Reveals Crop Growth Patterns and Improves Mapping Accuracy of Cropping Practices for Subtropical Small-Scale Fields in Japan. Remote Sens. 12, 2419. https://doi.org/10.3390/rs12152419

Sarris, A., Papadopoulos, N., Agapiou, A., Salvi, M.C., Hadjimitsis, D.G., Parkinson, W.A., Yerkes, R.W., Gyucha, A., Duffy, P.R., 2013. Integration of geophysical surveys, ground hyperspectral measurements, aerial and satellite imagery for archaeological prospection of prehistoric sites: the case study of Vésztő-Mágor Tell, Hungary. J. Archaeol. Sci. 40, 1454–1470. https://doi.org/10.1016/j.jas.2012.11.001

Savage, S.H., Levy, T.E., Jones, I.W., 2012. Prospects and problems in the use of hyperspectral imagery for archaeological remote sensing: a case study from the Faynan copper mining district, Jordan. J. Archaeol. Sci. 39, 407–420. https://doi.org/10.1016/j.jas.2011.09.028

Scintrex, 2018. CG-5 Autograv Gavity Meter. Available at: https://scintrexltd.com/wp-content/uploads/2018/11/CG-5-Brochure-R3.pdf

Scoular, J., Ghail, R., Mason, P., Lawrence, J., Bellhouse, M., Holley, R., Morgan, T., 2020. Retrospective InSAR Analysis of East London during the Construction of the Lee Tunnel. Remote Sens. 12, 849. https://doi.org/10.3390/rs12050849

Segal, D., 1982. Theoretical basis for differentiation of ferric-iron bearing minerals, using Landsat MSS data, in: Symposium for Remote Sensing of Environment. Presented at the 2nd Thematic Conference on Remote Sensing for Exploratory Geology, Fort Worth, Texas, p. 951.

Segev, A., Rybakov, M., 2011. History of faulting and magmatism in the Galilee (Israel) and across the Levant continental margin inferred from potential field data. J. Geodyn. 51, 264–284. https://doi.org/10.1016/j.jog.2010.10.001

Senthamarai Kannan, K., Manoj, K., Arumugam, S., 2015. Labeling Methods for Identifying Outliers. Int. J. Stat. Syst. 10, 231–238.

Sharafi, M., Khazaei, S., 2013. Detection of High Local Groundwater Inflow to Rock Tunnels using ASTER Satellite Images. Int. Arch. Photogramm. Remote Sens. Spat. Inf. Sci. XL-1/W3, 393–397. https://doi.org/10.5194/isprsarchives-XL-1-W3-393-2013

Shen, S.S., Roettiger, K.A., 2012. Detection of abandoned mines/caves using airborne LWIR hyperspectral data, in: Shen, S.S., Lewis, P.E. (Eds.), . Presented at the SPIE Optical Engineering + Applications, San Diego, California, USA, p. 85150D. https://doi.org/10.1117/12.946113

Shi, X., Huang, J., Huang, B., 2022. An Underground Abnormal Behavior Recognition Method Based on an Optimized Alphapose-ST-GCN. J. Circuits Syst. Comput. https://doi.org/10.1142/S0218126622502140

Shimoni, M., Haelterman, R., Perneel, C., 2019. Hypersectral Imaging for Military and Security Applications: Combining Myriad Processing and Sensing Techniques. IEEE Geosci. Remote Sens. Mag. 7, 101–117. https://doi.org/10.1109/MGRS.2019.2902525

Shirmard, H., Farahbakhsh, E., Müller, R.D., Chandra, R., 2022. A review of machine learning in processing remote sensing data for mineral exploration. Remote Sens. Environ. 268, 112750. https://doi.org/10.1016/j.rse.2021.112750

Sinclair, T., Andrews, D., 1984. Uplift of Tunnels and Pipes in Soft Clay. Presented at the Conference on Geomechanics, Perth, Australia, pp. 694–698.

Smith, A.M., Bourgeois, G., Teillet, P.M., Freemantle, J., Nadeau, C., 2008. A comparison of NDVI and MTVI2 for estimating LAI using CHRIS imagery: a case study in wheat. Can. J. Remote Sens. 34, 539–548. https://doi.org/10.5589/m08-071

Solymosi, K., Kövér, G., Romvári, R., 2019. The Progression of Vegetation Indices: a Short Overview. Acta Agrar. Kaposváriensis 23. https://doi.org/10.31914/aak.2264

Song, Y., Song, J., 2022. Analysis of surface temperature in an urban area using supervised spatial autocorrelation and Moran's I. Earth Sci Inform 15, 2545–2552. https://doi.org/10.1007/s12145-022-00856-x

Sousa, P.M., Barriopedro, D., García-Herrera, R., Ordóñez, C., Soares, P.M.M., Trigo, R.M., 2020. Distinct influences of large-scale circulation and regional feedbacks in two exceptional 2019 European heatwaves. Commun. Earth Environ. 1. https://doi.org/10.1038/s43247-020-00048-9

Sripada, R.P., Heiniger, R.W., White, J.G., Meijer, A.D., 2006. Aerial Color Infrared Photography for Determining Early In-Season Nitrogen Requirements in Corn. Agron. J. 98, 968–977. https://doi.org/10.2134/agronj2005.0200

Stagakis, S., Markos, N., Sykioti, O., Kyparissis, A., 2010. Monitoring canopy biophysical and biochemical parameters in ecosystem scale using satellite hyperspectral imagery: An application on a Phlomis fruticosa Mediterranean ecosystem using multiangular CHRIS/PROBA observations. Remote Sens. Environ. 114, 977–994. https://doi.org/10.1016/j.rse.2009.12.006

Stott, D., Boyd, D., Beck, A., Cohn, A., 2015. Airborne LiDAR for the Detection of Archaeological Vegetation Marks Using Biomass as a Proxy. Remote Sens. 7, 1594–1618. https://doi.org/10.3390/rs70201594

Stout, G., 2015. The Cistercian grange: a medieval farming system. Agric. Settl. Irel. 28–68.

Stray, G., 2018. Glastonbury Underground: Searching for the Lost Treasure of Avalon. Straydog Books, Glastonbury, UK.

Stray, G., 2025. Glastonbury Dowsing - Accuracy Statement, (pers. comm, 2 October 2025).

Štular, B., Kokalj, Ž., Oštir, K., Nuninger, L., 2012. Visualization of lidar-derived relief models for detection of archaeological features. J. Archaeol. Sci. 39, 3354–3360. https://doi.org/10.1016/j.jas.2012.05.029

Sun, H., Zhang, N., Li, D., Liu, S., Ye, Q., 2023. The first semi-airborne transient electromagnetic survey for tunnel investigation in very complex terrain areas. Tunn. Undergr. Space Technol. 132, 104893. https://doi.org/10.1016/j.tust.2022.104893

Supandi, S., 2021. Geotechnical profiling of a surface mine waste dump using 2D Wenner–Schlumberger configuration. Open Geosci. 13, 335–344. https://doi.org/10.1515/geo-2020-0234

Surmely, F., Chalin, J.-B., 2019. 3D Laser Scanning Contributions Toward Understanding and Preserving Medieval Tunnels of the French Massif Central. Lang. Lit. Cult., American Association for Science and Technology 2, 73–80.

Susantoro, T.M., Wikantika, K., Saepuloh, A., Harsolumakso, A.H., 2018. Selection of vegetation indices for mapping the sugarcane condition around the oil and gas field of North West Java Basin, Indonesia. IOP Conf. Ser. Earth Environ. Sci. 149, 012001. https://doi.org/10.1088/1755-1315/149/1/012001

Tan, K., Wan, Y., Zhou, X., Song, D., Duan, Q., 2006. The application of remote sensing technology in the archaeological study of the Mausoleum of Emperor Qinshihuang. Int. J. Remote Sens. 27, 3347–3363. https://doi.org/10.1080/01431160600554389

Tapete, D., Cigna, F., 2019. COSMO-SkyMed SAR for Detection and Monitoring of Archaeological and Cultural Heritage Sites. Remote Sens. 11, 1326. https://doi.org/10.3390/rs11111326

Themistocleous, K., Hadjimitsis, D.G., Melillos, G., 2018. Thermal remote sensing approach combined with field spectroscopy for detecting underground structures intended for defence and security purposes in Cyprus, in: Isaacs, J.C., Bishop, S.S. (Eds.), Detection and Sensing of Mines, Explosive Objects, and Obscured Targets XXIII. SPIE, Orlando, United States, p. 1. https://doi.org/10.1117/12.2303835

Thenkabail, P.S. (Ed.), 2024. Remote Sensing Handbook: Image Processing, Change Detection, GIS, and Spatial Data Analysis; Volume II, Second edition. ed. CRC Press, Taylor & Francis Group, Boca Raton.

Thenkabail, P.S., Gumma, M.K., Teluguntla, P., Awad, M., Jomaa, I., Arab, F., Zhang, C., Sánchez, N., Piles, M., Martínez-Fernández, J., Vall-llossera, M., Pipia, L., Camps, A., Aguasca, A., Pérez-Aragüés, F., Herrero, C.M., Marshall, M., Thenkabail, P., Saini, M., Christian, B., Joshi, N., Vyas, D., Marpu, P., Nadiminti, K., Aasen, H., Gnyp, M.L., Miao, Y., Bareth, G., Parshakov, I., Coburn, C., Staenz, K., 2014. 697 Hyperspectral Remote Sensing of Vegetation and Agricultural Crops. Photogramm. Eng.

Thenkabail, P.S., Lyon, J.G., Huete, A. (Eds.), 2012. Hyperspectral remote sensing of vegetation. CRC Press, Boca Raton, FL.

Thenkabail, P.S., Mariotto, I., Gumma, M.K., Middleton, E.M., Landis, D.R., Huemmrich, K.F., 2013. Selection of Hyperspectral Narrowbands (HNBs) and Composition of Hyperspectral Twoband Vegetation Indices (HVIs) for Biophysical Characterization and Discrimination of Crop Types Using Field Reflectance and Hyperion/EO-1 Data. IEEE J. Sel. Top. Appl. Earth Obs. Remote Sens. 6, 427–439. https://doi.org/10.1109/JSTARS.2013.2252601

Thenkabail, P.S., Smith, R.B., De Pauw, E., 2000. Hyperspectral Vegetation Indices and Their Relationships with Agricultural Crop Characteristics. Remote Sens. Environ. 71, 158–182. https://doi.org/10.1016/S0034-4257(99)00067-X

Thompson, J., Marvin, M., Club-Fellow, E., 2005. Experimental Research on the Use of Thermography to Locate Heat Signatures from Caves. National Cave and Karst Management Symposium. 102-115.

Thorp, K.R., French, A.N., Rango, A., 2013. Effect of image spatial and spectral characteristics on mapping semi-arid rangeland vegetation using multiple endmember spectral mixture analysis (MESMA). Remote Sens. Environ. 132, 120–130. https://doi.org/10.1016/j.rse.2013.01.008

Tobin, S., 1995. The Cistercians: monks and monasteries of Europe. Herbert, London.

Torrese, P., 2025. Near-surface cavity detection using ambient noise-based microseismic analysis in highly urbanized historical settings. J. Appl. Geophys. 241, 105858. https://doi.org/10.1016/j.jappgeo.2025.105858

Trier, Ø.D., Pilø, L.H., 2012. Automatic Detection of Pit Structures in Airborne Laser Scanning Data: Automatic detection of pits in ALS data. Archaeol. Prospect. 19, 103–121. https://doi.org/10.1002/arp.1421

Trier, Ø.D., Zortea, M., Tonning, C., 2015. Automatic detection of mound structures in airborne laser scanning data. J. Archaeol. Sci. Rep. 2, 69–79. https://doi.org/10.1016/j.jasrep.2015.01.005

Tucker, C.J., 1979. Red and photographic infrared linear combinations for monitoring vegetation. Remote Sens. Environ. 8, 127–150. https://doi.org/10.1016/0034-4257(79)90013-0

Tukey, J.W., 1970. Exploratory Data Analysis, Limited Preliminary Edition. ed. Addison-Wesley Publishing Company, Reading, Massachusetts.

UK Environment Agency, 2025a. 20250324-Glastonbury_DTM_1m_RFI-Adam_Morley-U, (pers. comm, 24 March 2025).

UK Environment Agency, 2025b. Geomatics LiDAR Accuracy Statement.

Ulusoy, İ., Labazuy, P., Aydar, E., 2012. STcorr: An IDL code for image-based normalization of lapse rate and illumination effects on nighttime TIR imagery. Comput. Geosci. 43, 63–72. https://doi.org/10.1016/j.cageo.2012.02.012

Ur, J., 2003. CORONA Satellite Photography and Ancient Road Networks: A Northern Mesopotamian Case Study. Antiquity 77, 102–115. https://doi.org/10.1017/S0003598X00061391

Urwin, J.H., 1936. Secret hiding places and underground passages. Billing and Sons Ltd, Guildford and Esher.

USGS, 1977. Water Dowsing. Available at: https://pubs.usgs.gov/gip/water_dowsing/pdf/water_dowsing.pdf.

Van der Meer, F., Hecker, C., van Ruitenbeek, F., van der Werff, H., de Wijkerslooth, C., Wechsler, C., 2014. Geologic remote sensing for geothermal exploration: A review. Int. J. Appl. Earth Obs. Geoinformation 33, 255–269. https://doi.org/10.1016/j.jag.2014.05.007

Van Niel, T.G., McVicar, T.R., Li, L., Gallant, J.C., Yang, Q., 2008. The impact of misregistration on SRTM and DEM image differences. Remote Sens. Environ. 112, 2430–2442. https://doi.org/10.1016/j.rse.2007.11.003

Verhoeven, G., Doneus, M., Atzberger, C., Wes, M., Ruš, M., Pregesbauer, M., Briese, C., 2013. New approaches for archaeological feature extraction of airborne imaging spectroscopy data, in: 10th International Conference on Archaeological Prospection. Austrian Academy of Sciences, pp. 13–15.

Verhoeven, G.J., 2012. Near-Infrared Aerial Crop Mark Archaeology: From its Historical Use to Current Digital Implementations. J. Archaeol. Method Theory 19, 132–160. https://doi.org/10.1007/s10816-011-9104-5

Vickery, A., Hobbs, B., 2002. The effect of subsurface pipes on apparent resistivity measurements. Eur. Assoc. Geosci. Eng. 50, 1–13.

Viezzoli, A., Christiansen, A.V., Auken, E., Sørensen, K., 2008. Quasi-3D modeling of airborne TEM data by spatially constrained inversion. Geophysics, 73, F105–F113. https://doi.org/10.1190/1.2895521

Vincent, N. (Ed.), 2021. The Letters and Charters of Henry II: King of England 1154-1189, First edition. ed. Oxford University Press, Oxford.

Vinesta, P., Milton-Joe, M., 2019. A Novel Modified Sobel Algorithm for Better Edge Detection of Various Images. Int. J. Emerg. Technol. Eng. Res. 7, 25–31.

Wainwright, F.T., 1953. Souterrains in Scotland. Antiquity 27, 219–232. https://doi.org/10.1017/S0003598X00025084

Wakefield, J., 1814. The Avalonian Guide to the town of Glastonbury and its Environs (1814). Kessinger Publishing.

Walter, C.A., Braun, A., Fotopoulos, G., 2019. Impact of three-dimensional attitude variations of an unmanned aerial vehicle magnetometry system on magnetic data quality. Geophys. Prospect. 67, 465–479. https://doi.org/10.1111/1365-2478.12727

Wang, W., Zhao, W., Huang, L., Vimarlund, V., Wang, Z., 2014. Applications of terrestrial laser scanning for tunnels: a review. J. Traffic Transp. Eng. Engl. Ed. 1, 325–337. https://doi.org/10.1016/S2095-7564(15)30279-8

Wang, Y., Khorrami, M., Tran, K.T., Horhota, D., 2023. Application of ambient noise tomography for deep void detection. J. Appl. Geophys. 209, 104922. https://doi.org/10.1016/j.jappgeo.2022.104922

Wang, Y., Tian, F., Huang, Y., Wang, J., Wei, C., 2015. Monitoring coal fires in Datong coalfield using multi-source remote sensing data. Trans. Nonferrous Met. Soc. China 25, 3421–3428. https://doi.org/10.1016/S1003-6326(15)63977-2

Waters, C.N., Graham, C., Tapete, D., Price, S.J., Field, L., Hughes, A.G., Zalasiewicz, J., 2019. Recognizing anthropogenic modification of the subsurface in the geological record. Q. J. Eng. Geol. Hydrogeol. 52, 83–98. https://doi.org/10.1144/qjegh2017-007

Waters, P., Greenbaum, D., Smart, P.L., Osmaston, H., 1990. Applications of remote sensing to groundwater hydrology. Remote Sens. Rev. 4, 223–264. https://doi.org/10.1080/02757259009532107

Weather Online, 2025. Weather Online. URL https://www.weatheronline.co.uk/ (accessed 2 Sep 25).

Webb, J.E., 1966. The Search for Iron Ore, Eyre Peninsula, South Australia†, in: Mining Geophysics Volume 1, Case Histories. Society of Exploration Geophysicists.

Weber, S.A., Yool, S.R., 1999. Detection of subsurface archaeological architecture by computer assisted airphoto interpretation. Geoarchaeology 14, 481–493. https://doi.org/10.1002/(SICI)1520-6548(199908)14:6<481::AID-GEA1>3.0.CO;2-3

Weishampel, J., Hightower, J., Chase, A., Chase, D., Patrick, R., 2011. Detection and Morphologic Analysis of Potential Below-Canopy Cave Openings in the Karst Landscape around the Maya Polity of Caracol using Airborne Lidar. J. Cave Karst Stud. 73, 187–196. https://doi.org/10.4311/2010EX0179R1

Werner, M., 2021. Caen – The Artists – Boudan, Louis. Travel Inf. Tips Fr. URL https://travelfrance.tips/caen-the-artists-boudan-louis/ (accessed 27 Jul 25).

White, A., Wilkinson, P., Boyd, J., Wookey, J., Kendall, J.M., Binley, A., Grossey, T., Chambers, J., 2023. Combined electrical resistivity tomography and ground penetrating radar to map Eurasian badger (Meles Meles) burrows in clay-rich flood embankments (levees). Eng. Geol. 323, 107198. https://doi.org/10.1016/j.enggeo.2023.107198

Wiig, F., Harrower, M., Braun, A., Nathan, S., Lehner, J., Simon, K., Sturm, J., Trinder, J., Dumitru, I., Hensley, S., Clark, T., 2018. Mapping a Subsurface Water Channel with X-Band and C-Band Synthetic Aperture Radar at the Iron Age Archaeological Site of ‘Uqdat al-Bakrah (Safah), Oman. Geosciences 8, 334. https://doi.org/10.3390/geosciences8090334

Wingfield, G., 2018. Glastonbury Isle of Avalon, 2nd ed. Wooden Books Ltd, Glastonbury, Somerset, UK.

Wright, J., 2021. The Tintern Tunnels - Triskele Heritage [WWW Document]. Mediev. Myth. Blog 5 Tintern Tunn. URL https://triskeleheritage.triskelepublishing.com/mediaeval-mythbusting-blog-5-the-tintern-tunnels/ (accessed 25 Jul 25).

Wynn, J.C., 1986. A review of geophysical methods used in archaeology. Geoarchaeology 1, 245–257. https://doi.org/10.1002/gea.3340010302

Wynne, J.J., Jenness, J., Sonderegger, D.L., Titus, T.N., Jhabvala, M.D., Cabrol, N.A., 2021. Advancing Cave Detection Using Terrain Analysis and Thermal Imagery. Remote Sens. 13, 3578. https://doi.org/10.3390/rs13183578

Wynne, J.J., Titus, T.N., Chong Diaz, G., 2008. On developing thermal cave detection techniques for earth, the moon and mars. Earth Planet. Sci. Lett. 272, 240–250. https://doi.org/10.1016/j.epsl.2008.04.037

Xu, X., Li, W., Ran, Q., Du, Q., Gao, L., Zhang, B., 2018. Multisource Remote Sensing Data Classification Based on Convolutional Neural Network. IEEE Trans. Geosci. Remote Sens. 56, 937–949. https://doi.org/10.1109/TGRS.2017.2756851

Xu, Y., Sun, D., Zeng, Z., Lv, H., 2019. Effect of temperature on thermal conductivity of lateritic clays over a wide temperature range. Int. J. Heat Mass Transf. 138, 562–570. https://doi.org/10.1016/j.ijheatmasstransfer.2019.04.077

Xue, J., Su, B., 2017. Significant Remote Sensing Vegetation Indices: A Review of Developments and Applications. J. Sens. 2017, 1353691. https://doi.org/10.1155/2017/1353691

Xue, W., Zhang, L., Mou, X., Bovik, A.C., 2014. Gradient Magnitude Similarity Deviation: A Highly Efficient Perceptual Image Quality Index. IEEE Trans. Image Process. 23, 684–695. https://doi.org/10.1109/TIP.2013.2293423

Yokoyama, R., Shirasawa, M., Pike, R., 2002. Visualizing Topography by Openness: A New Application of Image Processing to Digital Elevation Models. Photogramm. Eng. Remote Sens. 68, 257–265.

Young, G., 2024. 20240927-LiDAR Data_Carn_Euny-RFI-Adam_Morley-U, [Carn Euny HE Data, Historic England], (pers. comm, 27 September 2024).

Yuan, X., Chakravarty, A., Gu, L., Wei, Z., Lichtenberg, E., Chen, T., 2025. An Empirical Study of Methods for Small Object Detection from Satellite Imagery. https://doi.org/10.48550/arXiv.2502.03674

Zahorec, P., Papčo, J., Vajda, P., Szabó, S., 2019. High-precision local gravity survey along planned motorway tunnel in the Slovak Karst. Contrib. Geophys. Geod. 49, 207–227. https://doi.org/10.2478/congeo-2019-0011

Zaigham Abbas Naqvi, S.M., Awais, M., Khan, F.S., Afzal, U., Naz, N., Khan, M.I., 2021. Unmanned air vehicle based high resolution imagery for chlorophyll estimation using spectrally modified vegetation indices in vertical hierarchy of citrus grove. Remote Sens. Appl. Soc. Environ. 23, 100596. https://doi.org/10.1016/j.rsase.2021.100596

Zakšek, K., Oštir, K., Kokalj, Ž., 2011. Sky-View Factor as a Relief Visualization Technique. Remote Sens. 3, 398–415. https://doi.org/10.3390/rs3020398

Zanni, S., De Rosa, A., 2019. Remote Sensing Analyses on Sentinel-2 Images: Looking for Roman Roads in Srem Region (Serbia). Geosciences 9, 25. https://doi.org/10.3390/geosciences9010025

Zeng, S., Jiang, Y., Wu, Z., Zhang, C., Lv, T., 2023. Declining trees growth and vegetation productivity resulting from decreasing soil water contents induced by tunnels excavation in karst mountain areas. Ecol. Indic. 154, 110555. https://doi.org/10.1016/j.ecolind.2023.110555

Zhang, R., Bao, X., Hong, R., He, X., Yin, G., Chen, J., Ouyang, X., Wang, Y., Liu, G., 2024. Soil moisture retrieval over croplands using novel dual-polarization SAR vegetation index. Agricultural Water Management 306, 109159. https://doi.org/10.1016/j.agwat.2024.109159

Zhang, T., Zhang, C., Long, D., Wang, Y., Zhou, H., Wang, S., Li, G., Li, H., Zhou, F., Jiang, C., 2023. Application of Helicopter-Borne and Ground–Airborne Electromagnetic Detection to Tunnel Engineering Investigation. Appl. Sci. 13, 1886. https://doi.org/10.3390/app13031886

Zhao, J., Huang, L., Yang, H., Zhang, D., Wu, Z., Guo, J., 2016. Fusion and assessment of high-resolution WorldView-3 satellite imagery using NNDiffuse and Brovey algotirhms, in: 2016 IEEE International Geoscience and Remote Sensing Symposium. Presented at the IGARSS 2016, IEEE, Beijing, China, pp. 2606–2609. https://doi.org/10.1109/IGARSS.2016.7729673

Zhao, X., Dong, J., Yu, Y., Liao, M., Zhang, L., Gong, J., 2025. A review of SAR tomography. Geo-Spat. Inf. Sci. 1–44. https://doi.org/10.1080/10095020.2025.2510365